STRUCTURAL & GEOTECHNICAL ENGINEERING LABORATORY

LARGE-SCALE TESTING OF STEEL-REINFORCED CONCRETE (SRC) COUPLING BEAMS EMBEDDED INTO REINFORCED CONCRETE STRUCTURAL WALLS

Christopher J. Motter

John W. Wallace

University of California, Los Angeles
Department of Civil & Environmental Engineering

David C. Fields

John D. Hooper

Ron Klemencic

Magnusson Klemencic Associates, Inc.

Sponsor:

CHARLES PANKOW FOUNDATION
Building Innovation through Research

UCLA - SGEL
Report 2013/06

Large-Scale Testing of Steel-Reinforced Concrete (SRC) Coupling Beams Embedded into Reinforced Concrete Structural Walls

Christopher J. Motter
Department of Civil and Environmental Engineering
University of California, Los Angeles

David C. Fields
Magnusson Klemencic Associates, Inc.

John D. Hooper
Magnusson Klemencic Associates, Inc.

Ron Klemencic
Magnusson Klemencic Associates, Inc.

John W. Wallace
Department of Civil and Environmental Engineering
University of California, Los Angeles

Report to Charles Pankow Foundation
School of Engineering and Applied Science
University of California, Los Angeles

December 2013 Final Draft

ABSTRACT

Reinforced concrete structural walls provide an efficient lateral system for resisting seismic and wind loads. Coupling beams are commonly used to connect adjacent collinear structural walls to enhance building lateral strength and stiffness. Steel-Reinforced Concrete (SRC) coupling beams provide an alternative to reinforced concrete coupling beams, diagonally-reinforced for shorter spans and longitudinally-reinforced for longer spans, and offer potential advantages of reduced section depth, reduced congestion at the wall boundary region, improved degree of coupling for a given beam depth, and improved deformation capacity.

Four large-scale, flexure-yielding, cantilever SRC coupling beams embedded into reinforced concrete structural walls were tested by applying quasi-static, reversed-cyclic loading to the coupling beam (shear) and the top of the wall (moment, shear, and constant axial load) to create cyclic tension and compression fields across the embedment region. The primary test variables were the structural steel section embedment length, beam span length (aspect ratio), quantities of wall boundary longitudinal and transverse reinforcement, and applied wall loading (moment, shear, and axial load). Based on test results, long embedment length, sufficient wall boundary reinforcement, and low-to-moderate wall demands across the embedment region are all associated with favorable coupling beam performance, characterized by minimal pinching and strength degradation in the load-deformation response and plastic hinge formation at the beam-wall interface with a lack of damage (plasticity) in the embedment region. The variation in aspect ratio was not found to significantly affect performance.

Detailed design and modeling recommendations for steel reinforced concrete (SRC) coupling beams are provided for both code-based (prescriptive) design and alternative (non-prescriptive) design. For both code-based and alternative design, modeling a rigid beam for flexure and shear deformations with rotational springs at the beam-wall interfaces is recommended for stiffness, as test results indicate that the majority of the coupling beam deformations were associated with interface slip/extension. Alternative stiffness modeling recommendations are provided, in which an effective bending stiffness that accounts for the aspect ratio or beam length is used instead of interface rotational springs. A capacity design approach, in which the provided embedment strength exceeds the expected beam strength, is recommended for determining the required embedment length of the steel section into the structural wall. Recommendations for computing the nominal and expected (upper bound) flexure and shear strengths are provided. For alternative design, additional parameters are provided to define the strength and deformation capacity (to complete the backbone relations) and to address cyclic degradation for each of the test beams.

ACKNOWLEDGEMENTS

The Charles Pankow Foundation provided funding for the development of this document (Grant No. 02-08). This support is gratefully acknowledged, with special thanks extended to Dr. Robert Tener, former Executive Director of the Charles Pankow Foundation, Mark Perniconi, the current Executive Director of the Charles Pankow Foundation, and Dean Browning, the Project Director for the Charles Pankow Foundation.

Laboratory testing was conducted in the Structural/Earthquake Engineering Research Laboratory at UCLA. Thanks are extended to Charles Pankow Builders for construction of the test specimens. Material donations from Herrick Steel are also greatly appreciated. Special thanks are extended to Steve Keowen, Alberto Salamanca, and Harold Kasper for their help with the test set-up and testing. Anne Lemnitzer, Chris Segura, Chris Hilson, Ryon Marapao, Luis Herrera, Ian Wallace, Charys Clay, Kelsey Sakamoto, and Estefan Garcia are thanked for their assistance with the construction and/or testing phase of the research. Testing was performed in a collaboratory renovated with funds provided by the National Science Foundation under Grant No. 0963183, which is an award funded under the American Recovery and Reinvestment Act of 2009 (ARRA). Any opinions, findings, and conclusions expressed in this material are those of the authors and do not necessarily reflect those of the National Science Foundation.

TABLE OF CONTENTS

LIST OF FIGURES

LIST OF TABLES

LIST OF SYMBOLS

$(EA)_{eff}$	coupling beam effective elastic shear stiffness
$(EI)_{eff}$	coupling beam effective elastic bending stiffness
A	cross-sectional area
a	distance from the point of shear load application to the beam-wall or beam-column interface for a cantilever test beam, i.e., the cantilever length
a_1	depth of uniform magnitude (Whitney) stress block, determined as the product of the neutral axis depth, x, and the ACI stress block factor, β_1
A_1	effective rotational stiffness term used for backbone modeling, expressed as K / M_{pe}
A_2	effective bending stiffness term used for backbone modeling, expressed as $(EI)_{eff}$ / $E_s I_{trans}$
a_c	length of the concrete bearing zone for a steel beam embedded through a reinforced concrete column (i.e., a reinforced concrete column to steel beam connection)
A_{cv}	area of concrete section of structural wall resisting shear
A_f	flange area of steel section
A_g	area of a gross reinforced concrete section, neglecting the impact of reinforcement (i.e., not considering a transformed section)
A_s	area of wall longitudinal reinforcement
A_{sc}	cross-sectional area of a stud shear connector
A_{st}	area of transverse reinforcement provided at a center-to-center spacing of s

A_{tb} required area of transfer reinforcement for steel or SRC coupling beams, to be attached at each of the top and bottom flange locations at each of two regions, the first of which is located at the longitudinal wall reinforcement closest to the face of the wall and the second of which is located at a distance no less than one-half the depth of the steel section (d/2) from the end of the embedded member

A_w area of steel section resisting shear, taken as the product of the section depth, d, and web thickness, t_w

b bearing width for a steel section embedded into a reinforced concrete member (e.g., column or wall)

B_1 load at yield plateau used for backbone modeling, expressed as M / M_{pe} or V / $V@M_{pe}$

b_c width of an SRC coupling beam, taken as the width of concrete encasement

b_{eff} effective bearing width for a steel section embedded into a reinforced concrete member (e.g., column or wall), measured to the outside of the confining hoops and ties in the reinforced concrete member

b_f flange width of steel section

b_j' effective joint width for a steel beam embedded through a reinforced concrete column (i.e., a reinforced concrete column to steel beam connection)

b_w width (thickness) of a reinforced concrete wall into which the steel section of an SRC coupling beam is embedded

c for a steel section embedded into a reinforced concrete member (e.g., column or wall), the clear cover measured from the edge of the concrete member to the outside of the transverse reinforcement (at the boundary for walls) if present or to

the outside of the outermost longitudinal reinforcement if transverse reinforcement is not present

C resultant compressive force

C_1 strength drop for backbone modeling, expressed as expressed as M / M_{pe} or V / $V@M_{pe}$

C_b resultant concrete bearing force developed within the embedment region of a steel section embedded into a reinforced concrete member (e.g., column or wall), located near the back of the embedded steel section, and acting normal to the flange of the embedded steel section

C_c resultant concrete compressive force

Cc_1 resultant compression force in concrete cover, used when computing M_p or M_{pe} using plastic section analysis for an SRC coupling beam

Cc_2 resultant compression force in concrete at depth of steel flange, used when computing M_p or M_{pe} using plastic section analysis for an SRC coupling beam

Cc_3 resultant compression force in concrete at depth of steel web, used when computing M_p or M_{pe} using plastic section analysis for an SRC coupling beam

C_f resultant concrete bearing force developed within the embedment region of a steel section embedded into a reinforced concrete member (e.g., column or wall), located near the front of the embedded steel section, and acting normal to the flange of the embedded steel section

Cs_f resultant tension force in web of steel section, used when computing M_p or M_{pe} using plastic section analysis for an SRC coupling beam

Cs_w	resultant tension force in web of steel section, used when computing M_p or M_{pe} using plastic section analysis for an SRC coupling beam
d	depth (height) of steel section
D_1	for backbone modeling, the chord rotation (in radians) over which the strength drop, C_1, occurs
d_b	nominal bar diameter of reinforcement
d_c	depth of longitudinal tension reinforcement in an SRC coupling beam cross-section, measured from the extreme concrete compression fiber to the center of the longitudinal tension reinforcement
E	modulus of elasticity
e	distance from the applied beam shear load to the center of the embedment length (either modified or unmodified for concrete spalling at the beam-wall or beam-column interface) for a cantilever steel section embedded into a reinforced concrete member (e.g. column or wall)
E_c	modulus of elasticity of concrete
E_s	modulus of elasticity of steel
e_{wall}	distance of eccentrically applied structural wall axial load from the edge of the wall during SRC coupling beam testing
f'_c	specified compressive strength of concrete
$f'_{c,test}$	as-tested compressive strength of concrete
f'_{ce}	expected compressive strength of concrete
f_b	concrete bearing strength in the embedment region of a steel section embedded into a reinforced concrete member (e.g. column or wall)

f_c	concrete compressive stress
$F_{lat.}$	wall lateral shear load
F_s	steel stress
F_u	specified minimum tensile strength of structural steel
$f_{u,test}$	as-tested tensile strength of reinforcement
$F_{u,test}$	as-tested tensile strength of structural steel
F_{uc}	specified minimum tensile strength of a stud shear connector
F_{ue}	expected tensile strength of structural steel
F_y	specified minimum yield strength of structural steel
f_y	specified yield strength of reinforcement
$f_{y,test}$	as-tested yield strength of reinforcement
$F_{y,test}$	as-tested yield strength of structural steel
f_{ye}	expected yield strength of reinforcement
F_{ye}	expected yield strength of structural steel
f_{yt}	specified yield strength of transverse reinforcement
f_{ytb}	specified yield strength of transfer reinforcement attached to the flanges of an SRC coupling beam
f_{yte}	expected yield strength of transverse reinforcement
G_s	shear modulus of steel
h	the overall section depth of an SRC coupling beam, taken as the section height of concrete encasement
h_c	depth (height) of reinforced concrete column
h_w	structural wall height

h_x maximum center-to-center horizontal spacing of crossties or hoop legs

I moment of inertia

$I_{g,c}$ moment of inertia of a gross reinforced concrete section, neglecting the impact of reinforcement (i.e., not considering a transformed section)

$I_{g,s}$ moment of inertia of a steel section, neglecting the impact of reinforced concrete encasement for an SRC coupling beam

I_{trans} moment of inertia of an SRC coupling beam computed using a transformed section, with concrete in compression transformed into an equivalent area of steel based on the modular ratio of steel to concrete, and neglecting concrete tensile strength, i.e., neglecting cracked concrete

k ratio of applied wall shear load, V_{wall}, to applied beam shear load, V_{beam}, during testing of SRC coupling beams

K stiffness of rotational springs located at the beam-wall interfaces of an SRC coupling beam which are used to model slip/extension, with the stiffness expressed in units of interface moment per radian or per unit chord rotation

k' a modification factor used when computing an effecting bending stiffness, $(EI)_{eff}$, for a steel or SRC coupling beam to account for shear deformations when modeling shear stiffness as rigid

k_b the ratio of the distance from the embedded end to the resultant back bearing force to the distance from the embedded end to the neutral axis of the embedment length, x_b, for a steel section embedded into a reinforced concrete member (e.g., column or wall)

L coupling beam clear span, measured as the distance between the beam-wall interfaces

L_c coupling beam effective clear span, computed based on increasing the clear span, L, to account for spalling of wall clear cover, c, at the beam-wall interfaces

L_e embedment length of a steel section embedded into a reinforced concrete member (e.g., column or wall), measured from the beam-wall interface to the embedded end of the steel section

$L_{e,c}$ effective embedment length of the steel section of an SRC coupling beam into the structural wall, determined based on modification of the embedment length, L_e, to account for spalling of wall cover concrete, c

L_{eff} coupling beam effective clear span, computed based on taking fixity at $L_e/3$ or $0.3L_e$ within the beam-wall interfaces in order to account for gapping between the flange of the steel section and the bearing concrete in the portion of the embedment regions near the beam-wall interfaces and the associated lack of fixity at the beam-wall interfaces

l_w structural wall length

$L_{w,avg}$ average length of two walls coupled by a coupling beam

M moment

$M@V_{ne,limit}$ moment developed in an SRC coupling beam at the beam-wall interfaces when the limiting shear strength, $V_{ne,limit}$, of the coupling beam is reached

M_n nominal flexural strength of an SRC coupling beam

M_p nominal plastic flexural strength of an SRC coupling beam cross-section

M_{pe} expected plastic flexural strength of an SRC coupling beam cross-section

M_u required flexural strength (factored moment)

M_{wall} applied wall moment

M_y flexural yielding strength of an SRC coupling beam, determined using plane-strain moment-curvature analysis

M_{y1} flexural strength of a structural wall at first yield of reinforcement (i.e., when the outermost longitudinal wall bar reaches yield), determined using plane-strain moment-curvature analysis (considering the wall axial load)

P axial load

P_{cyclic} reversed cyclic wall axial load applied during coupling beam testing

$P_{gravity}$ constant wall axial load applied during coupling beam testing

P_u required axial strength (factored axial force)

P_{wall} applied wall axial load

Q_n nominal strength of one stud shear connector embedded in solid concrete

Q_{total} total nominal strength of stud shear connectors

R_t ratio of the expected tensile strength of structural steel F_{ue}, to the specified minimum tensile strength of structural steel, F_u

R_y ratio of the expected yield strength of structural steel, F_{ye}, to the specified minimum yield strength of structural steel, F_y

s center-to-center spacing of transverse reinforcement

T resultant tensile force

t thickness of a reinforced concrete member (e.g., column or wall) into which a steel section is embedded

t_f flange thickness of steel section

T_f	resultant tension force in flange of steel section, used when computing M_p or M_{pe} using plastic section analysis for an SRC coupling beam
t_w	web thickness of steel section
T_w	resultant tension force in web of steel section, used when computing M_p or M_{pe} using plastic section analysis for an SRC coupling beam
V	shear force
$V@M_n$	SRC coupling beam shear force developed when the nominal flexural strength, M_n, is developed at the beam-wall interfaces and the nominal plastic flexural strength, M_p, is developed at $L_e/3$ inside of the beam-wall interfaces
$V@M_p$	SRC coupling beam shear force developed when the nominal plastic flexural strength, M_p, is developed at the beam-wall interfaces
$V@M_{pe}$	SRC coupling beam shear force developed when the expected flexural strength, M_{pe}, is developed at the beam-wall interfaces
$V@M_y$	SRC coupling beam shear force developed when the flexural yielding strength, M_y, is developed at the beam-wall interfaces
V_b	beam shear load
V_{beam}	applied beam shear load
$V_{c,wall}$	contribution to nominal shear strength of a structural wall provided by concrete
V_{fiber}	the shear strength of an SRC coupling beam computed using fiber modeling
V_n	nominal shear strength of an SRC coupling beam cross-section, including the contribution of structural steel, concrete, and transverse reinforcement to shear strength

$V_{n(ACI)}$ The nominal shear strength of a diagonally-reinforced concrete coupling beam determined using ACI 318-08

$V_{n,embed}$ the embedment strength of a steel section embedded into a reinforced concrete member (e.g., column or wall), which is the peak beam shear load that the embedment can resist

$V_{n,embed,test}$ the peak embedment strength measured during testing for a steel section embedded into a reinforced concrete member (e.g., column or wall)

$V_{n,wall}$ nominal shear strength of a structural wall

V_{ne} expected shear strength of an SRC coupling beam cross-section, including the contribution of structural steel, concrete, and transverse reinforcement

$V_{ne,embed(M\&G)}$ the embedment strength of an SRC coupling beam determined based on the Mattock and Gaafar (1982) approach

$V_{ne,embed(M\&M)}$ the embedment strength of an SRC coupling beam determined based on the Marcakis and Mitchell (1980) approach

$V_{ne,limit}$ limiting shear strength of an SRC coupling beam, taken as the smaller of V_{ne} (the expected shear strength) and $V@M_{pe}$ (the coupling beam shear force developed when the expected flexural strength, M_{pe}, is developed at the beam-wall interfaces)

V_p nominal shear strength of a steel section, used to determine the shear strength of an SRC coupling beam

V_p' maximum shear capacity of a steel section, taken as 1.25 times the nominal shear strength of the steel section

V_{RC} the nominal shear strength of the reinforced concrete encasement used in an SRC coupling beam, including the contribution of concrete and transverse reinforcement

$V_{s,wall}$ contribution to nominal shear strength of a structural wall provided by reinforcement

V_{steel} the nominal shear strength of the steel beam used in an SRC coupling beam

V_{test} the peak shear strength of an SRC coupling beam measured during testing

V_{wall} applied wall shear load

x neutral axis depth, which is the distance from the extreme compression fiber to the neutral axis

x_b distance from the embedded end to the neutral axis of the embedment length for a steel section embedded into a reinforced concrete member (e.g., column or wall)

Z_x plastic section modulus (about x-axis) of a steel section

α the span-to-depth (aspect) ratio of an SRC coupling beam, i.e., the ratio of the clear span, L, to the overall beam height including concrete encasement, h

α_b ratio of equivalent stress to specified compressive strength of concrete, f'_c, for an equivalent stress block located along the back portion of a steel section embedded into a reinforced concrete member (e.g., column or wall) and acting normal to the embedment length

α_c coefficient defining the relative contribution of concrete strength to nominal wall shear strength

β_1 ACI stress block factor, taken as the ratio of the uniform magnitude (Whitney) stress block depth, a_1, to the neutral axis depth, x

β_b ratio of the equivalent stress block depth to the distance from the embedded end to the neutral axis of the embedment length, x_b, for an equivalent stress block located along the back portion of a steel section embedded into a reinforced concrete member (e.g., column or wall) and acting normal to the embedment length

δ coupling beam lateral displacement

$\delta_{applied}$ displacement applied to coupling beam during testing

$\delta_{measured}$ cantilever coupling beam lateral displacement measured during testing

$\delta_{relative}$ cantilever coupling beam lateral displacement, adjusted relative to the measured displacement, $\delta_{meas.}$, to include the effects of wall deformation, δ_{wall}

δ_{shear} vertical coupling beam displacement at point of cantilever load application due to shear deformation only

δ_{wall} cantilever coupling beam lateral displacement due to wall deformation

ε_0 concrete compressive strain corresponding to the specified compressive strength of concrete, f'_c

$\varepsilon_{0,test}$ concrete compressive strain corresponding to the as-tested compressive strength of concrete, $f'_{c,test}$

ε_b concrete compressive strain at the embedded end of a steel section embedded into a reinforced concrete member (e.g., column or wall)

ε_c concrete compressive strain

ε_s steel strain

$\varepsilon_{s,bl}$ maximum tensile strain on wall longitudinal reinforcement at the location of the embedded SRC coupling beam, computed as the mean of the maximum for the building model subjected to the requisite number of base acceleration histories

$\varepsilon_{s,max}$ maximum tensile strain on wall longitudinal reinforcement at the location of the embedded SRC coupling beam, determined analytically based on plane-strain moment-curvature analysis of the structural wall for the observed maximum structural wall loading demands

ε_y yield strain of wall boundary longitudinal reinforcement

θ coupling beam chord rotation

$\theta_{p,bl}$ maximum plastic rotation of wall at the location of the embedded SRC coupling beam, computed as the mean of the maximum for the building model subjected to the requisite number of base acceleration histories

θ_w wall rotation

θ_y coupling beam chord rotation at yield

$\theta_{y,w}$ wall yield rotation

λ the cross-section shape factor for shear, taken as 1.5 for W-shapes

λ_c modification factor reflecting the reduced mechanical properties of light-weight concrete relative to normal-weight concrete of the same compressive strength

μ statistical average

ρ_{bound} the wall boundary longitudinal reinforcement ratio, taken as the total area of wall boundary longitudinal reinforcement divided by the gross concrete area of the wall boundary

ρ_l ratio of area of distributed wall longitudinal reinforcement to gross area of concrete perpendicular to that reinforcement

ρ_t ratio of area of distributed wall transverse reinforcement to gross area of concrete perpendicular to that reinforcement

σ	statistical standard deviation
φ	strength reduction factor
ϕ	curvature

1 Introduction

This chapter provides background information, including the motivation and objectives for the research, and a brief summary of report organization.

1.1 BACKGROUND

For reinforced concrete residential and office building construction, use of coupled walls (often core walls) along with post-tensioned floor slabs and gravity columns is very common because it minimizes story heights and provides for a flexible floor plan. Use of a post-tensioned floor slab allows for slab span-to-depth ratios of 40 to 45 (CRSI, 2008). Use of coupling beams is required for taller buildings to increase the lateral stiffness to meet code drift limits and to provide a mechanism to dissipate energy due to earthquakes. Coupling beams provide an effective means to resist overturning moment due to lateral loading, as a portion of the total overturning moment is resisted though axial tension-compression couples between coupled wall piers, which form as a result of the vertical forces imparted to the walls due to beam shear (Figure 1.1). Harries (2001) refers to the "degree of coupling" as the ratio of moment demand resisted by coupling action to the total moment demand resisted by both coupling action and the individual wall piers.

The ductility capacity of a coupled wall system increases with increasing degrees of coupling (Harries, 1998), and the degree of coupling is often designed to achieve a target value.

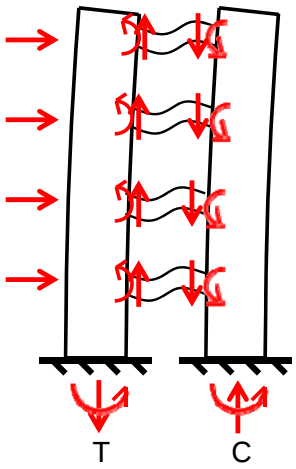

Figure 1.1: Coupled Wall Behavior

The preferred overall behavior of coupled walls subjected to Design Earthquake (DE) or Maximum Considered Earthquake (MCE) shaking involves yielding of coupling beams over the full building height and yielding at the base of the individual wall piers (Paulay, 1986). Because coupling beams tend to be much weaker than the large wall sections they connect, and due to geometric considerations, coupling beams yield prior to yielding at the base of wall piers and are subjected to large inelastic rotational demands. The coupling beams act as fuses to limit the lateral force demands on a building and dissipate earthquake energy. Favorable performance of coupling beams is characterized by large inelastic deformation capacity (large ductility) and stable energy dissipation with minimal post-yield strength degradation and pinching of load-deformation behavior, in addition to predictable strength and stiffness.

Design of reinforced concrete coupling beams is currently based on ACI 318-11 code provisions. The coupling beam length-to-depth (aspect) ratio typically dictates whether the member will be controlled by yielding in flexure or shear, with longer aspect ratio beams yielding in flexure and shorter aspect ratio beams yielding in shear. ACI 318-11 Section 21.9.7.2 requires the use of diagonal reinforcement (Figure 1.2) in reinforced concrete coupling beams when shear demand is high ($> 4\sqrt{f'_c}$) and aspect ratio is low (< 2.0). For cases in which the reinforced concrete coupling beam aspect ratio is large ($\geq$ 4.0), ACI 318-11 Section 21.9.7.1 (which references Section 21.5) specifies that straight bars be used, since the diagonal reinforcement becomes less effective at a low angle of inclination. For cases in which the coupling beam aspect ratio is between two and four, ACI 318-11 Section 21.9.7.3 allows the use of either straight or diagonal reinforcement. Recent tests show that coupling beams constructed with diagonal or straight reinforcement maintain reliable strength through loading cycles at 6% or 4% beam chord rotation, respectively (Naish et al, 2009 and Naish et al, 2013a).

Figure 1.2: Diagonally-Reinforced Concrete Coupling Beam

(photo courtesy of NEESR at the University of Michigan)

Although diagonally-reinforced concrete coupling beams are frequently used in mid- and high-rise buildings to resist lateral loads due to earthquakes, the congestion associated with

embedding diagonal coupling beam reinforcement into RC wall boundary zones creates constructability challenges, thereby increasing construction time and cost. Additionally, as coupling beams are typically located between vertically stacked door or corridor openings, story height limits beam depth, which may lead to heavily reinforced members in order to achieve the desired flexural capacity. The use of steel reinforced concrete (SRC) coupling beams (Figure 1.3) provides a viable design alternative to conventionally- or diagonally-reinforced concrete coupling beams since use of an SRC coupling beam reduces section depth, simplifies construction (and reduces cost) by reducing congestion in the wall boundary zone, improves the degree of coupling for a given beam depth, and offers potentially superior ductility.

A steel-reinforced concrete (SRC) coupling beam refers to a structural steel coupling beam encased with reinforced concrete and embedded into the boundary zones of reinforced concrete structural walls. An SRC coupling beam may also be referred to as a "concrete-encased steel coupling beam" or simply "composite coupling beam." The embedded steel sections transfer coupling forces to structural walls through bearing, which avoids the need for welded and bolted connections while benefiting from the ductility of properly selected structural steel sections. Encasing the steel wide-flange section in concrete provides greater stability against buckling, which results in increased beam deformation capacity prior to strength degradation.

Figure 1.3: Steel Reinforced Concrete (SRC) Coupling Beam

(photo courtesy of Magnusson Klemencic Associates)

Although neither the ACI 318-11 (concrete) nor the 2010 AISC (steel) building codes include provisions for SCR coupling beams, the 2010 AISC *Seismic Provisions for Structural Steel Buildings* (referred to simply as the "2010 AISC Seismic Provisions" for the remainder of this manuscript) provide design guidelines, including recommendations for computing SRC coupling beam strength (flexure and shear), effective (elastic) stiffness, embedment length into the structural walls, and embedment detailing requirements. With regard to embedment detailing, AISC requires the use of auxiliary transfer bars attached perpendicular to the flanges of the steel section and the use of face bearing plates (Figure 1.4), both of which assist with load transfer between the embedded steel section and the structural wall. Face bearing plates are welded to the steel section, whereas the auxiliary transfer bars may be welded or attached using mechanical half-couplers. A more extensive overview of the requirements provided in the 2010 AISC Seismic Provisions as related to SRC coupling beams is provided in Chapter 2.

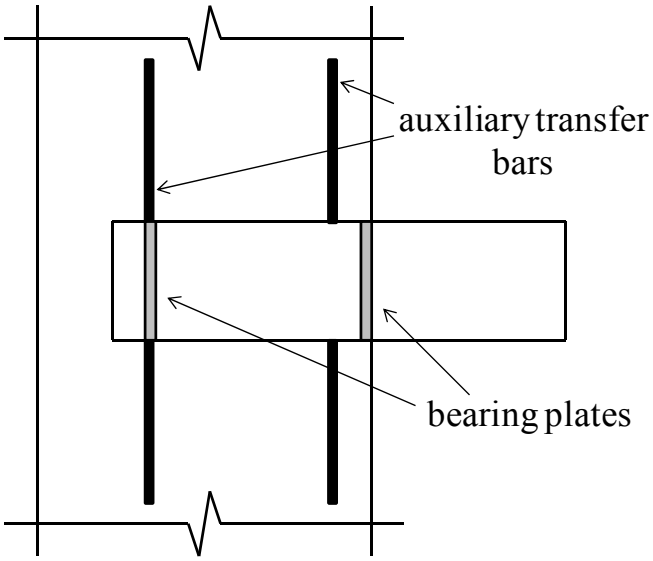

Figure 1.4: Face Bearing Plates and Auxiliary Transfer Bars

Another alternative to diagonally-reinforced concrete coupling beams is steel-plate reinforced concrete coupling beams, in which a vertical steel plate is used to provide a ductile shear-yielding mechanism for the member. Since the steel plate contributes less flexural strength than an I-beam, straight reinforcement is often used (as needed) to increase the flexural capacity of the member, in order to ensure shear-yielding behavior.

1.2 OBJECTIVES AND SCOPE

Prior tests conducted to assess the behavior and design of SRC coupling beams, which were the basis for the design equation provided in the 2010 AISC Seismic Provisions to determine the required embedment length of the steel section into the structural wall, were often conducted at relatively small-scale (e.g., 9-in steel section depth with a section weight of 27-plf (pounds per

linear foot) for Shahrooz et al, 1993; 6-in steel section depth with a section weight of 20-plf for Gong and Shahrooz, 2001a,b,c). To assess whether it is appropriate to extrapolate these results on small-scale test specimens to beams with much larger cross-sections, this research study strives to assess the validity of the available embedment equations at the largest scale possible given laboratory constraints (determined to be about one-half scale).

Additionally, prior tests were often conducted for steel sections embedded into walls or reaction blocks that did not accurately represent local stress/strain fields within the embedment region (Harries et al, 1993; Harries et al, 1997; Gong and Shahrooz, 2001a; Fortney et al, 2007). Because local stress/strain fields could impact the required embedment length, the test set-up used for this study was designed to include a wall subjected to lateral loading (shear), moment, and axial load to more realistically represent embedment region conditions (Figure 1.5).

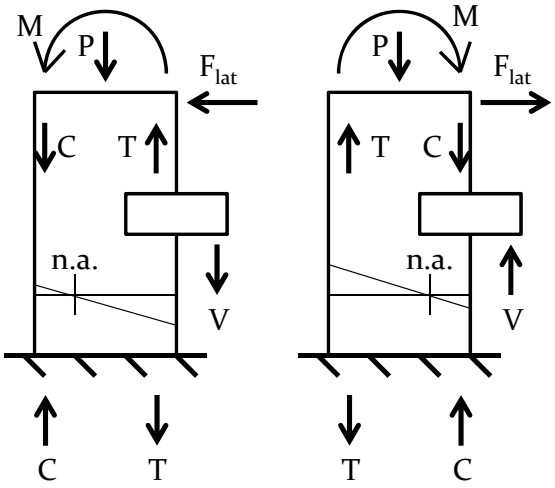

Figure 1.5: Wall Strains at Embedment Zone

The auxiliary transfer bars and face bearing plates (Figure 1.4), mandated by the 2010 AISC Seismic Provisions within the embedment zone of SRC coupling beams, provide an additional beam-to-wall force-transfer mechanism other than bearing. Because existing embedment models suggest that providing sufficient embedment length enables load transfer through bearing alone, transfer bars and bearing plates, which increase construction costs, were not used in the test beams in this study, in an effort to assess whether or not (or under what conditions) these details are necessary.

Nonlinear modeling of coupling beams has become increasingly important as performance-based design of tall core-wall buildings has become more commonplace. Modeling parameters to formulate backbone curves for diagonally-reinforced concrete coupling beams are provided in FEMA 356 (2000), ASCE 41-06 (2007), and Naish et al (2013b); however, similar parameters for SRC coupling beams are not currently available to practicing engineers. In this study, experimental results are used to develop appropriate nonlinear modeling parameters. Current SRC coupling beam recommendations (2010 AISC Seismic Provisions) for effective stiffness and member strength suggest symmetric load-displacement response. However, because cyclic wall loading creates alternating compression and tension demands acting normal to the embedment length (Figure 1.5), beam strength and stiffness may be larger with compression, rather than tension, acting across the embedment length. If testing demonstrates that the asymmetry is significant, modeling recommendations should be developed to reflect this asymmetry.

Based on the preceding discussion, the primary objectives of this SRC coupling beam research are to:

(1) Design and test specimens that explore limitations of prior research on SRC coupling beams, particularly with regard to embedment length and load transfer to structural walls.

(2) Test at the largest scale feasible (limited by laboratory constraints and other test objectives) in order to assess the reliability of embedment models at realistic scale.

(3) Embed the SRC coupling beams into reinforced concrete structural walls in order to apply reversed-cyclic loading to the structural wall (in addition to the coupling beam) in order to create realistic boundary conditions, i.e., alternating compression/tension normal to the embedment length (Figure 1.5).

(4) Test flexure-yielding members, since the recommendations in the 2010 AISC Seismic Provisions for computing the capacity of flexure-yielding members, unlike for shear-yielding members, are not currently supported by test data.

(5) Develop stiffness and strength recommendations and compare to these recommendations with commonly used recommendations (e.g., 2010 AISC Seismic Provisions).

(6) Use load-displacement responses obtained through testing to provide modeling recommendations, including backbone modeling recommendations of the type presented in ASCE 41-06 (2007), that may be used by practicing engineers for conducting nonlinear analysis of coupled core-wall structures.

(7) Assess the need for auxiliary transfer bars and bearing plates in the embedment zone.

(8) Provide improved design guidelines that practicing engineers may use when designing SRC coupling beams.

With these objectives in mind, four one-half scale SRC coupling beams, embedded into reinforced concrete structural walls, were designed, constructed, and tested in the UCLA Structural Earthquake Engineering Research Laboratory. Testing was quasi-static, with reversed-cyclic loading applied to the coupling beam, while simultaneous constant axial load and reversed-cyclic loading (moment and shear) was applied to the structural wall in order to simulate the effects of cyclic wall compression/tension normal to the embedment length (Figure 1.5).

1.3 ORGANIZATION

This report is organized into eight chapters and two appendices. The introduction provided in Chapter 1 is followed by a literature review of SRC coupling beams in Chapter 2, which includes a summary of existing design guidelines (2010 AISC Seismic Provisions). The design of the test specimens is presented in Chapter 3, while the experimental program, including details of the test set-up and testing protocol, is summarized in Chapter 4. Chapter 5 presents the test results obtained from the experimental program. Chapter 6 provides code-based (prescriptive) design recommendations while Chapter 7 provides alternative (non-prescriptive) design recommendations, which include backbone curves that may be used to conduct nonlinear analysis of structures with SRC coupling beams, intended for use by practicing engineers designing SRC coupling beams. Chapter 8 provides conclusions and recommendations.

Material testing results are provided in Appendix A, while Appendix B provides a sample computation for SRC coupling beam flexural strength.

2 Literature Review

This chapter provides a synopsis of previous research related to reinforced concrete coupling beams with embedded structural steel I-beams (either rolled wide-flange sections or built-up sections) and is divided into four sections. The first section (Section 2.1) provides a summary of the development of the embedment length equations, while the second section (Section 2.2) provides an overview of previous testing programs and design recommendations relevant to SRC coupling beams. The third section (Section 2.3) provides an overview of the design recommendations for SRC coupling beams provided in the 2010 AISC Seismic Provisions, and the final section (Section 2.4) provides a brief summary of this chapter.

2.1 EMBEDMENT LENGTH

For SRC coupling beams, the strength of the beam-to-wall connection is dependent on the embedment length, L_e, of the steel section into the wall. Adequate embedment length is defined here as the length necessary to create reliable transfer of forces from the beam to the wall without excessively damaging the wall. This section provides a summary of the development of the Mattock and Gaafar (1980) and Marcakis and Mitchell (1982) load transfer models (Figure 2.1) to determine the required embedment length. Although these embedment models were

developed based on the transfer of forces from unencased cantilever steel sections to reinforced concrete columns, the force transfer mechanism is effectively the same as for steel or SRC coupling beams embedded into reinforced concrete structural walls. These embedment models and the corresponding embedment equations are used as the basis for determining the required embedment of SRC coupling beams into structural walls.

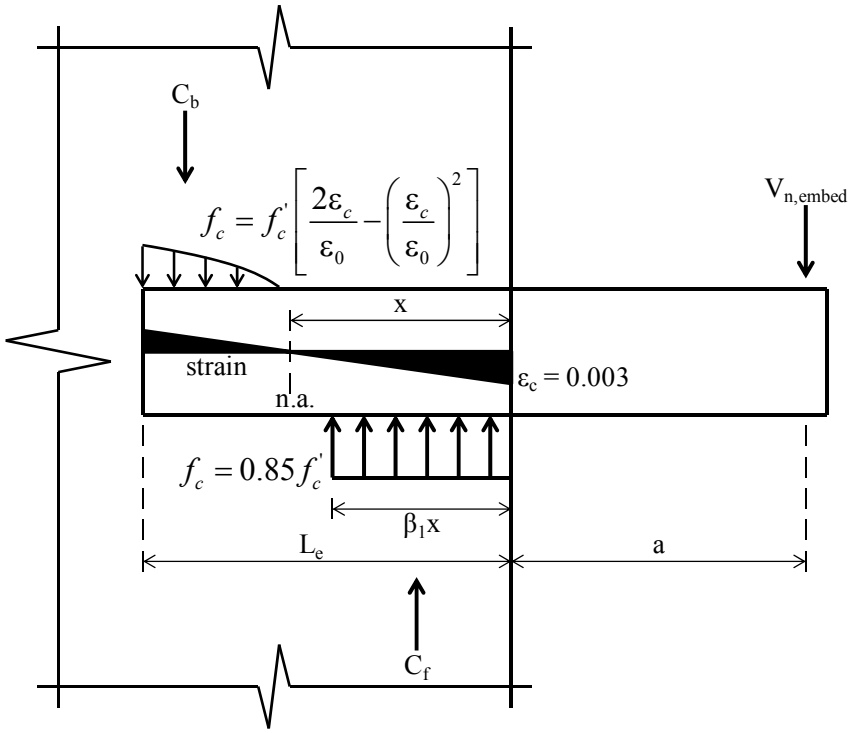

Figure 2.1: Marcakis and Mitchell (1980) and Mattock and Gaafar (1982) Embedment Model

Both the Marcakis and Mitchell (1980) and Mattock and Gaafar (1982) embedment models (Figure 2.1) are based on satisfying force and moment equilibrium of the embedded member, where the embedment strength, $V_{n,embed}$, is expressed as a shear force applied on a cantilever beam a distance, a, from the beam-wall interface. Both models assume a linear strain distribution in the embedment region with a strain of 0.003 at the outer face, from which a

uniform magnitude (Whitney) stress block, with a stress magnitude of $0.85f'_c$, where f'_c is the specified strength of concrete, is assumed along the front portion of the embedded member. The ACI stress block factor, β_1, is used to relate the depth of the Whitney stress block to the neutral axis depth, x. The following parabolic stress-strain relationship (Hognestad, 1955) is used to determine the stress distribution along the back portion of the embedded member (since the peak strain at the back end of the embedded member is less than 0.003, negating the use of a Whitney stress block):

$$f_c = f_c^{'}\left[2\frac{\varepsilon_c}{\varepsilon_0} - \left(\frac{\varepsilon_c}{\varepsilon_0}\right)^2\right] \tag{2.1}$$

where ε_0 is the strain corresponding to f'_c, and f_c is the concrete compressive stress computed at the strain of interest, ε_c. If material testing data are unavailable for concrete, a value of 0.002 is often assumed for ε_0 and was used by Mattock and Gaafar (1982) to simplify the Hognestad (1955) stress-strain relationship as follows:

$$f_c = 1000 f_c^{'}\left[\varepsilon_c(1 - 250\varepsilon_c)\right] \tag{2.2}$$

Marcakis and Mitchell (1980) replaced the parabolic stress distribution at the back of the connection with an equivalent uniform stress distribution for convenience. The equivalent distribution has a uniform stress of $\alpha_b f'_c$ acting over a depth of $\beta_b x_b$, measured from the back of the embedment, where x_b is the distance from the back end of the embedded member to the

neutral axis, and the stress block factors, α_b and β_b, are determined from the following relationships:

$$\alpha_b \beta_b = \frac{\varepsilon_b}{\varepsilon_0} - \frac{1}{3}\left(\frac{\varepsilon_b}{\varepsilon_0}\right)^2 \tag{2.3}$$

$$\beta_b = \frac{4 - \frac{\varepsilon_b}{\varepsilon_o}}{6 - 2\frac{\varepsilon_b}{\varepsilon_o}} \tag{2.4}$$

where ε_b is the strain at the back of the connection. Noting that the magnitude and location are identical for the equivalent and parabolic stress distributions, the resultant force at the back of the connection, C_b, and the distance of this force from the back of the connection, $\beta_b/2$, expressed as a fraction of x_b, are computed as:

$$C_b = \alpha_b f_c^{'} b \beta_b x_b \tag{2.5}$$

$$\frac{\beta_b}{2} = \frac{1 - \frac{\varepsilon_b}{4\varepsilon_o}}{3 - \frac{\varepsilon_b}{\varepsilon_o}} \tag{2.6}$$

respectively, where b is the bearing width, with further explanation provided later in this section.

Mattock and Gaafar (1982) similarly replaced the parabolic stress distribution at the back of the connection with a resultant force vector. The magnitude, C_b, and the distance from the back of the connection, k_b, expressed as a fraction of x_b, are computed as:

$$C_b = \frac{500}{3} f_c^{'}[3\varepsilon_b - 500\varepsilon_b{}^2]x_b b \tag{2.7}$$

$$k_b = \frac{1 - 0.375\left(\frac{L_e}{x} - 1\right)}{3 - 1.5\left(\frac{L_e}{x} - 1\right)} \tag{2.8}$$

respectively. Taking ε_0 = 0.002 within the Marcakis and Mitchell (1980) approach and recognizing that $\varepsilon_b = 0.003(L_e - x)/x$ demonstrates that the resultant back bearing force, C_b, and its location for both the Marcakis and Mitchell (1980) and Mattock and Gaafar (1982) embedment models are equivalent.

For both the Marcakis and Mitchell (1980) and the Mattock and Gaafar (1982) embedment models, the front bearing force, C_f, which is located at $\beta_1 x/2$ from the beam-wall interface, is computed as:

$$C_f = 0.85 f_c^{'} \beta_1 x b \tag{2.9}$$

Based on a free body diagram of the embedded member, force and moment equilibrium may be used to determine the neutral axis depth and the embedment strength for a given embedment length and cantilever distance. Although a convenient closed-form solution cannot be obtained, Marcakis and Mitchell (1980) noted that the following two equations, based on force and moment equilibrium, respectively, could be used to solve for the two unknowns (x and $V_{n,embed}$):

$$V_{n,embed} = C_f - C_b = 0.85 f_c' b \beta_1 x - \alpha_b f_c' b \beta_b x_b \tag{2.10}$$

$$\begin{aligned} V_{n,embed} a &= C_b (L_e - \beta_b x_b / 2) - C_f (\beta_1 x / 2) \\ &= (\alpha_b f_c' b \beta_b x_b)(L_e - \beta_b x_b / 2) - 0.85 f_c' b \beta_1 x (\beta_1 x / 2) \end{aligned} \tag{2.11}$$

Alternatively, Mattock and Gaafar (1982) provided a third-order equation to solve for the neutral axis depth as:

$$\begin{aligned} &1.7\beta_1 \left(\frac{x}{L_e}\right)^2 \left[\frac{a}{L_e} + \frac{\beta_1}{2}\left(\frac{x}{L_e}\right)\right] \\ &\quad - \left(1 - \frac{x}{L_e}\right)^2 \left[\left(\frac{a}{L_e} + 1\right)\left(4.5 - 1.5\frac{L_e}{x}\right) - \left(1 - \frac{x}{L_e}\right)\left(1.375 - 0.375\frac{L_e}{x}\right)\right] = 0 \end{aligned} \tag{2.12}$$

which may then be used to compute the embedment strength as:

$$V_{n,embed} = 0.85 f_c' \beta_1 b L_e \left(\frac{x}{L_e}\right) \left[\frac{1 - k_b\left(1 - \frac{x}{L_e}\right) - \frac{\beta_1}{2}\left(\frac{x}{L_e}\right)}{1 - k_b\left(1 - \frac{x}{L_e}\right) + \frac{a}{L_e}}\right] \tag{2.13}$$

noting that this expression for $V_{n,embed}$ was determined by summing moments about C_b (Mattock and Gaafar, 1982).

Recognizing the need for a convenient design equation, Mattock and Gaafar (1982) conducted a sensitivity study on the ratio of neutral axis depth to embedment length, x/L_e. For this study, the ratio of cantilever length to embedment length was varied between 0.1 and 0.5 for a range of f'_c

values between 4000 and 7000 psi. The average value of neutral axis to embedment length was found to be 0.66 with a coefficient of variation of 3.5%. Due to the minor variance in this parameter over a practical range of values, Mattock and Gaafar (1982) modeled this ratio as a constant, using 0.66. This led to the following preliminary expression to compute embedment strength:

$$V_{n,embed} = 0.85 f_c' \beta_1 b L_e \left(\frac{0.58 - 0.22\beta_1}{0.88 + a / L_e} \right) \tag{2.14}$$

Although not specifically noted by Mattock and Gaafar (1982), it is interesting to note that the associated ratio of the front bearing force to the embedment capacity, $C_f/V_{n,embed}$, is:

$$\frac{C_f}{V_{n,embed}} = \left[\frac{1 - k_b \left(1 - \frac{x}{L_e} \right) - \frac{\beta_1}{2} \left(\frac{x}{L_e} \right)}{1 - k_b \left(1 - \frac{x}{L_e} \right) + \frac{a}{L_e}} \right]^{-1} \tag{2.15a}$$

$$\frac{C_f}{V_{n,embed}} = \left(\frac{0.88 - 0.33\beta_1}{0.88 + a / L_e} \right)^{-1} = \left[\frac{1}{0.66} \left(\frac{0.58 - 0.22\beta_1}{0.88 + a / L_e} \right) \right]^{-1} \tag{2.15b}$$

and, similarly, by force equilibrium (i.e., $C_f = C_b + V_{n,embed}$), the ratio of the back bearing force to the embedment capacity, $C_b/V_{n,embed}$, is:

$$\frac{C_b}{V_{n,embed}} = \frac{C_f}{V_{n,embed}} - 1 = \left[\frac{1 - k_b\left(1 - \frac{x}{L_e}\right) - \frac{\beta_1}{2}\left(\frac{x}{L_e}\right)}{1 - k_b\left(1 - \frac{x}{L_e}\right) + \frac{a}{L_e}} \right]^{-1} - 1 \qquad (2.16a)$$

$$\frac{C_b}{V_{n,embed}} = \frac{C_f}{V_{n,embed}} - 1 = \left(\frac{0.88 - 0.33\beta_1}{0.88 + a / L_e} \right)^{-1} - 1 = \left(\frac{a / L_e + 0.33\beta_1}{0.88 - 0.33\beta_1} \right) \qquad (2.16b)$$

The ratio $C_b/V_{n,embed}$ in Equation (2.16b) is used in Section 6.4.1 to develop a design recommendation related to the magnitude of the back bearing force, C_b.

Both pairs of researchers (Marcakis and Mitchell (1980) and Mattock and Gaafar (1982)) used test results to calibrate embedment strength design equations. Marcakis and Mitchell (1980) tested 25 steel sections embedded into reinforced concrete columns. The small-scale test specimens included four (4) HSS4x4x1/4, thirteen (13) HSS6x4x3/8, two (2) W6x25 with flanges trimmed to 4" (corresponding to ~W6x18 in terms of section depth and section weight), three (3) 4"x4" steel bars, and three (3) 3/4"x4" steel plates. The primary test variables were column axial load, connection width, influence of auxiliary transfer bars (attached to the embedded steel section in the embedment zone), shape of embedded member, and eccentricity of loading. All specimens were loaded monotonically to failure. Additional details may be found in Marcakis and Mitchell (1980) and Marcakis (1979).

Mattock and Gaafar (1982) tested five steel sections embedded into 10"x12" concrete columns with four #6 bars as longitudinal reinforcement and #3 hoops spaced at 8" as transverse reinforcement. The small-scale steel specimens included the following: two (2) rectangular

sections with (width x height) dimensions 2"x4.45" and 5"x3.24"; two (2) I-beams both with 4" height, 3" flange width and 1" flange and web thicknesses; and one (1) wide-flange section with 6" depth and 4" flange width with a section weight of approximately 12-plf (i.e., ~W6x12 in terms of depth and weight). All members had a 6" cantilever length and a 10" embedment length, except for the wide-flange member, which had an 8" cantilever length and an 8" embedment length. All specimens were loaded monotonically to failure. Additional details may be found in Mattock and Gaafar (1982).

Marcakis and Mitchell (1980) used test results to plot the normalized connection strength, $V_{n,embed}/(\varphi f'_c b L_e)$, as a function of the normalized cantilever length, a/L_e, noting that φ is the strength reduction factor. Slightly conservative curve-fitting led to the following design equation:

$$V_{n,embed} = \frac{0.85 f'_c b_{eff} L_e}{1 + 3.6e / L_e} \tag{2.17}$$

where $e=a+L_e/2$ and the bearing width, b, is taken as the effective width, b_{eff}, which accounts for load spreading. During testing, Marcakis and Mitchell (1980) observed spalling of cover concrete to the outside of the column confining ties in the connection region, indicating load spreading to this effective width. For cases in which the confined width significantly exceeds the embedded member width, they estimated the limits of load spreading to be 3.2 times the width of the embedded member. For design purposes, Marcakis and Mitchell (1980) suggested taking the effective width, b_{eff}, as the width of the confined region, not to exceed 2.5 times the width of the embedded member.

To account for the effects of confinement (i.e., similar to the load spreading / effective width concept), Mattock and Gaafar (1982) considered an increase in connection bearing stress due to lateral confining effects. Transverse reinforcement in the RC column was provided as #3 hoops spaced at 8", which was close to the minimum amount required by ACI 318-77. By assuming that an increase in bearing stress is proportional to an increase in connection capacity, Mattock and Gaafar (1982) calculated the bearing strength, f_b, based on the measured embedment strength, $V_{n,embed,test}$, as follows:

$$\frac{f_b}{0.85f_c^{'}} = \frac{V_{n,embed,test}}{V_{n,embed}} \tag{2.18}$$

Curve-fitting to test results produced the following expression to determine the bearing stress as a function of the ratio b_f/t:

$$\frac{f_b}{0.85f_c^{'}} = \left(\frac{b_f}{t}\right)^{-0.66} \tag{2.19}$$

where b_f is the width of the embedded section and t is the column width. This led to the modified design equation, accounting for the effects of lateral confinement:

$$V_{n,embed} = 0.85f_c^{'}\left(\frac{t}{b_f}\right)^{0.66} \beta_1 b_f L_e \left(\frac{0.58-0.22\beta_1}{0.88+a/L_e}\right) \tag{2.20}$$

In this expression, the bearing width, b, is essentially represented by an effective width of $b_f(t/b_f)^{0.66}$.

Mattock and Gaafar (1982) noted that the research of Kriz and Raths (1963), Hawkins (1970), and Williams (1979) suggested that concrete bearing strength under strip loading is proportional to concrete tensile strength rather than compressive strength. In keeping with Kriz and Raths (1963) and Hawkins (1970), the tensile strength of concrete was assumed proportional to $\sqrt{f_c'}$. Assuming f'_c=4-ksi, Mattock and Gaafar (1982) presented the following design equation:

$$V_{n,embed} = 54\sqrt{f_c'}\left(\frac{t}{b_f}\right)^{0.66} \beta_1 b_f L_e \left(\frac{0.58 - 0.22\beta_1}{0.88 + a/L_e}\right) \tag{2.21}$$

Because both embedment models were based on the same assumptions, leading to identical free-body diagrams, the Marcakis and Mitchell (1980) and Mattock and Gaafar (1982) design equations yield similar results, particularly when f'_c is around 4.0-ksi. Note that the primary difference between the two equations is the use of f'_c versus $\sqrt{f_c'}$. Since Mattock and Gaafar (1982) established the relationship between $0.85f'_c$ and $54\sqrt{f_c'}$ using f'_c = 4.0-ksi, the use of $\sqrt{f_c'}$ causes the Mattock and Gaafar (1982) embedment equation to be more conservative than the Marcakis and Mitchell (1980) equation for increasing f'_c greater than 4.0-ksi.

Harries et al (1993) and Harries et al (2000) recommended modifying the embedment model to include the effects of concrete spalling at the face of the connection (Figure 2.2). Spalled

concrete serves to increase the cantilever distance and reduce the embedment length. The degree of spalling depends upon the confinement provided.

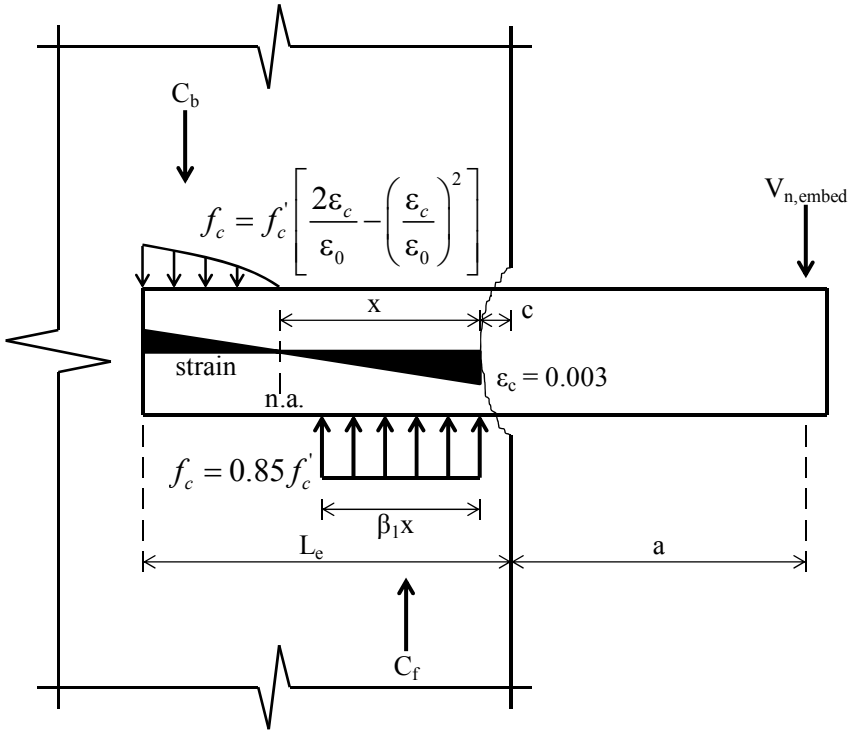

Figure 2.2: Modified Embedment Model to Account for Concrete Spalling

The Marcakis and Mitchell (1980) embedment equation modified to include spalling is as follows:

$$V_{n,embed} = \frac{0.85 f_c' b_{eff} (L_e - c)}{1 + 3.6\left(\frac{e}{(L_e - c)}\right)} \tag{2.22}$$

where $e=a+c+(L_e-c)/2$ and c is the distance of concrete spalling taken as the concrete clear cover to the outermost layer of transverse reinforcement. It is noted that the modified Marcakis and Mitchell (1980) embedment equation provided by Harries et al (1993) and Harries et al (2000) explicitly includes a strength reduction factor, φ, that was excluded in Equation (2.22).

Similarly, the Mattock and Gaafar (1982) embedment equation modified to include spalling is:

$$V_{n,embed} = 54\sqrt{f_c'}\left(\frac{t}{b_f}\right)^{0.66}\beta_1 b_f (L_e - c)\left(\frac{0.58 - 0.22\beta_1}{0.88 + (a+c)/(L_e - c)}\right) \tag{2.23}$$

It is noted that the modified Mattock and Gaafar (1982) embedment equation provided by Harries et al (2000) implicitly includes a strength reduction factor, $\varphi = 0.9$, that was not included in Equation (2.23). The expression provided by Harries (2000) should include modification of a and L_e, to $a + c$ and $L_e - c$, respectively, to be consistent with the embedment model presented for the modified Mattock and Gaafar (1982) approach which includes spalling (i.e., Figure 8 in Harries et al, 2000). It is noted that the embedment equation provided in the 2010 AISC Seismic Provisions (Equation H4-2 in Section H4.5b(1)(3) with modification per Section H4.5b(2)(2); Equation (2.35) in this document) is consistent with Equation (2.23). Additional details on the 2010 AISC Seismic Provisions, including this equation, are provided in Section 2.3.

2.2 EXPERIMENTAL STUDIES

Design recommendations for moment connections between steel beams and reinforced concrete columns were provided by Deierlein et al (1989) and ASCE (1994) based on 15 tests conducted on two-third-scale specimens under either monotonic or reversed-cyclic loading using the test set-up shown in Figure 2.3 (Sheikh et al, 1989; Sheikh, 1987; Deierlein, 1988). The specimens were composite in the sense that a steel beam was embedded through a reinforced concrete column; however, the beam itself was not composite, since it was not encased in concrete. In order to study joint strength, beam flexural and shear strengths were designed to exceed joint strength, with some joints designed to fail in panel shear and others in bearing. The joints failing in bearing were of particular interest within the scope of this research, since the mechanism is similar to that for embedded steel coupling beams.

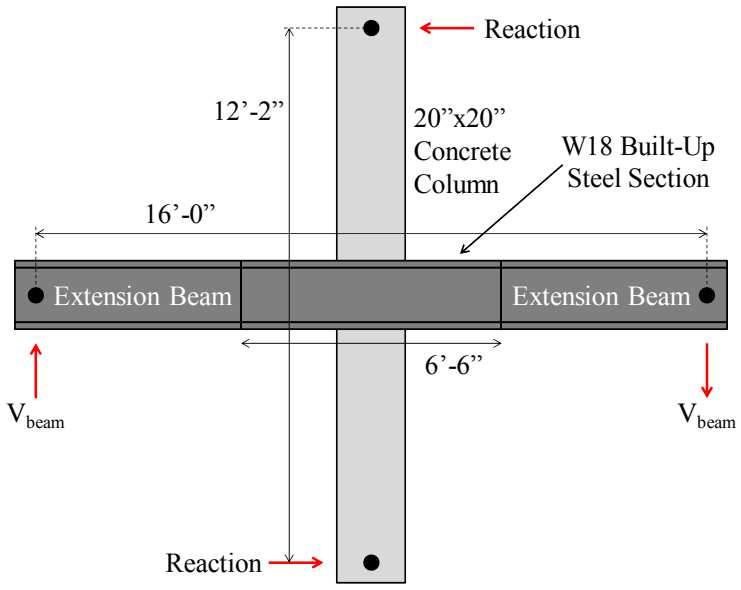

Figure 2.3: Typical Test Set-Up for Sheikh et al (1989), Sheikh (1987), and Deierlein (1988)

Sheikh (1987) presented a "lever arm mechanism," in which equal and opposite bearing forces were assumed to develop at opposite sides of the embedded member; Deierlein (1989) recommended using an equivalent rectangular stress block to compute the magnitude of the resultant bearing forces as:

$$C_c = 2 f_c^{'} a_c b_j^{'} \tag{2.24}$$

where C_c is the resultant concrete bearing force, f'_c is the specified compressive strength of concrete, b_j' is the effective width of the joint, and a_c is the bearing zone length, which is varied to provide force equilibrium for the applied load, but shall not exceed $0.3h_c$, where h_c is the column depth. More details on the computation of b_j' may be found in Deierlein et al (1989), as well as design equations to quantify the increase in capacity provided by vertical transfer bars attached to the beam flanges and developed into the column.

Deierlein (1988) reported that the use of face bearing plates welded to the steel section at the beam-column interfaces and web stiffeners increased the capacity of the joint panel by 70% and 50%, respectively. Extending the face bearing plates above and below the steel beam led to a 130% increase in strength, with the strength increase found to be proportional to the increase in bearing plate width. The use of vertical reinforcement attached to the beam flanges (often termed "auxiliary transfer bars" or "transfer bars" in this document) in the joint was found to decrease the bearing stress on the beam flanges. For cases in which joint failure was governed by bearing, the vertical transfer bars increased the strength of the joint, noting that Deierlein et al (1989) provided design equations to quantify this strength increase. Sheikh et al (1989) noted

that providing additional detailing resulted in up to a 180% increase in strength over a plain steel beam. Based on these studies, face bearing plates (web stiffeners at or just inside of the beam-wall interface) and/or auxiliary transfer bars, as well as back bearing plates (web stiffeners near the end of the embedded member), were often used in future experimental studies on SRC coupling beams in an effort to improve performance (Shahrooz et al, 1993; Harries et al, 1993; Harries et al, 1997; Shahrooz et al, 2001a,b,c).

Shahrooz et al (1993) tested three (unencased) steel coupling beams embedded into reinforced concrete structural walls. The one-half-scale built-up steel coupling beams (9" section depth and 27-plf section weight, i.e., ~W9x27 in terms of depth and weight) were flexure-controlled with a length-to-depth (aspect) ratio of 2.33. Minimum required embedment lengths were computed using the embedment model of Mattock and Gaafar (1982). None of the specimens included face or back bearing plates, and one of the specimens had auxiliary transfer bars in the embedment zone welded to the flanges of the steel section.

A schematic of the Shahrooz et al (1993) test set-up is shown in Figure 2.4. Reversed-cyclic wall moment and axial load were simulated, creating cyclic compression and tension demand acting normal to the embedded steel coupling beam. Consistent with actual coupled core walls, in which the beam shear forces from the coupling beams impart axial demand into the structural walls, wall axial compression corresponded to downward (negative) beam loading. The ratio of the cyclically-applied wall moment to coupling beam moment was maintained constant throughout each individual test to reflect the dependency suggested by analytical analysis of the prototype structure (Remmetter et al. 1992). To assess the influence of the magnitude of wall

stresses on the performance of the embedded member, one of the beams without transfer bars was tested under low wall demands, while the other was tested under much larger wall demands which included wall axial gravity load (indicated as the "constant" load on Figure 2.4). The beam with transfer bars was tested under identical large wall demands (including axial gravity load) to directly assess the impact of transfer bars. Note also that the eccentricity of the applied wall loads differed among the tests. Specifically, the distance from the edge of the wall to the applied wall load, indicated as e_{wall} in Figure 2.4, was larger by a factor of 1.49 (24.25" versus 16.25") for the condition with larger wall demands compared to the condition with smaller wall demands.

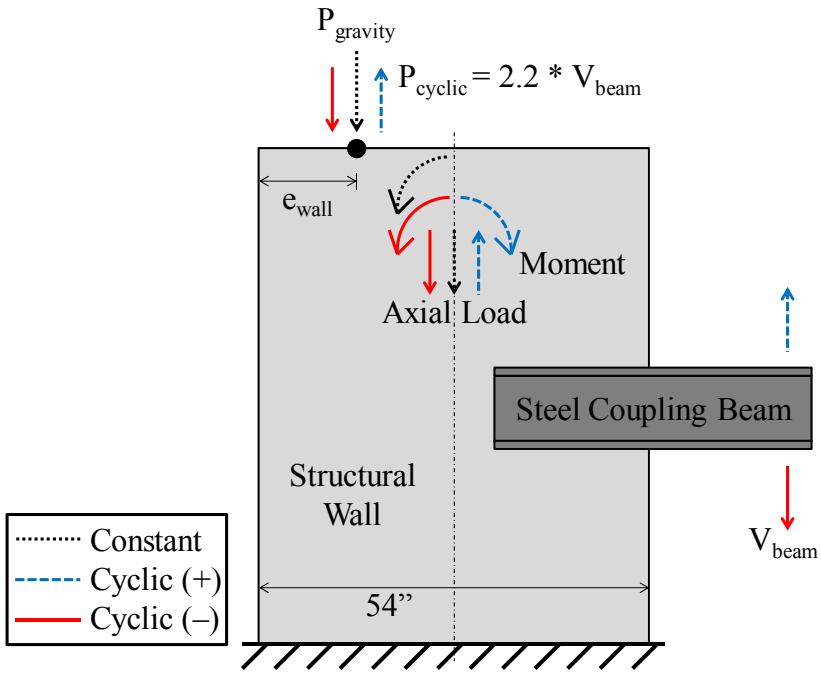

Figure 2.4: Test Set-Up for Shahrooz et al (1993)

All three beams (Shahrooz et al, 1993) were tested to peak chord rotations between 2.0% and 3.33%, corresponding to displacement ductility values in excess of four, with very minimal strength degradation observed. The beams without transfer bars displayed load-displacement asymmetry, characterized by reduced strength and stiffness when the wall demands created tension normal to the embedment length compared to compression. This asymmetry was more pronounced for the beam with larger wall loading. For the two beams with identical wall loads, the beam with transfer bars, relative to the beam without transfer bars, displayed less load-displacement asymmetry, less pinching, and greater strength and stiffness, with roughly 10% and 20% greater strength at 2.0% chord rotation for wall tensile and compressive stresses, respectively, normal to the embedment length. The wall axial compressive gravity load was observed to increase the initial coupling beam stiffness and to delay cracking and reduce crack propagation.

It was observed for all three tests (Shahrooz et al, 1993) that the coupling beams were not fixed at the face of the walls. Shahrooz et al (1993) considered effective fixity at one-third of the embedment length ($L_e/3$) from the beam-wall interface for modeling purposes. Despite the lack of fixity at the beam-wall interface, the majority of the total dissipated energy was attributed to the formation of plastic hinges in the steel member rather than damage within the connection region, suggesting adequacy of the embedment length in all cases. Comparing the two beams without transfer bars, it is interesting to note that the maximum beam shear load developed in the positive loading direction was larger for the beam with larger wall loading, suggesting that the effective point of fixity was closer to the beam-wall interface due to the large compression on the connection. In other words, the development of lower peak beam shear in the positive loading

direction for the beam with lower wall loads suggests that this member had a longer effective cantilever length than the beam with larger wall demands.

Harries et al (1993) tested two (unencased) built-up (14" section depth and 36-plf or 35-plf section weight, i.e., ~W14x36 or ~W14x35 in terms of depth and weight), shear-yielding, embedded steel coupling beams with a length-to-depth (aspect) ratio of 3.43 using the test set-up shown in Figure 2.5. The steel sections embedded into post-tensioned wall segments; therefore, constant compression was maintained in the wall segments such that cyclic tension/compression across the embedment length was not simulated. The embedment length was determined using the Marcakis and Mitchell (1980) embedment equation. Both beams included face bearing plates, but neither utilized back bearing plates or auxiliary transfer bars. The area of wall vertical reinforcement crossing the embedded section was selected to have a total yield force, $A_s f_y$, equal to the plastic shear capacity of the embedded beam.

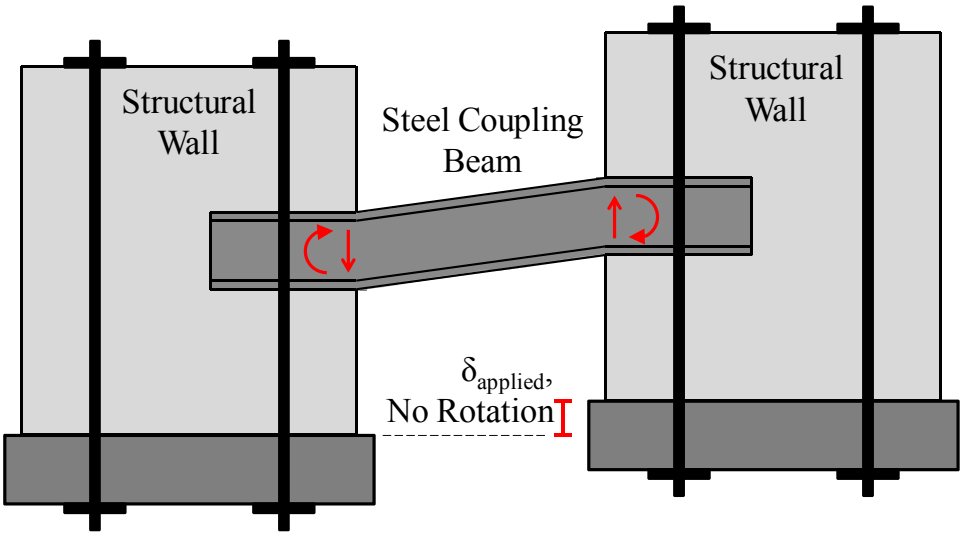

Figure 2.5: Test Set-up for Harries et al (1993) and Harries et al (1997)

For the first test specimen (Harries et al, 1993), web crippling of the steel section slightly inside of the beam-wall interface was observed after spalling of the wall cover concrete, and plastic deformations within the embedment region were also observed. For the second test beam, a web stiffener was added at each end of the beam slightly inside of the beam-wall interface in order to prevent web crippling, and plates were added in the embedment region to thicken the web of this member, thereby preventing shear yielding from occurring within the embedment region. Additionally, the minimum required embedment length was computed to include wall spalling at the beam-wall interface (Figure 2.2). The overall performances of both beams were excellent, characterized by stable load-displacement hysteresis with little-to-no strength degradation up to ~8% chord rotation, corresponding to displacement ductility values of about eight. The second beam showed a slight improvement in energy dissipation over the first, and no plastic deformation occurred in the embedment zone for the second beam. It is noted that wall vertical steel crossing the embedment zone did not yield at any point during testing.

Harries et al (1993) recommended modifying the Marcakis and Mitchell (1980) embedment equation to include the effect of wall spalling at the beam-wall interface (Equation (2.22)) and to include a strength reduction factor, φ=0.85, for concrete in bearing (mentioned previously in Section 2.1 but not included in Equation (2.22)). Harries et al (1993) also recommended providing an area of vertical reinforcement, A_s, crossing the embedment zone that resists a force, $A_s f_y$, equal to or exceeding the maximum shear capacity of the steel section, V_p' (to be taken as 1.25 times the nominal shear strength), with two-thirds of this reinforcement located within the front one-half of the embedment length; the inclusion of a strength reduction factor, φ=0.85, was also recommended. In equation form, this recommendation is:

$$A_s f_y \geq \frac{V_p'}{\phi} \tag{2.25}$$

Harries et al (1997) conducted two additional tests on unencased steel coupling beams (14" section depth and 21-plf section weight, i.e., ~W14x21 in terms of depth and weight). The Marcakis and Mitchell (1980) embedment equation, modified to include wall spalling and a strength reduction factor per Harries et al (1993) (i.e., Equation (2.22) modified to include a strength reduction factor of φ=0.85), was used to determine the embedment lengths. One beam was shear-controlled with a length-to-depth (aspect) ratio of 1.29 and the other was flexure-controlled with an aspect ratio of 3.43. Both beams included face bearing plates but excluded auxiliary transfer bars. The shear-controlled beam included back bearing plates (in addition to another set of web stiffeners between the face and back bearing plates), while the flexure-controlled beam did not. The flexure-controlled beam included steel plates added to the flanges within the embedment zone to increase the flexural capacity of the beam, ensuring that beam yielding would not occur in the embedment region.

The shear-controlled beam (Harries et al, 1997) displayed stable hysteresis with minimal-to-no strength degradation and pinching up to a displacement ductility of eight (~7.0% chord rotation), and a tearing failure occurred during the first loading cycle at a displacement ductility of ten (~8.75% chord rotation). The flexure-controlled beam was tested under reversed-cyclic loading to a displacement ductility of three (~3.2% chord rotation). Although no significant strength degradation or pinching was observed, a switch from cyclic to monotonic loading was made due to out-of-plane web local buckling during the third cycle at this level, which occurred after

flange local buckling two cycles previous (Harries, 1995). Subsequent monotonic loading to a displacement ductility of seven (~7.5% chord rotation) resulted in ~20% strength degradation.

Based on test results (Harries et al, 1993; Harries et al, 1997), Harries (1995) and Harries et al (2000) proposed modeling the effective bending stiffness, $(EI)_{eff}$, of an unencased steel coupling beam as:

$$\left(EI\right)_{eff} = 0.6k'E_sI_{g,s} = 0.6E_sI_{g,s}\left(1+\frac{12E_sI_{g,s}\lambda}{L_c{}^2G_sA_w}\right)^{-1} \tag{2.26}$$

where *k'* represents the reduction in flexural stiffness due to shear deformations, $I_{g,s}$ is the moment of inertia of the gross steel section (neglecting reinforced concrete encasement, where applicable), E_s is the modulus of elasticity of steel, G_s is the shear modulus of steel, A_w is the area of the steel section resisting shear (taken as the product of the steel section depth, d, and web thickness, t_w), λ is the cross-section shape factor for shear (1.5 for W-shapes), L_c is the effective clear span of the coupling beam, computed as $L_c = L + 2c$ to account for spalling of the wall clear cover, c, where L is the clear span. Given that the effective bending stiffness is reduced to account for shear deformations using *k'*, the beam shear stiffness should be modeled as rigid, unless shear deformations are modeled separately, in which case $k' = 1$. Modeling an effective shear stiffness of $0.6G_sA_w/\lambda$ when $k' = 1$ is consistent with Equation (2.26).

Harries et al (2000) referenced the work of Harries (1995), Harries et al (1997), and Shahrooz et al (1993) in stating that auxiliary transfer bars attached to the beam flanges in the embedment zone (Figure 1.4) are not necessary so long as adequate embedment length of the steel section is

provided and wall boundary reinforcement satisfies the recommendations of Harries et al (1993) and Harries et al (1997), i.e., the required area of vertical reinforcement crossing the embedment length is not less than the expected coupling beam shear strength, with two-thirds of this steel located over the first one-half of the embedment length, and the width of the boundary element reinforcement does not exceed 2.5 times the coupling beam flange width. Satisfying these recommendations provides adequate control of the gap that opens at the beam flanges without reliance on auxiliary transfer bars (Harries et al, 2000). If transfer bars are provided, Harries et al (2000) recommended neglecting the contribution of transfer bars when computing the minimum required embedment length in order to be conservative, even though Marcakis and Mitchell (1980) and Qin (1993) account for a reduction in the minimum required embedment length due to the additional load-transfer mechanism provided by transfer bars.

Gong and Shahrooz (2001a) tested four one-third-scale, shear-yielding, built-up (6" section depth and 20-plf section weight, i.e., ~W6x20 in terms of depth and weight) steel coupling beams designed considering a 20-story prototype structure. The primary test variables were the number and spacing of web stiffeners and the presence or lack of concrete encasement, noting that three of the four beams included encasement. The same steel section and cantilever length were used for all four tests, and the span-to-length (aspect) ratios for the concrete-encased and unencased beams were 4.0 and 5.33, respectively. All four steel coupling beams included auxiliary transfer bars welded to the embedded flanges. Face and back bearing plates were used at the location of the transfer bars in all four specimens (noting that the face bearing plates were slightly inside of the beam-wall interface in this instance), and web stiffeners were included in the beam span of three of the four specimens. The Mattock and Gaafar (1982) equation

(Equation (2.21)) was used to determine the embedment length. The influence of concrete encasement was neglected when computing the member capacity used to determine the minimum required embedment length on the basis that encasement was not expected to contribute significantly to strength and stiffness and the design was more conservative by neglecting encasement. Therefore, all four beams had the same embedment length. The cantilever test beams were embedded into a portion of a structural wall, which was loaded under constant axial compression without applied bending moment (Figure 2.6).

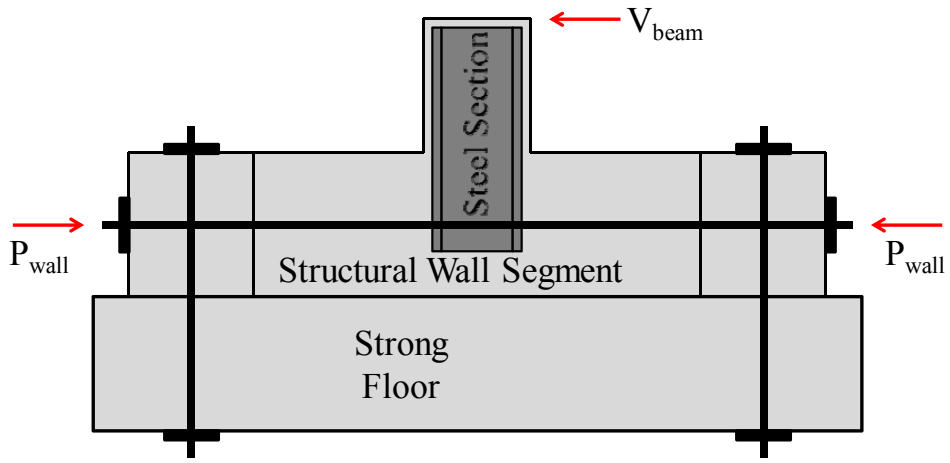

Figure 2.6: Test Set-Up for Gong and Shahrooz (2001a)

The four tests beams (Gong and Shahrooz, 2001a) displayed stable hysteretic loops and testing was stopped at roughly 5% to 6% chord rotation. Gong and Shahrooz (2001a) found that lightly-reinforced concrete encasement was adequate to prevent web buckling in the beam span at advanced yielding, suggesting that web stiffeners are unnecessary if concrete encasement is provided. Concrete encasement served to increase the coupling beam shear capacity by 10% to 25% and the initial stiffness by roughly 25%. By comparing modeling predictions to test data,

Gong and Shahrooz (2001a) found the effective point of fixity to be 1/4 and 1/3 of the embedment length inside of the wall for unencased and encased steel coupling beams, respectively. This is consistent with the findings of Shahrooz et al (1993), suggesting effective fixity at 1/3 of the embedment length inside of the wall, and also with observations made during testing (Gong and Shahrooz, 2001a). Specifically, at advanced rotational demands, concrete at the beam-wall interface spalled off and the steel flanges were separated from the surrounding concrete. Wall boundary transverse reinforcement passing through the embedded web and mechanical half couplers (welded to the flanges of the beam section and used to attach auxiliary longitudinal bars) had fractured, suggesting movement of the embedded steel section relative to the surrounding concrete and an associated lack of fixity at the beam-wall interface.

Gong and Shahrooz (2001c) noted that the effects of additional stiffness due to coupling beam encasement impact the entire structure. Aside from producing smaller vibration periods, the additional stiffness leads to increased wall axial load and increased wall shear. Specifically, for elastic analysis of the 20-story prototype structure (Gong and Shahrooz, 2001c), the wall axial load on the first floor increased by 40% while the increase in wall shear force was roughly 10% due to concrete encasement. It is noted that cracking, which decreases the stiffness of the coupling beams, was not accounted for in the elastic analysis.

With regard to energy dissipation, the concrete-encased steel coupling beams did not perform as well as the unencased steel coupling beam (Gong and Shahrooz, 2001a). Test data suggest that significant inelasticity occurred in the embedment region for the concrete-encased beams, suggesting that the embedment length was inadequate and should have been increased to account

for the increased coupling beam shear strength provided by concrete encasement. If the additional shear strength associated with encasement is not considered, damage occurs in the embedment region prior to mobilizing the full capacity of the SRC coupling beam. This was confirmed by observation; during the latter stages of testing, concrete spalling was observed in the embedment zone. Gong and Shahrooz (2001a) recommended a capacity design approach, in which the required embedment length is computed based on the expected strength of the SRC coupling beam, i.e., the embedment strength was designed to meet or exceed the expected shear strength.

Gong and Shahrooz (1998, 2001b) suggested determining the expected shear strength of an SRC coupling beam, V_{ne}, as:

$$V_{ne} = 1.6(V_{steel} + V_{RC}) \tag{2.27}$$

where V_{steel} is the nominal shear strength of the steel section, and V_{RC} is the nominal shear strength of the reinforced concrete encasement, computed as:

$$V_{steel} = 0.6F_y(d - 2t_f)t_w \tag{2.28}$$

$$V_{RC} = 2\sqrt{f_c'}b_c d_c + \frac{A_{st} f_{yt} d_c}{s} \tag{2.29}$$

respectively, where F_y is the specified minimum yield strength of structural steel, d is the depth of the steel section, t_f is the flange thickness, t_w is the web thickness, b_c is the overall beam width

(i.e., the width of concrete encasement), d_c is the effective depth of concrete encasement (i.e., the distance from the extreme compression fiber to the center of the beam longitudinal tension reinforcement), A_{st} is the area of transverse reinforcement, f_{yt} is the specified yield strength of the transverse reinforcement, and s is the spacing of transverse reinforcement. Equation (2.27) was developed by Gong and Shahrooz (2001b) based on a parametric study that considered numerous SRC coupling beams (24 cases) and was conducted in order to calibrate V_{ne}, against V_{fiber}, the shear strength computed using fiber modeling based on modified compression field theory (Collins and Mitchell, 1991). This calibration yielded a coefficient of 1.6 in Equation (2.27), corresponding to a V_{ne}/V_{fiber} ratio of 0.991 with a standard deviation of 0.075.

Gong and Shahrooz (2001b) tested three concrete-encased, shear-yielding coupling beams (6" section depth and 20-plf section weight, i.e., ~W6x20 in terms of depth and weight) with a length-to-depth (aspect) ratio of 4.0. The embedment length for the test specimens was determined using the Mattock and Gaafar embedment equation (Equation (2.21)) with an embedment strength of V_{ne}, computed based on Equation (2.27). These test beams were identical to those tested previously by Gong and Shahrooz (2000a), except for a 59% increase in the provided embedment length. All specimens included auxiliary transfer bars, two included face and back bearing plates at the location of the transfer bars (noting that the face bearing plates were slightly inside of the beam-wall interface in this instance), and one of the two with bearing plates included an RC floor slab along the entire length of the wall at the location of the coupling beam. Although previous research (Sheikh, 1987; Deierlein 1988; Sheikh et al, 1989; Deierlein et al, 1989; ASCE 1994) suggested that face bearing plates at each side of the column increase the strength and ductility of the connection between steel beams and reinforced concrete

columns, Gong and Shahrooz (2001b) noted that the typical column width to beam depth ratio is about twice the typical wall width to coupling beam depth ratio, suggesting that the benefit of face bearing plates may be less significant for coupling beams.

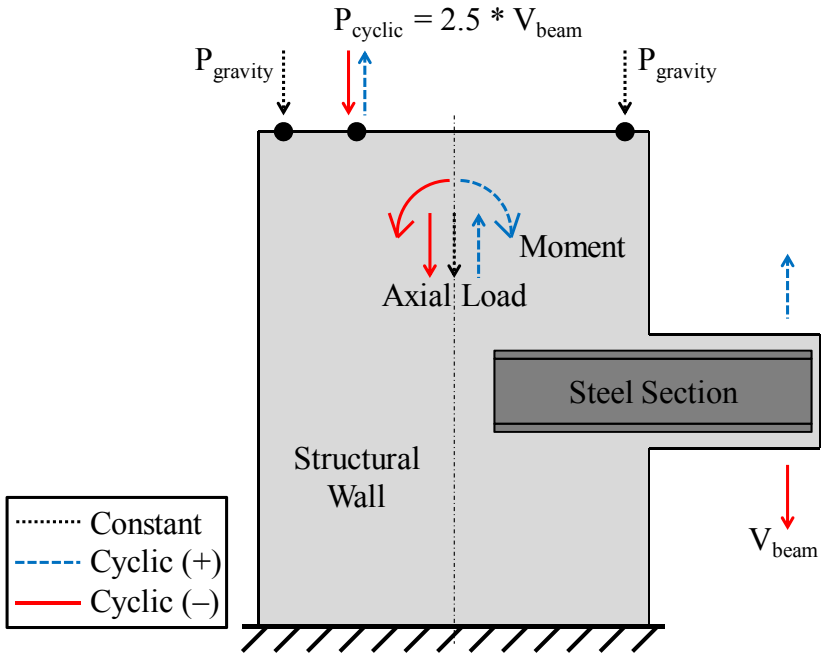

Figure 2.7: Test Set-Up for Gong and Shahrooz (2001b)

Each test specimen (Gong and Shahrooz, 2001b) contained one wall pier with an embedded one-half-length cantilever coupling beam. Using the test set-up shown in Figure 2.7, reversed-cyclic shear loading was applied to the coupling beam, and simultaneous, reversed-cyclic axial load and overturning moment (due to the eccentricity of the applied axial load), in addition to constant (axial) gravity load, were applied to the structural wall. Wall shear load was not applied, as it was expected to have minimal influence on coupling beam performance. The ratio between the cyclic force and moment applied to the wall and that applied to the coupling beam was

determined based on dynamic analysis of the prototype structure for several ground motions (Gong and Shahrooz, 1998).

All test specimens (Gong and Shahrooz, 2001b) exhibited stable load-displacement hysteresis with very minimal pinching but noticeable asymmetry. Since the effect of wall overturning moment on the coupling beam was simulated, the embedment zone was subjected to compression when the beam was loaded up (positive) and tension when the beam was loaded down (negative). When the wall demands produced compressive stresses normal to the embedded steel section, the bearing force transfer mechanism improved and a larger force was developed. Alternatively, when the wall overturning moment produced tension at the boundary, the coupling beam developed a lower shear force. For the two specimens without the floor slab, the capacity developed in the negative loading direction was ~2/3 of the capacity developed in the positive loading direction, and the beam with face bearing plates displayed slightly higher capacity and less strength degradation in the positive loading direction than did the beam without face bearing plates. Very similar rates of strength degradation in the negative loading direction, i.e., when the connection was in tension, were evident from the load-deformation responses of the three test specimens.

Gong and Shahrooz (2001b) noted that diagonal cracking was observed in the embedment region for the test beams, suggesting that concrete struts were mobilized by face-bearing plates. Test data suggested that face bearing plates delay stiffness degradation due to less reliance on bearing stresses and increased participation of the connection toward dissipating energy. Also, face bearing plates mitigate the impact of wall overturning moment on connection capacity, since the

resistance provided by compression struts associated with the bearing plates is not dependent on the direction of wall overturning moment. (Gong and Shahrooz, 2001b)

The test results of Gong and Shahrooz (2001b) indicated that the floor slab contributed additional strength in positive bending (slab in compression) but provided little benefit in negative bending (opposite to that for conventional RC beams due to the large area of steel in composite beams). The slab contribution to strength diminished at large deformations. The floor slab served to eliminate the participation of the connection region toward dissipating energy. Therefore, Gong and Shahrooz (2001b) recommended determining the required embedment length based on the expected shear strength of the coupling beam (V_{ne} per Equation (2.27)), ignoring the increase in strength provided by the floor slab. The floor slab initially increased the coupling beam stiffness, as the effective fixity for the beam with the floor slab was initially found to be at the beam-wall interface. However, the additional stiffness was lost after exceeding small deformations. According to Gong and Shahrooz (2001b), modeling the increase in stiffness is unnecessary, and modeling effective fixity at 1/3 of the embedment length from the beam-wall interface is recommended. Harries et al (2000) conversely stated that until further data are established, including the participation of the floor slab in determining the SRC coupling beam stiffness is recommended. Using the effective flange width for T-beams (ACI 318) was recommended, as well as checking deflection limits without including the floor slab (Harries et al, 2000).

Comparing the test results of Gong and Shahrooz (2001b) to Gong and Shahrooz (2001a), it is evident that the increased embedment length resulted in a significant improvement in ductility

(deformation capacity) and energy dissipation, along with less strength degradation. Computing the minimum required embedment length to develop $V_{n,embed}$ in Equation (2.21) equal to V_{ne} in Equation (2.27) was deemed acceptable (Gong and Shahrooz, 2001b). El-Tawil et al (2010) modified this recommendation slightly, to compute the expected capacity of shear-yielding SRC coupling beams as:

$$V_{ne} = 1.1R_y V_p + 1.56V_{RC} \tag{2.30}$$

where R_y is ratio of the expected yield strength of structural steel, F_{ye}, to the specified minimum yield strength of structural steel, F_y. V_p is computed as:

$$V_p = 0.6F_y dt_w \tag{2.31}$$

which differs from the computation of V_{steel} (Equation (2.28)) in that V_p is based on the section depth, d, rather than the web height, $d - 2t_f$, of the steel section.

Fortney et al (2007) tested an unencased, shear-yielding steel coupling beam that was roughly one-half-scale (14" section depth and 54-plf section weight i.e., ~W14x54 in terms of depth and weight) with a length-to-depth (aspect) ratio of 2.57. The steel beam embedded into wall segments that were not cyclically loaded during testing, and the embedment length for the test specimen was determined using the Mattock and Gaafar (1982) embedment equation (Equation (2.21)). The test specimen included auxiliary transfer bars as well as face and back bearing plates (noting that the back bearing plates were located at one-half of the embedment length

inside of the beam-wall interface in this instance). Reversed-cyclic loading was applied up to 4% rotation, at which point a switch was made due to concerns regarding the stability of the loading frame and load, and monotonic loading was conducted up to 11% rotation. The performance of this member was excellent with no significant degradation or pinching observed in the load-deformation response.

Table 2.1: Summary of Previous Testing Programs

Testing Program	Test #	Steel Section	Concrete Encasement	Yield Mode	Face & Back Bearing Plates	Auxiliary Transfer Bars	Floor Slab	Wall (Cyclic)
Shahrooz et al (1993)	1	~W8x27	No	Flexure	No & No	No	No	Yes
	2		No			No		
	3		No			Yes		
Harries et al (1993) & (1997)	1	~W14x36	No	Shear	Yes & No	No	No	No
	2		No	Shear	Yes & No			
	3	~W14x21	No	Shear	Yes & Yes			
	4		No	Flexure	Yes & No			
Gong & Shahrooz (2001a)	1	~W6x20	No	Shear	Yes & Yes	Yes	No	No
	2		Yes					
	3		Yes					
	4		Yes					
Gong & Shahrooz (2001b)	5	~W6x20	Yes	Shear	No & No	Yes	No	Yes
	6		Yes		Yes & Yes		No	
	7		Yes		Yes & Yes		Yes	
Fortney et al (2007)	1	~W14x54	No	Shear	Yes & Yes	Yes	No	No

A summary of the testing programs discussed in this section is provided in Table 2.1, including such variables as the size of the steel section, the yielding mode of the coupling beam (flexure or shear), and the inclusion/exclusion of concrete encasement, face and back bearing plates,

auxiliary transfer bars, a floor slab, and a cyclically-loaded wall. Referring to Table 2.1, note the absence of tests on flexure-yielding, concrete-encased coupling beams embedded into cyclically-loaded structural walls, which were tested in this study.

2.3 AISC SEISMIC PROVISIONS

The 2010 AISC Seismic Provisions for Structural Steel Buildings provide design guidelines for structural steel coupling beams (both with and without concrete encasement) embedded into reinforced concrete shear walls. The design guidelines differ depending upon whether the coupling beams connect ordinary shear walls (Section H4) or special shear walls (Section H5). The 2010 AISC Seismic Provisions state that special shear walls are designed in accordance with ACI 318 including Chapter 21 (Section H5.2), whereas ordinary shear walls exclude Chapter 21 provisions (Section H4.2). The term "structural wall" rather than "shear wall" is typically used in this document, as ACI 318-11 uses the term "structural wall" and notes that a shear wall is a structural wall (in the definition for "structural wall" provided in ACI 318-11 Chapter 2). The differences between coupling beam design for ordinary and special structural walls are noted herein. It is noted that the 2010 AISC Seismic Provisions typically refer to SRC coupling beams as "composite coupling beams."

The 2010 AISC Seismic Provisions recommend obtaining effective stiffness values for use in elastic analysis from ACI 318 Chapter 10 for wall piers and SRC coupling beams. Uncracked values are to be used with ordinary structural walls (Section H4.3(1)), whereas cracked values are to be used with special structural walls (Section H5.3(1)). ACI 318-11 Section 10.10.4.1

specifies an effective moment of inertia of $0.70I_{g,c}$ and $0.35I_{g,c}$ for uncracked and cracked walls, respectively, and $0.35I_{g,c}$ for beams, where $I_{g,c}$ is the moment of inertia of the gross concrete section neglecting the impact of reinforcement (a transformed section analysis is not required). The connection flexibility and the shear distortion of the beam are to be taken into account in the analysis (Section H4.3(3) and Section H5.3(2)). Details as to how this shall be accomplished are not included, although recommendations related to connection flexibility are provided in Commentary Section 4.3. Specifically, when L_e is known, using an effective clear span, $L_{eff} = L + 0.6L_e$, to account for connection flexibility is recommended and consistent with Shahrooz et al (1993) and Gong and Shahrooz (2001b). When L_e is unknown, the effective bending stiffness, $(EI)_{eff}$, for either steel or SRC coupling beams may be determined based on Equation (2.26) (presented previously), where k' (included in Equation (2.26) and defined in Section 2.2) is used to account for shear deformations. Although not explicitly stated in Commentary Section 4.3, it appears that $(EI)_{eff}$ is presented as a suggested alternative to using ACI recommendations to determine effective stiffness (per Section H4.3(1) and Section H5.3(1)).

For design purposes, it is permissible to redistribute coupling beam forces vertically to adjacent floors, provided individual beam shears are never reduced by more than 20% and the total (summed) shear capacity of all coupling beams exceeds the total (summed) coupling beam shear demand determined from analysis (Section H4.4). The limiting shear strength of an SRC coupling beam, $V_{ne,limit}$, which is used to compute the minimum required embedment length, is computed as (Equation H4-3, Section H4.5b(2)(1)):

$$V_{ne,limit} = \frac{2M_{pe}}{L} \leq V_{ne} \tag{2.32}$$

where L is the clear span, M_{pe} is the expected plastic flexural strength of the SRC coupling beam, and V_{ne} is the expected shear strength of the SRC coupling beam. M_{pe} is to be computed using the plastic stress distribution or the strain compatibility method, including appropriate R_y factors for various elements of the cross-section (i.e., flanges, web). No further details on the computation of M_{pe} are provided in the 2010 AISC Seismic Provisions. For ordinary structural walls, V_{ne} is computed as (Equation H4-4 per Section H4.5b(2)(1)):

$$V_{ne} = R_y V_p + 2\sqrt{f_c'} b_c d_c + \frac{A_{st} f_{yt} d_c}{s} \tag{2.33}$$

and for special structural walls, V_{ne} includes overstrength and is computed as (Equation H5-3 per Section H5.5d):

$$V_{ne} = 1.1 R_y V_p + 1.56\left(2\sqrt{f_c'} b_c d_c + \frac{A_{st} f_{yt} d_c}{s}\right) \tag{2.34}$$

where A_{st} is the area of transverse reinforcement, f_{yt} is the specified yield strength of transverse reinforcement, b_c is the width of concrete encasement, d_c is the effective depth of concrete encasement, s is the spacing of transverse reinforcement, R_y is the ratio of the expected yield strength to the specified minimum yield strength of structural steel, and V_p is the nominal shear strength of the steel section, computed as $0.6F_yA_w$, where F_y is the specified minimum yield strength of structural steel and A_w is the web area. Note that in the 2010 AISC Seismic Provisions no difference in the computation of M_{pe} is mentioned for special structural walls

compared to ordinary structural walls, meaning that flexure-controlled sections will have the same embedment length for either ordinary or special structural walls.

Per Section H4.5b(2)(2) in the 2010 AISC Seismic Provisions, the minimum required embedment length, L_e, is determined using Equation H4-2 (Section H4.5b(1)(3)), by taking $V_{n,embed}$ equal to $V_{ne,limit}$ (which is computed using Equation (2.32)):

$$V_{n,embed} = 1.54\sqrt{f_c'}\left(\frac{b_w}{b_f}\right)^{0.66} \beta_1 b_f L_{e,c}\left[\frac{0.58 - 0.22\beta_1}{0.88 + \frac{L_c}{2L_{e,c}}}\right] \tag{2.35}$$

where b_w is the wall thickness, b_f is the beam flange width, β_1 is the depth factor, relating the depth of the Whitney stress block to the neutral axis depth, and f'_c is in units of *ksi*. To account for spalling, the modified embedment length, $L_{e,c}$, excludes the concrete cover thickness, and the modified clear span, L_c, includes the concrete cover thickness (Commentary H4.5b), i.e., $L_{e,c} = L_e - c$ and $L_c = L + 2c$. The concrete cover thickness is to be measured from the wall face to the first layer of confinement or to the outermost wall vertical reinforcement if wall boundary confinement is not present (Commentary H4.5b). It is unclear as to whether the concrete cover is to be measured to the center of this reinforcement or the outside edge (i.e., as for clear cover). To be consistent with Harries et al (1993), which is the basis for this recommendation, the concrete cover is assumed to be taken to the outside edge of this reinforcement, meaning that the parameter c in Figure C-H4.6 (Commentary H4.5b) represents the wall clear cover;. Note that Equation (2.35) is generally consistent with Equation (2.23) but differs relative to Equation

(2.23) in that it includes an inherent strength reduction factor, $\varphi = 0.9$, requires f'_c to be input in units of *ksi* rather than *psi* (leading to change in the leading coefficient from 54 to 1.54, consistent with f'_c = 4-ksi and $\varphi = 0.9$, i.e., $1.54\sqrt{4\ ksi} = (\phi = 0.9)(54)\sqrt{4000\ psi}\ /\ (1000\ psi\ /\ ksi)$), and uses the modified coupling beam clear span, L_c, which is twice the modified cantilever length ($a + c$) of a one-half-length test beam.

Per Section H4.5b(1)(4) vertical wall reinforcement with nominal $A_s f_y$ greater than or equal to the limiting shear strength, $V_{ne,limit}$, of the SRC coupling beam must be provided over the embedment length of the beam, with at least two-thirds of this reinforcement located over the first one-half of the embedment length. This vertical wall reinforcement must extend at least one tension development length above and below the beam flanges.

For special structural walls only, face bearing plates and auxiliary transfer bars must be provided (Section H5.5c per Section H5.5d). Theses face bearing plates and transfer bars provide additional force-transfer mechanisms that improve load transfer between the embedded steel section and the reinforced concrete structural wall. Specifically the auxiliary transfer bars enable load transfer through shear and bond, while the bearing plates allow the formation of a diagonal strut between the two plates. These plates also act as web stiffeners, since the transfer bars create concentrated loads on the steel section. Additional detailing requirement related to auxiliary transfer bars and bearing plates are provided in the following paragraphs.

Per Section H5.5c, as required by Section H5.5d, face bearing plates shall be provided on both sides of the embedded steel section at the face of the reinforced concrete wall. The face bearing

plates must be detailed to satisfy Section F3.5b(4); namely, the combined width of the stiffeners must be at least $b_f - 2t_w$ and the plate thickness must be at least $0.75t_w$ or 3/8", where b_f is the flange width and t_w is the web thickness of the embedded member. Although the code does not explicitly state this, the Commentary H5.5c states that stiffener plates similar to the face bearing plates must also be provided near the end of the embedded section at the location of the vertical transfer reinforcement.

Per Section H5.5c, embedded steel sections must be provided with two regions of vertical transfer reinforcement attached to both the top and bottom flanges. The first region is located at the location of the longitudinal wall reinforcement closest to the face of the wall. The second region is located at a distance no less than $d/2$ from the end of the embedded member, where d is the overall depth of the steel section. All transfer reinforcement must extend a full tension development length from the flanges of the embedded section. The required area of vertical transfer reinforcement is (Equation H5-1 per Section H5.5c):

$$A_{tb} \geq 0.03 f_c' L_{e,c} b_f / f_{ytb} \tag{2.36}$$

where A_{tb} is the required area of transfer reinforcement attached at each of the two regions at each of the top and bottom flange locations, and f_{ytb} is the specified yield strength of transfer reinforcement. The total area of transfer reinforcement is not to exceed (Equation H5-2 per Section H5.5c)

$$\Sigma A_{tb} < 0.08 L_{e,c} b_w - A_s \tag{2.37}$$

where ΣA_{tb} is the sum of all transfer reinforcement in both regions attached to both the top and bottom flange, A_s is the area of wall longitudinal reinforcement provided over the modified embedment length, $L_{e,c}$, and b_w is the wall width. Note that Figure C-H5.2 in the Commentary H5.5c illustrates these transfer bar requirements.

The 2010 AISC Seismic Provisions note in Commentary Section H4.1 that it is not necessary or practical to pass boundary element transverse reinforcement through the web of the embedded steel I-beam (as noted by Harries et al, 2000). Using hooked ties with a short vertical bar between the beam flanges that anchors the ties is specified as a practical alternative (as noted by El-Tawil et al, 2010, with reference to Lehmkuhl, 2002).

2.4 SUMMARY

This chapter presented a literature review for SRC coupling beams. Based on this literature review, it was noted that previous tests were often conducted for relatively small-scale coupling beams and/or coupling beams that were not embedded into cyclically-loaded structural walls. Additionally, a lack of previous testing of flexure-yielding members without concrete encasement was identified. The test specimens in this study, the design of which is covered in the next chapter, were flexure-yielding, concrete-encased members embedded into cyclically-loaded structural walls, due to the lack of previous testing for such members. The provisions for SRC coupling beams found in the 2010 AISC Seismic Provisions were also summarized in this chapter; one of the goals of this research is to assess and improve upon these existing recommendations.

3 Specimen Design

3.1 DESIGN OF OVERALL TEST SET-UP

As mentioned previously in Chapter 1, because prior testing on SRC coupling beams was often conducted on small-scale specimens (Shahrooz et al, 1993; Gong and Shahrooz, 2001a,b,c), this testing program was intended to assess the reliability of the embedment equations at large-scale. Additionally, because previous tests were often carried out for steel sections embedded into uncracked walls or reaction blocks (Harries et al, 1993; Harries et al, 1997; Gong and Shahrooz, 2001a; Fortney et al, 2007), the test set-up for this study was designed such that the steel sections were embedded into a wall subjected to reversed cyclic lateral loading and overturning moment, in order to subject the embedment region to strains/stresses representative of actual conditions (illustrated previously in Figure 1.5).

The test set-up (Figure 3.1) was developed based on extraction of the test specimen sub-assembly from a coupled core wall (Figure 3.2). Note that this general test configuration, i.e., including a cyclically-loaded structural wall, has been used by previous research teams (Shahrooz et al, 1993; Gong and Shahrooz, 2001b), as presented in Section 2.2. A more detailed presentation of the test set-up is provided in Section 4.3. Two test specimen sub-assemblies were designed, constructed and tested in the UCLA Structural/Earthquake Engineering Research

Laboratory. Referring to Figure 3.1, each sub-assembly contained a reinforced concrete structural wall with two one-half span, cantilever SCR coupling beams embedded into the wall (one on each side of the wall). Each beam was tested individually, with the two beams in each test specimen sub-assembly tested sequentially, meaning that a total of four SRC coupling beams were tested. The beams were tested by applying a reversed-cyclic shear load at a location representing the coupling beam midspan (the inflection point for a coupling beam spanning between two walls, as indicated in Figure 3.2). A "test specimen" essentially constitutes one coupling beam and the structural wall, since the other coupling beam is not loaded during testing and is expected to have no significant impact on the test. In this sense, each test specimen sub-assembly contains two test specimens. Beam 1 (SRC1) and Beam 2 (SRC2), the two test specimens from the first sub-assembly, were tested prior to the design and construction of Beam 3 (SRC3) and Beam 4 (SRC4), the two test specimens from the second sub-assembly.

It is noted that the quantity of wall boundary longitudinal and transverse reinforcement typically decreases over the height of a structural wall. ACI 318-11 Section 21.9.6 provides detailing requirements for the boundaries of structural walls, with Sections 21.9.6.2 and 21.9.6.3 used to assess the need for special boundary elements in structural walls. In mid- to high-rise construction in Seismic Design Category D, E, and F, the lower stories of structural walls typically require special boundary elements, which are to be detailed in accordance with the provisions of Section 21.9.6.4. For locations in which special boundary elements are not required, an intermediate level of boundary transverse reinforcement is required when the longitudinal reinforcement ratio at the wall boundary is greater than $400/f_y$, per Section 21.9.6.5. This intermediate level of confinement is often referred to as an "ordinary boundary element"

(see NIST Technical Brief #6 (Moehle et al, 2011)). As indicated in Figure 3.2, intermediate-level stories often contain ordinary boundary elements, and upper-level stories may contain ordinary boundary elements or may contain no boundary element if the longitudinal reinforcement ratio is less than or equal to $400/f_y$.

Wall boundary longitudinal and transverse reinforcement provided in the test specimens was a function of the assumed SRC coupling beam location in an actual coupled core wall. As indicated in Figure 3.2, the specimens tested in this study either had ordinary boundary elements or no boundary elements. Special boundary elements were not used for any of the test specimens, which is conservative in the sense that a special boundary element provides a greater level of confinement and restraint against buckling of longitudinal reinforcement than that provided by an ordinary boundary element. As well, the structural wall boundary reinforcement was not symmetric within each test specimen sub-assembly, since the quantity of longitudinal reinforcement provided at the wall boundary crossing the SRC beam embedment zone was considered to be an important parameter. On the other hand, the loading protocol for the structural wall was selected to ensure that the behavior at the opposite boundary did not greatly influence the performance of the coupling beam being tested, meaning that the wall boundary reinforcement at the opposite wall boundary was not an important parameter for that coupling beam test.

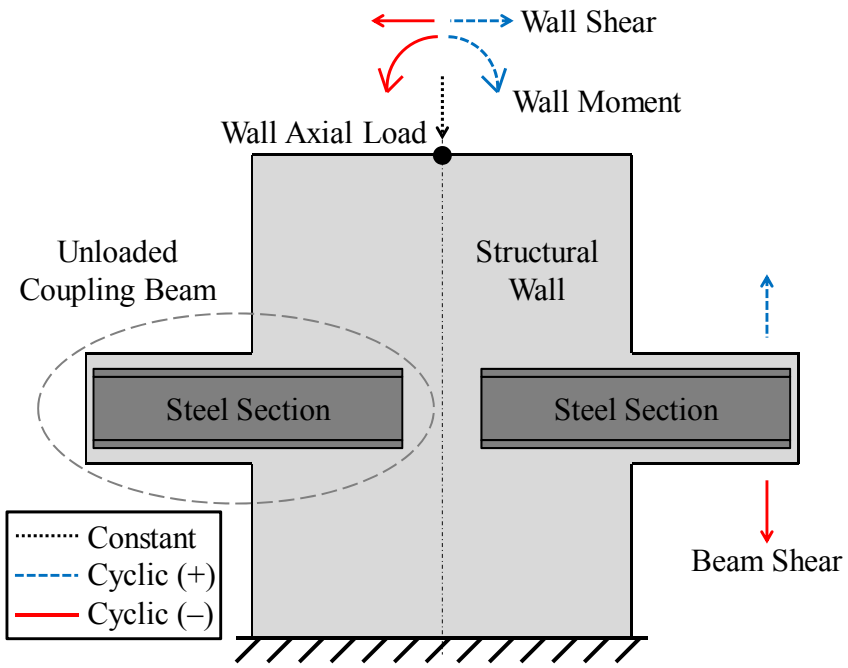

Figure 3.1: General Schematic of the Test Set-Up

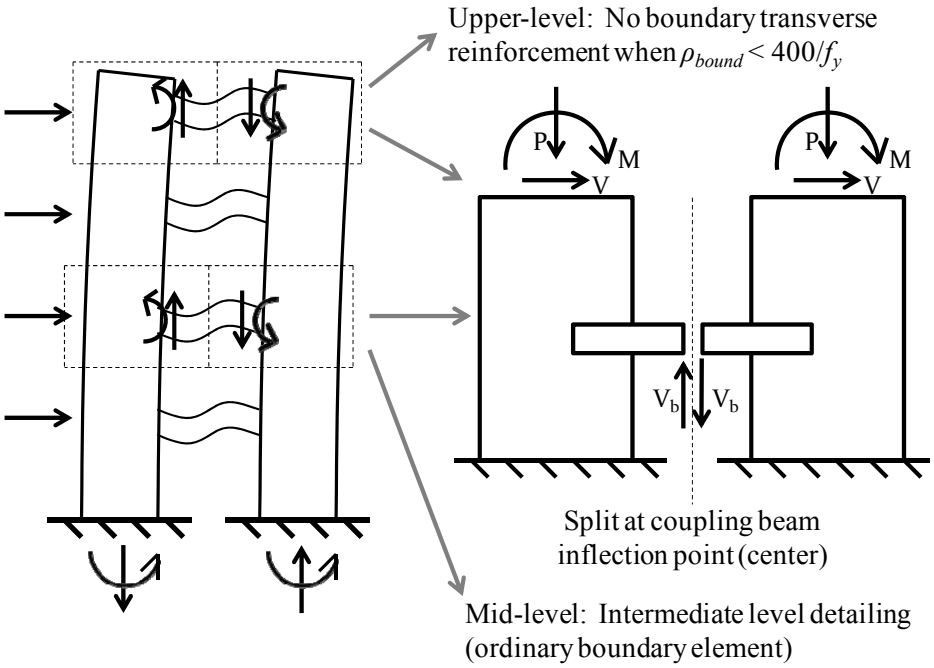

Figure 3.2: Extraction of the Test Sub-Assembly from a Coupled Core Wall

3.2 TEST SPECIMEN OVERVIEW AND TEST MATRIX

Figure 3.3 and Figure 3.4 show an elevation view of the first and second test specimen sub-assemblies, respectively, while Figure 3.5 and Figure 3.6 show the respective structural wall cross-sections, noting that the first sub-assembly included SRC1 and SRC2, while the second included SRC3 and SRC4. Figure 3.7 shows the coupling beam cross-section, which was the same for all four test beams.

The test matrix for the four specimens is shown in Table 3.1 and illustrated in Figure 3.8. Test variables included embedment length of the steel section into the structural wall (L_e), coupling beam span-to-depth (aspect) ratio (α), longitudinal reinforcement ratio at the wall boundary into which the steel section is embedded (ρ_{bound}), quantity of wall boundary transverse reinforcement at the boundary into which the steel section is embedded (categorized as "SBE" for special boundary element, "OBE" for ordinary boundary element, or "Other" for any conditions that do not satisfy SBE or OBE), the as-tested concrete compressive strength for the 4.5-ksi mix design ($f'_{c,test}$), and the applied peak structural wall demands ($\varepsilon_{s,max}/\varepsilon_y$). In the term $\varepsilon_{s,max}/\varepsilon_y$, $\varepsilon_{s,max}$ is the tensile strain in the outermost wall longitudinal bars at the location of the coupling beam centerline, and is normalized by ε_y, the yield strain of the wall boundary longitudinal reinforcement. $\varepsilon_{s,max}$ was computed analytically using plane-strain moment-curvature analysis based on the peak wall moment (including the influence of axial load, where applicable) reached during testing when loading in the negative direction, i.e., when the beam was loaded downward with wall tension acting normal to the embedment length. More detailed information on the applied wall demands is provided in Section 4.5.

SRC1 was intended to test a favorable scenario, characterized by long embedment and low wall demands, while SRC2 was intended to test a more critical scenario, characterized by potentially inadequate embedment length and larger wall demands. SRC3 tested a lower aspect ratio beam, while SRC4 tested the effects of reduced wall boundary longitudinal reinforcement with no wall boundary transverse reinforcement. The embedment capacities for SRC3 and SRC4 were intended to be consistent with SRC2; specifically, the embedment lengths for the beams with varying aspect ratio were designed to develop the same flexural capacity at the beam-wall interface, contingent upon consistent $f'_{c,test}$. Due to significant discrepancy in $f'_{c,test}$, the provided embedment capacity was significantly larger for SRC2 than SRC3 and SRC4. It should be noted that there was a construction joint in the structural wall at the top of the coupling beam, and $f'_{c,test}$ in Table 3.1 is for the concrete below this construction joint. More detailed information on the construction procedure and material testing is provided in Chapter 4, and more details on the design of the coupling beams, structural walls, and embedment detailing are provided in the following sections.

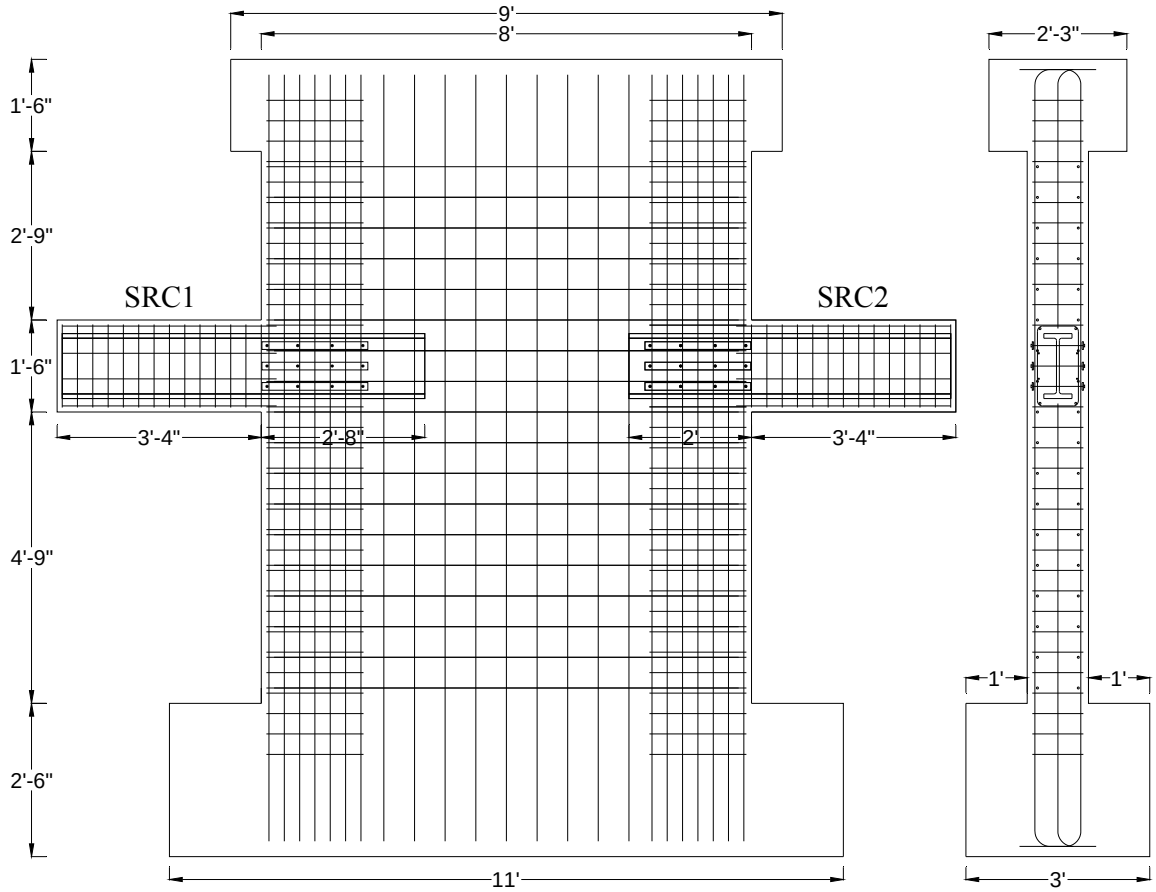

Figure 3.3: Elevation View of First Sub-Assembly (SRC1 and SRC2)

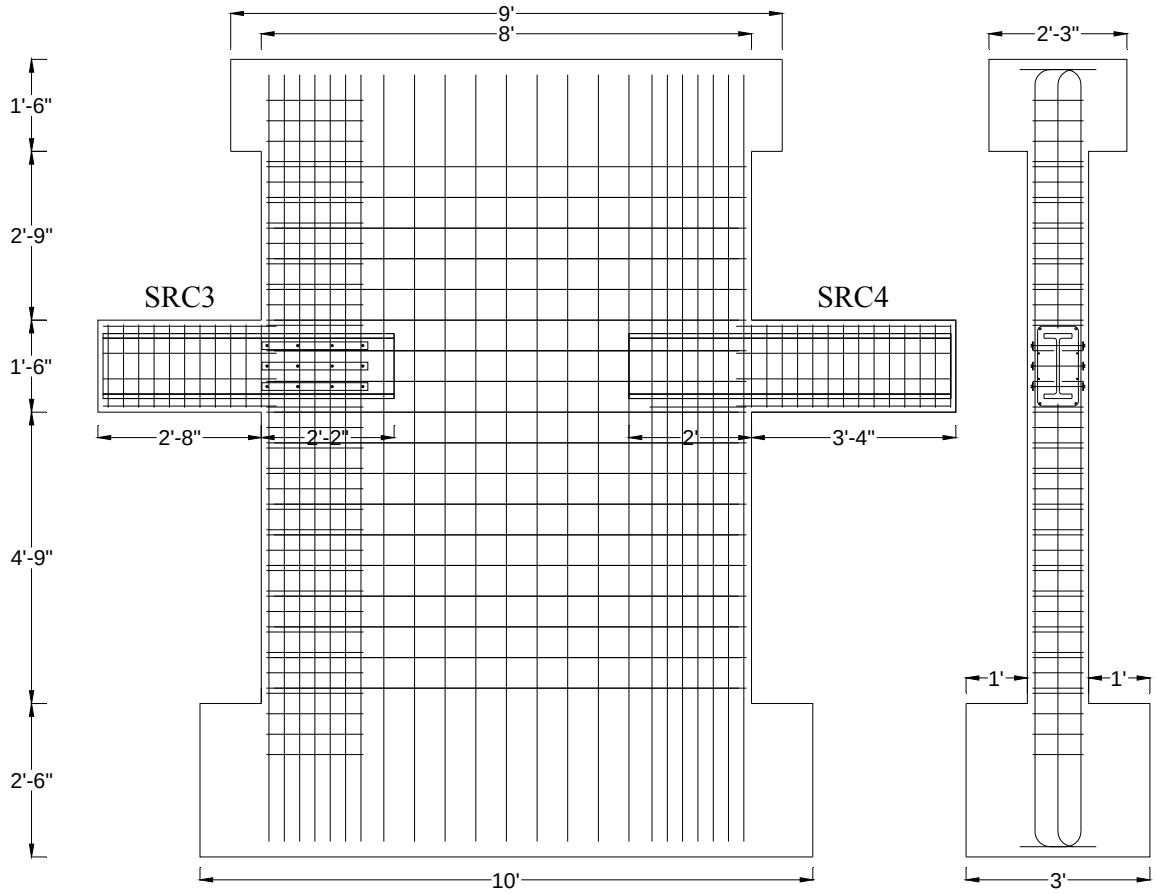

Figure 3.4: Elevation View of Second Sub-Assembly (SRC3 and SRC4)

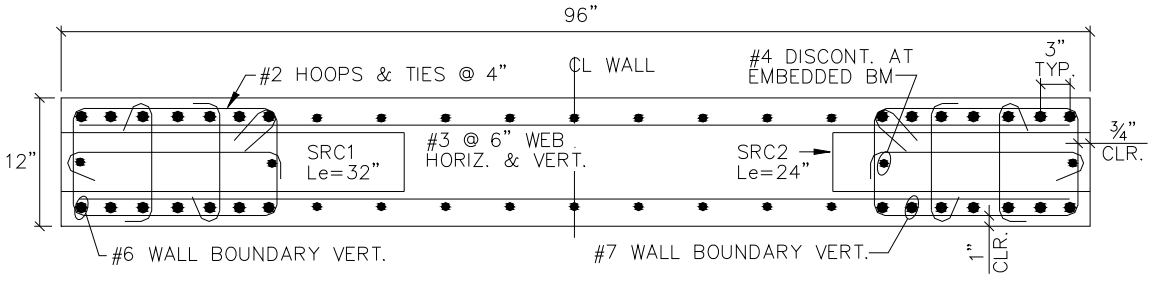

Figure 3.5: Structural Wall Cross-Section for First Sub-Assembly (SRC1 and SRC2)

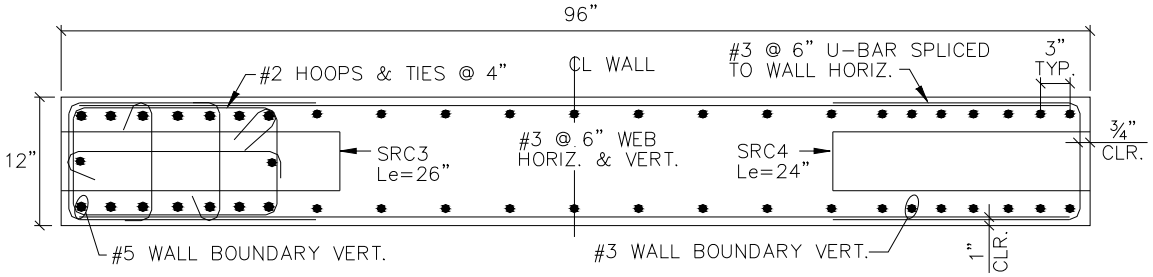

Figure 3.6: Structural Wall Cross-Section for Second Sub-Assembly (SRC3 and SRC4)

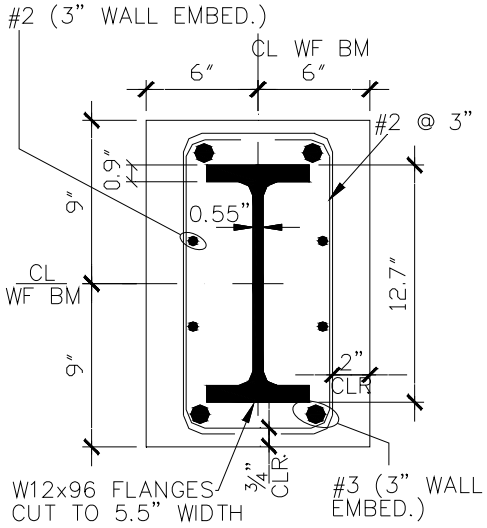

Figure 3.7: Coupling Beam Cross-Section (Same for All Test Specimens)

Table 3.1: Test Matrix

	$\alpha = L/h$	L_e (in.)	ρ_{bound}	bound trans.	f'_c (ksi)	$\varepsilon_{s,max}/\varepsilon_y$
SRC1	3.33	32	0.024	OBE	7.4	0.53
SRC2	3.33	24	0.033	OBE	7.4	0.83
SRC3	2.40	26	0.017	OBE	5.0	1.09
SRC4	3.33	24	0.006	Other	4.6	0.57

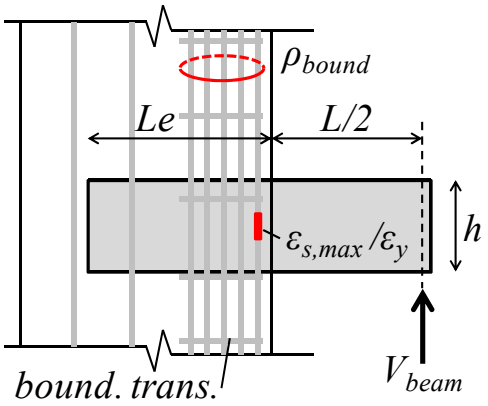

Figure 3.8: Test Variables

3.3 COUPLING BEAMS

The steel section (Figure 3.7) used in all four test beams was a W12x96 AISC (A992, grade 50) section (d = 12.7", t_w = 0.55", b_f = 12.2", and t_f = 0.90") with flanges trimmed to a width of 5.5". This section was selected to approximately represent a one-half-scale W24x250 AISC section (d = 26.3", t_w = 1.04", b_f = 13.2", and t_f = 1.89"), which was assumed for a hypothetical prototype beam. Table 3.2 compares section properties, including an indication of scaling, for the prototype and the test specimen and includes comparisons for two additional steel sections that were considered for the test specimen, namely a W16x50 and a built-up section. The W16x50

was attractive because no modification (i.e., trimmed flanges) was required. However, it is clear from Table 3.2 that better overall scaling of section properties was achieved through the use of the W12x96 with trimmed flanges, noting that the smaller web thickness of the W16x50 was of particular concern. The prototype beam was flexure-controlled for the aspect ratios used in this study, i.e., 2.40 and 3.33 (Table 3.1), while some degree of shear yielding was possible for a W16x50 due to the thin web. The term "flexure-controlled" indicates that the flexural strength of the beam was expected to be reached prior to shear yielding of the beam.

Using a built-up section offered the benefit of precise scaling; however, due to differences in fabrication processes and material properties for wide flange sections and built-up sections, the use of a built-up section was deemed undesirable. With regard to fabrication processes, wide-flange sections are milled or rolled, whereas built-up sections are comprised of three plates welded together. With regard to material properties, wide-flange sections would typically be specified as A992 structural steel, whereas built-up sections would typically be built from A572 grade 50 plates. Liu et al (2007) conducted a survey of mill certificates and a review of published tensile property surveys in order to determine the actual material properties for common structural steel specifications. The results provided a mean and a coefficient of variation, as well as maxima and minima, for the actual yield strength and the actual tensile strength. These results were reflected in the R_y and R_t parameters of the 2005 AISC Seismic Provisions. For structural steel, R_y is the ratio of the average expected yield strength (F_{ye}) to the specified minimum yield strength (F_y), and R_t is the ratio of the average expected tensile strength (F_{ue}) to the specified minimum tensile strength (F_u). As shown in Table 3.3, the mean and standard deviation, based on the results of Liu et al (2007), for the actual yield strength and the

actual tensile strength are larger for A572 grade 50 plate material than for A992 wide flange material.

Table 3.2: Scaling of the Test Specimen to the Assumed Prototype

	W24x250	**W16x50**			**W12x96 w/5.5" width**			**Built-Up Section**		
	Prototype	Specimen	Ratio	Scale	Specimen	Ratio	Scale	Specimen	Ratio	Scale
Z_x (in^3)	744	93.1	0.13	0.50	75.9	0.10	0.47	93.1	0.13	0.50
A (in^2)	73.5	14.7	0.20	0.45	16.1	0.22	0.47	16.1	0.22	0.47
d (in)	26.3	16.3	0.62	0.62	12.7	0.48	0.48	13.0	0.49	0.49
t_w (in)	1.04	0.38	0.37	0.37	0.55	0.53	0.53	0.50	0.48	0.48
b_f (in)	13.2	7.07	0.54	0.54	5.50	0.42	0.42	6.50	0.49	0.49
t_f (in)	1.89	0.63	0.33	0.33	0.90	0.48	0.48	1.00	0.53	0.53

Table 3.3: Actual Yield Strength and Tensile Strength for A992 WF and A572 Gr. 50 Plate (Obtained from Liu et al, 2007)

	Actual Yield Strength (ksi)		Actual Tensile Strength (ksi)	
	A992	A572 Gr. 50	A992	A572 Gr. 50
	(Wide Flange)	(Built-Up)	(Wide Flange)	(Built-Up)
μ	55.0	58.0	72.8	81.9
σ	2.8	4.1	2.9	5.7

An aspect ratio (beam span-to-depth ratio) of 3.33 was used for SRC1, SRC2, SRC4, while an aspect ratio of 2.40 was used for SRC3 (Table 3.1), noting that aspect ratios of 3.33 and 2.40 are typical for office and residential buildings, respectively, in the United States. 12" by 18" reinforced concrete encasement was used for the test beams, which is consistent with an assumed 24" by 36" prototype, leading to 30" and 21.6" cantilever lengths (measured from the beam-wall interface to the point of load application) for the test beams with aspect ratio 3.33 and 2.4,

respectively. In keeping with the prototype, all four test beams were flexure-controlled for the aspect ratios considered. Because the contribution of concrete to shear strength was not required to achieve flexure-controlled beams, coupling beam stirrups, #2 A36 undeformed bars spaced at 3", were fabricated as two U-bars rather than hoops (for ease of construction). #3 beam longitudinal bars were used at each corner of the beam (Figure 3.7) to anchor beam stirrups; these bars extended only 3" into the wall so that they would not contribute significantly to beam flexural strength and increase the demands on the embedment zone. The side clear cover for the coupling beam (Figure 3.7) is 2", which scales to 4" and is much larger than minimum cover requirements. Because the #3 longitudinal bars embedded a few inches into the wall, the large cover was used to avoid having to bend these bars in order to place them inside the wall boundary longitudinal bars.

Table 3.4 was used to guide the selection of the embedment lengths for the first two test beams. The embedment lengths in Table 3.4 were computed by equating $V_{ne,limit}$ to $V_{n,embed}$ in Equation (2.22) and Equation (2.23), the modified (for wall spalling per Harries et al (1993) and Harries et al (2000)) Marcakis and Mitchell (1980) and Mattock and Gaafar (1982) embedment equations, respectively. Equation (2.32) (Equation H4-3 in Section H4.5b(2)(1) of the 2010 AISC Seismic Provisions) was used to determine the limiting shear strength, $V_{ne,limit}$, of the test beams, where $V_{ne,limit}$ is taken as the smaller of the expected shear strength, V_{ne}, and the shear at the expected plastic flexural strength, $V@M_{pe}$, where $V@M_{pe} = 2M_{pe}/L = M_{pe}/a$, noting that $a = L/2$ for the one-half-length cantilever test beams. $V_{ne,limit}$ was equal to $V@M_{pe}$ in all instances (Table 3.4), since the test beams were flexure-controlled (i.e., $V@M_{pe}$ was less than V_{ne}).

Table 3.4: Member Capacity and Corresponding Embedment Length

			μ-2σ	μ-σ	μ	μ+σ	μ+2σ	des. w/o φ	des. w/ φ = 0.9
M_{pe} without Strain Hardening	V_{ne}	k	332.1	346.0	360.0	373.9	387.9	334.6	334.6
	$V@M_{pe}$	k	171.7	178.4	185.1	191.7	198.3	172.9	172.9
	$V_{ne,limit}$	k	171.7	178.4	185.1	191.7	198.3	172.9	172.9
	L_e (M&M)	in	25.3	25.9	26.5	27.1	27.6	25.4	27.1
	L_e (M&G)	in	29.0	29.7	30.4	31.1	31.7	29.1	31.1
M_{pe} with Strain Hardening	V_{ne}	k	332.1	346.0	360.0	373.9	387.9	334.6	334.6
	$V@M_{pe}$	k	160.4	168.2	175.9	183.6	191.3	161.8	161.8
	$V_{ne,limit}$	k	160.4	168.2	175.9	183.6	191.3	161.8	161.8
	L_e (M&M)	in	24.3	25.0	25.7	26.4	27.0	24.5	26.0
	L_e (M&G)	in	27.8	28.6	29.4	30.2	31.0	27.9	29.8

Because M_{pe} and V_{ne} are both sensitive to the yield and tensile strength of structural steel, a range of structural steel properties for the A992 wide flange section was considered in order to account for material uncertainty (reflected in Table 3.4). Specifically, the test results of Liu et al (2007) that were presented previously in Table 3.3 were used to determine the yield strength and tensile strength over a statistical range that included μ-2σ, μ-σ, μ, μ+σ, and μ+2σ. The specified minimum yield and tensile strengths, F_y=50-ksi and F_u=65-ksi, respectively, were also analyzed with and without the inclusion of a strength reduction factor of φ=0.9 in the embedment equations (Equation (2.22) and Equation (2.23)), noting that the selection of φ=0.9 is consistent with the value of the capacity reduction factor inherently included in Equation (2.35) (Equation H4-2 in the 2010 AISC Seismic Provisions) relative to Equation (2.23). A specified compressive strength of concrete of 6-ksi was used for the design calculations. The selected concrete mix design had a lower specified compressive strength of 4.5-ksi with a slightly higher expected 28-day strength of 6.4-ksi. This concrete mix design was selected in an effort to limit the degree to which the actual concrete strength would exceed the strength used for calculations. More details on the concrete mix are provided in Section 4.4.1 and Appendix A.

The values for V_{ne} in Table 3.4 were computed using Equation (2.34) (Equation H5-3 in the 2010 AISC Seismic Provisions), with a sample computation for the test beam cross-section provided here (considering specified material properties):

$$V_{ne} = 1.1R_yV_p + 1.56\left(2\sqrt{f_c'}b_cd_c + \frac{A_{st}f_{yt}d_c}{s}\right)$$
$$= (1.1)(1.1)(0.6)(50ksi)(12.7")(0.55")$$
$$+ (1.56)(2)\frac{\sqrt{6000\,psi}}{1000\,psi/ksi}(12")(17.125") + (1.56)\frac{(2*0.049in^2)(36ksi)(17.125")}{3}$$
$$= 253.56k + 49.66k + 31.42k$$
$$= 334.6k$$

It is interesting to note that over 75% of the provided shear strength is attributed to the web of the embedded steel section.

To determine M_{pe}, the 2010 AISC Seismic Provisions allow the use of either a strain compatibility approach or a plastic analysis approach, both of which were used (Table 3.4). When using the plastic analysis approach, the flexural strength of the beam was computed based on a fully plastic steel section and a uniform stress block for concrete in compression. The strain compatibility approach was based on a plane section analysis of the cross-section assuming no slip between concrete and steel, i.e., a reinforced concrete beam analysis in which structural steel was treated as reinforcement. Sample computations using both approaches are provided in Appendix B. The influence of strain hardening of steel may be included in the moment-curvature analysis. If strain hardening of steel is not considered, the two analytical approaches produce nearly identical results for the sections in this study. In Table 3.4, M_{pe} values were

computed using the plastic analysis approach without consideration of strain hardening of steel and also using the moment-curvature approach with consideration of strain hardening. For cases in which strain hardening was considered, the onset of strain hardening was taken at a strain of 0.005 and the elastic modulus and strain-hardened modulus were taken as 29000-ksi and 1000-ksi, respectively.

Computing M_{pe} using a plastic analysis approach and a strain compatibility approach was done with the assistance of a simple computer spreadsheet, using iteration to determine the neutral axis depth required to achieve section equilibrium. For the strain compatibility approach, the concrete compression zone was divided into five slices, the web of the steel section was divided into ten equivalent slices, and the flanges were taken as a single slice for analytical purposes. The analytical strain-compatibility results were verified using BIAX software (Wallace 1992), by converting the steel section into an equivalent area of reinforcement (with modified material properties) to perform strain-compatibility moment-curvature analysis.

It is noted that both the strain compatibility approach and the plastic analysis approach, used to determine M_{pe}, assume monotonic loading and the development of full composite action (i.e., no slip) between the concrete and steel. Since cyclic loading was applied during coupling beam testing and shear studs were not provided to enhance composite action, these analytical methods were expected to over-predict M_{pe} and subsequently $V_{ne,limit}$, which is conservative for computing minimum required embedment lengths. Additionally, because $V@M_{pe}$ was obtained by dividing M_{pe} by the cantilever distance, a, the intended yield and failure mechanisms are assumed to occur at the beam-wall interface rather than within the wall, suggesting that plastic hinge formation

does not occur within the connection. Since this may not always be the case (as mentioned in Chapter 2, Shahrooz et al (1993) note fixity at $L_e/3$ within the beam-wall interface), this approach was expected to potentially lead to an overestimate of $V@M_{pe}$ and subsequently $V_{ne,limit}$, which is also conservative for computing minimum required embedment lengths.

Prior to construction of the first test specimen sub-assembly, which included the first two test beams, Table 3.4 was used to guide the selection of the embedment lengths for SRC1 and SRC2. Based on the range of required embedment lengths provided in Table 3.4, obtained using a range of structural steel properties (Liu et al 2007) in the two analysis methods (strain compatibility and plastic analysis), a conservative embedment length of 32" was selected for SRC1. An embedment length of 24" was selected for SRC2, in order to assess the degree of conservatism inherent in the embedment equations and better understand embedment behavior.

Testing of SRC2 (which was conducted prior to the design and construction of the second test specimen sub-assembly) suggested that the 24" embedment length was satisfactory. Therefore, for the second test specimen sub-assembly, the embedment lengths for SRC3 and SRC4 were selected to provide the same ratio of embedment strength to limiting shear strength, $V_{n,embed}/V_{ne,limit}$, as SRC2. A 24" embedment length was used for SRC4, since the aspect ratio for SRC4 is the same as for SRC2. By assuming fixity at the beam-wall interface, meaning that the flexure-yielding cantilever coupling beams develop M_{pe} at the beam-wall interface, $V_{ne,limit}$ for SRC3 is larger than for SRC4 by a factor of 3.33/2.4, i.e., the ratio of the coupling beam aspect ratios. Assuming f'_c is constant, the embedment strength is proportional to the cantilever length and the required embedment length as follows:

$$V_{n,embed} = Const.* \frac{(L_e - c)}{0.78 + (a + c)/(L_e - c)} \qquad \text{(Marcakis and Mitchell, 1980)}$$

$$V_{n,embed} = Const.* \frac{(L_e - c)}{0.88 + (a + c)/(L_e - c)} \qquad \text{(Mattock and Gaafar, 1982)}$$

For this test set-up, an increase in limiting shear strength, $V_{ne,limit}$, due to a reduction in cantilever length, a, both proportional to 3.33/2.4, caused the 24" embedment length for SRC2 to increase to 26.4" (10.0% increase) and 26.2" (9.1% increase) for SRC3 using the modified (for spalling) Marcakis and Mitchell (1980) and Mattock and Gaafar (1982) embedment equations (Equation (2.22) and Equation (2.23)), respectively. Thus, a 26" embedment length was selected for SRC3, which was intended to be consistent with the level of embedment strength, $V_{n,embed}/V_{ne,limit}$, provided by the 24" embedment length of SRC2.

3.4 STRUCTURAL WALLS

Figure 3.5 and Figure 3.6 show the structural wall cross-sections for both test specimen sub-assemblies. The wall cross-section dimensions were 12"x96" (1'x8') with ¾" clear cover, representative of a one-half scale 24"x192" (2'x16') prototype with 1.5" clear cover. For the first test specimen sub-assembly, prototype wall boundary longitudinal reinforcement was initially assumed to be 22-#11 bars (A_s = 34.32 in^2) leading to 20-#6 bars (A_s = 8.80 in^2) for the scaled specimen, noting that the area of reinforcement reduces by one-quarter at one-half scale due to similitude concepts. 20#6 bars (A_s = 8.80 in^2) were modified to 14-#7 (A_s = 8.54 in^2) bars to allow the use of fewer bars and increase bar spacing. This arrangement was further modified

to 14-#7 (A_s = 8.54 in^2) at one wall boundary and 14-#6 (A_s = 6.16 in^2) at the opposite wall boundary. Asymmetry in the provided area of wall boundary longitudinal reinforcement was desired in order to make for a more interesting structural wall test (one additional variable), as the structural wall was repaired and tested to failure after the completion of the first two coupling beam tests.

ACI 318 Chapter 21 and Appendix A (strut-and-tie modeling) code provisions were used to further guide the design of the structural wall. Within the embedment zone, coupling beam bearing forces were assumed to transfer into wall vertical reinforcement. A conceptual load path for the structural wall, including the coupling beam bearing forces, is shown in Figure 3.9. When the coupling beam is loaded upward (positive), the structural wall demands create compression across the embedment zone. In this case the coupling beam bearing forces reduce the magnitude of wall compression across the connection, possibly even creating local tension across the connection if the wall demands are small relative to the beam demands. When the coupling beam is loaded downward (negative), the structural wall demands create tension across the connection. In this case the coupling beam bearing forces increase local wall tensile demands across the embedment zone, potentially causing local yielding of the wall boundary longitudinal reinforcement.

Assuming that the first two test beams (SRC1 and SRC2) would develop the same strength during testing, strain compatibility fiber analysis of the embedment zone suggested that the coupling beam bearing forces would be larger for the section with shorter embedment length. This makes sense conceptually, as larger bearing forces are required to satisfy moment

equilibrium since the distance between the two resultant bearing forces is shorter. The larger bearing forces of SRC2 relative to SRC1 were expected to impart larger local tensile demands into wall boundary longitudinal reinforcement. For this reason, 14#7 wall verticals were used on the side of the wall with SRC2, and 14#6 wall verticals were used on the side with SRC1.

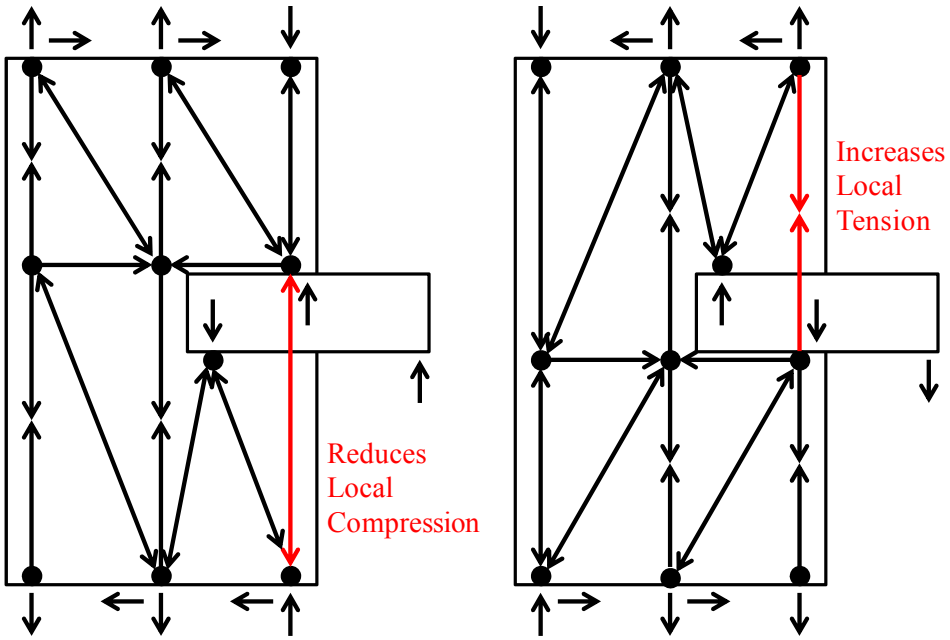

Figure 3.9: Conceptual Load Path

An intermediate level of wall boundary transverse reinforcement is representative of a mid-to-upper-level story for a high-rise reinforced concrete building in Seismic Design Category C, D, E, and F. For SRC1, SRC2, and SRC3, boundary transverse reinforcement was provided to satisfy provisions for an intermediate level of boundary confinement (often referred to as an "ordinary boundary element"), namely ACI 318-11 Section 21.9.6.5, which requires an 8" maximum vertical spacing. Assuming #4 hoops and ties at 8" spacing for the prototype suggested #2 hoops and ties at 4" spacing. ACI 21.9.6.5 also requires that $h_x \leq 14$" (per ACI

21.6.4.2 as mandated within ACI 21.9.6.5), which scaled to $h_x \leq 7$". h_x is defined as the maximum center-to-center horizontal spacing of cross-ties or hoop legs. Two cross-ties were used for the test specimen in the short direction as shown in Figure 3.5 and Figure 3.6; therefore, $h_x = 7.125$" for the #7 verticals (deemed close enough to 7"). A central cross-tie was also needed in the long direction to satisfy the h_x requirement. Discontinuous (due to the embedded steel section) #4 vertical bars were used as placeholders for this cross-tie and were embedded into the footing and the concrete top beam.

Coupling beam strengths do not typically reduce significantly over the height of the building, although the wall strength reduces significantly as height increases. SRC4 was intended to represent the upper-level stories in a typical high-rise coupled core wall, in which the coupling beam shear strength is larger relative to the wall, which is lightly-reinforced, sometimes excluding boundary transverse reinforcement. Per ACI 318-11 Section 21.9.6.5(a), wall boundary transverse reinforcement is not required when the longitudinal reinforcement ratio at the wall boundary, ρ_{bound}, does not exceed $400/f_y$ (which corresponds to $\rho_{bound} = 0.0067$ for grade 60 reinforcement). Therefore, boundary transverse reinforcement (hoops and ties) was not required for SRC4 since 14#3 bars were used for boundary longitudinal reinforcement ($\rho_{bound} = 0.0061$). It is noted that bar buckling of wall boundary longitudinal reinforcement is influenced by the ratio of the spacing of wall boundary transverse reinforcement, s, to wall boundary longitudinal bar diameter, d_b. The s/d_b ratios for SRC1, SRC2, SRC3, and SRC4 were 5.3, 4.6, 6.4, and 16.0, respectively, suggesting that the likelihood of bar buckling is significantly increased for SRC4 relative to the other beams due to the lack of an ordinary boundary element. Generally, this is not an issue at upper levels of the wall, since wall boundary longitudinal

reinforcement does not yield. However, SRC coupling beams can increase local tension (Figure 3.9), leading to yielding of boundary longitudinal reinforcement and greater likelihood of bar buckling.

For SRC3, since the primary test variable was intended to be the aspect ratio, consideration was given to using 14#7 as wall boundary longitudinal reinforcement to be consistent with SRC2. However, the use of 14#7 (ρ_{bound} = 0.0333) on one side of the wall with 14#3 (ρ_{bound} = 0.0061) on the other side would have created a significant mismatch (with reinforcement ratios differing by a factor of 5.5), and the use of 14#5 (ρ_{bound} = 0.0172) was selected as an appropriate middle ground (with reinforcement ratios differing by a factor of 2.8). With 14#5 the ratio of wall boundary longitudinal reinforcement was well above $400/f_y$, consistent with the use of an intermediate level of boundary confinement (i.e., an ordinary boundary element), #2@4" hoops and ties (per ACI 318-11 Section 21.9.6.5), consistent with SRC1 and SRC2.

For all specimens, the wall web longitudinal and transverse reinforcement ratios, ρ_l and ρ_t, respectively, were selected to satisfy the code minimum, which is ρ_l = 0.0025 and ρ_t = 0.0025 per ACI 318-11 Section 21.9.2.1. At one-half-scale, #6@12" spacing (ρ_l = 0.0031 and ρ_t = 0.0031) scaled to #3@6" spacing (ρ_l = 0.0031 and ρ_t = 0.0031). For the second specimen sub-assembly, #3 U-bars engaging wall boundary longitudinal reinforcement were spliced to the #3 wall web horizontal reinforcement at both ends of the wall per ACI 318-11 Section 21.9.6.5(b). Although code mandated, this detail was omitted for the first specimen sub-assembly, and the horizontal web bars were embedded (without hooks) into the cores of the ordinary boundary elements.

It is noted that, in certain instances, wall thickness may place limitations on the maximum flange width of the embedded steel coupling beam, since the beam flange must fit within the opening between wall boundary longitudinal reinforcement. For the structural wall prototype (24" wall thickness, #11 wall vertical reinforcement, #4 wall boundary transverse reinforcement, and 1.5" clear cover), the maximum embedded flange width was computed to be 17.2", and for the test specimen with the largest wall boundary longitudinal bars, namely SRC2 (12" wall thickness, #7 wall boundary longitudinal reinforcement, #2 wall boundary transverse reinforcement, and 0.75" clear cover), the maximum flange width of the embedded steel section was computed to be 8.25". For both the prototype and the test specimen, the flange (trimmed in the case of the test specimen) could easily fit between the wall boundary longitudinal reinforcement. For thin walls, this is not always the case.

3.5 EMBEDMENT DETAILING

Figure 3.10 shows the wall boundary detailing at the connection zone. Due to the presence of the embedded steel section, standard hoops and cross-ties could not be placed. In order to maintain wall boundary confinement through the depth of the embedded beam, pre-drilled holes through the web of the steel section allowed the use of threaded rods and steel plates. The threaded rods were sized to achieve the desired level of confinement, while the A36 steel plates measured 0.25"x1.5"x20.5". This detailing was used for SRC1, SRC2, and SRC3, but was not necessary for SRC4, since SRC4 did not include boundary transverse reinforcement (i.e., an ordinary boundary element).

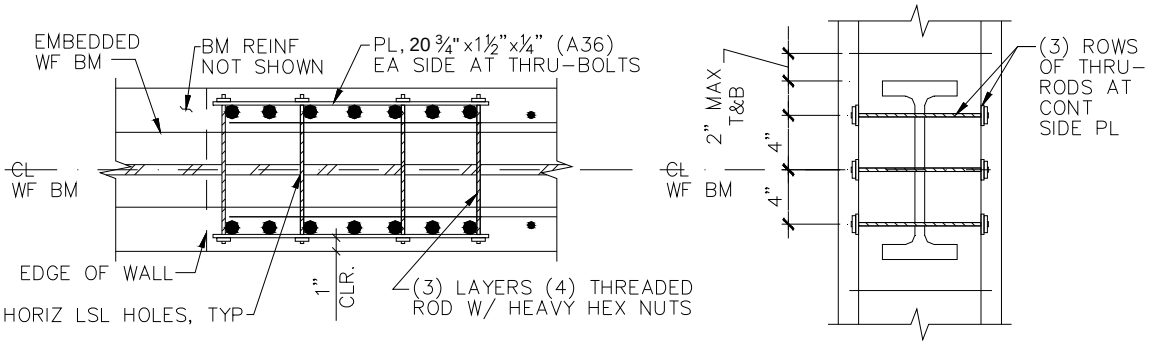

Figure 3.10: Embedment Detail (Plan View and Elevation View)

For the first test specimen sub-assembly, 5/16" diameter A307 Grade A threaded rod was selected in an effort to provide a level of confinement equivalent to that provided by the A36 ¼"-diameter smooth bar used as wall boundary transverse reinforcement. The minor diameter for 5/16"-18 threaded rod is 0.24". Interestingly, A36 or F1554 grade 36 threaded rod was not available in diameters less than ½". Table 2-5 in the 2005 AISC Steel Construction Manual indicates no specified yield strength and a tensile strength of 60-ksi for A307 Grade A, consistent with the specified tensile strength of 58-80 ksi for A36 and F1154 Grade 36. Material testing after the completion of construction indicated that the A307 Grade A threaded rods were stronger and less ductile than expected. More information on material testing is provided in Chapter 4 and Appendix A.

The surprising material test results for the A307 Grade A threaded rods prompted a more thorough investigation regarding threaded rods prior to constructing the second test specimen. Through material testing and interaction with material suppliers, interesting information was determined regarding threaded rods. Material suppliers categorize and sell/distribute threaded rod based on the certification of the stock bar, prior to machining the bar into the finished

product. The machining process typically alters the material properties of the threaded rod due to work hardening. For this reason, threaded rod typically displays higher strength and lower ductility than the specified material properties would suggest. In order to carefully select a threaded rod with strength and ductility similar to the 1/4"-diameter smooth rod used as wall boundary transverse reinforcement, tensile testing was conducted on numerous threaded rod specimens. Namely, the following specimens were tested: 3/8" and 5/16" low strength steel; 1/4" B7 alloy; 1/4" grade 8; 5/16", 1/4", #12-24, #10-32, #10-24, and #8-32 grade 18-8 stainless steel. The results of all tensile tests are shown in Appendix A. #12-24 grade 18-8 threaded rod was selected for the second test specimen sub-assembly (referring to the plot in Appendix A), as this rod best matched the strength of the A36 smooth bar and was deemed to display adequate ductility (tensile failure at ~6% strain) to be used as wall boundary transverse reinforcement.

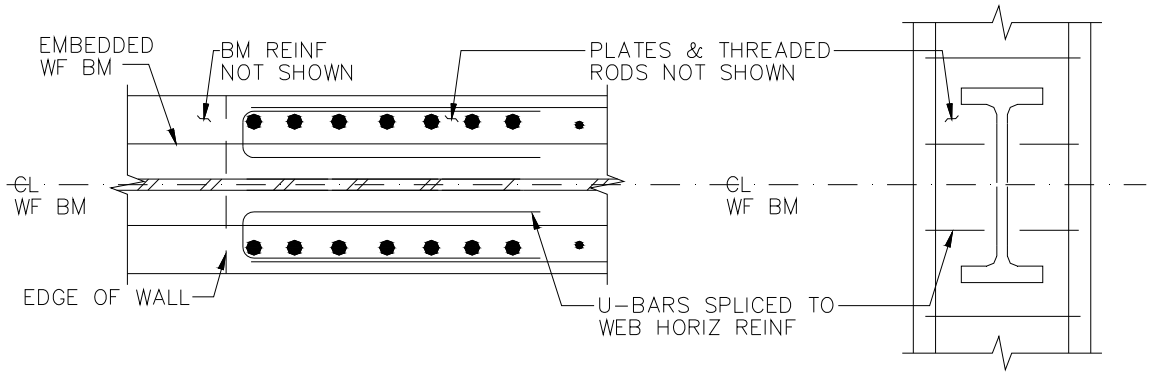

Figure 3.11: U-Bars Spliced to Web Horizontal Reinforcement at Embedded Steel Section

At wall boundary locations where web horizontal reinforcement is required to be provided with either 90-degree hooks or spliced to U-bars per ACI 318-11 Section 21.9.6.5(b), due to the difficulty associated with passing 90-degree hooks or U-bars through the web of the embedded steel section, an alternative detail (Figure 3.11), where individual U-bars spliced to individual

horizontal web bars in the embedment region (without passing the U-bar through the web of the steel section), was used.

Despite the detailing requirements of the 2010 AISC Seismic Provisions, auxiliary transfer bars and bearing plates (Figure 1.4) were not provided in the embedment zone for the test specimens. Transfer bars and bearing plates provide load transfer mechanisms in addition to bearing. This study was intended to assess the reliability of the embedment equations without the added benefit of additional load-transfer mechanisms.

4 Experimental Program

4.1 MATERIALS

4.1.1 Concrete

As mentioned previously, design calculations were based on 6-ksi compressive strength of concrete. A mix design with 4.5-ksi specified minimum strength, f'_c, and an expected 28-day compressive strength of 6.4-ksi based on laboratory tested cylinders was selected. The mix design for the normal-weight concrete is provided in Appendix A. Each test specimen sub-assembly was constructed in three pours, creating construction joints at the foundation-wall interface and at the top of the coupling beams, consistent with typical construction practice for coupled core walls. 6" by 12" concrete cylinders were cast for each pour. Within +/- one day of specimen testing, standard compression testing of the concrete cylinders was conducted at the UCLA material testing laboratory, including one cylinder from the foundation pour, three cylinders from the lower wall pour (which includes the coupling beam concrete), and three cylinders from the upper wall pour. For all test specimens, the as-tested compressive strength of concrete, $f'_{c,test}$, and the corresponding strain, $\epsilon_{0,test}$, are shown in Table 4.1 for all cylinder tests, and average values for the lower wall and upper wall cylinder tests are shown in Table 4.2. The stress-strain plots for individual cylinder tests are provided in Appendix A.

Referring to Table 4.2, it is important to note the significant difference between $f'_{c,test}$ for SRC1 and SRC2 compared to SRC3 and SRC4. Since embedment strength is proportional to concrete strength per the Marcakis and Mitchell (1980) and Mattock and Gaafar (1982) embedment models, this difference in $f'_{c,test}$ is significant with regard to embedment strength. This issue is discussed in greater detail in Chapter 5.

Table 4.1: Concrete Cylinder Test Results

Beam		Footing	Lower #1	Lower #2	Lower #3	Upper #1	Upper #2	Upper #3
SRC1	$f'_{c,test}$ (ksi)	6.6	7.7	7.6	6.9	7.8	7.7	7.6
	$\varepsilon_{0,test}$ (in/in)	0.0026	0.0029	0.0030	0.0023	0.0032	0.0030	0.0030
SRC2	$f'_{c,test}$ (ksi)	5.9	7.7	7.2	N.A.	7.9	7.4	7.8
	$\varepsilon_{0,test}$ (in/in)	0.0023	0.0030	0.0027	N.A.	0.0032	0.0028	0.0032
SRC3	$f'_{c,test}$ (ksi)	5.2	4.9	5.2	5.0	4.7	4.6	4.2
	$\varepsilon_{0,test}$ (in/in)	0.0013	0.0021	0.0027	0.0022	0.0019	0.0020	0.0009
SRC4	$f'_{c,test}$ (ksi)	6.2	5.1	4.2	4.5	5.6	5.4	5.2
	$\varepsilon_{0,test}$ (in/in)	N.A.	N.A.	0.0015	0.0018	0.0028	0.0022	0.0024

Table 4.2: Average Values Obtained from Concrete Cylinder Testing

	SRC1		SRC2		SRC3		SRC4	
	Lower	Upper	Lower	Upper	Lower	Upper	Lower	Upper
$f'_{c,test}$ (ksi)	7.4	7.7	7.4	7.7	5.0	4.5	4.6	5.4
$\varepsilon_{0,\ test}$ (in/in)	0.0027	0.0031	0.0029	0.0031	0.0023	0.0016	0.0016	0.0024

4.1.2 Steel

All four embedded structural steel sections were cut from the same ASTM A992 Grade 50 W12x96 stock beam. Three steel coupons were cut from both the flange and the web of the stock beam in accordance with the recommended American Society of Testing and Materials (ASTM) A370-07a coupon dimensions. These coupons were tested at Twining Laboratories in Long Beach, CA. Important parameters obtained from material testing are provided in Table 4.3. More detailed information on material testing is provided in Appendix A.

Table 4.3: Structural Steel Material Testing Results

	Flange				Web			
	#1	#2	#3	Average	#1	#2	#3	Average
$F_{y,test}$ (ksi)	62.0	51.3	51.3	54.9	62.0	63.9	55.5	60.5
$F_{u,test}$ (ksi)	84.5	75.7	76.5	78.9	80.2	81.8	76.6	79.5
% elong.	26.3	27.5	23.8	25.8	22.5	17.5	23.8	21.3

With the exception of the #2 undeformed bars and the threaded rods in the embedment zones, all steel reinforcement used to construct the test specimens conformed to the American Society of Testing and Materials (ASTM) designation A615 or A706 Grade 60. Upon delivery of all ASTM A615/A706 Grade 60 deformed bars, Pacific Coast Steel provided mill certificates from suppliers Nucor Steel Kingman, LLC, Gerdau Ameristeel, and Cascade Steel Rolling Mills, Inc. The #2 bars used for coupling beam shear reinforcement and structural wall boundary transverse reinforcement, which were ASTM A36 smooth bar rather than deformed bar, due to the lack of availability of #2 deformed bar, were obtained from a local material supplier. Three samples

each of the #2 smooth bars were tested in the UCLA material testing laboratory. Important parameters obtained from mill certificates and material testing are summarized in Table 4.4, with more detailed information on material testing of the #2 undeformed bars provided in Appendix A. Values shown for the #2 bar in Table 4.4 were based on the average of three tests.

Table 4.4: Structural Steel Material Testing Results

	SRC1 and SRC2					SRC3 and SRC4		
Bar Size	#7	#6	#4	#3	#2 (1/4") undef.	#5	#3	#2 (1/4") undef.
$F_{y,test}$ (ksi)	71.0	77.5	72.0	63.9	50.9	61.8	68.0	50.9
$F_{u,test}$ (ksi)	95.5	104.0	109.0	102.5	72.3	83.6	105.0	72.3
% elong.	19	14	13	14	21	19	14	21

For SRC1 and SRC2, the 5/16"-diameter threaded rods used in the embedment zone were A307 Grade A, due to the lack of availability of A36 or F1554 Grade 36 threaded rod in diameters less than ½". These threaded rods were attached with A563 Grade A heavy hex nuts during construction. For SRC3, the #12 (0.216" diameter) threaded rods were American Iron and Steel Institute (AISI) Type 18-8 stainless steel. These threaded rods were secured during construction with AISI Type 18-8 stainless steel heavy hex nuts. The steel plates used with the threaded rods to provide confinement of the wall boundary at the embedment zone were A36. No material testing was performed for this A36 plate steel. Three samples each of the 5/16"-diameter and #12 (0.216"-diameter) threaded rod were tested in the UCLA material testing laboratory. More detailed material information is provided in Appendix A.

4.2 CONSTRUCTION

All test specimens were constructed in the UCLA Structural Earthquake Engineering Laboratory by Charles Pankow Builders, Ltd. Construction of the first test specimen sub-assembly was completed in September, 2011 and testing of SRC1 and SRC2 took place in March, 2012 and April, 2012, respectively. Construction of the second test specimen sub-assembly was completed in December, 2013, and testing of SRC3 and SRC4 took place in February, 2013 and April, 2013, respectively.

A general summary of the construction sequence is as follows:

1. Footing formwork constructed
2. Footing reinforcement assembled (floor-level) and placed
3. Wall formwork constructed for one face of wall
4. Wall boundary element reinforcement assembled (floor-level) and placed
5. Wall web bars placed individually (no floor-level assembly)
6. Concrete poured to top of footing
7. Coupling beam formwork constructed
8. Embedded steel sections placed
9. Coupling beam reinforcement assembled (floor-level) and placed
10. Formwork closed to top of coupling beams
11. Concrete poured to top of coupling beams
12. Top beam reinforcement assembled (floor-level) and placed
13. Top beam formwork constructed around top beam reinforcement
14. Formwork closed to top of specimen

15. Concrete poured to top of specimen

One of the noteworthy difficulties encountered during the construction process was the installation of the threaded rod and steel plate embedment detail. Formwork was built to full-height of the wall along one long face and both sides of the structural wall, leaving access from only one wall face. This made it very difficult to thread the nuts onto the threaded rods due to the congestion in this region. If possible, leaving both sides of the formwork open or leaving a temporary gap in the formwork at the embedment region could provide easy access to this area and speed up the installation process.

Construction photos are shown in Figure 4.1 through Figure 4.10. Figure 4.1 shows the coupling beam cross-section. Figure 4.2 and Figure 4.3 show the structural wall reinforcement for both test specimen sub-assemblies prior to the installation of the coupling beams. Figure 4.4 shows the threaded rod and side plate embedment detail. Figure 4.5 through 4.8 show the embedded steel section and reinforcement for all four test beams. Figure 4.9 and Figure 4.10 show the wall boundary reinforcement for an intermediate level of wall boundary confinement (ordinary boundary element) and no wall boundary confinement, respectively.

Figure 4.1: Typical Coupling Beam Cross-Section

Figure 4.2: Structural Wall Reinforcement for Sub-Assembly #1 (with SRC1 and SRC2)

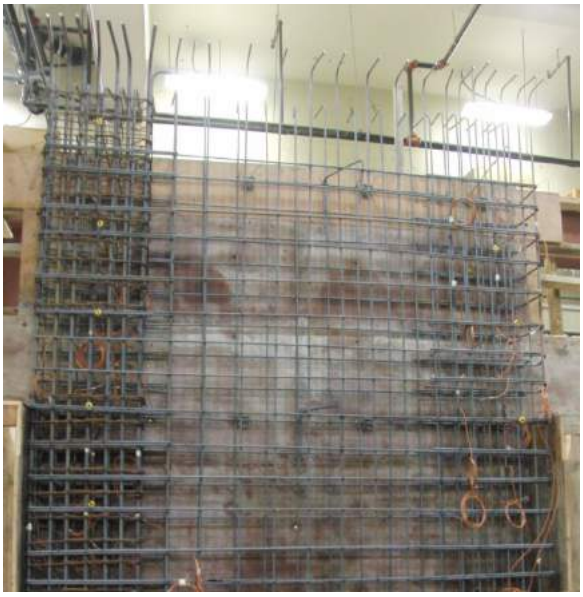

Figure 4.3: Structural Wall Reinforcement for Sub-Assembly #2 (with SRC3 and SRC4)

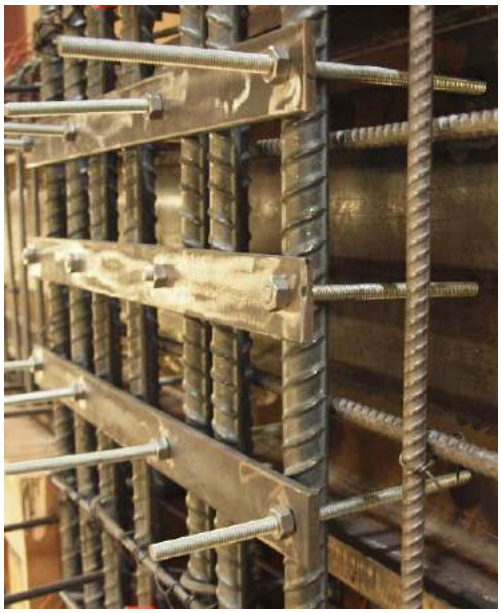

Figure 4.4: Close-Up of Embedment Detail

Figure 4.5: SRC1 Embedded Steel Section and Reinforcement

Figure 4.6: SRC2 Embedded Steel Section and Reinforcement

Figure 4.7: SRC3 Embedded Steel Section and Reinforcement

Figure 4.8: SRC4 Embedded Steel Section and Reinforcement

Figure 4.9: Intermediate Wall Boundary Transverse Reinforcement (Ordinary Boundary Element)

Figure 4.10: No Wall Boundary Transverse Reinforcement

4.3 TEST SET-UP

The overall test set-up is shown in a schematic in Figure 4.11 and a photo in Figure 4.12. The test specimen consisted of a reinforced concrete structural wall with two one-half-length SRC coupling beams (one on each side of the wall) which were tested individually. A 200-kip (max.) actuator with +/- 12" stroke was used to apply vertical load to the cantilever coupling beam. The point of load application represents the midpoint, which is also an inflection point for the full-span-length coupling beam, assuming that the full-length coupling beam has fixed-fixed end conditions and develops equal moment capacity at the beam-wall interface in positive moment at one end and negative moment at the other end. Six-inch wide steel bearing plates, shown in Figure 4.13, were used to apply load to the coupling beam. A 275-k upper bound estimate of the peak applied load was based on the mean plus two standard deviation $V_{ne,limit}$ from Table 3.4, modified to account for the difference in aspect ratio of SRC3 and the other test beams (198.3-k * 3.33/2.4 = 275-k). Based on the 275-k load and the 72-in^2 bearing area for each plate, the applied stress was not expected to exceed 3.8-ksi, which is slightly lower than f'_c.

To generate wall overturning moment, two 400-kip (max.) actuators with +/- 24" stroke were used to apply equal and opposite vertical loads. The wall lateral shear force (and additional moment) was applied by a 300-kip (max.) actuator with +/- 12" stroke. To support the lateral reaction from the 300-kip actuator, reaction blocks were stacked, grouted at the interfaces, and post-tensioned to the laboratory strong-floor with 1.25" diameter high-strength Dywidag rod. The "concrete top beam" in Figure 4.11 refers to a thickened portion at the top of the structural wall (poured continuously with the upper wall), which was constructed to facilitate anchorage to

the steel loading beam (positioned across the top of the specimen). The top beam and footing were post-tensioned to the steel loading beam and the laboratory strong floor, respectively.

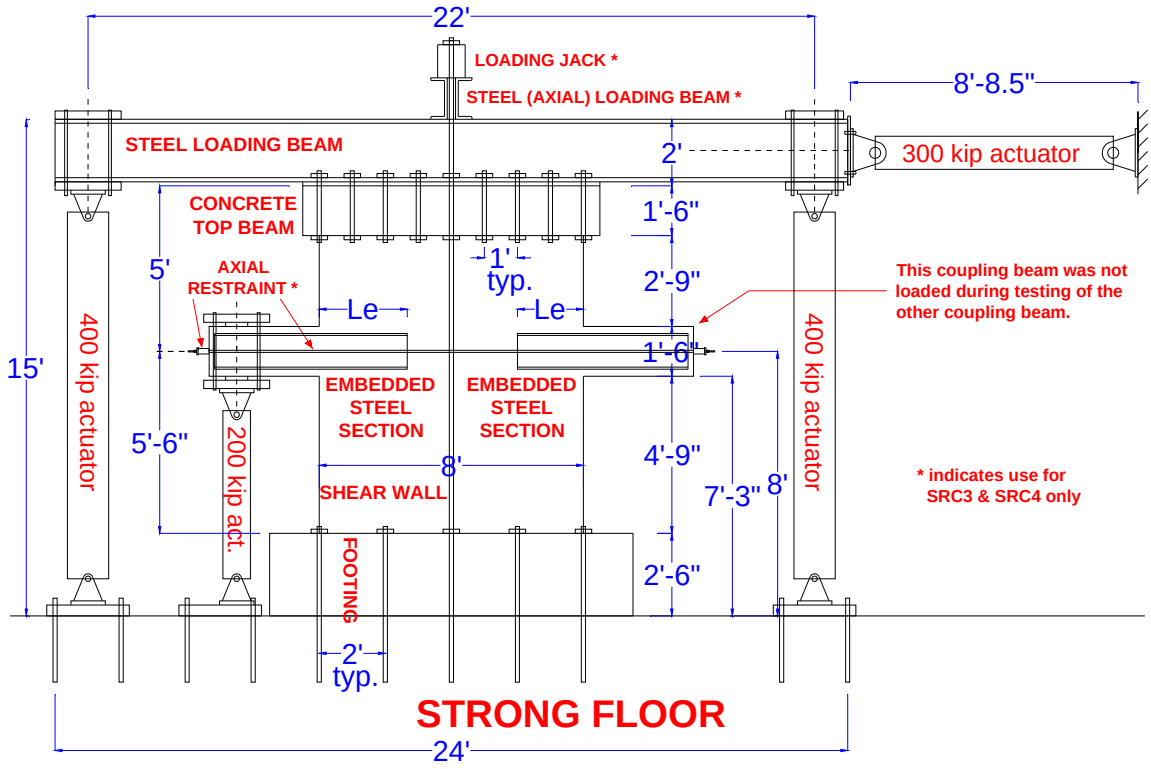

Figure 4.11: Test Set-Up

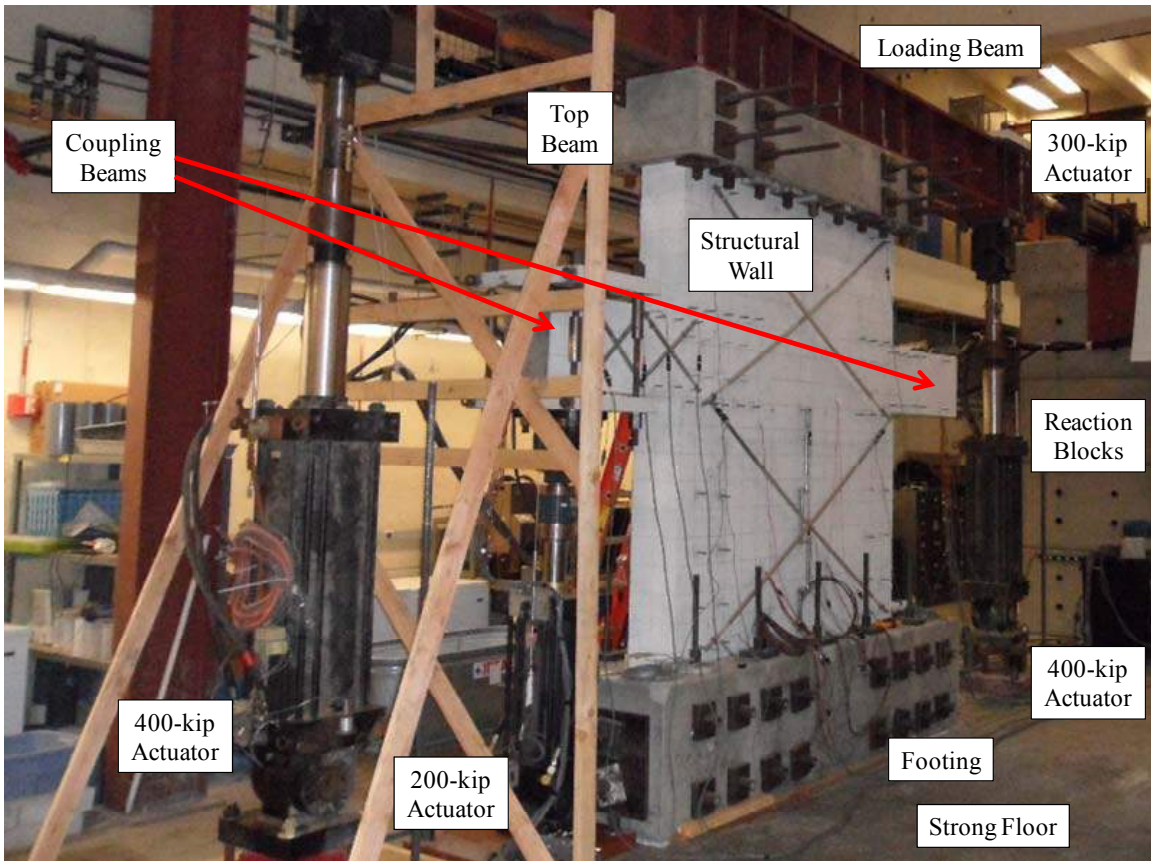

Figure 4.12: Photo of the Test Set-Up

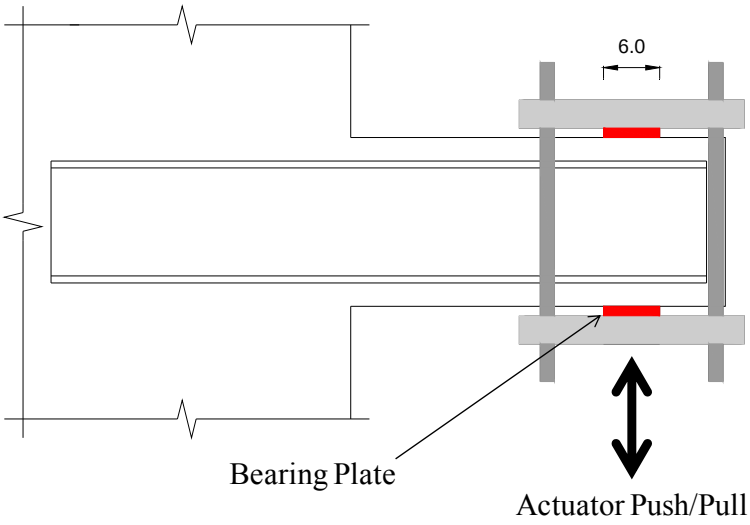

Figure 4.13: Application of Coupling Beam Load

A steel brace was attached to the loading beam to prevent out-of-plane displacement or torsion of the specimen during testing. During testing of SRC3 and SRC4, the loading jack at the top of the wall, which was controlled by a (manual) hand pump, was used to apply axial compressive load to the wall. For SRC3 and SRC4 additional axial load was initially applied by the two vertical 400-kip actuators before they were used for the remainder of the test to apply equal and opposite vertical loads to create reversed-cyclic structural wall overturning moment.

Because coupling beam axial load is dependent on structural lay-out, geometry, applied loads, and in-plane diaphragm restraint, it was not simulated for SRC1 and SRC2 due to the lack of a specific prototype structure. However, due to the large axial growth of SRC2 (discussed in detail in Chapter 5), axial restraint in the form of two 3/8"-diameter ASTM A193 Grade B7 threaded rods (one on each side of the wall) was added for SRC3 and SRC4. The threaded rods spanned across the test specimen sub-assembly, from end-to-end of the two coupling beams, and were located at the beam centerline. These rods were not post-tensioned, meaning that the coupling beam axial load was initially zero but increased as the beam elongated axially, similar in theory to an actual coupling beam. These rods were sized to never provide greater than ~20-kips (~$0.02A_g f'_c$) of total axial restraint. Analysis suggests that this level of axial load has little P-M effect on the section, increasing the flexural capacity of the coupling beam by ~2%. This level of axial restraint is likely significantly less than what exists in actual structures, where restraint is provided by a floor slab and the adjacent structural wall into which the steel section is embedded. Material testing on the threaded rods was carried out at the UCLA materials testing laboratory, and the results are included in Appendix A.

4.4 INSTRUMENTATION

The specimen was instrumented with linear variable differential transformers (LVDTs) and strain gages to record global and local deformations in the beams and the wall. Figure 4.14 shows the layout of LVDTs used in the test specimen. 3/8”-diameter threaded rods were embedded through the wall and SRC beams during construction, oriented horizontally relative to the strong floor, to provide attachment points for LVDTs. These rods extended through the specimen to allow the measurement of an average strain over the gage length. Longitudinal sensors measured flexural deformations, while diagonal sensors measured shear deformations. Sensors oriented across an interface detected slip/extension deformations, and sensors mounted to an external reference frame (not the specimen) at one end measured global deformations.

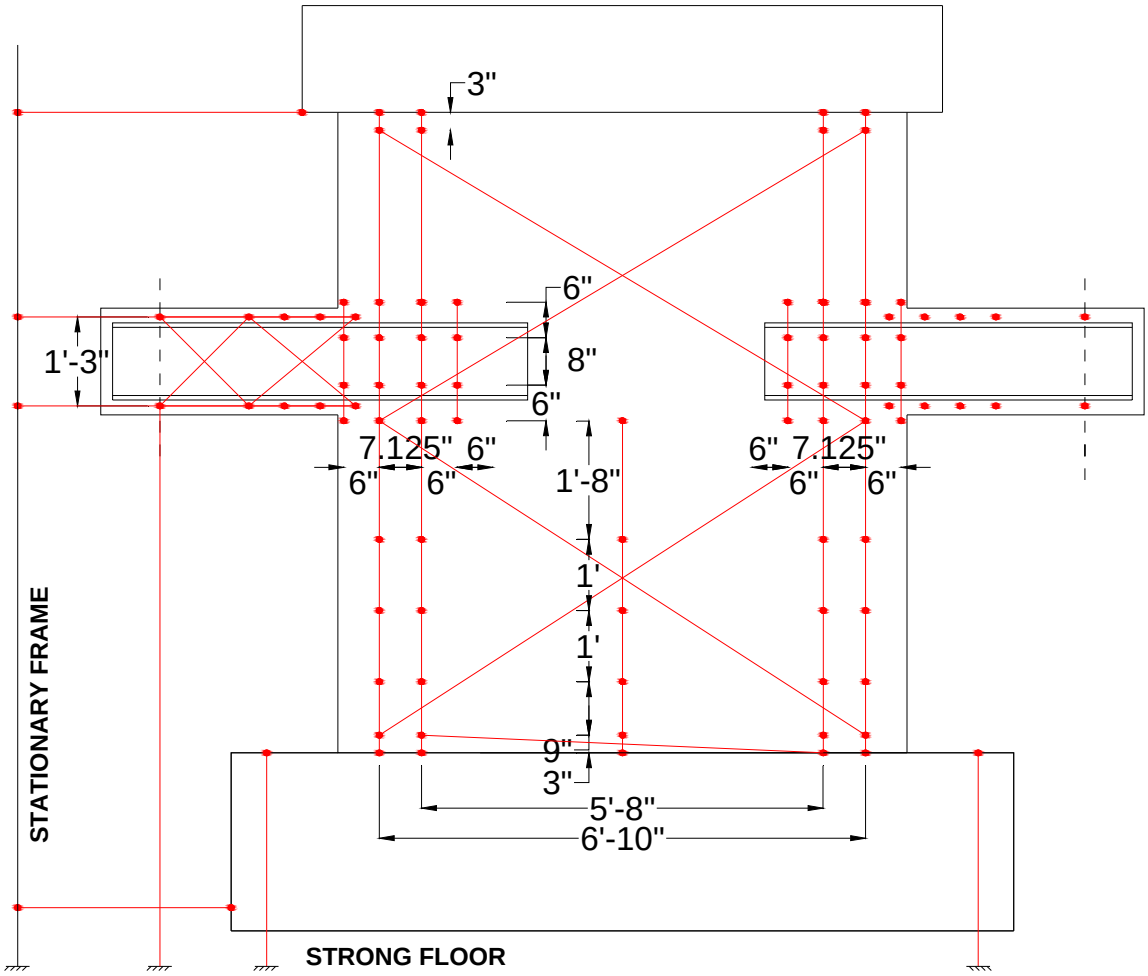

Figure 4.14: Typical LVDT Layout

Figure 4.15 and Figure 4.16 show the layout of strain gages in the first and second test specimen sub-assemblies, respectively, while Figure 4.17 and Figure 4.18 show the corresponding layout of strain gages on the embedded steel sections, noting that additional strain gages were added to the second test specimen sub-assembly relative to the first test specimen sub-assembly. Strain gages were installed on the steel sections at the quarter points along the embedded length in order to measure the strain profiles at these cross-sections. A photo of the two embedded steel sections with strain gages prior to installation in the second test sub-assembly is shown in Figure

4.19, noting that the strain gages shown at the intersection of the flange and the web in Figure 4.17 and Figure 4.18 were installed on the inside of the flange roughly halfway between the web and the edge of the flange. The strain gages on the wall boundary longitudinal bars in the vicinity of the embedded steel sections were intended to measure the local strains imparted into the wall from the coupling beam bearing stresses. The strain gages near the base of the wall were intended to be most useful for the structural wall test (after completion of the beam test and repair of the damage), since these sensors were located within the expected plastic hinge region of the structural wall. In addition to the strain gages installed on steel, two vertically-oriented embedded (concrete) strain gages were installed directly beneath the embedded end of each steel beam, as shown in Figure 4.20. In an effort to study the spread of bearing strain in the out-of-plane direction, one gage was installed directly beneath the beam centerline (aligned with the web) and the other was installed below the outside of the flange.

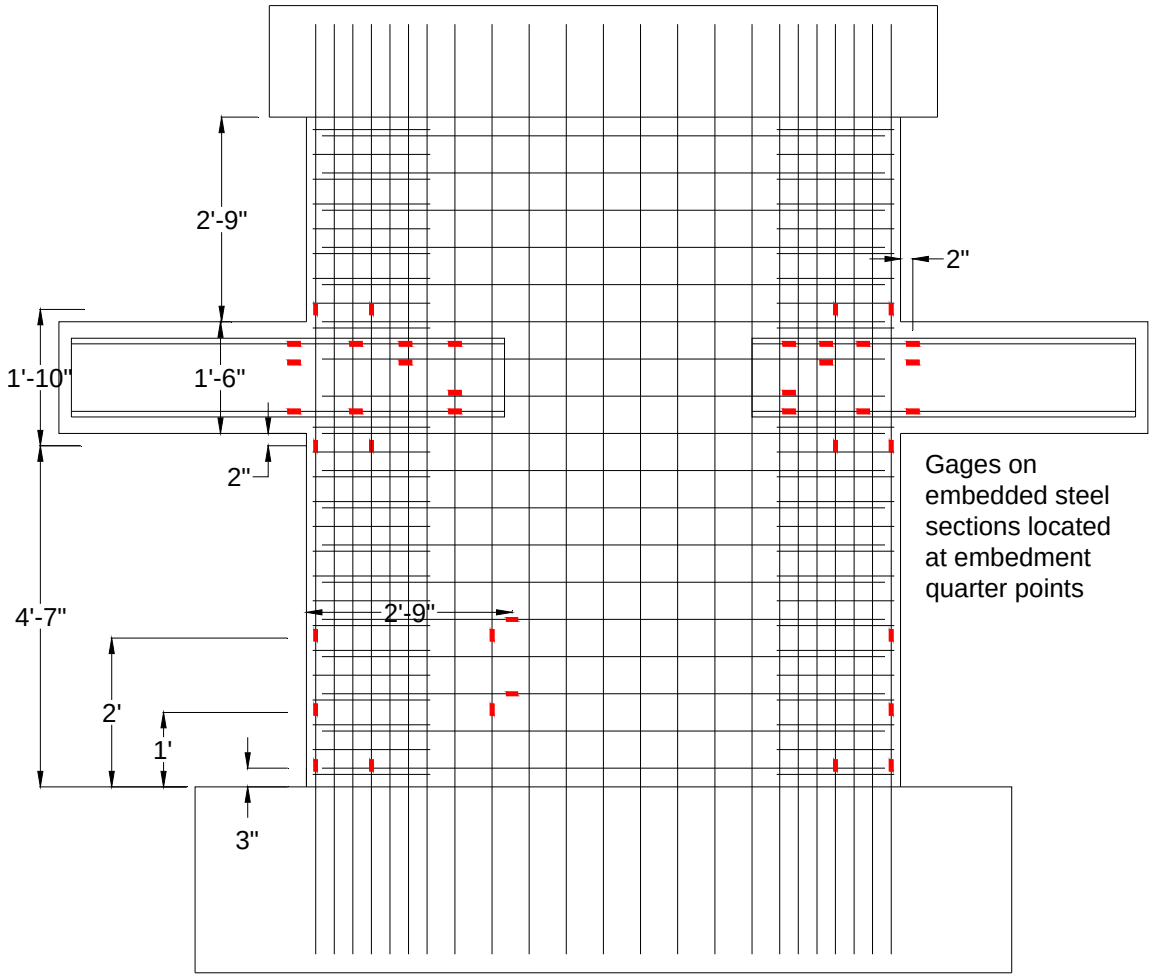

Figure 4.15: Strain Gage Layout for Sub-Assembly #1

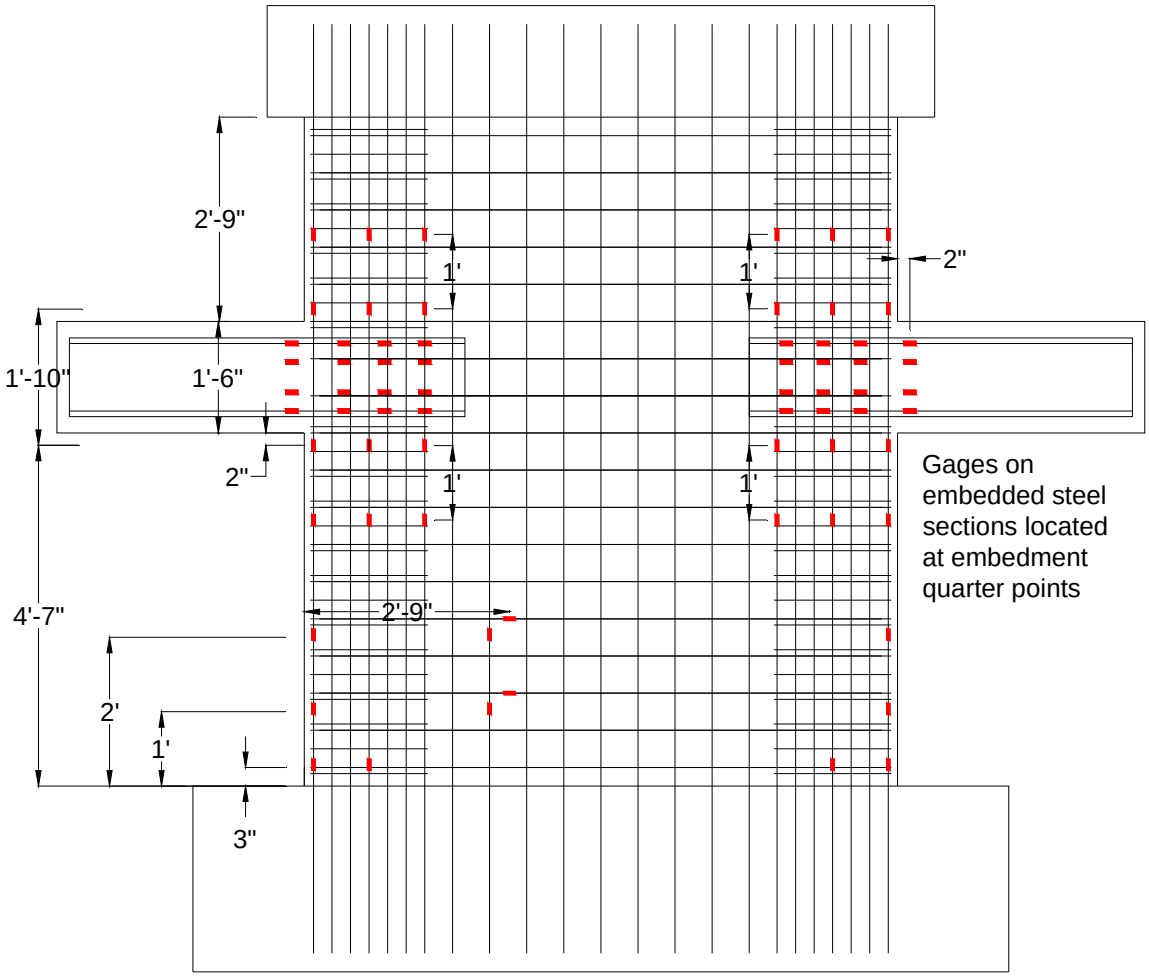

Figure 4.16: Strain Gage Layout for Sub-Assembly #2

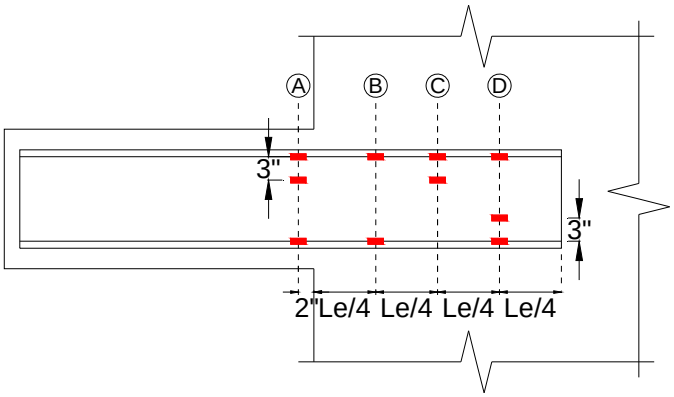

Figure 4.17: Strain Gage Layout for Embedded Steel Section, SRC1 and SRC2

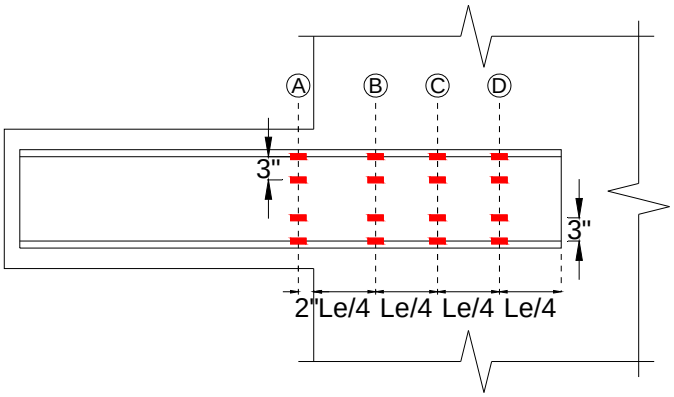

Figure 4.18: Strain Gage Layout for Embedded Steel Section, SRC3 and SRC4

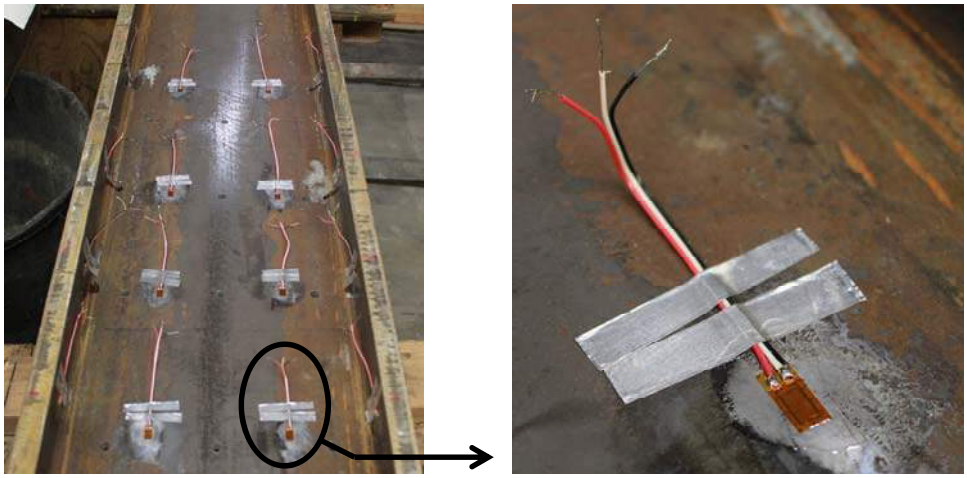

Figure 4.19: Photos of Embedded Steel Section Instrumented with Strain Gages

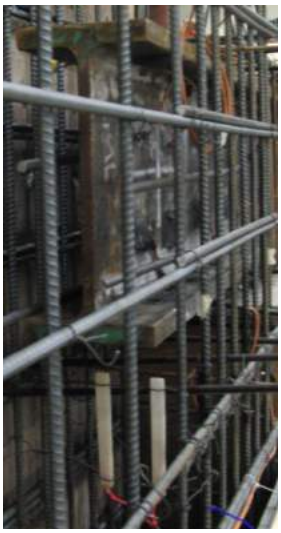

Figure 4.20: Embedded (Concrete) Strain Gages below Embedded Steel Section

The two 3/8”-diameter threaded rods providing coupling beam axial restraint during testing of SRC3 and SRC4 were each instrumented with a load cell. One of the load cells is shown in Figure 4.21. Each load cell was devised of an 8” length of 5/8”-diameter smooth high-strength rod with threaded ends. Two strain gages were attached on opposite sides of the rod along the smooth section and prior to installation in the test set-up a calibration between force and average strain was obtained through tensile testing (in the UCLA materials testing laboratory) in the elastic range. Each load cell was attached along the length of the threaded rods in the axial restraining system, and the larger diameter of the load cell rods relative to the threaded rods ensured that the load cells would remain elastic during testing. These load cells were used to measure the axial force in the coupling beam during testing (by summing the values from each load cell).

Figure 4.21: Load Cell Used to Determine Coupling Beam Axial Load

4.5 TESTING PROTOCOL

4.5.1 Wall Loads

The coupling beam actuator was used to control the test, and the three wall actuators were slaved to this actuator based on the force ratios shown in Figure 4.22 and Figure 4.23. Based on these load ratios, a free body diagram for the structural wall is shown in Figure 4.24, and the resulting demands on the structural wall, including the moment and axial load diagram for both positive and negative loading, are shown in Figure 4.25.

The computation of the wall shear strength is dependent on the height-to-length aspect ratio of the wall, h_w / l_w. The h_w / l_w ratio was reduced for the test specimen relative to the prototype (see Figure 3.2), and moment was applied to the top of the wall to simulate the demands from the stories above. Based on the values for V_{wall} and M_{wall} indicated in Figure 4.24, the moment and shear demands at the top of the 9' tall test specimen structural wall are equivalent to those of a

20.3’ tall wall with an applied cantilever shear load (M_{wall} / V_{wall} = 11.3’ per Figure 4.24, and 9’ + 11.3’ = 20.3’). For a 20.3’ tall wall, h_w / l_w = 2.54. This value is used to determine the nominal shear strength of the wall, $V_{n,wall}$, which is computed in accordance with ACI 318-11 Section 21.9.4.1 as follows:

$$V_{n,wall} = A_{cv}(\alpha_c \lambda_c \sqrt{f_c'} + \rho_t f_y) = V_{c,wall} + V_{s,wall}$$

$$\alpha_c = 2.0 \text{ for } \frac{h_w}{l_w} \geq 2.0$$

$$\lambda_c = 1.0 \text{ for normal-weight concrete}$$

$$V_{c,wall} = A_{cv}\alpha_c\lambda_c\sqrt{f_c'} = (96")(12")(2.0)(1.0)\frac{\sqrt{6000^{psi}}}{1000^{lb/k}} = 178.5^k$$

$$V_{s,wall} = A_{cv}\rho_t f_y = (96")(12")(0.0031)(60^{ksi}) = 211.2^k$$

$$V_{n,wall} = V_{c,wall} + V_{s,wall} = 178.5^k + 211.2^k = 389.7^k$$

where $V_{c,wall}$ is the contribution to nominal shear strength of a structural wall provided by concrete, $V_{s,wall}$ is the contribution to nominal shear strength of a structural wall provided by reinforcement, A_{cv} is the area of concrete section of structural wall resisting shear, α_c is the coefficient defining the relative contribution of concrete strength to nominal wall shear strength, λ_c is the modification factor reflecting the reduced mechanical properties of light-weight concrete relative to normal-weight concrete of the same compressive strength, and ρ_t is the ratio of area of distributed transverse reinforcement to gross concrete area perpendicular to that reinforcement. Note that α_c is taken as 2.0 when h_w / $l_w \geq$ 2.0.

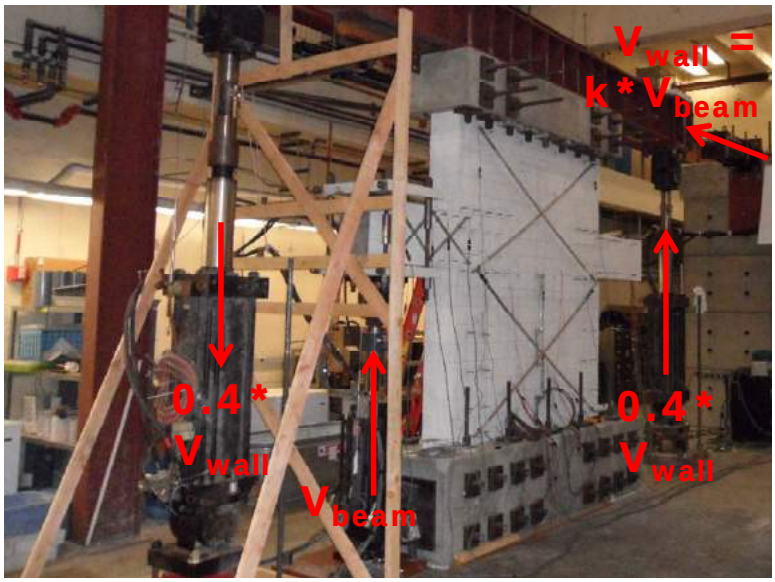

Figure 4.22: Test Photo with Indication of Applied Loads

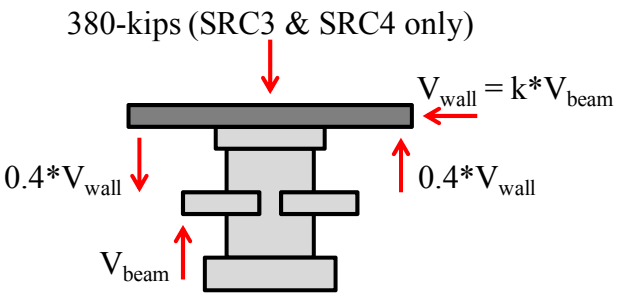

$k = V_{wall} / V_{beam} =$

	(+), Up	(-), Down
SRC1	0.5	0.5
SRC2	1.25	1.25
SRC3	0.5	1.0
SRC4	0.5	1.0

Figure 4.23: Applied Loads

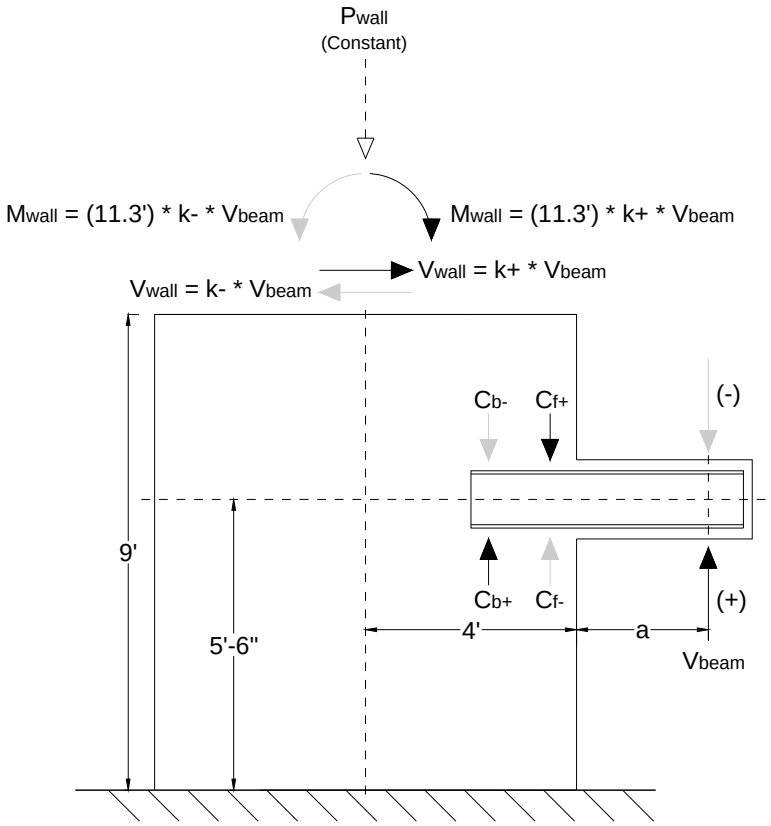

Figure 4.24: Free Body Diagram of Structural Wall

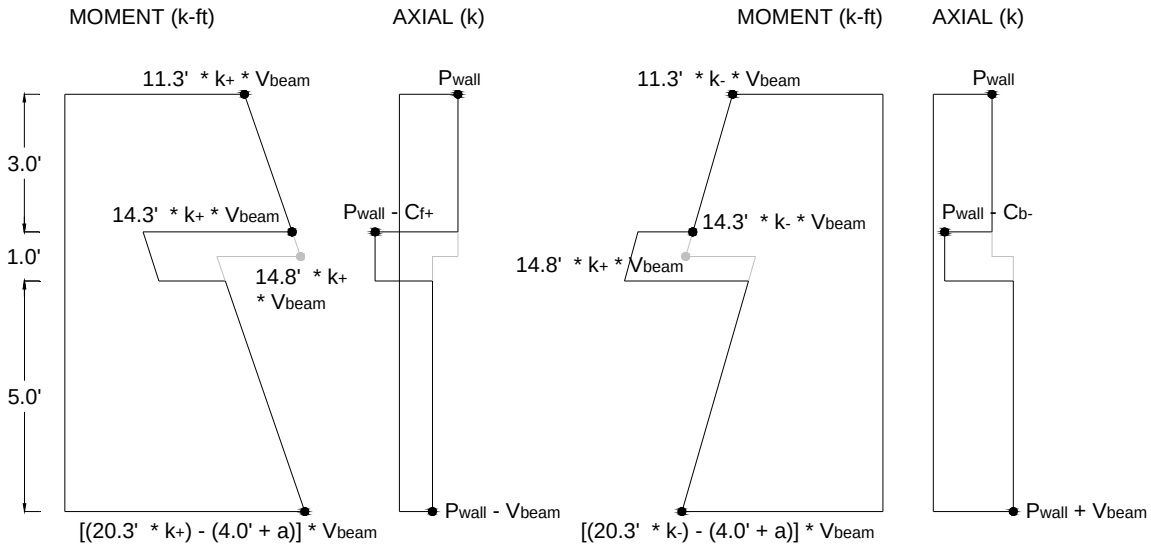

Figure 4.25: Moment and Axial Load Diagrams for the Structural Wall

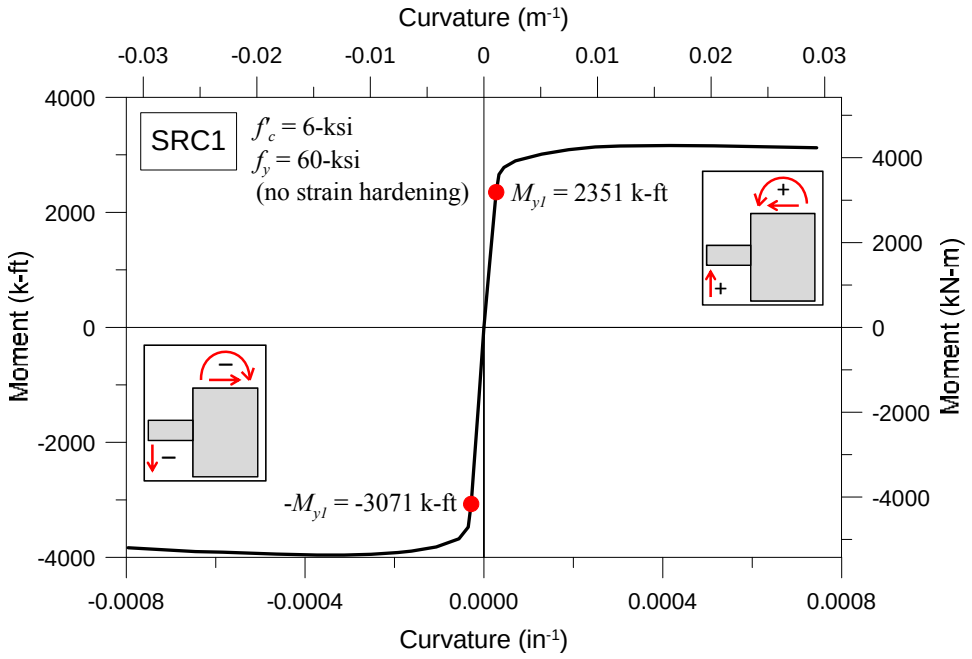

Figure 4.26: Structural Wall Analytical Moment-Curvature Plot: a) SRC1

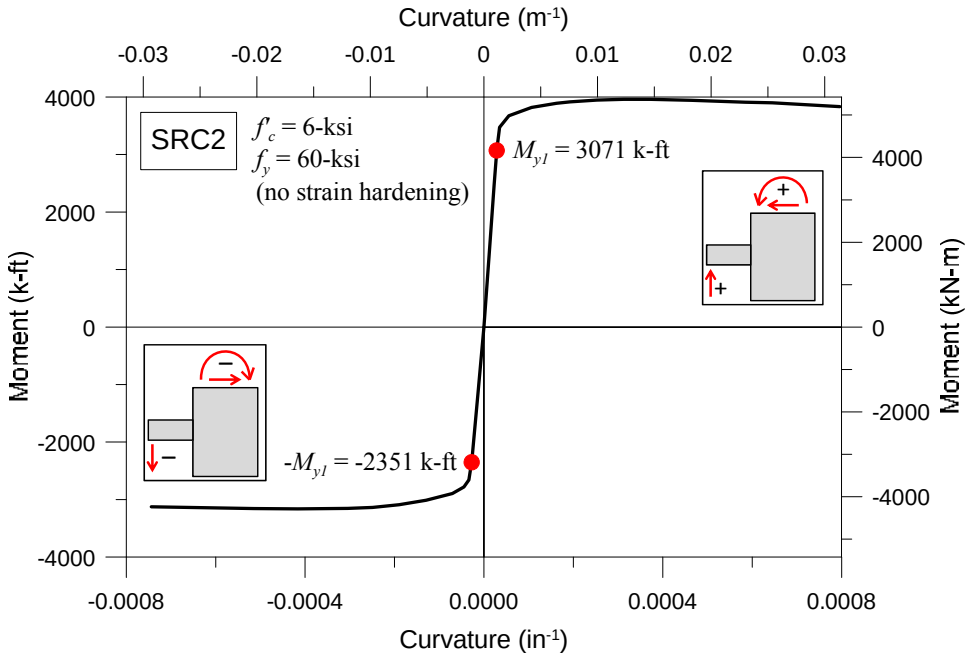

Figure 4.26: Structural Wall Analytical Moment-Curvature Plot: b) SRC2

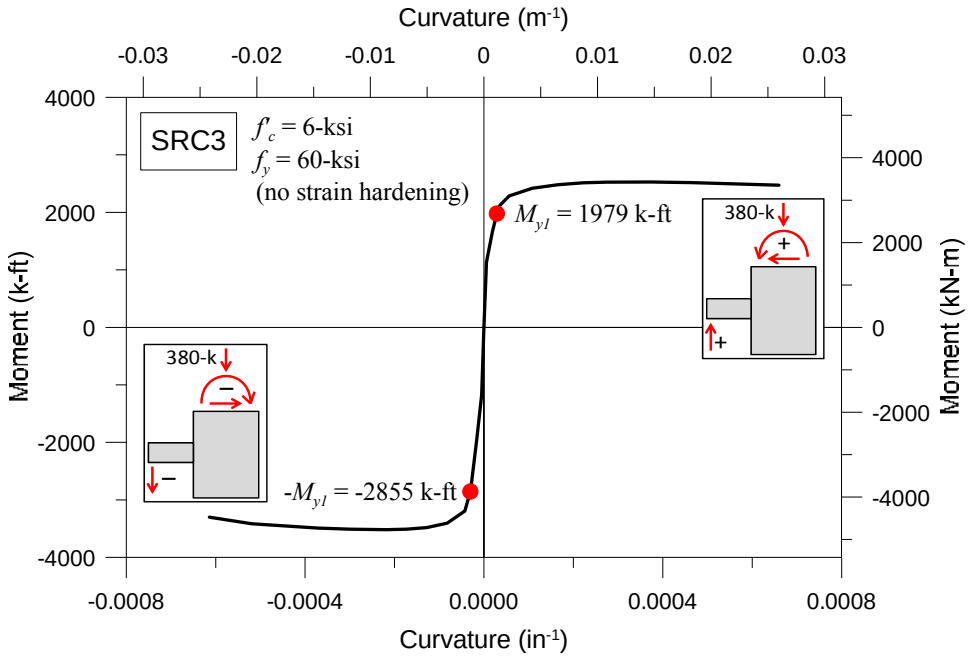

Figure 4.26: Structural Wall Analytical Moment-Curvature Plot: c) SRC3

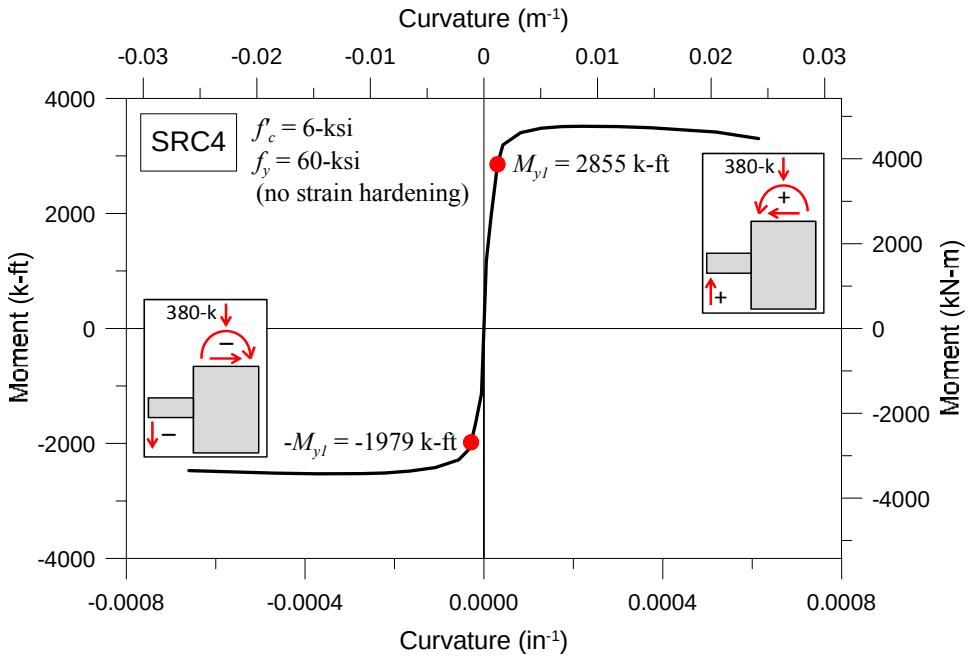

Figure 4.26: Structural Wall Analytical Moment-Curvature Plot: d) SRC4

The ratio between wall overturning moment and wall shear was held constant for all three tests (Figure 4.22 and Figure 4.23). This ratio was selected to achieve a modest shear demand in the wall (not expected to approach $V_{n,wall}$ but expected to potentially exceed $V_{c,wall}$, which corresponds to a shear stress of $2\sqrt{f_c'}$, during peak loading for SRC2, SRC3, and SRC4), while also targeting a specific moment demand at the location of the coupling beam. Care was also taken to avoid yielding the wall near the base, as this was of particular concern when the coupling beam was loaded upward, since the upward coupling beam loading imparts axial tension in the lower portion of the wall, thereby reducing the wall yield moment relative to the segment of the wall above the coupling beam.

Axial (gravity) load was not applied at the top of the wall for SRC1 and SRC2. Because the wall boundary longitudinal reinforcement was reduced for the second test specimen sub-assembly (with SRC3 and SRC4) relative to the first (with SRC1 and SRC2), a constant wall axial load of 380-k ($0.073A_g f'_c$) was applied for SRC3 and SRC4 in order to increase the yield strength of the wall, allowing the application of appreciable wall overturning moment that prevented the wall from going into reverse curvature in the lower portion (due to the wall moment imparted by the coupling beam).

The ratio $k = V_{wall}/V_{beam}$ (Figure 4.22 and Figure 4.23) differed for each of the four beam tests, based on the desired level of wall overturning moment at the coupling beam. k was 0.5 for SRC1 and 1.25 for SRC2. For SRC3 and SRC4, k_+ was 0.5 when the beam was loaded up (positive) and k_- was 1.0 when loaded down (negative); the switch was made after each one-half cycle when the coupling beam load was zero. For SRC3, the different positive and negative k-values

were due to the significant difference in the quantity of wall boundary longitudinal reinforcement (#5 v. #3). For SRC4, k was initially set at 1.0 for both positive and negative; however, due to the embedment damage from testing SRC3, large wall rotations during positive loading were initially causing large beam rotations, leading to unreliable test data. Reducing the applied wall loads in the positive direction (i.e., reducing k_+) corrected this problem, while still allowing for an appreciable compression stress along the embedment length.

The determination of k was primarily based on the desired wall overturning moment demand at the coupling beam location under negative loading. Because coupling beam bearing forces were expected to impart additional local tensile stresses into the wall boundary (consistent with the load paths shown in Figure 3.9), the negative loading direction was determined to be the more critical of the two loading directions, since the wall boundary is in tension. The wall moment diagrams shown in Figure 4.25 were used to determine the wall demand. These diagrams consider a front and back bearing force imparted into the structural wall by the embedded member, but also show the axial and moment diagrams without including the local bearing force effects, i.e., "global" axial and moment diagrams. At the location of the coupling beam centerline, the moment demand was computed as $(14.8')kV_{beam}$ based on the global moment diagrams.

Plane section moment-curvature analysis was used to compute the yield moment of the wall cross-section. For the applied wall axial load (0-kips for SRC1 and SRC2 and 380-kips for SRC3 and SRC4), the moment at first yield of the structural wall (i.e., when the outermost longitudinal bar reaches yield), M_{y1}, for negative loading was computed to be 2351 k-ft, 3071 k-

ft, 2855 k-ft, and 1979 k-ft for SRC1, SRC2, SRC3, and SRC4, respectively (Figure 4.26). These values were calculated using f'_c=6-ksi and f_y=60-ksi. The wall moment demand at the coupling beam was normalized by the wall yield moment to assess the overall level of wall demand provided. Although there are reasons why this general approach may be unreliable (e.g., plane sections not remaining plane, the effect of the local bearing forces), this simple approach was deemed a reasonable means to assess the wall demand applied to the embedment connection and to compute "target" moment demands at this location for testing purposes.

At the expected maximum coupling beam load, the wall demands for SRC1 were intended to exceed the wall cracking moment and reach approximately one-half of first yield in tension of boundary longitudinal reinforcement, i.e., since no axial load was applied at the top of the wall, the maximum tensile strain in the outermost #6 wall vertical reinforcement would be ~0.001 at the location of the coupling beam. For SRC2 the wall forces were 2.5 times larger than for SRC1 in order to approach first yield at the coupling beam, noting that the wall yield moment is significantly larger with the #7 bars rather than the #6 bars in tension. In comparing the SRC1 and SRC2 testing approaches, larger walls loads in combination with shorter embedment length were expected to create the more critical scenario for the coupling beam connection.

The observed peak coupling beam shear in the negative loading direction was 167-kips for SRC1 and 138-kips for SRC2, corresponding to peak wall moment demands (based on (14.8')kV_{beam}) that were roughly 53% and 83% of the yield moments (2351 k-ft and 3071 k-ft, respectively), respectively (consistent with $\varepsilon_{s,max}/\varepsilon_y$ in Table 3.1). Therefore, the wall demands for SRC2 were less than the target value. As SRC3 and SRC4 were expected to perform no better than SRC2,

the wall demands for SRC3 and SRC4 were adjusted by a factor of 1.20 (1.00/0.83=1.20) relative to SRC2 to target yield of boundary longitudinal reinforcement in tension. An adjustment was also made based on the wall yield moments, as the wall yield moment for SRC3 and SRC4 (which included applied axial load at the top of the wall) was 93% and 64% of SRC2, respectively. Assuming flexural capacity is reached at the beam-wall interface, k was also adjusted for SRC3 relative to SRC2 based on the ratio of the coupling beam aspect ratios, 2.4/3.33=0.72. Therefore, relative to SRC2, k was scaled by a factor of 0.80 in the negative loading direction for both SRC3 and SRC4 relative to SRC2 (based on 1.20*0.72*0.93=0.80 for SRC3 and 1.20*0.64=0.77 for SRC4) in an effort to approach wall yield at the location of the embedded coupling beam.

The actual peak wall demands developed during testing were indicated previously in Table 3.1, expressed in terms of the ratio of the strain in the outermost vertical wall bar $\varepsilon_{s,max}$, to the yield strain of reinforcement, ε_y. These values were computed using plane section moment-curvature (including P-M interaction) analysis based on the global axial demand and peak global moment demand in the negative loading direction at the coupling beam centerline. Note that the actual wall demands for SRC4 were much less than the targeted yield value due to reduced capacity of this member and the linear relationship between applied beam shear load and wall demands. Detailed discussion on the performance of SRC4 and the other test beams is provided in subsequent chapters.

4.5.2 Beam Testing Protocol

The calculated shear force at flexural yield of the coupling beam, $V@M_y$, was used in the development of the testing protocol. The yielding moment, M_y, for the cross-section was estimated to be ~400-k-ft based on the moment-curvature plot in Figure 4.27, which was developed using plane-strain analysis with f'_c = 6-ksi and F_y = 55.0-ksi without consideration of strain hardening. The use of F_y = 55.0-ksi in this instance was based on the average steel yield strength from Liu et al (2007) (Table 3.3). This approach was expected to potentially overestimate the actual yield strength due to the assumption of fully-composite action associated with plane-strain analysis. Assuming yielding at the beam-wall interface, $V@M_y$ was ~160-k for SRC1, SRC2, and SRC4 with aspect ratio 3.33 and ~220-k for SRC3 with aspect ratio 2.4.

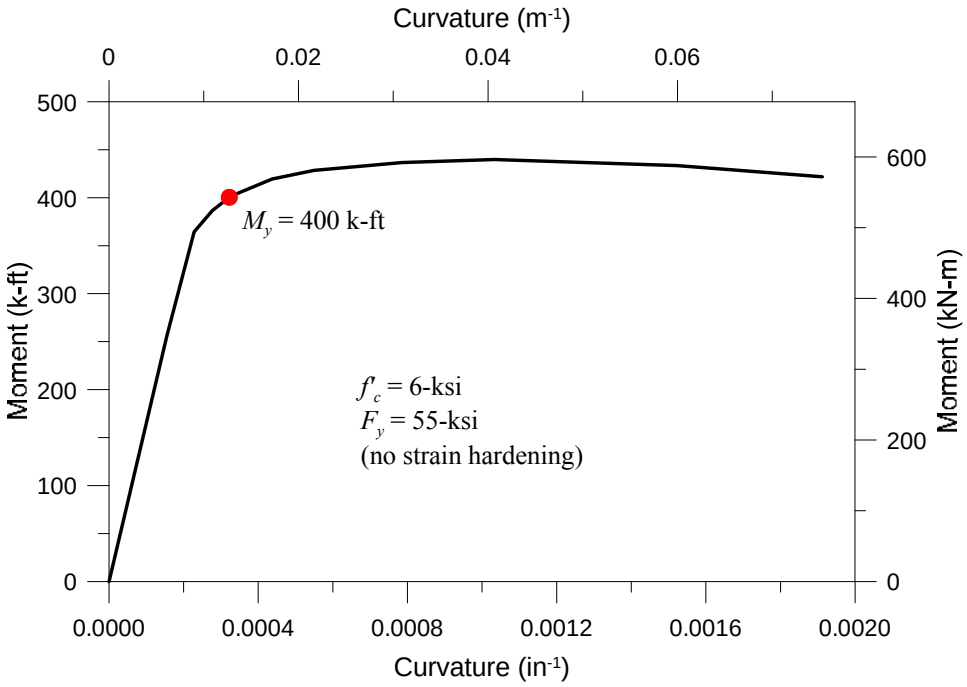

4.27: Analytical Moment-Curvature Plot for Test Beams

The reversed-cyclic loading protocol for all four beams is shown in Figure 4.28. For each test, pre-yield cycles were conducted under load control at increments of $V@M_y$ * 1/8, 1/4, 1/2, and 3/4. For load-controlled cycles, due to the difference in stiffness between the positive (upward) and negative (downward) loading, the loading in the negative direction was displacement-controlled based on the observed displacement for the positive direction (which was load-controlled). The term "rotation" refers to the chord rotation of the cantilever coupling beam, which was computed as the beam displacement at the point of load application divided by the cantilever length. Upon completion of the load-controlled cycles, based on the observed stiffness at $3(V@M_y)/4$, the yield rotation was estimated and the tests proceeded as displacement-controlled. The yield rotations for SRC1, SRC2, SRC3, and SRC4 were estimated as 1.67%, 0.67%, 1.33%, and 1.33%, respectively, and the completed loading protocols for the four beams were as follows:

SRC1: 20-k, 40-k, 80-k, 120-k, 1.67%, 2.25%, 3.0%, 4.0%, 6.0%, 8.0%, 10.0%, 13.0%

SRC2: 20-k, 40-k, 80-k, 120-k, 0.67%, 1.0%, 1.5%, 2.0%, 3.0%, 4.0%, 6.0%, 8.0%, 10.0%

SRC3: 27.5-k, 55-k, 110-k, 165-k, 1.33%, 2.0%, 3.0%, 4.0%, 6.0%, 8.0%, 10.0%

SRC4: 20-k, 40-k, 80-k, 120-k, 1.33%, 2.0%, 3.0%, 4.0%, 6.0%, 8.0%

For all beams three cycles were carried out at each increment up through 4.0% rotation. At 6.0% and 8.0% rotation, two cycles were completed. SRC1 included two cycles each at 10.0% and 13.0% rotation, and SRC2 included three cycles at 10.0% rotation. SRC3 included one cycle at 10.0% rotation, and SRC4 was stopped after 8.0% rotation due to significant damage.

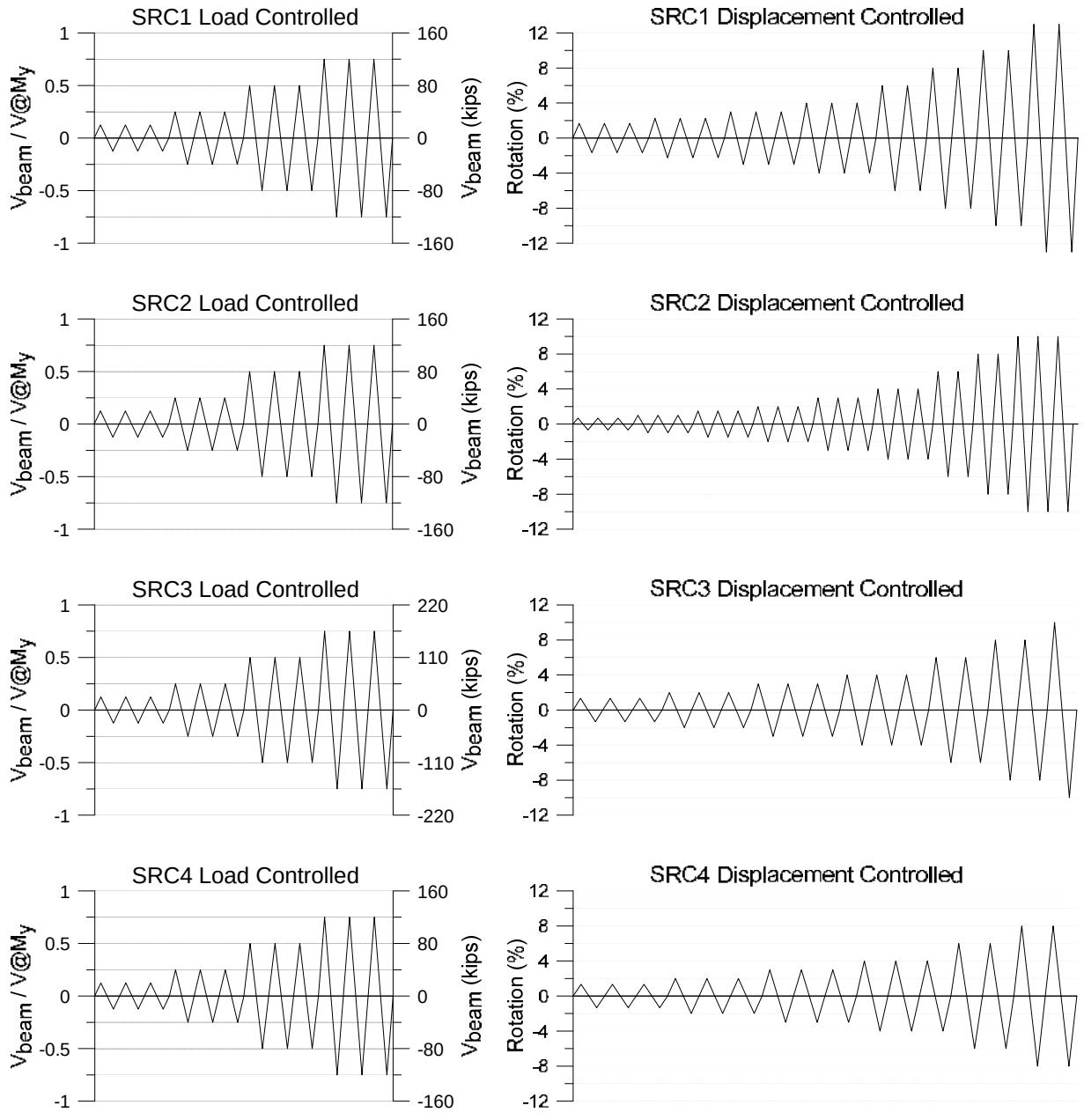

Figure 4.28: Loading Protocol for All Beams

It is noted that the peak chord rotations imposed on the coupling beams tested in this study were larger than typical rotational demands imposed on coupling beams in actual structures. Assuming the formation of plastic hinges at the beam-wall interfaces and at the base of the

coupled structural walls (at the wall centerlines) in actual structures, the coupling beam chord rotation, θ, may be estimated from the wall rotation, θ_w, as:

$$\theta = \theta_w \left(2 + \frac{L_{w,avg}}{L} \right) \tag{4.1}$$

where $L_{w,avg}$ is the average length of the two walls coupled by the coupling beam, and L is the length of the coupling beam clear span. For tall core wall buildings (e.g., 30 to 40 storeis), average wall rotation is on the order of 1%, and $L_{w,avg}/L$ does not typically exceed four to five. Relative to tall buildings, drift may be larger in low-rise buildings, but $L_{w,avg}/L$ is typically smaller. Therefore, coupling beam chord rotations generally do not exceed 6%, which is a limit commonly used to define strength loss of diagonally-reinforced coupling beams (Naish et al, 2013).

During testing of the specimens in this study, the applied wall demands were expected to create wall rotation in the opposite direction of the applied beam rotation, such that the relative cantilever displacement of the coupling beam would include the measured displacement plus any additional opposing displacement due to wall deformation (Figure 4.29). Footing uplift/rotation was expected to similarly affect beam displacement/rotation measurements. In previous testing programs involving SRC coupling beams embedded into cyclically-loaded structural walls, it is unclear whether the effects of wall rotation and footing rotation/uplift were taken into consideration when determining the coupling beam chord rotation.

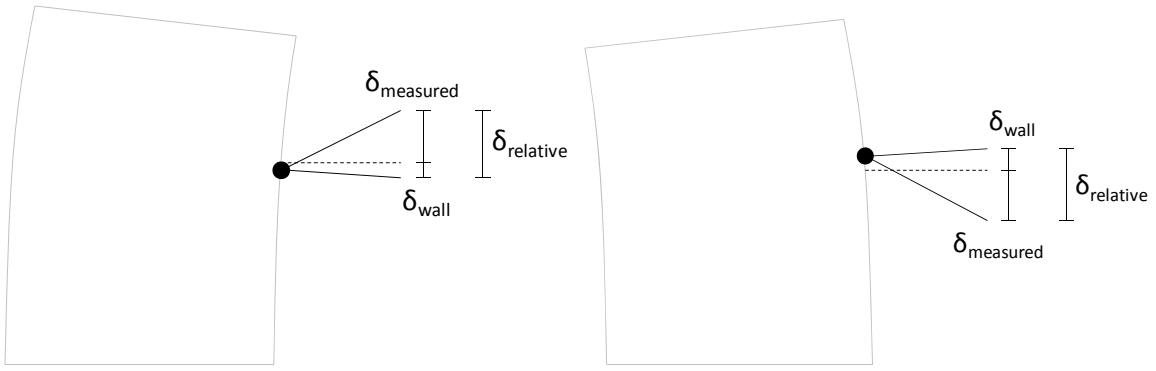

Figure 4.29: Influence of Wall Rotation on Coupling Beam Displacement

During testing, the beam displacement/rotation data were corrected in real time to exclude footing rotation and uplift; this correction assumed rigid body motion of the footing. Throughout testing of SRC1, a real-time modification to the measured beam displacement was made to account for beam displacement due to wall rotation and wall axial displacement, and this modification was based on a plane strain assumption for the structural wall at the location of the coupling beam centerline. The modification was also used during the early phases of SRC2 testing but was abandoned mid-test for SRC2 and not used during testing of SRC3 and SRC4 due to the lack of plane section behavior in the structural wall at the location of the coupling beam (details provided in Section 5.11). For SRC2 (after the modification for wall rotation was abandoned), SRC3, and SRC4, a real-time modification was instead made for wall extension/contraction measured between the footing and the base of the coupling beam. Of the ten, vertical, collinear LVDTs in the wall located roughly 7" from the outer edge of the wall nearest the test beam (Figure 4.14), the lower five were used to make this modification. Due to the lack of plane section behavior in the structural wall in the vicinity of the coupling beam, data were corrected after the completion of testing to remove this modification for extension/contraction. Similarly, the test data for SRC1 and the early stages of SRC2 were

corrected to remove the modification for wall rotation. Therefore, post-processing of test data leads to reported deformations/rotations that differ from the values used to control the tests; more details are provided in Section 5.1.

5 Experimental Results

Experimental results are presented and discussed in this chapter. Corrections to the measured coupling beam chord rotations are made in order to account for wall rotations (Section 5.1). A discussion of observed damage is provided (Section 5.2). Load-deformation responses of the test beams are presented and compared (Section 5.3.1), as well as test results obtained from a previous study (Naish et al, 2013b) of reinforced concrete coupling beams (Section 5.3.2). The influence of the uncertainty in measured coupling beam chord rotation for the test results presented in this study is assessed in Section 5.3.3. Plots of dissipated energy versus chord rotation are used as a means to quantifiably assess energy dissipation for the beams tested in this study (Section 5.4), and results and discussion related to the measured axial deformation of the test beams are provided (Section 5.5). Moment-curvature plots and curvature profiles are used to assess the spread of plasticity in the coupling beam (Section 5.6). Shear load versus shear deformation responses are presented and discussed (Section 5.7), as are plots of the structural wall rotation (measured over the clear height of the wall) versus the coupling beam rotation (Section 5.8). Data obtained from embedded (concrete) strain gages are used to assess the variation of bearing stresses measured beneath the flange of the embedded steel section (Section 5.9), while data obtained from strain gages attached to the embedment region of the steel section are used to assess the extent to which the steel section yielded within the embedment zone

(Section 5.10). Local wall yielding in the vicinity of the embedment region is assessed based on data obtained from strain gages attached to wall longitudinal reinforcement (Section 5.11), and wall strain profiles are used to assess plane section behavior at ten cross-sections over the height of the structural wall (Section 5.12).

5.1 CORRECTING BEAM ROTATIONS FOR WALL DEFORMATION

Ideally, coupling beam chord rotation should be measured relative to the wall rotation at the location of the embedded beam (consistent with the behavior of coupled walls, in which wall rotation imposes beam rotation). However, as mentioned previously in Section 4.5.2, test data indicate a lack of plane-section behavior in the vicinity of the coupling beam (i.e. due to the local effects of the embedded SRC coupling beam on the structural wall), discussed in more detail in Section 5.11. As the wall rotation and axial displacement at the location of the coupling beam is between that measured at the top and bottom of the structural wall, the wall rotation and axial displacement at the location of the beam was estimated as the average of that measured relative to these two reference planes. Results presented in the remainder of this report were adjusted in this manner to account for the contribution of wall deformations to the coupling beam tip displacement (Figure 4.29). In general, results obtained were not overly sensitive to this adjustment, with the exception of the elastic stiffness of SRC2 (see Section 6.5.4) and the measured coupling beam post-yield chord rotations (affecting ductility) for SRC3 and SRC4 (see Section 5.3.3).

It is noted that the adjusted coupling beam chord rotations imposed on each beam at each displacement-controlled loading cycle differed from the target values indicated in Section 4.5.2 (including Figure 4.28). The adjusted coupling beam chord rotation and load reached at the peak of each individual cycle are provided in Table 5.1, noting that chord rotation is provided relative to the base of the wall, the top of the wall, and the average of the two. For each load or displacement level, an indication of the average coupling beam chord rotation applied for all cycles in the positive and negative loading direction is provided in Table 5.1, noting that these values are used as callouts in Section 5.2.

As mentioned in Section 4.5.2, a change to the parameter *k*, which related the magnitude of the applied wall loads to the applied beam load, was made during the early stages of testing for SRC4 due to large wall rotation in the positive loading direction. It is noted that the test results prior to the loading change were deemed unimportant to the remainder of this document and are not typically included, except in Section 5.2 and Section 5.3. Plots and analysis for SRC4 do not consider these data unless specifically noted.

Table 5.1: Load-Displacement Peak Values: a) SRC1

Cyclic Increment Avg. Rotation	Positive (+)					Negative (-)				
	Cycle	Rotation (%)			Load (k)	Cycle	Rotation (%)			Load (k)
		Rel. to Bot. of Wall	Rel. to Top of Wall	Rel. to Top/Bot. Avg.			Rel. to Bot. of Wall	Rel. to Top of Wall	Rel. to Top/Bot. Avg.	
+0.11% –0.11%	1	0.104	0.111	0.108	20.0	1	-0.104	-0.114	-0.109	-20.0
	2	0.115	0.124	0.120	20.0	2	-0.105	-0.114	-0.110	-20.0
	3	0.112	0.120	0.116	20.0	3	-0.117	-0.127	-0.122	-20.0
+0.30% –0.25%	1	0.271	0.286	0.279	40.0	1	-0.235	-0.259	-0.247	-40.1
	2	0.294	0.311	0.302	40.1	2	-0.241	-0.265	-0.253	-40.1
	3	0.299	0.315	0.307	40.0	3	-0.243	-0.267	-0.255	-40.1
+0.67% –0.60%	1	0.606	0.638	0.622	80.0	1	-0.534	-0.621	-0.578	-80.0
	2	0.671	0.690	0.680	80.0	2	-0.560	-0.654	-0.607	-80.0
	3	0.707	0.724	0.715	79.9	3	-0.563	-0.658	-0.610	-78.8
+1.09% –1.03%	1	1.072	1.099	1.086	120.1	1	-0.930	-1.154	-1.042	-120.0
	2	1.091	1.103	1.097	112.5	2	-0.936	-1.162	-1.049	-116.2
	3	1.095	1.103	1.099	109.8	3	-0.889	-1.105	-0.997	-108.1
+1.61% –1.32%	1	1.622	1.644	1.633	144.1	1	-1.176	-1.456	-1.316	-135.6
	2	1.567	1.584	1.576	135.6	2	-1.178	-1.462	-1.320	-133.6
	3	1.602	1.619	1.610	137.4	3	-1.170	-1.452	-1.311	-130.6
+2.20% –1.82%	1	2.159	2.184	2.171	152.1	1	-1.656	-1.995	-1.825	-147.4
	2	2.181	2.199	2.190	146.1	2	-1.647	-1.987	-1.817	-144.9
	3	2.227	2.248	2.238	146.5	3	-1.644	-1.981	-1.813	-142.9
+3.00% –2.55%	1	2.961	2.986	2.974	159.9	1	-2.335	-2.711	-2.523	-156.1
	2	2.992	3.016	3.004	154.0	2	-2.371	-2.748	-2.559	-152.8
	3	3.018	3.040	3.029	150.3	3	-2.371	-2.745	-2.558	-149.3
+4.05% –3.51%	1	4.020	4.044	4.032	166.7	1	-3.310	-3.719	-3.514	-160.6
	2	4.027	4.041	4.034	152.9	2	-3.312	-3.714	-3.513	-154.5
	3	4.066	4.073	4.069	148.3	3	-3.307	-3.704	-3.505	-151.2
+6.07% –5.50%	1	6.070	6.072	6.071	163.6	1	-5.259	-5.696	-5.478	-163.5
	2	6.080	6.065	6.073	153.7	2	-5.303	-5.740	-5.522	-158.7
+8.10% –7.51%	1	8.090	8.043	8.066	154.5	1	-7.281	-7.750	-7.516	-163.7
	2	8.174	8.098	8.136	150.2	2	-7.261	-7.731	-7.496	-158.9
+10.15% –9.51%	1	10.177	10.073	10.125	151.5	1	-9.232	-9.725	-9.478	-160.8
	2	10.229	10.106	10.168	147.6	2	-9.297	-9.796	-9.546	-159.4
+13.17% –12.50%	1	13.250	13.112	13.181	147.6	1	-12.230	-12.751	-12.490	-157.4
	2	13.234	13.090	13.162	144.2	2	-12.258	-12.772	-12.515	-149.4

Table 5.1: Load-Displacement Peak Values: b) SRC2

Cyclic Increment Avg. Rotation	Positive (+)					Negative (-)				
	Cycle	Rotation (%)			Load (k)	Cycle	Rotation (%)			Load (k)
		Rel. to Bot. of Wall	Rel. to Top of Wall	Rel. to Top/Bot. Avg.			Rel. to Bot. of Wall	Rel. to Top of Wall	Rel. to Top/Bot. Avg.	
+0.09% –0.10%	1	0.058	0.122	0.090	20.0	1	-0.061	-0.133	-0.097	-17.2
	2	0.056	0.126	0.091	20.0	2	-0.061	-0.127	-0.094	-16.2
	3	0.056	0.125	0.090	20.4	3	-0.061	-0.126	-0.094	-16.2
+0.18% –0.14%	1	0.098	0.251	0.174	40.0	1	-0.100	-0.205	-0.152	-25.9
	2	0.102	0.254	0.178	39.2	2	-0.092	-0.182	-0.137	-22.8
	3	0.107	0.265	0.186	40.5	3	-0.090	-0.177	-0.133	-22.0
+0.39% –0.26%	1	0.207	0.545	0.376	80.1	1	-0.194	-0.372	-0.283	-40.6
	2	0.225	0.555	0.390	78.0	2	-0.176	-0.329	-0.252	-34.8
	3	0.239	0.580	0.409	80.1	3	-0.171	-0.317	-0.244	-33.0
+0.63% –0.36%	1	0.340	0.859	0.599	120.5	1	-0.264	-0.504	-0.384	-48.7
	2	0.365	0.875	0.620	117.8	2	-0.249	-0.464	-0.356	-42.8
	3	0.395	0.924	0.660	122.0	3	-0.234	-0.436	-0.335	-39.8
+1.01% –0.43%	1	0.636	1.298	0.967	150.3	1	-0.291	-0.636	-0.464	-61.6
	2	0.690	1.343	1.017	147.9	2	-0.263	-0.589	-0.426	-57.2
	3	0.732	1.387	1.060	147.9	3	-0.246	-0.560	-0.403	-54.8
+1.29% –0.84%	1	1.162	1.904	1.533	164.1	1	-0.459	-1.058	-0.758	-93.4
	x	0.806	1.189	0.997	78.1	2	-0.550	-1.227	-0.888	-103.7
	x	0.639	0.812	0.725	36.3	3	-0.552	-1.209	-0.881	-99.3
+1.29% –1.26%	x	0.637	0.817	0.727	36.5	1	-0.844	-1.700	-1.272	-124.4
	2	0.925	1.396	1.161	104.4	2	-0.852	-1.669	-1.260	-116.1
	3	0.928	1.398	1.163	103.3	3	-0.856	-1.657	-1.256	-113.5
+1.70% –1.81%	1	1.389	2.063	1.726	151.3	1	-1.313	-2.314	-1.813	-135.6
	2	1.401	1.991	1.696	134.6	2	-1.332	-2.274	-1.803	-125.7
	3	1.406	1.972	1.689	128.4	3	-1.346	-2.260	-1.803	-120.9
+2.20% –2.32%	1	1.892	2.526	2.209	144.6	1	-1.819	-2.825	-2.322	-131.5
	2	1.903	2.487	2.195	134.4	2	-1.829	-2.813	-2.321	-127.7
	3	1.907	2.473	2.190	131.1	3	-1.833	-2.805	-2.319	-124.8
+3.20% –3.33%	1	2.906	3.512	3.209	141.3	1	-2.802	-3.872	-3.337	-134.7
	2	2.913	3.488	3.200	135.8	2	-2.796	-3.867	-3.332	-133.0
	3	2.917	3.471	3.194	132.3	3	-2.793	-3.842	-3.317	-128.9
+4.21% –4.33%	1	3.932	4.506	4.219	140.1	1	-3.772	-4.884	-4.328	-134.2
	2	3.912	4.453	4.182	134.9	2	-3.861	-4.945	-4.403	-130.8
	3	3.967	4.481	4.224	132.7	3	-3.751	-4.789	-4.270	-121.8

Table 5.1: Load-Displacement Peak Values: b) SRC2 (Continued)

+6.22% –6.17%	1	5.964	6.478	6.221	133.9	1	-5.634	-6.730	-6.182	-126.2
	2	5.995	6.457	6.226	125.5	2	-5.626	-6.680	-6.153	-119.4
+8.25% –8.15%	1	8.019	8.466	8.242	125.0	1	-7.616	-8.690	-8.153	-120.4
	2	8.056	8.451	8.254	118.3	2	-7.645	-8.639	-8.142	-107.3
+10.22% –10.10%	1	10.024	10.387	10.205	113.0	1	-9.662	-10.647	-10.155	-105.3
	2	10.079	10.374	10.226	101.7	2	-9.605	-10.467	-10.036	-87.1
	3	10.144	10.394	10.269	88.0	3	-9.564	-10.316	-9.940	-73.9

Table 5.1: Load-Displacement Peak Values: c) SRC3

Cyclic Increment Avg. Rotation	Positive (+)					Negative (-)				
	Cycle	Rotation (%)			Load (k)	Cycle	Rotation (%)			Load (k)
		Rel. to Bot. of Wall	Rel. to Top of Wall	Rel. to Top/Bot. Avg.			Rel. to Bot. of Wall	Rel. to Top of Wall	Rel. to Top/Bot. Avg.	
+0.11% –0.09%	1	0.104	0.119	0.112	27.5	1	-0.062	-0.118	-0.090	-31.4
	2	0.098	0.114	0.106	27.5	2	-0.057	-0.107	-0.082	-27.5
	3	0.105	0.121	0.113	28.5	3	x	x	x	x
+0.21% –0.24%	1	0.186	0.219	0.202	55.0	1	-0.178	-0.281	-0.230	-55.0
	2	0.192	0.226	0.209	55.0	2	-0.194	-0.299	-0.247	-55.2
	3	0.199	0.236	0.218	55.0	3	-0.191	-0.286	-0.238	-51.7
+0.47% –0.52%	1	0.444	0.507	0.475	110.1	1	-0.422	-0.627	-0.524	-87.5
	2	0.449	0.500	0.474	91.7	2	-0.436	-0.625	-0.530	-81.9
	3	0.445	0.494	0.470	88.1	3	-0.428	-0.608	-0.518	-76.6
+1.05% –1.26%	1	1.021	1.098	1.060	165.1	1	-0.939	-1.556	-1.247	-140.2
	2	1.035	1.056	1.046	145.5	2	-0.956	-1.581	-1.268	-129.5
	3	1.043	1.067	1.055	147.3	3	-0.958	-1.552	-1.255	-122.7
+1.35% –1.66%	1	1.336	1.373	1.355	177.2	1	-1.225	-2.113	-1.669	-151.7
	2	1.341	1.348	1.344	163.9	2	-1.226	-2.082	-1.654	-146.6
	3	1.337	1.340	1.338	158.7	3	-1.226	-2.066	-1.646	-143.0
+1.94% –2.62%	1	1.999	2.012	2.006	202.7	1	-1.823	-3.441	-2.632	-181.3
	2	2.004	1.825	1.914	161.1	2	-1.826	-3.424	-2.625	-175.1
	3	2.001	1.784	1.892	153.7	3	-1.827	-3.371	-2.599	-167.2
+2.70% –4.05%	1	2.997	2.764	2.880	209.2	1	-2.777	-5.365	-4.071	-192.3
	2	2.974	2.262	2.618	138.5	2	-2.809	-5.278	-4.044	-182.0
	3	2.998	2.209	2.603	139.1	3	-2.825	-5.230	-4.027	-175.5
+3.40% –5.39%	1	3.959	3.125	3.542	182.2	1	-3.801	-7.113	-5.457	-192.2
	2	3.987	2.726	3.357	142.4	2	-3.831	-6.947	-5.389	-176.9
	3	3.957	2.662	3.309	134.7	3	-3.863	-6.794	-5.329	-169.0
+5.27% –7.75%	1	6.012	4.752	5.382	191.5	1	-5.827	-9.896	-7.861	-192.5
	2	5.976	4.336	5.156	153.6	2	-5.844	-9.438	-7.641	-170.7
+7.25% –9.63%	1	7.991	6.418	7.204	180.6	1	-7.710	-11.843	-9.777	-178.5
	2	8.076	6.505	7.291	163.1	2	-7.691	-11.273	-9.482	-157.1
+9.46% –11.46%	1	10.133	8.788	9.461	167.6	1	-9.562	-13.365	-11.464	-161.5

Table 5.1: Load-Displacement Peak Values: d) SRC4 before Loading Change

Cyclic Increment Avg. Rotation	Positive (+)					Negative (-)				
	Cycle	Rotation (%)			Load (k)	Cycle	Rotation (%)			Load (k)
		Rel. to Bot. of Wall	Rel. to Top of Wall	Rel. to Top/Bot. Avg.			Rel. to Bot. of Wall	Rel. to Top of Wall	Rel. to Top/Bot. Avg.	
+0.07% –0.08%	1	0.049	0.094	0.072	20.2	1	-0.050	-0.096	-0.073	-20.0
	2	0.046	0.087	0.067	20.3	2	-0.055	-0.106	-0.080	-20.3
	3	0.047	0.086	0.067	20.1	3	-0.056	-0.106	-0.081	-20.0
+0.14% –0.15%	1	0.096	0.193	0.145	40.4	1	-0.107	-0.185	-0.146	-29.8
	2	0.096	0.188	0.142	39.7	2	-0.105	-0.183	-0.144	-28.3
	3	0.096	0.185	0.141	39.4	3	-0.107	-0.187	-0.147	-28.5
+0.26% –0.22%	1	0.132	0.422	0.277	80.5	1	-0.171	-0.271	-0.221	-36.5
	2	0.139	0.381	0.260	72.4	2	-0.176	-0.276	-0.226	-34.9
	3	0.147	0.322	0.234	59.6	3	-0.174	-0.273	-0.224	-33.5
+0.46% –0.30%	1	0.170	0.743	0.456	120.3	1	-0.240	-0.352	-0.296	-39.6

Table 5.1: Load-Displacement Peak Values: e) SRC4

Cyclic Increment Avg. Rotation	Positive (+)					Negative (-)				
	Cycle	Rotation (%)			Load (k)	Cycle	Rotation (%)			Load (k)
		Rel. to Bot. of Wall	Rel. to Top of Wall	Rel. to Top/Bot. Avg.			Rel. to Bot. of Wall	Rel. to Top of Wall	Rel. to Top/Bot. Avg.	
+0.09%	1	0.087	0.087	0.087	20.0	1	x	x	x	x
+0.25% –0.30%	1	0.252	0.266	0.259	42.2	1	-0.238	-0.358	-0.298	-39.1
	2	0.245	0.254	0.250	41.2	2	-0.240	-0.358	-0.299	-38.3
	3	0.244	0.250	0.247	41.2	3	-0.240	-0.355	-0.297	-36.9
+0.49% –0.59%	1	0.478	0.514	0.496	80.1	1	-0.466	-0.710	-0.588	-60.7
	2	0.479	0.484	0.481	74.0	2	-0.467	-0.694	-0.581	-54.9
	3	0.481	0.485	0.483	73.9	3	-0.482	-0.711	-0.597	-55.0
+0.91% –1.23%	1	0.920	0.955	0.937	120.0	1	-0.909	-1.524	-1.217	-82.9
	2	0.925	0.867	0.896	106.4	2	-0.920	-1.536	-1.228	-79.2
	3	0.921	0.851	0.886	103.6	3	-0.927	-1.541	-1.234	-77.8
+1.26% –1.85%	1	1.324	1.257	1.290	128.2	1	-1.327	-2.399	-1.863	-92.2
	2	1.333	1.165	1.249	112.9	2	-1.335	-2.388	-1.861	-88.8
	3	1.332	1.145	1.239	110.1	3	-1.324	-2.352	-1.838	-85.6
+1.81% –2.86%	1	1.988	1.782	1.885	133.3	1	-1.977	-3.734	-2.856	-101.3
	2	1.991	1.581	1.786	110.6	2	-1.999	-3.751	-2.875	-95.2
	3	1.982	1.525	1.753	102.8	3	-2.000	-3.707	-2.853	-92.0
+2.58% –4.39%	1	2.968	2.449	2.709	128.0	1	-3.006	-5.693	-4.349	-103.9
	2	2.924	2.136	2.530	100.0	2	-3.083	-5.745	-4.414	-100.5
	3	2.897	2.096	2.497	93.5	3	-3.099	-5.743	-4.421	-97.0
+3.48% –5.78%	1	3.901	3.021	3.461	115.0	1	-4.081	-7.500	-5.791	-105.3
	2	4.000	3.020	3.510	106.1	2	-4.130	-7.491	-5.811	-101.6
	3	3.955	2.976	3.466	106.3	3	-4.114	-7.354	-5.734	-95.6
+5.25% –8.00%	1	5.916	4.745	5.330	126.6	1	-6.027	-10.307	-8.167	-103.6
	2	5.909	4.424	5.166	108.3	2	-5.925	-9.737	-7.831	-87.2
+7.50% –9.32%	1	8.025	6.493	7.259	112.1	1	-7.772	-11.505	-9.639	-84.3
	2	8.110	7.379	7.745	39.0	2	-7.818	-10.167	-8.992	-51.0

5.2 OBSERVED DAMAGE

Figure 5.1 shows damage photos at zero rotation for all beams after the completion of each load or displacement level applied. For SRC1 and SRC2, damage concentrated primarily at the beam-wall interface. After completing cycles at ~3% rotation, SRC1 showed significant cracking but minimal spalling, while SRC2 showed more spalling and wider cracking, at the beam-wall interface. After completing cycles at ~6% rotation, significant spalling and gapping (axial deformation) at the beam-wall interface, as well as cracking in the embedment region, was evident for SRC1 and was more extensive for SRC2, noting that there was no spalling or significant damage in the embedment region during either test.

Damage in the embedment region was more extensive for SRC3 and SRC4 than for SRC1 and SRC2. SRC3 showed extensive cracking in the embedment region after completing cycles at ~3% rotation with significant crack opening evident after completing cycles at ~6% rotation. Spalling of cover concrete and buckling of wall boundary longitudinal reinforcement in the SRC3 embedment region appeared imminent when testing of SRC3 terminated; this damage was observed during testing of SRC4. Extensive cracking in the embedment region was also seen for SRC4 after completing cycles at ~3% beam rotation, and damage after completing cycles at ~6% rotation included extensive concrete spalling and crushing as well as buckling of wall longitudinal reinforcement at the embedment region, which had initiated during loading cycles at ~4% rotation.

Aside from the damage at the beam-wall interface, only minor hairline cracking was observed within the beam span for all four tests. Although significant outward ratcheting of the steel

section was observed during testing of SRC2 and to some extent for SRC1, the axial restraining system for SRC3 and SRC4 was effective in reducing the gap opening at the beam-wall interface. Because this level of axial restraint was presumably less than that provided in actual structures, outward ratcheting does not appear problematic for SRC coupling beams.

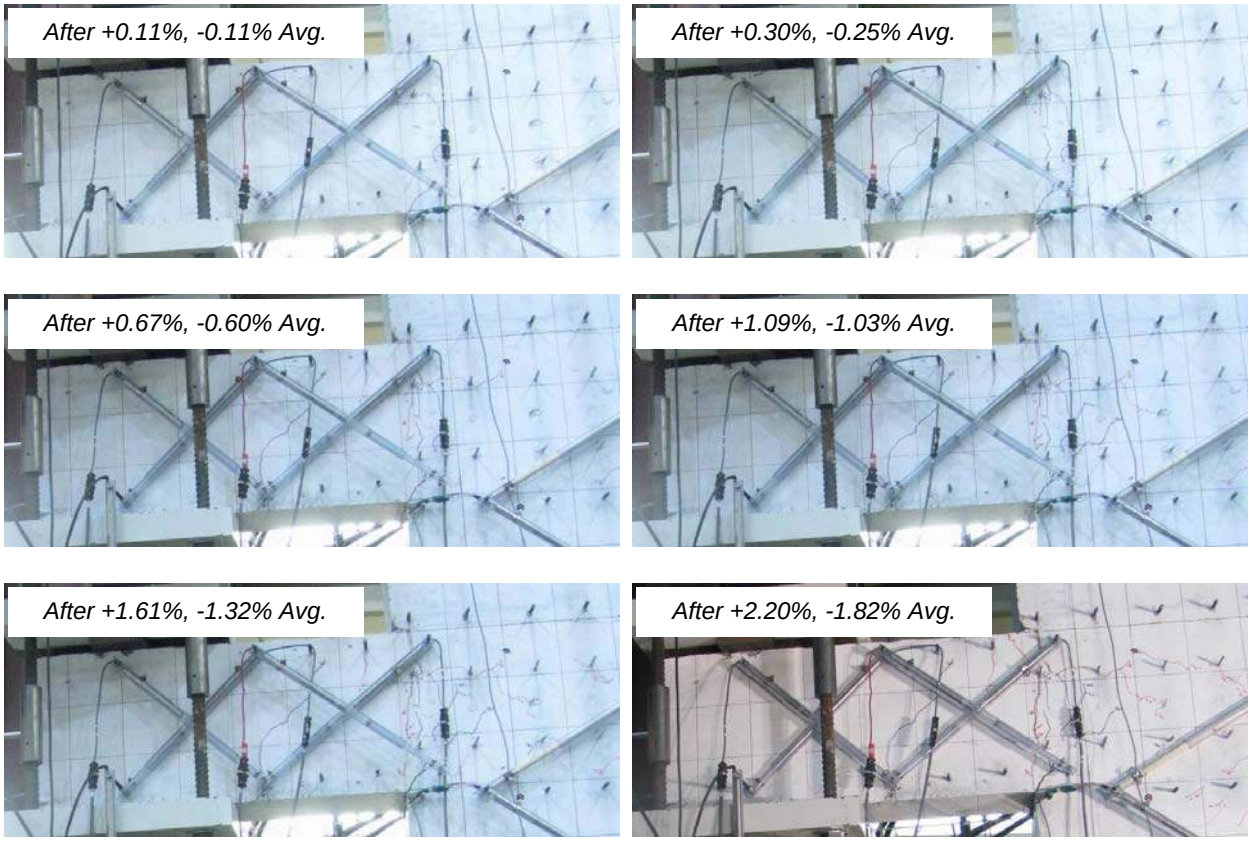

Figure 5.1: Damage Photos at Zero Rotation: a) SRC1

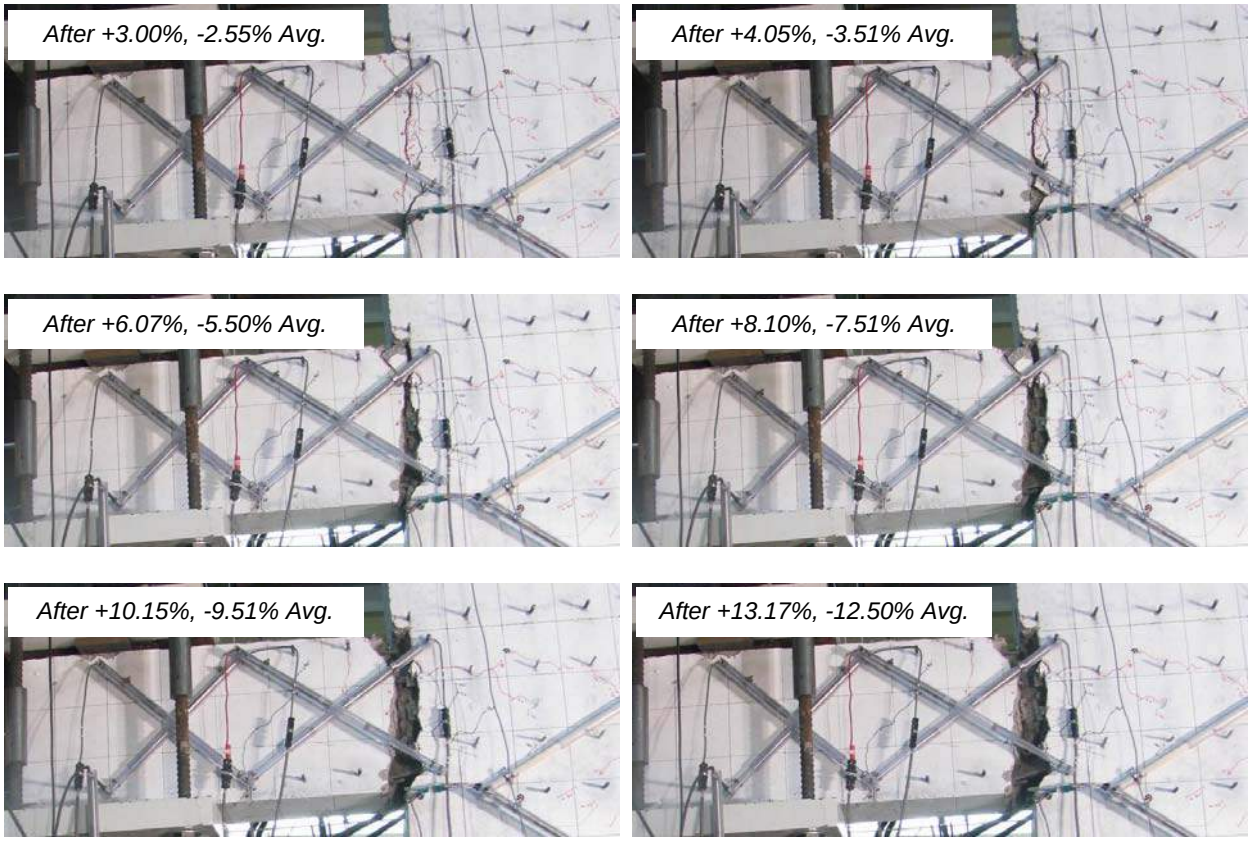

Figure 5.1: Damage Photos at Zero Rotation: a) SRC1 (Continued)

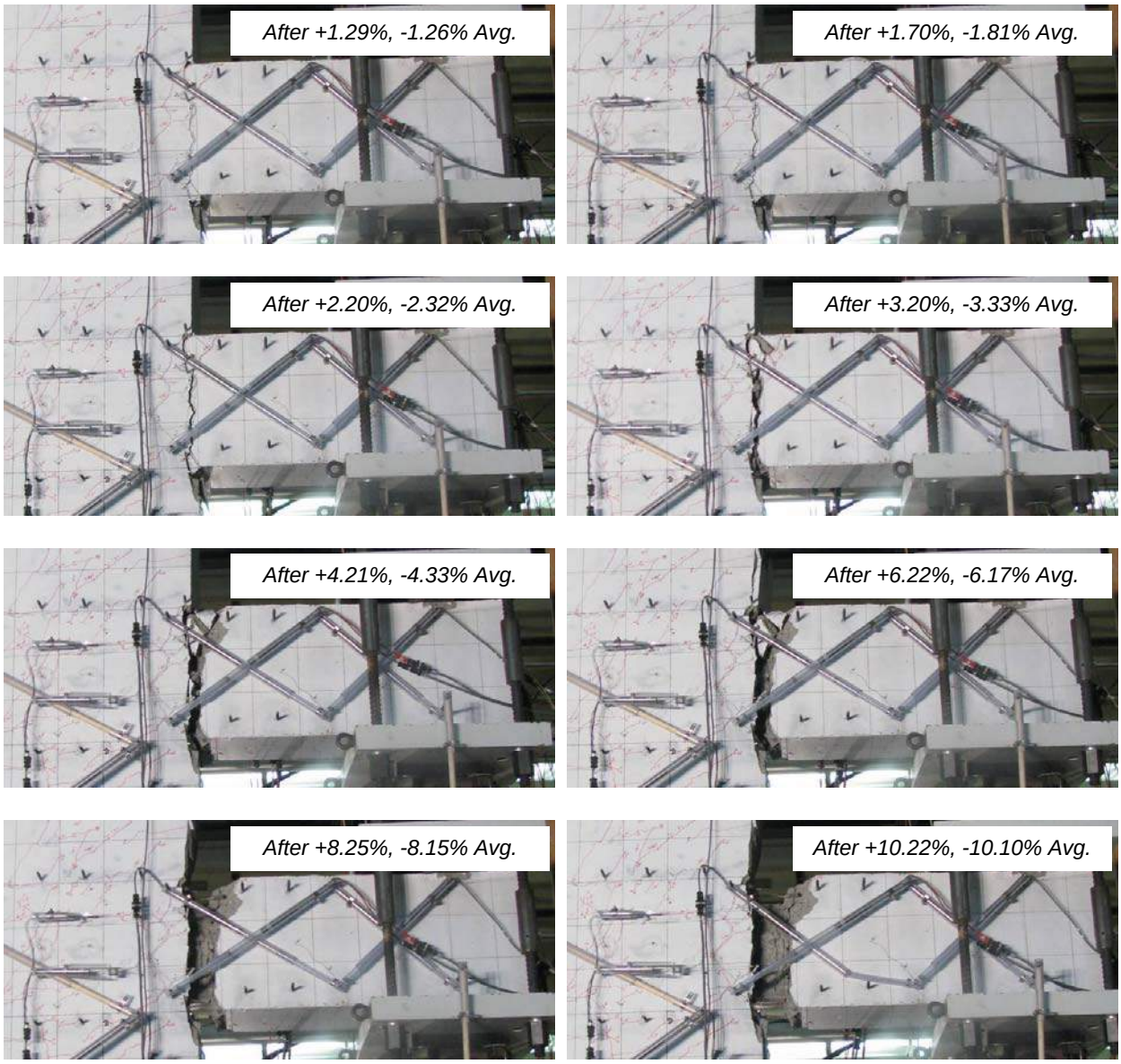

Figure 5.1: Damage Photos at Zero Rotation: b) SRC2

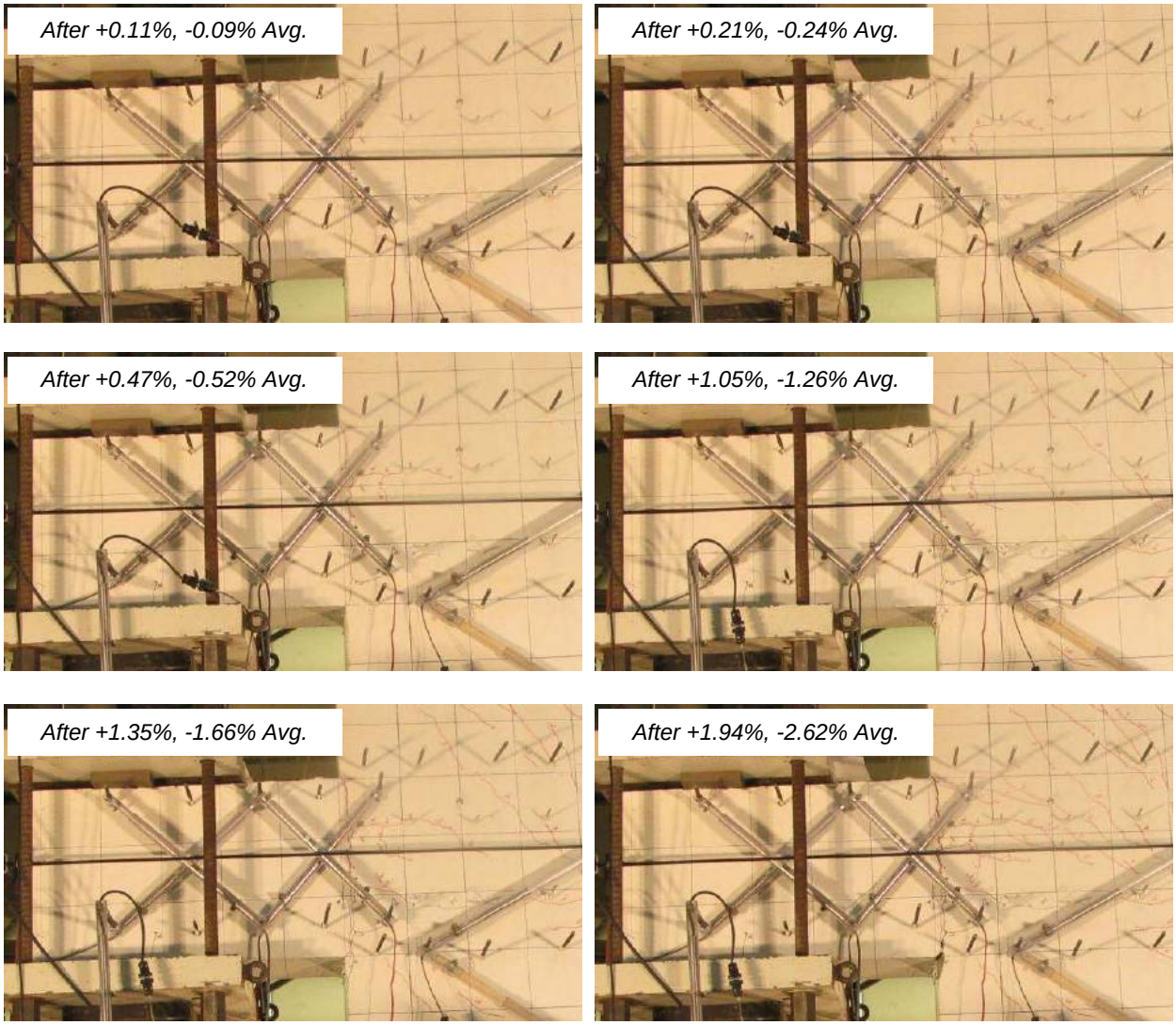

Figure 5.1: Damage Photos at Zero Rotation: c) SRC3

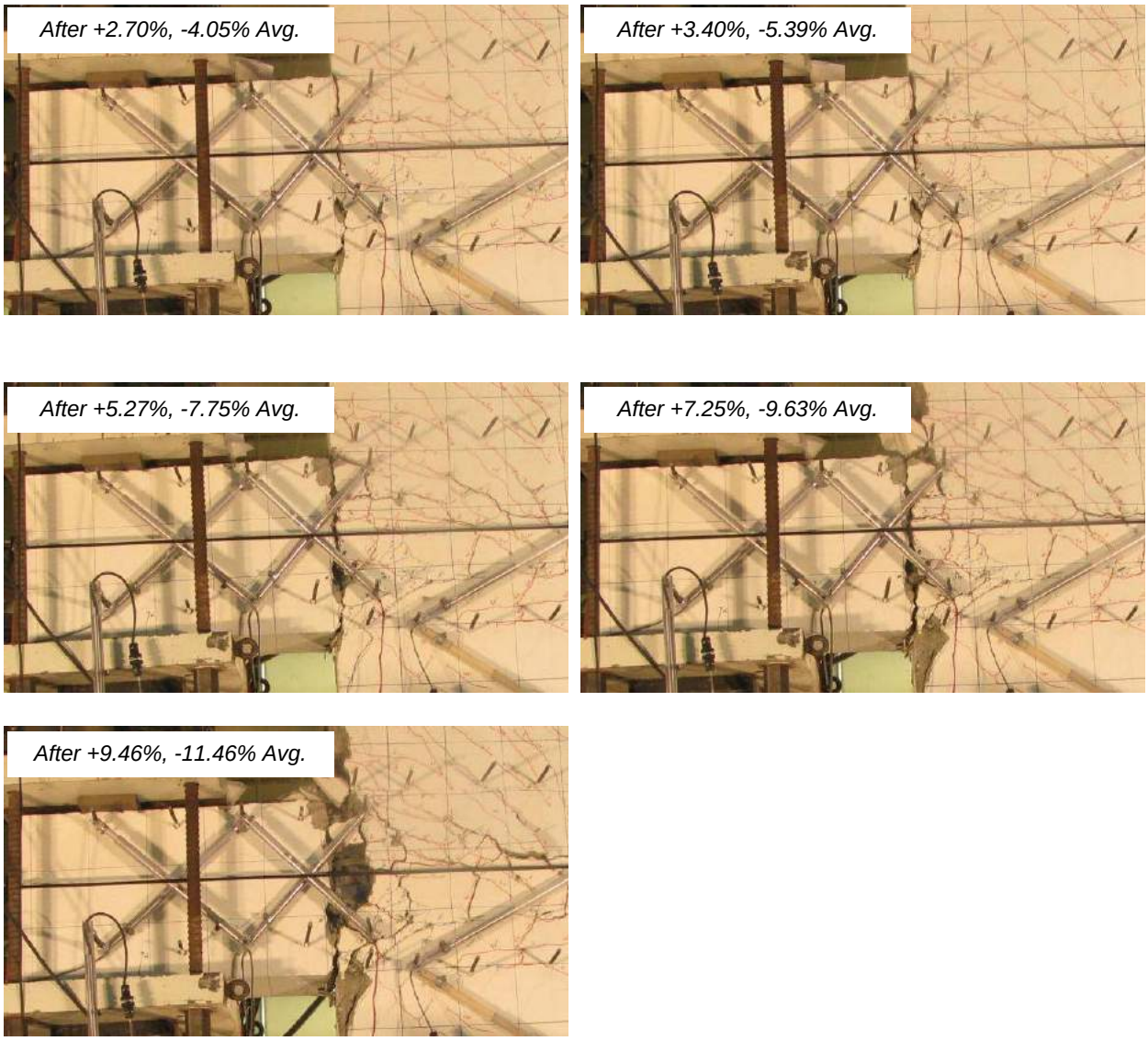

Figure 5.1: Damage Photos at Zero Rotation: c) SRC3 (Continued)

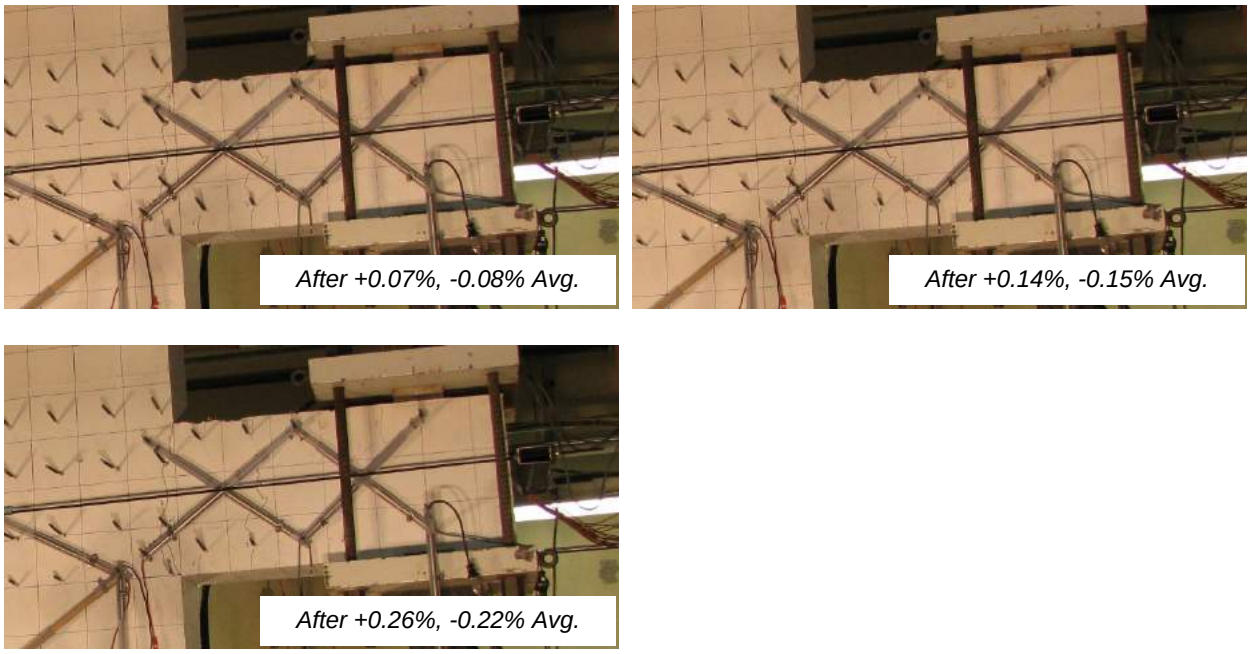

Figure 5.1: Damage Photos at Zero Rotation: d) SRC4 prior to Loading Protocol Adjustment

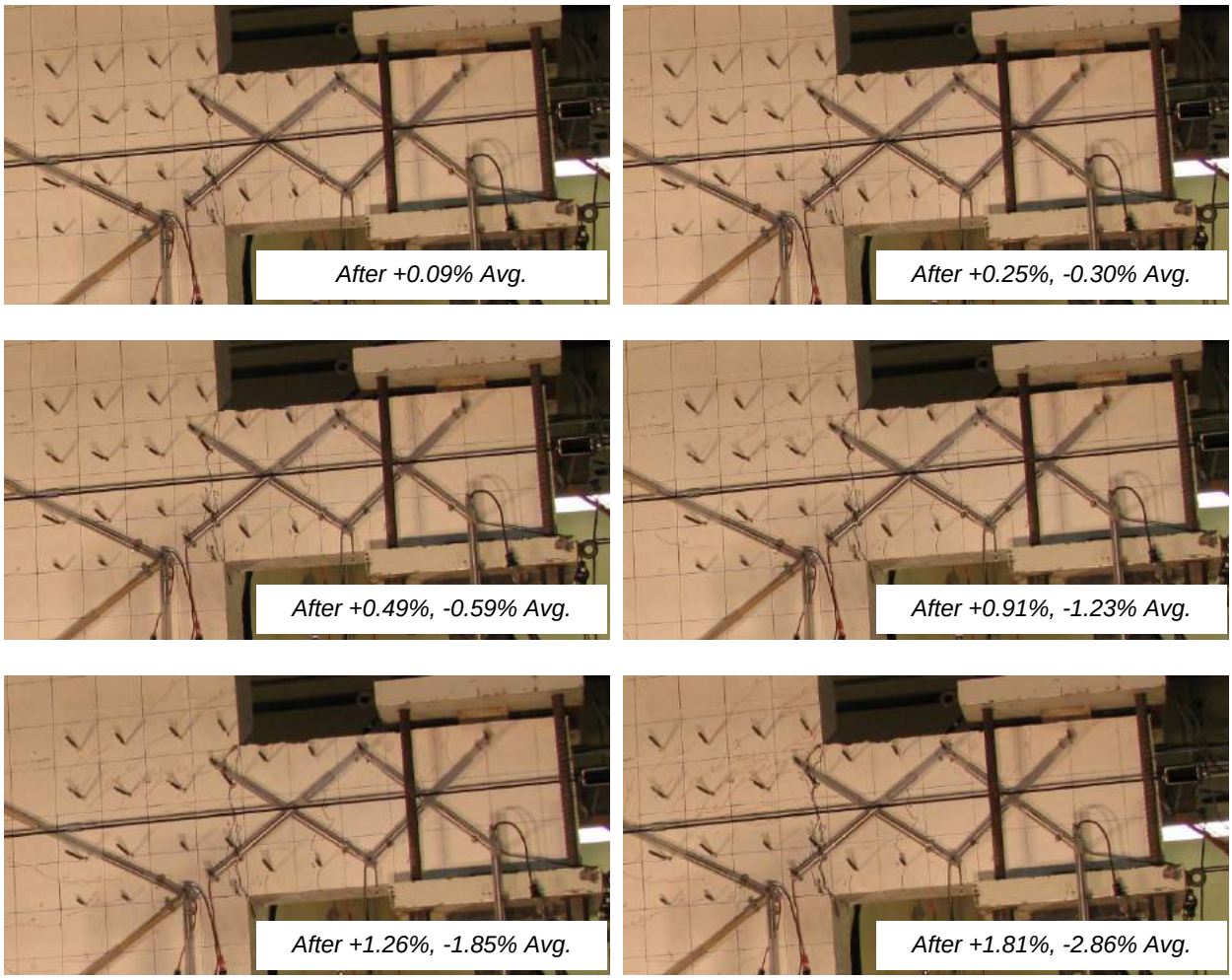

Figure 5.1: Damage Photos at Zero Rotation: e) SRC4

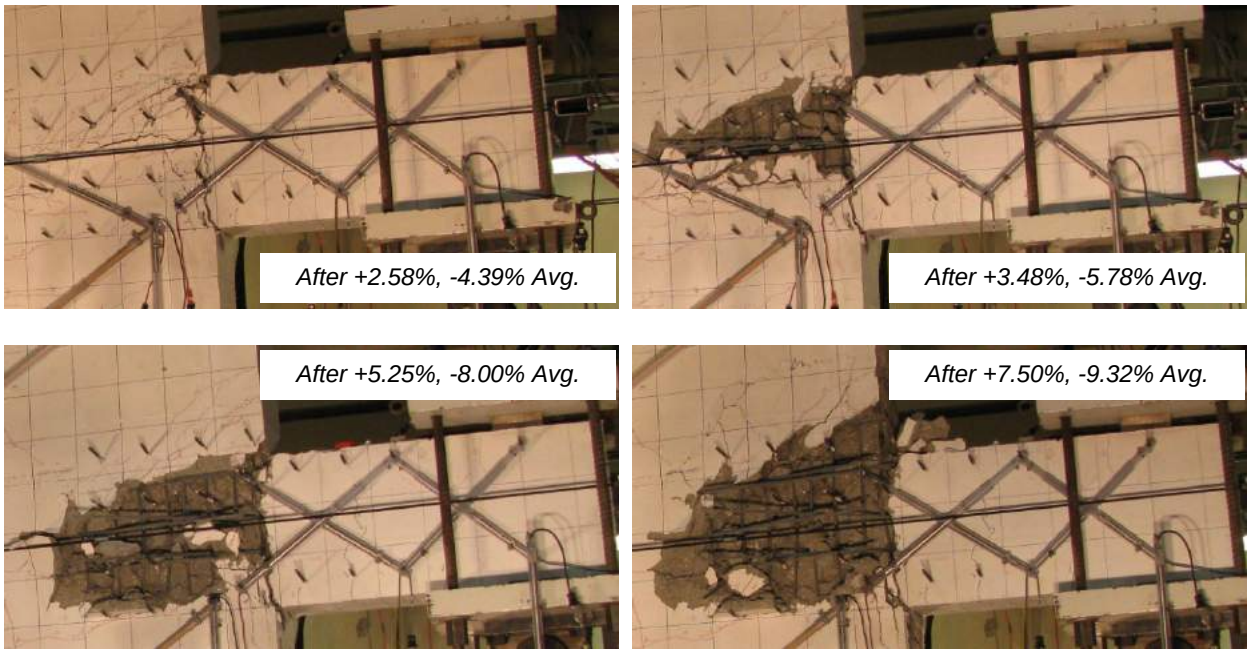

Figure 5.1: Damage Photos at Zero Rotation: e) SRC4 (Continued)

Figure 5.2: Photo Showing Gapping Between Steel Flange and Concrete (SRC2)

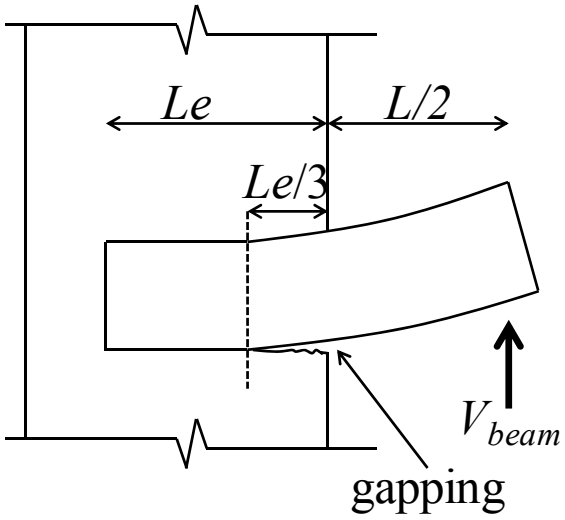

Figure 5.3: Effective Fixity Point (Shahrooz et al (1993) and Harries et al (2000))

Significant gapping between the steel flange and wall concrete at the beam-wall interface (Figure 5.2) occurred in all tests and is consistent with the modeling recommendation of Shahrooz et al (1993) and Harries et al (2000), in which the effective point of fixity is taken at $L_e/3$ inside of the beam-wall interface (Figure 5.3). This modeling recommendation, which was later considered in Section 6.2.1, increases the beam clear span by $2L_e/3$ for a coupling beam in an actual structure

and increases the effective cantilever lengths of the one-half-length test beams in this study by $L_e/3$.

The noted embedment damage for SRC3 and SRC4 is undesirable. Properly designed coupling beams should display damage patterns similar to SRC1 and SRC2, where damage concentrates at the beam-wall interface. The measured crack widths at the beam-wall interface are an important metric for relating the damage observed in the test specimens to the expected repair procedures required after an earthquake. The residual crack widths measured at zero load, rather than the crack widths measured at peak loads, provide a better indicator of the damage that will exist after earthquake shaking has stopped. For the beams in this study, residual crack widths at the beam-wall interface generally did not exceed 1/8" and 1/4" at ~1.5% and ~2.5% rotation or less, respectively (Table 5.2). For the beams with axial restraint (SRC3 and SRC4), residual crack widths at the beam-wall interface generally did not exceed 1/2" until rotations exceeded ~5% (Table 5.2). The measured crack widths and observed damage patterns are useful in developing fragility curves, which may be used to relate observed damage to repair procedures for structural components following an earthquake. As the development of fragility curves requires sufficient data to construct probability density functions based on meaningful statistical analysis, the development of fragility curves was not possible at this time due to the lack of available test data.

Table 5.2: Measured Residual Crack Widths at Beam-Wall Interface: a) SRC1

Avg. Rotation	1st Cycle		2nd Cycle		3rd Cycle		Residual	
	Pos. (+)	Neg. (-)	Pos. (+)	Neg. (-)	Pos. (+)	Neg. (-)	Pos. (+)	Neg. (-)
0.11%, -0.11%	0.002	0.020	x	x	x	x	x	x
0.30%, -0.25%	0.010	0.020	0.020	0.020	x	0.030	x	x
0.67%, -0.60%	0.040	0.060	x	x	x	x	x	x
1.09%, -1.03%	0.094	0.125	x	x	x	x	x	x
1.61%, -1.32%	0.188	0.188	x	x	x	x	x	x
2.20%, -1.82%	0.250	0.250	0.250	x	x	x	x	x
3.00%, -2.55%	0.375	0.313	0.375	0.313	0.313	x	x	0.188
4.05%, -3.51%	0.375	0.500	1.250	0.438	1.250	0.500	1.000	0.313
6.07%, -5.50%	1.500	0.750	2.000	1.000			2.000	1.000
8.10%, -7.51%	3.000	1.250	3.000	3.000			2.500	3.000
10.15%, -9.51%	3.000	4.500	3.750	4.750			3.000	4.500
13.17%, -12.50%	x	x	x	x			x	x

Table 5.2: Measured Residual Crack Widths at Beam-Wall Interface: b) SRC2

Avg. Rotation	1st Cycle		2nd Cycle		3rd Cycle		Residual	
	Pos. (+)	Neg. (-)	Pos. (+)	Neg. (-)	Pos. (+)	Neg. (-)	Pos. (+)	Neg. (-)
0.09%, -0.10%	x	x	x	x	x	0.013	x	x
0.18%, -0.14%	x	x	x	x	x	x	x	x
0.39%, -0.26%	x	0.030	0.040	x	x	x	x	x
0.63%, -0.36%	0.094	0.040	0.100	x	0.090	0.050	x	x
1.01%, -0.43%	x	0.120	0.150	0.125	0.120	x	x	x
1.29%, -1.26%	x	0.160	0.140	0.160	0.180	0.200	0.080	0.070
1.70%, -1.81%	0.260	0.250	0.250	0.250	0.280	0.230	0.140	0.130
2.20%, -2.32%	0.330	0.380	0.360	0.380	0.450	0.370	0.270	0.250
3.20%, -3.33%	0.600	0.500	2.000	2.000	2.000	3.000	1.900	2.500
4.21%, -4.33%	2.750	3.500	2.750	3.750	3.000	3.750	2.500	4.000
6.22%, -6.17%	4.000	5.000	4.000	5.000			3.250	5.000
8.25%, -8.15%	4.750	6.000	5.000	7.000			4.250	6.500
10.22%, -10.10%	5.750	7.500	6.000	8.000			x	x

Table 5.2: Measured Residual Crack Widths at Beam-Wall Interface: c) SRC3

Avg. Rotation	1st Cycle				2nd Cycle				3rd Cycle			
	Positive (+)		Negative (-)		Positive (+)		Negative (-)		Positive (+)		Negative (-)	
	Peak	Resid.	Peak	Resid.	Peak	Resid.	Peak	Resid.	Peak	Resid.	Peak	Resid.
0.11%, -0.09%	x	x	x	x	x	x	x	x	x	x	x	x
0.21%, -0.24%	0.013	x	0.020	0.013	0.016	x	0.030	0.011	0.020	0.009	0.030	0.013
0.47%, -0.52%	0.040	0.013	0.060	0.030	0.040	0.020	0.050	0.030	0.050	0.016	0.060	0.040
1.05%, -1.26%	0.125	0.040	0.155	0.060	0.128	0.050	0.143	0.073	0.152	0.072	0.131	0.076
1.35%, -1.66%	0.190	0.070	0.217	0.093	0.188	0.050	0.167	0.097	0.184	0.060	0.238	0.096
1.94%, -2.62%	0.250	0.119	0.278	0.173	0.302	0.163	0.304	0.186	0.211	0.092	0.317	0.150
2.70%, -4.05%	0.300	0.173	0.463	0.314	0.355	0.198	0.482	0.266	0.322	0.206	0.525	0.315
3.40%, -5.39%	0.458	0.296	0.648	0.413	0.460	0.305	0.760	0.361	0.486	0.313	0.640	0.375
5.27%, -7.75%	0.753	0.443	1.042	0.866	0.876	0.637	1.210	0.713				
7.25%, -9.63%	0.877	0.757	1.834	1.313	1.060	0.775	0.782	0.714				
9.46%, -11.46%	x	x	x	x								

Table 5.2: Measured Residual Crack Widths at Beam-Wall Interface: d) SRC4 prior to Loading Protocol Adjustment

Avg. Rotation	1st Cycle				2nd Cycle				3rd Cycle			
	Positive (+)		Negative (-)		Positive (+)		Negative (-)		Positive (+)		Negative (-)	
	Peak	Resid.	Peak	Resid.	Peak	Resid.	Peak	Resid.	Peak	Resid.	Peak	Resid.
0.07%, -0.08%	x	x	x	x	x	x	x	x	x	x	x	x
0.14%, -0.15%	x	x	x	x	x	x	x	x	x	x	x	x
0.26%, -0.22%	0.025	0.011	0.025	0.013	0.030	0.011	0.030	0.016	0.030	0.011	0.030	0.020
0.46%, -0.30%	0.060	0.020	0.050	0.020								

Table 5.2: Measured Residual Crack Widths at Beam-Wall Interface: e) SRC4

Avg. Rotation	1st Cycle				2nd Cycle				3rd Cycle			
	Positive (+)		Negative (-)		Positive (+)		Negative (-)		Positive (+)		Negative (-)	
	Peak	Resid.	Peak	Resid.	Peak	Resid.	Peak	Resid.	Peak	Resid.	Peak	Resid.
0.09%	x	x	x	x	x	x	x	x	x	x	x	x
0.25%, -0.30%	x	x	x	x	x	x	x	x	x	x	x	x
0.49%, -0.59%	0.086	0.040	0.060	0.050	0.087	0.060	0.092	0.040	0.089	0.060	0.085	0.068
0.91%, -1.23%	0.152	0.080	0.211	0.050	0.153	0.092	0.172	0.060	0.167	0.096	0.106	0.060
1.26%, -1.85%	0.231	0.147	0.218	0.090	0.234	0.126	0.231	0.099	0.220	0.186	0.253	0.100
1.81%, -2.86%	0.321	0.201	0.377	0.130	0.356	0.195	0.417	0.226	0.346	0.256	0.403	0.169
2.58%, -4.39%	0.465	0.359	0.666	0.276	0.423	0.386	0.719	0.284	0.661	0.351	0.838	0.535
3.48%, -5.78%	0.673	0.488	1.081	0.458	0.632	0.512	1.125	0.428	0.558	0.539	1.344	0.667
5.25%, -8.00%	0.953	0.601	1.743	0.823	0.912	0.796	1.806	1.320				
7.50%, -9.32%	x	x	x	x	x	x	x	x				

5.3 LOAD-DISPLACEMENT

The load-displacement response of seismic force-resisting members is one of the primary means used to assess performance. Favorable load-deformation response is characterized by predictable strength and stiffness with minimal pinching and large ductility. Large ductility is characterized by minimal cyclic degradation and strength degradation, noting that strength degradation refers to a reduction in strength due to an increase in imposed beam rotation, whereas cyclic degradation refers to a reduction in strength (due to a reduction in stiffness) between subsequent loading cycles at roughly equivalent imposed beam rotation.

5.3.1 Test Beams

The load-deformation response for each of the test beams is presented in Figure 5.4, with three strength-based limit states indicated on the plots, including two limit states for embedment strength, $V_{ne,embed(M\&M)}$ and $V_{ne,embed(M\&G)}$, and one limit state for flexural strength, $V@M_p$. The nominal plastic flexural strength, M_p, of the cross-section was computed to be 391.7 k-ft using the specified minimum yield strength, F_y (50-ksi), for structural steel and the specified compressive strength of concrete, f'_c (4.5-ksi), with a uniform magnitude stress block for concrete in compression. A sample computation for the method used to determine M_p is provided in Appendix B. The shear corresponding to the development of the nominal plastic flexural strength, $V@M_p$, was based on fixity at the beam-wall interface. The embedment strengths, $V_{ne,embed(M\&M)}$ and $V_{ne,embed(M\&G)}$, were computed based on the provided embedment length, L_e, and the as-tested concrete compressive strength, $f'_{c,test}$ (Table 3.1) using Equation

(2.22) and Equation (2.23), the modified (to account for wall spalling per Harries et al, 1993, and Harries et al, 2000) Marcakis and Mitchell (1980) and Mattock and Gaafar (1982) embedment equations, respectively. The computed values for the three limit states are indicated in Table 5.3, as is the maximum positive and negative beam shear loads, V_{test}, developed during testing. Included in Table 5.3 is a comparison of these observed capacities to the limit states for flexure and embedment strength, as well as an indication of the ratio of observed negative capacity to observed positive capacity, which was included as a means to assess the asymmetry in member capacity.

As the load-deformation response for each test beam is presented individually in Figure 5.4, the first- and second-cycle load-deformation backbone plots for all four beams are plotted together in Figure 5.5 for comparative purposes. Note that the backbone plots are comprised of load-displacement pairs at the peak of each loading cycle and that the load is normalized by $V@M_p$ in order to facilitate comparison between the four flexure-controlled beams of identical cross-section and varying aspect ratio. Figure 5.4, Figure 5.5, and Table 5.3 are collectively used to assess and compare the performances of the four beams.

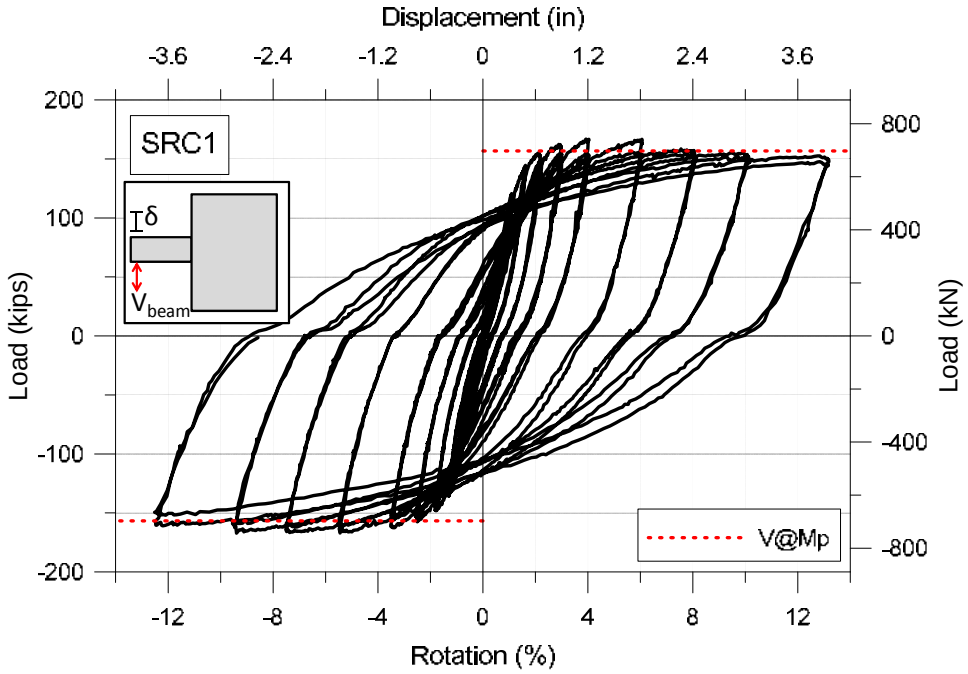

Figure 5.4: Load-Displacement: a) SRC1

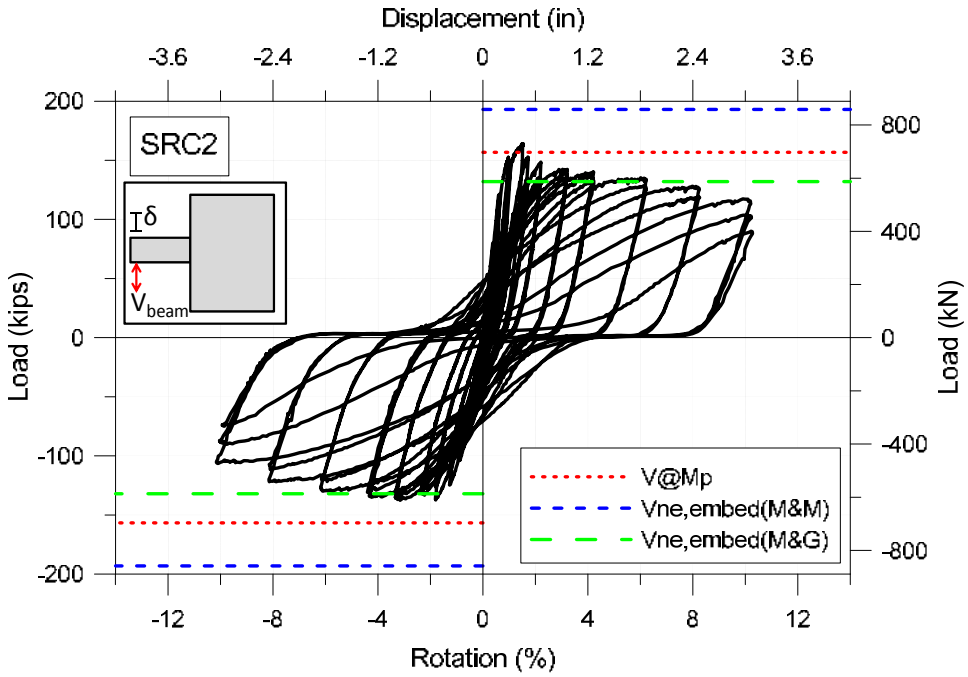

Figure 5.4: Load-Displacement: b) SRC2

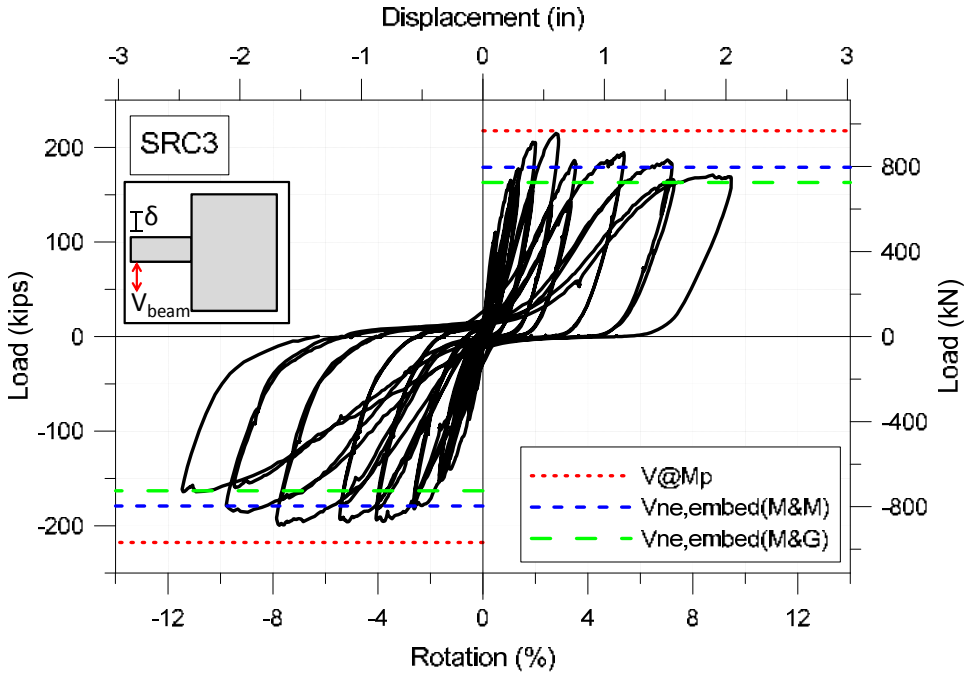

Figure 5.4: Load-Displacement: c) SRC3

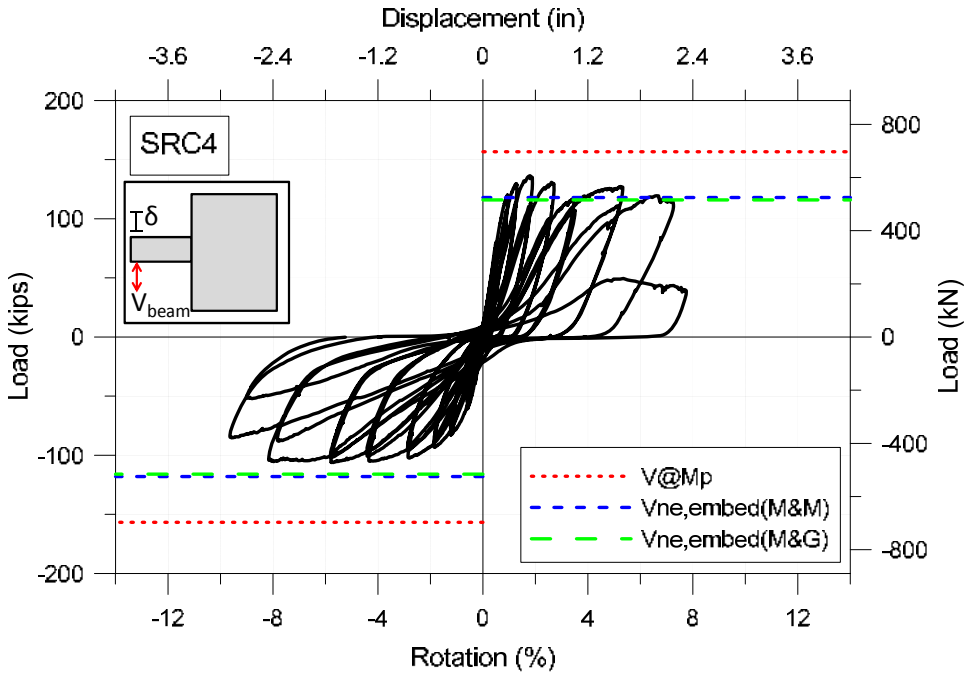

Figure 5.4: Load-Displacement: d) SRC4

Table 5.3: Comparison of Observed Peak Loads to Limit States

	M_{test} (k-ft)		V_{test} (kips)			$V@M_p$ (kips)	$V_{ne,embed\ (M\&M)}$ (kips)	$V_{ne,embed\ (M\&G)}$ (kips)	$V_{ne,embed\ (M\&G)} / V_{ne,embed\ (M\&M)}$	$V_{test} / V@M_p$		$V_{test} / V_{ne,embed\ (M\&M)}$		$V_{test} / V_{ne.embed\ (M\&G)}$	
	(+)	(-)	(+)	(-)	(-)/(+)					(+)	(-)	(+)	(-)	(+)	(-)
SRC1	418	418	167	167	1.00	157	310	210	0.68	1.07	1.07	0.54	0.54	0.80	0.80
SRC2	410	345	164	138	0.84	157	193	132	0.68	1.05	0.88	0.85	0.71	1.24	1.04
SRC3	387	360	215	200	0.93	218	179	163	0.91	0.99	0.92	1.20	1.12	1.32	1.23
SRC4	340	265	136	106	0.78	157	120	117	0.97	0.87	0.68	1.13	0.88	1.17	0.91

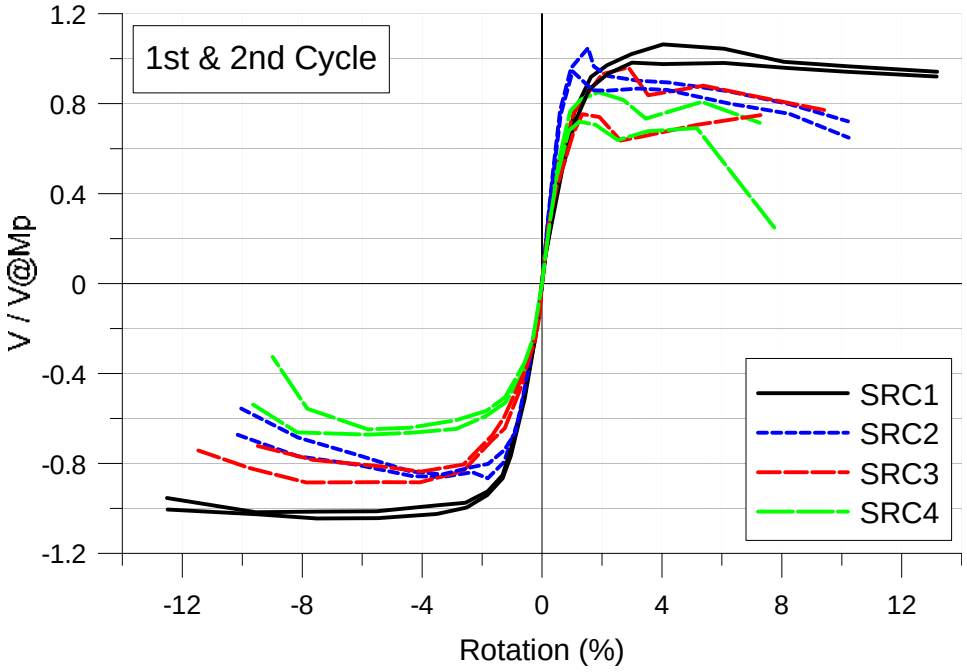

Figure 5.5: Load-Displacement Backbone Test Data for All Beams

It is evident from Figure 5.4, Figure 5.5, and Table 5.3 that there are significant differences in the performances of the four beams. The overall performance of SRC1 was excellent. The load-deformation response displays symmetry with no significant strength degradation, cyclic degradation, or pinching up to rotation levels beyond 12%, which is well beyond any practical

design level. V_{test} for SRC1 was equivalent in both the positive and negative loading directions and was reasonably estimated (within 7%) by $V@M_p$. The limit states for embedment strength were computed to be well in excess of V_{test} (Table 5.3) and are, therefore, not included on the load-displacement plot in Figure 5.4. As SRC1 tested a conservative design, with long embedment length and low wall demands relative to the other test beams (Table 3.1), the excellent performance of SRC1 was believed to be indicative of a peak performance level for flexure-controlled SRC coupling beams without auxiliary transfer bars or face-bearing plates, which appear to increase flexural strength, as later demonstrated in Section 6.2.1.

Relative to SRC1, the load-displacement response for SRC2 displays more pinching, greater strength degradation, slightly greater cyclic degradation, and noticeable asymmetry. The pinching is consistent with the observed gapping between the steel flanges and bearing concrete (Figure 5.2) and is greater for SRC2 than SRC1 due to shorter embedment length and larger wall demands (Table 3.1). While the positive capacity of SRC1 is similar to SRC2 (Table 5.3) and is reasonably estimated by $V@M_p$ (within 5%), the reduced negative capacity, ~15% less than the positive capacity, suggests that the fixity point for negative loading may be inside the face of the wall (Figure 5.3). Despite the reduction in performance of SRC2 relative to SRC1, the overall performance of SRC2 was very favorable, characterized by damage concentration at the beam-wall interface and the development of shear loads of at least 75% of the peak values in both loading directions at all cycles through 6% rotation.

Note that the as-tested compressive strength of concrete ($f'_{c,test}$) of 7.4-ksi for SRC1 and SRC2 (Table 3.1) caused a significant discrepancy between $V_{ne,embed(M\&M)}$ and $V_{ne,embed(M\&G)}$ (Table 5.3).

As discussed in Chapter 2, the use of $\sqrt{f_c'}$ in the Mattock and Gaafar (1982) embedment equation versus f'_c in the Marcakis and Mitchell (1980) equation generally produces more conservatism (i.e. leads to a lower calculated embedment strength for a given embedment length) for values of f'_c in excess of 4-ksi, with the difference between the two equations increasing with increasing f'_c. This trend is evident when comparing $V_{ne,embed(M\&M)}$ / $V_{ne,embed(M\&G)}$ (Table 5.3) versus $f'_{c,test}$ (Table 3.1) for the four beams. Although the SRC2 embedment length was selected to be potentially less-than-adequate based on pre-test analysis (Table 3.4), $V_{ne,embed(M\&G)}$ was exceeded during testing but $V_{ne,embed(M\&M)}$ was not. Of the four beams tested, this is the only instance in which one embedment limit state was exceeded while the other was not. Significant embedment damage was not observed for SRC2, suggesting that the embedment strength was adequate. However, based on this one particular test at this one particular loading level, it is not appropriate to generalize the Mattock and Gaafar (1982) equation as being overly conservative for high-strength concrete. Aside from the tests on embedded steel plates done by Marcakis and Mitchell (1980), neither Marcakis and Mitchell (1980) nor Mattock and Gaafar (1982) tested specimens with f'_c larger than 6-ksi when developing the embedment equations.

Relative to SRC1 and SRC2, the load-displacement responses of SRC3 and SRC4 both displayed greater pinching, cyclic degradation, and strength degradation, consistent with the observed damage in the embedment zone (Figure 5.1). The observed damage was due primarily to the combination of reduced embedment strength (Table 5.3) and decreased area of wall boundary longitudinal reinforcement (Table 3.1). Although SRC3 and SRC4 were designed to provide the same level of embedment strength as SRC2, $f'_{c,test}$ for both SRC3 and SRC4 was lower than SRC2 by at least 30% (Table 3.1), leading to reduced embedment strength (Table 5.3). For

SRC3, and to a lesser extent for SRC4, cyclic degradation is particularly apparent between the first and second positive cycles and is larger than in the negative loading direction. This suggests that the completion of the initial cycle in the negative loading direction is causing new damage which corresponds to cyclic degradation for the subsequent cycle in the positive loading direction, noting that loading in the positive direction preceded loading in the negative direction for each cycle. In other words, it appears that the majority of the observed damage for the test beams is attributable to the initial negative loading cycles. In terms of quantifying strength and cyclic degradation, both beams developed post-peak shear loads above 80% percent of V_{test} for initial loading cycles (strength degradation) and 60% of V_{test} for subsequent loading cycles (cyclic degradation) in both the positive and negative loading directions through 6% rotation.

For SRC3, both embedment limit states were exceeded during testing, which, in addition to 33% larger peak wall demands ($\varepsilon_{s,max}/\varepsilon_y$ from Table 3.1) and a 30% reduction in the provided area of wall boundary longitudinal reinforcement (ρ_{bound} in Table 3.1), contributed to the decrease in performance of SRC3 relative to SRC2. The observed positive capacity for SRC3 matches $V@M_p$ (within 1%), and it is interesting to note that SRC3 is more symmetric than SRC2 in terms of capacity, as the ratio of observed negative to positive capacity is 0.93 compared to 0.84 (Table 5.3), respectively. Damage in the negative loading direction likely contributed to reduced capacity in the positive loading direction for SRC3, consistent with the minor reduction in V_{test} / $V@M_p$ (Table 5.3) in the positive loading direction for SRC3 relative to SRC2.

Of the four beams tested, SRC4 displayed the lowest capacity, 19% and 36% lower than SRC1 and 12% and 26% lower than SRC3 in the positive and negative loading directions, respectively,

and the greatest asymmetry between positive and negative capacity, with a 22% reduction in negative capacity relative to positive capacity (Table 5.3). The decrease in capacity relative to SRC3 is attributed to the 65% decrease in the area of wall boundary longitudinal reinforcement (ρ_{bound} in Table 3.1) rather than the embedment strength, as the limit state for embedment strength was not exceeded in the negative loading direction and was exceeded to a lesser extent than SRC3 in the positive direction. This suggests that damage in the negative loading direction led to strength reduction in the positive loading direction. In addition to the reduced area of wall boundary longitudinal reinforcement relative to SRC3, the smaller diameter longitudinal boundary bars and lack of an ordinary boundary element for SRC4 greatly increased the propensity for buckling of boundary longitudinal reinforcement (noting that s/d_b = 16 for SRC4, versus 6.4 for SRC3, where s is the spacing of the wall boundary transverse reinforcement and d_b is the bar diameter of the wall boundary longitudinal reinforcement), leading to more extensive observed damage (Figure 5.1).

Because the coupling beam bearing forces create additional local tension in the wall boundary longitudinal reinforcement at the connection (Figure 3.9), the provided quantity of boundary longitudinal reinforcement in combination with the demand on that reinforcement may limit the capacity of the coupling beam under negative (downward) loading. Increasing the quantity of wall longitudinal reinforcement is expected to increase the capacity of SRC4 and to reduce the local yielding of wall longitudinal reinforcement (confirmed to have occurred by visual observation of bar buckling and use of strain gage data in Section 5.12) and the associated embedment damage. Sufficient wall longitudinal reinforcement must be provided to resist the

wall demand and the additional local coupling beam bearing force demand; further discussion, as well as a design recommendation, is provided in Section 6.4.1.

SRC2, SRC3, and SRC4 all displayed load-displacement asymmetry, including reduced capacity in the negative (downward), relative to the positive (upward), loading direction. During positive (upward) beam loading, the wall loads created a compression field normal to the embedment length, while a tension field was induced during negative (downward) beam loading (Figure 1.5). This leads to asymmetric load-displacement response of the coupling beam, as the effective point of fixity moves further inside the beam-wall interface when the embedment length is under tensile, rather than compressive, demands. This effect was not apparent for SRC1, due to the combination of lower wall demands and a sufficient quantity of wall boundary reinforcement. The global wall demands for SRC1, which were lower than for SRC2 and SRC3, were comparable for SRC4 ($\varepsilon_{s,max}/\varepsilon_y$ in Table 3.1). However, the provided area of wall boundary longitudinal reinforcement (ρ_{bound} in Table 3.1) for SRC1 was four times that of SRC4, meaning that the local increase in wall demands due to bearing force effects was much smaller for SRC1 than SRC4. Although the wall demands (tension/compression effects) and longitudinal wall reinforcement are important factors influencing asymmetry, it is unclear to what degree increasing the embedment lengths for SRC2, SRC3, and SRC4 might reduce this asymmetry.

5.3.2 Comparison to Reinforced Concrete Coupling Beams

Given that one of the primary research objectives was to improve upon existing building code provisions for coupling beams, comparing the performance of SRC coupling beams to that of

reinforced concrete coupling beams designed to satisfy ACI 318-11 is of interest. SRC1 was used for comparative purposes, as this member was intended to be representative of peak performance. In comparing the load-deformation response of SRC1 to that of the conventionally-reinforced coupling beam tested by Naish et al (2013a) (Figure 5.6), the overall performance of the SRC coupling beam is better, noting that the conventionally-reinforced coupling beam displays noticeably more pinching and greater strength and cyclic degradation beyond 4% rotation. In comparing the load-deformation response of SRC1 to that of a diagonally-reinforced coupling beam tested by Naish et al (2013a) (Figure 5.7), the overall performance is comparable, with minimal pinching, strength degradation, and cyclic degradation through 6% rotation. The strength and cyclic degradation of the diagonally-reinforced coupling beam (DRCB) that occurs beyond 6% rotation was deemed insignificant, given that the demands on coupling beams during MCE level events do not typically exceed 6% rotation (discussed in Section 4.5.2). Given that the performance of SRC coupling beams meets or exceeds that of DRCBs, the cost savings associated with using SRC coupling beams versus DRCBs becomes very attractive for designers.

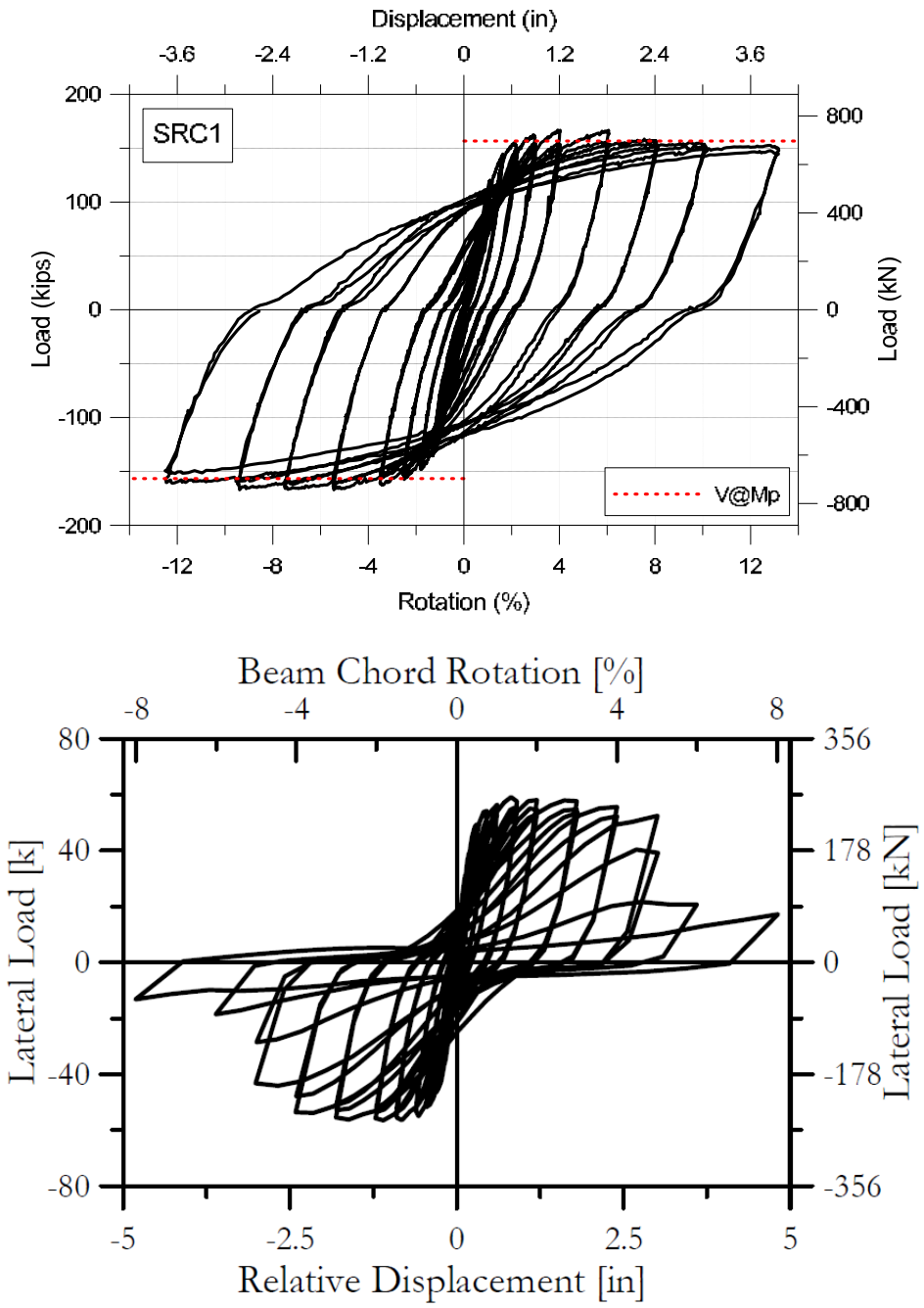

Figure 5.6: Comparison of SRC and Conventionally-Reinforced Concrete Coupling Beams

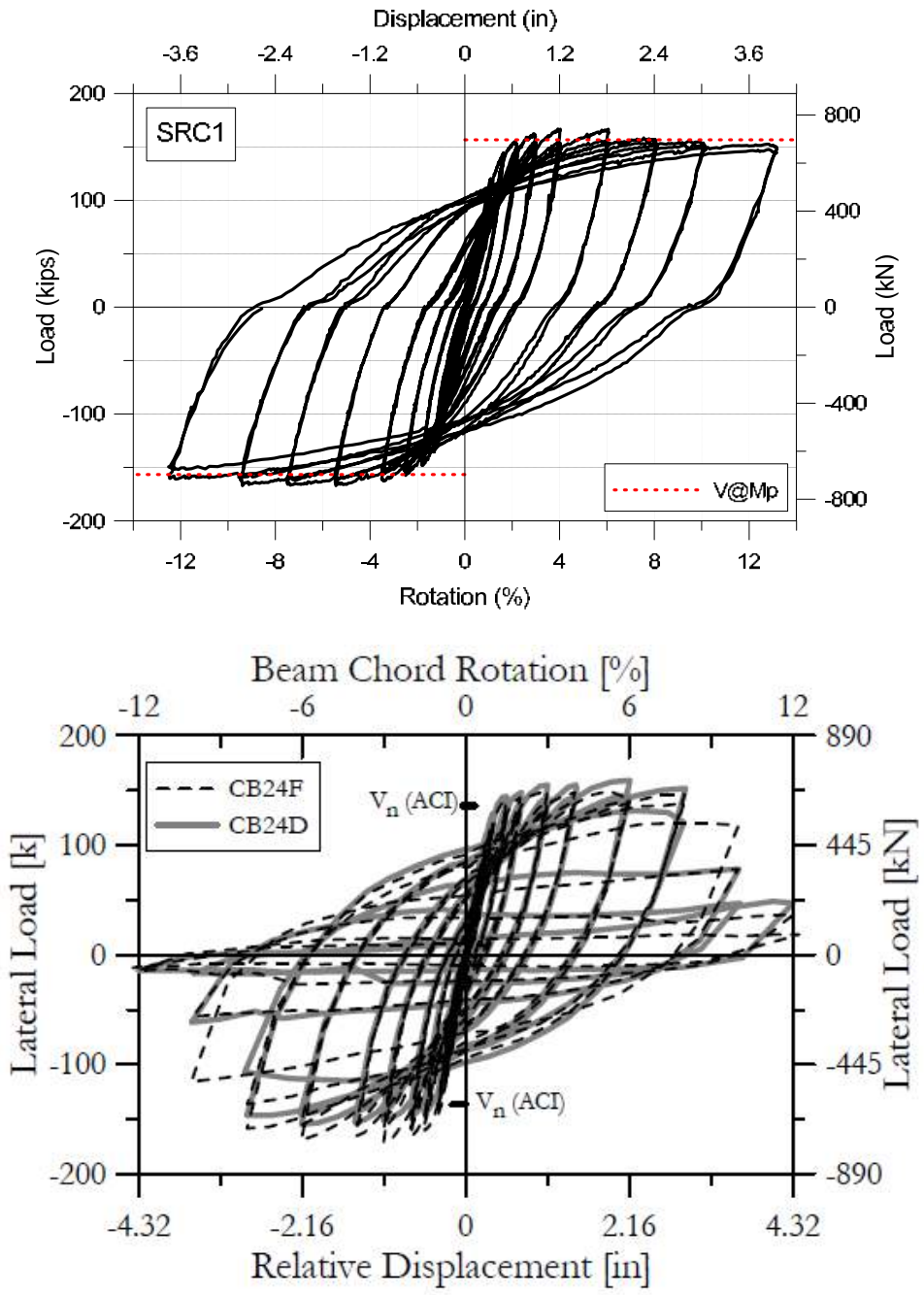

Figure 5.7: Comparison of SRC and Diagonally-Reinforced Concrete Coupling Beams

5.3.3 Influence of Wall Deformations

As mentioned previously in Section 5.1, the uncertainty in the measured coupling beam chord rotation, shown in the load-deformation response in Figure 5.8, is due to uncertainty in the measured wall deformations. Note that the large uncertainty for SRC4 prior to the loading protocol adjustment (Figure 5.8d) prompted a change in the loading protocol. It should also be noted that the values provided in Table 5.1 for load and displacements at the peak of each cycle were based on the plots shown in Figure 5.8. Consistent with the plots in Figure 5.8, the uncertainty in measured coupling beam chord rotation is plotted as a function of the average rotation in Figure 5.9, with the uncertainty in measured rotations determined as the difference between the rotations measured relative to the top and bottom of the wall. For SRC1, the uncertainty is larger in the negative loading direction. For SRC2, the uncertainty versus deformation response matches the shape of the load versus deformation response, indicating that uncertainty is varying linearly with load and is therefore due to elastic deformations (flexibility) in the wall. For SRC3 and SRC4, members for which wall yielding was observed in the negative loading direction (Section 5.8), the uncertainty is larger in the negative rather than the positive direction, and appears to vary almost linearly with beam chord rotation in the negative loading direction.

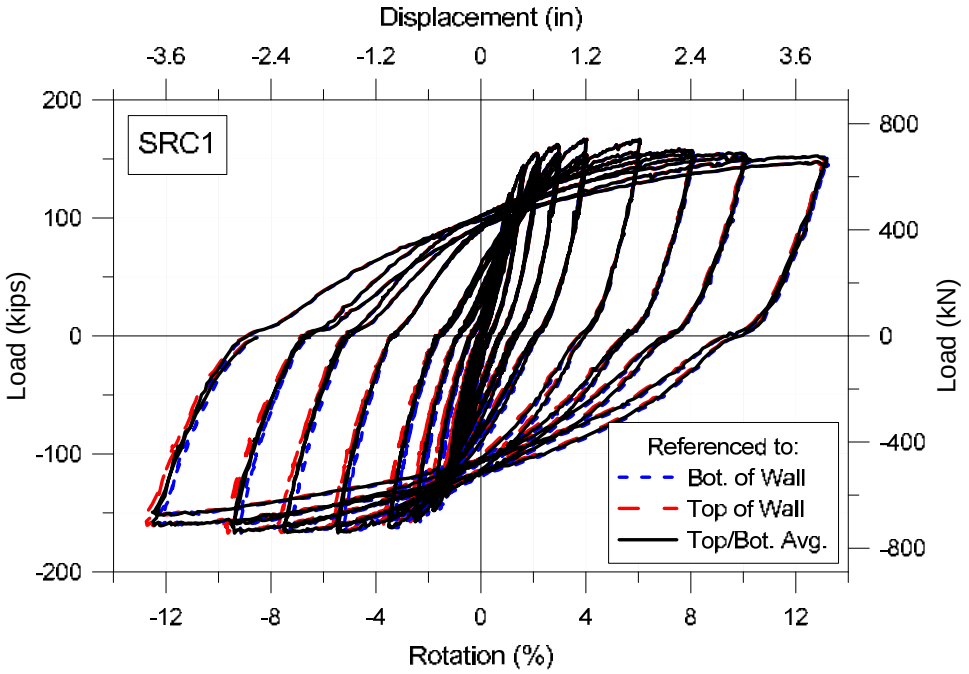

Figure 5.8: Sensitivity of Measured Beam Displacements to Wall Rotation: a) SRC1

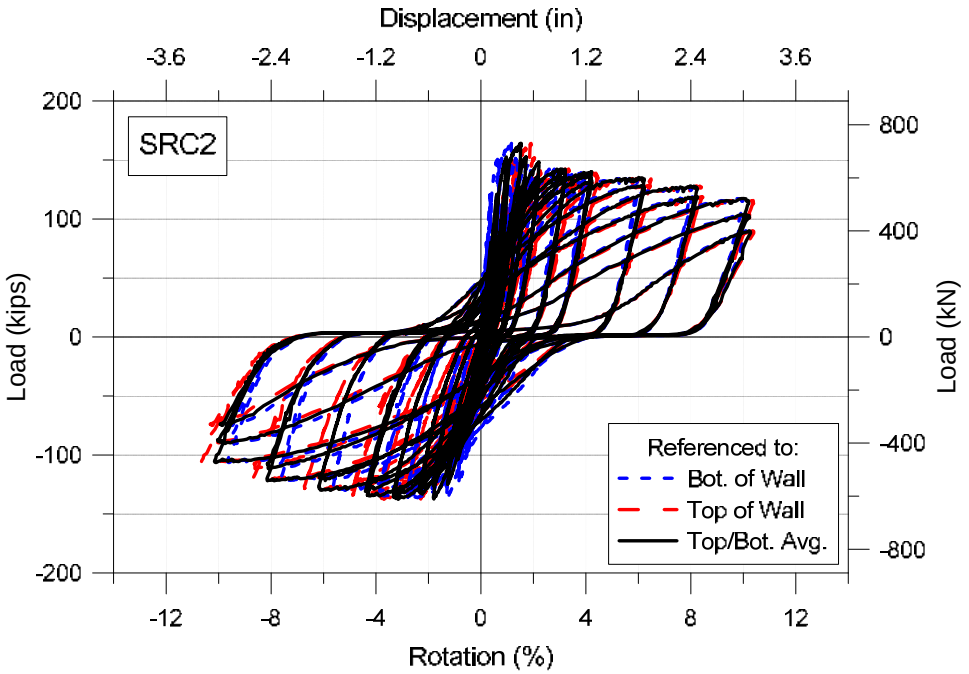

Figure 5.8: Sensitivity of Measured Beam Displacements to Wall Rotation: b) SRC2

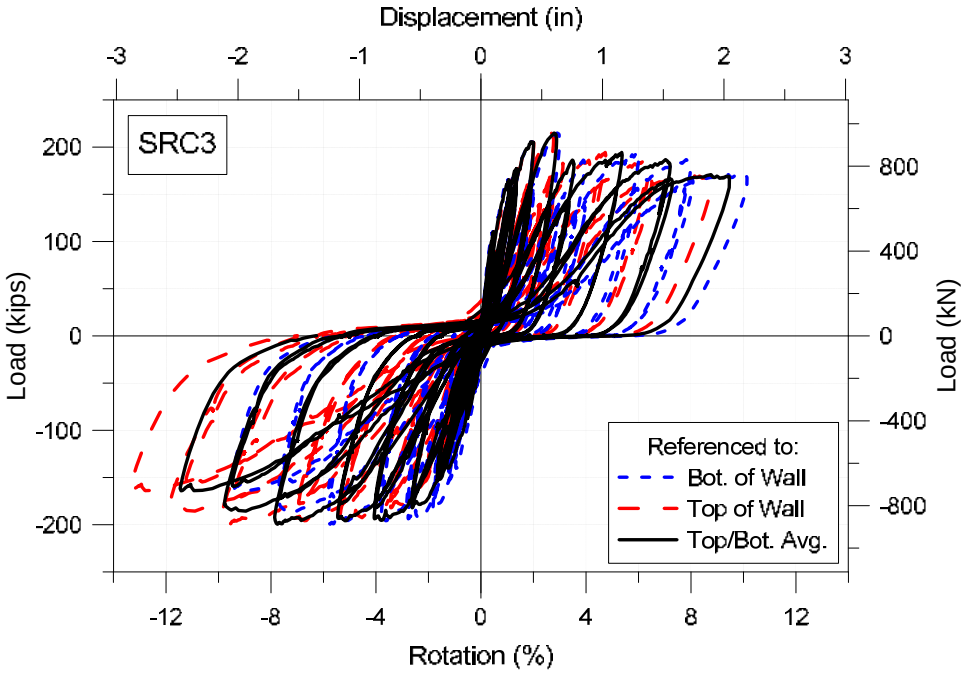

Figure 5.8: Sensitivity of Measured Beam Displacements to Wall Rotation: c) SRC3

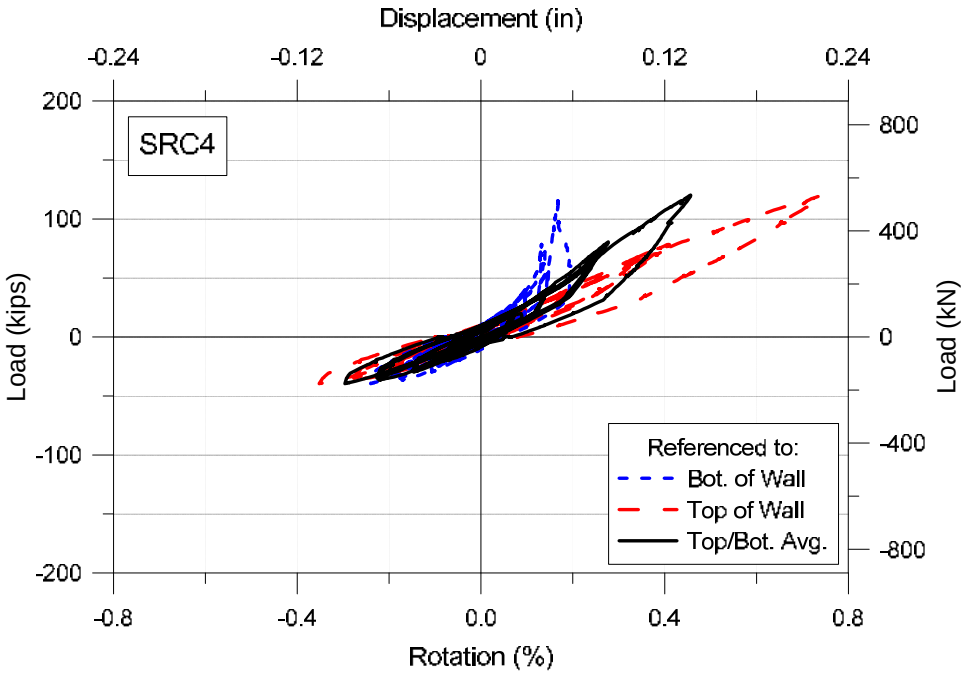

Figure 5.8: Sensitivity of Measured Beam Displacements to Wall Rotation: d) SRC4 prior to Loading Protocol Adjustment

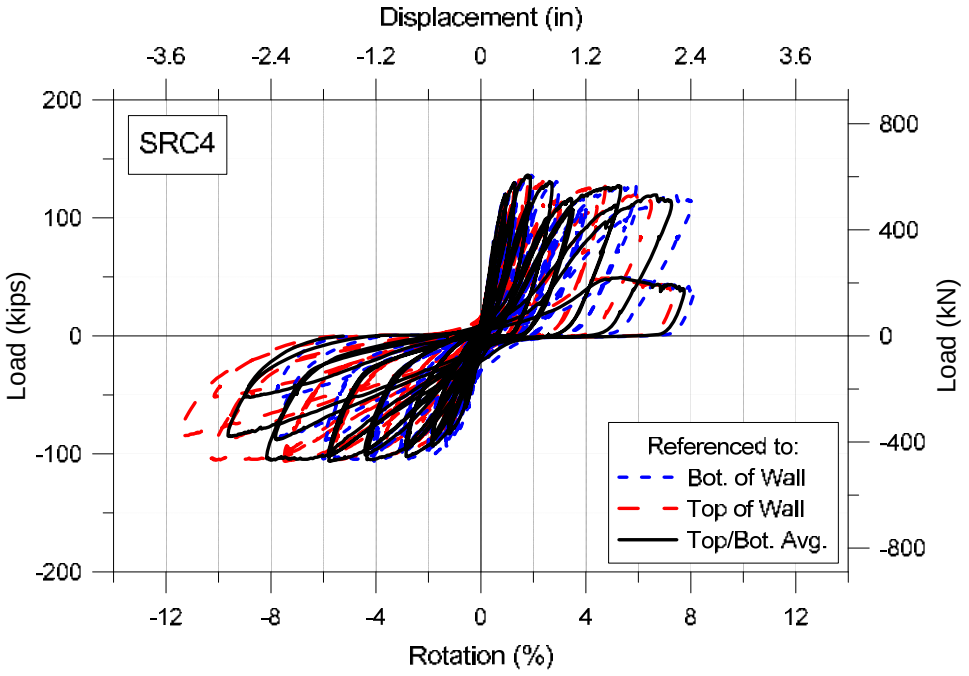

Figure 5.8: Sensitivity of Measured Beam Displacements to Wall Rotation: e) SRC4

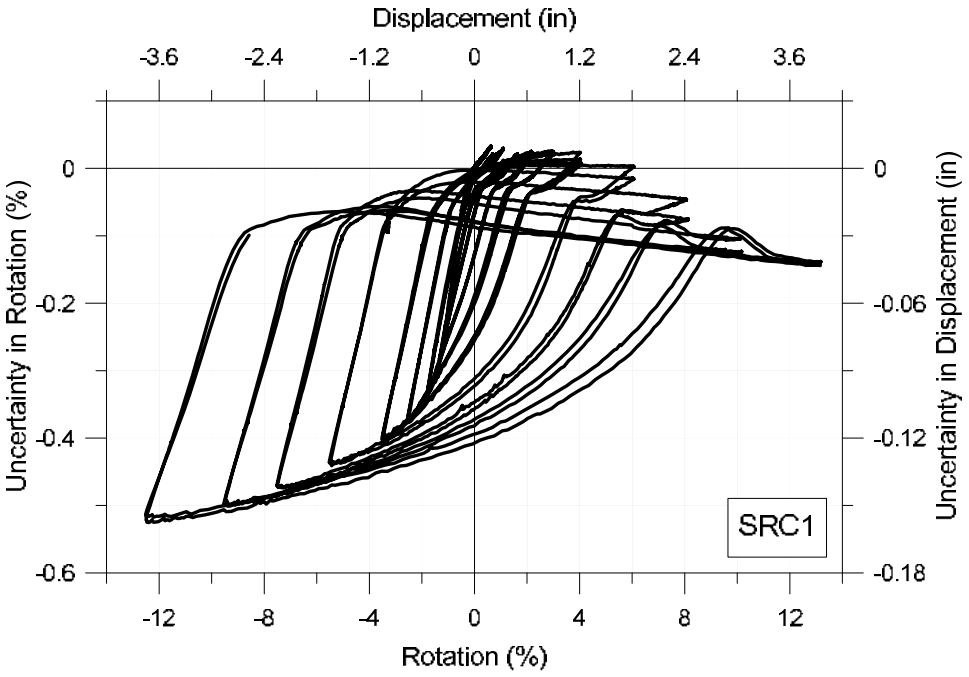

Figure 5.9: Uncertainty in Measured Rotation: a) SRC1

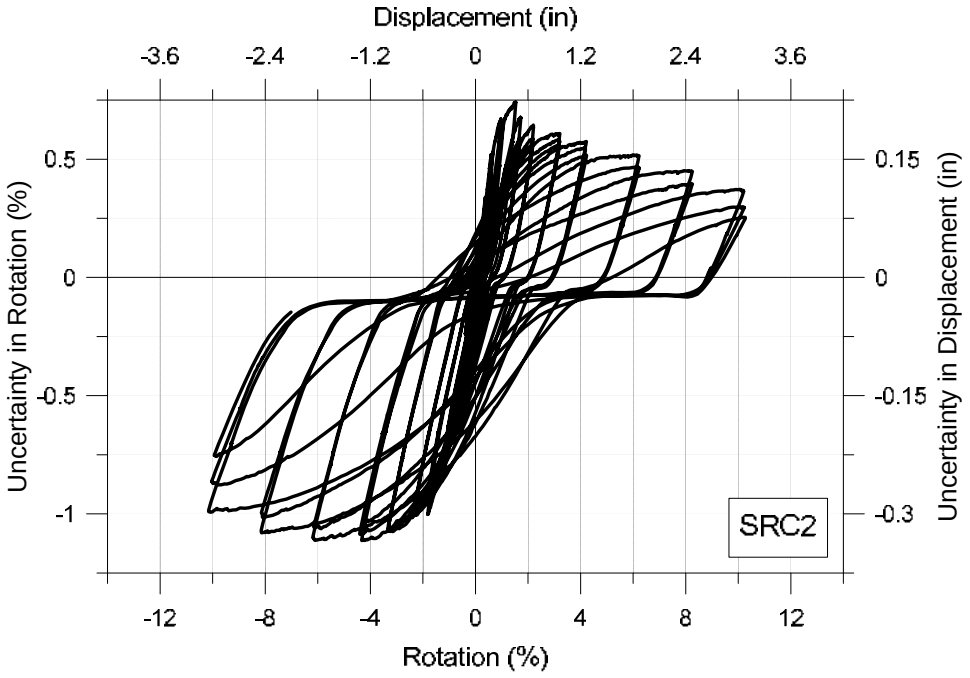

Figure 5.9: Uncertainty in Measured Rotation: b) SRC2

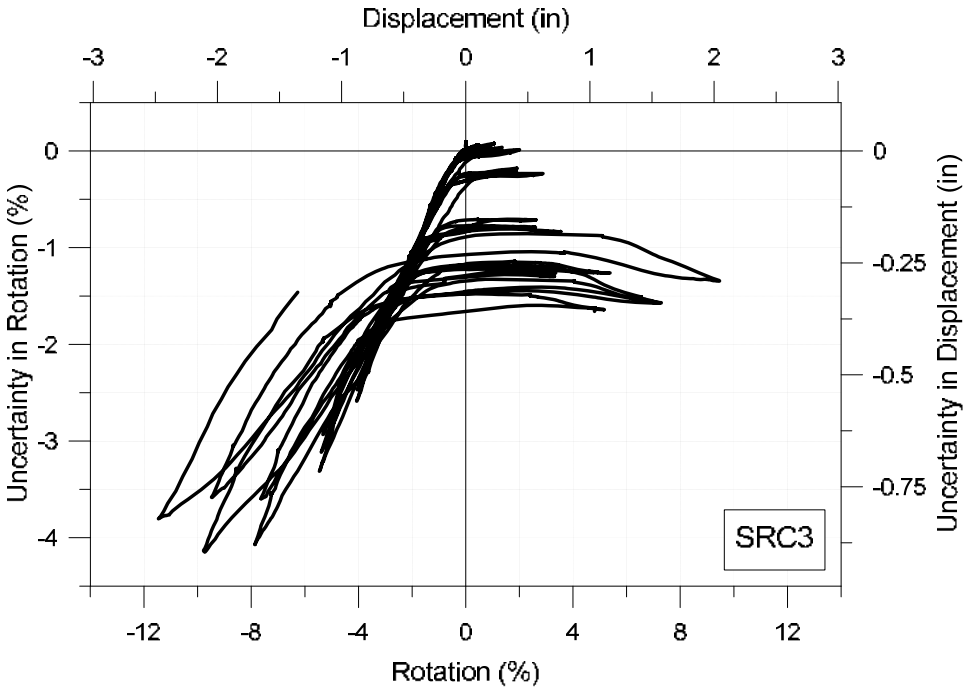

Figure 5.9: Uncertainty in Measured Rotation: c) SRC3

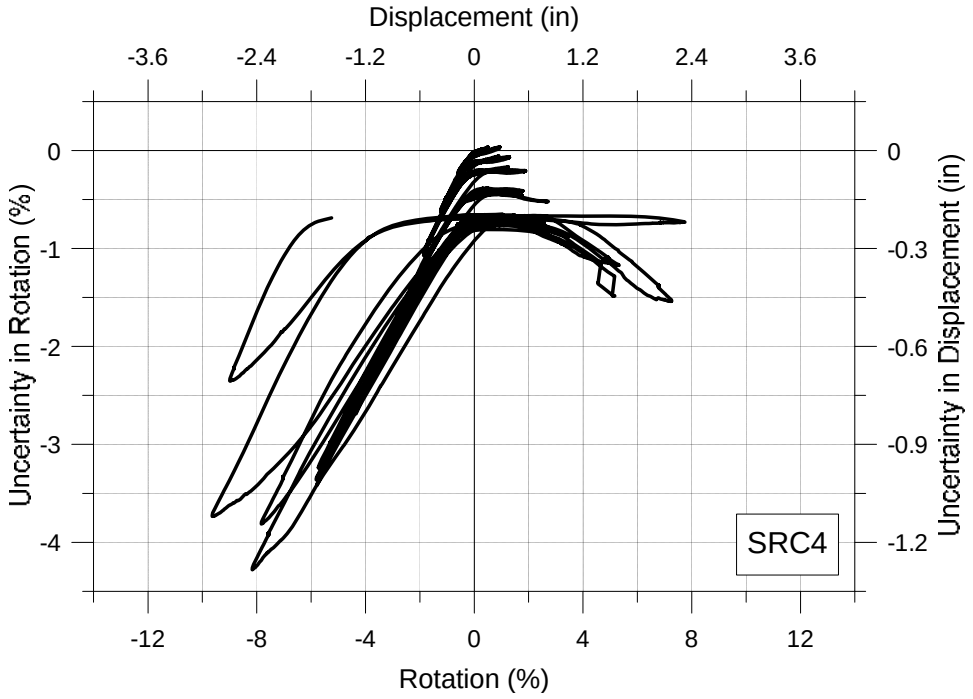

Figure 5.9: Uncertainty in Measured Rotation: d) SRC4

In Figure 5.10, uncertainty in the beam rotation is plotted for all beams in terms of a percent error, which was computed as the difference in the rotations measured relative to the top and bottom of the wall divided by the average of the rotation measured relative to the top and bottom of the wall. The plots in Figure 5.10 include only the peak values of the first loading cycle of each load or displacement level applied. It is evident from Figure 5.10 that the uncertainty in the elastic range is largest for SRC2, on the order of roughly 60-90% (+/- 30-45%), which moderately influences the effective elastic stiffness (further discussion and analysis provided in Section 6.5.4), while uncertainty in the post-yield range is largest for SRC3 and SRC4, on the order of roughly 50-60% (+/- 25-30%) up to 8% chord rotation, which moderately influences the ductility. Given the large ductility displayed by the SRC coupling beams tested in this study, this

level of uncertainty in post-yield rotations is not expected to have a significant influence on overall system performance.

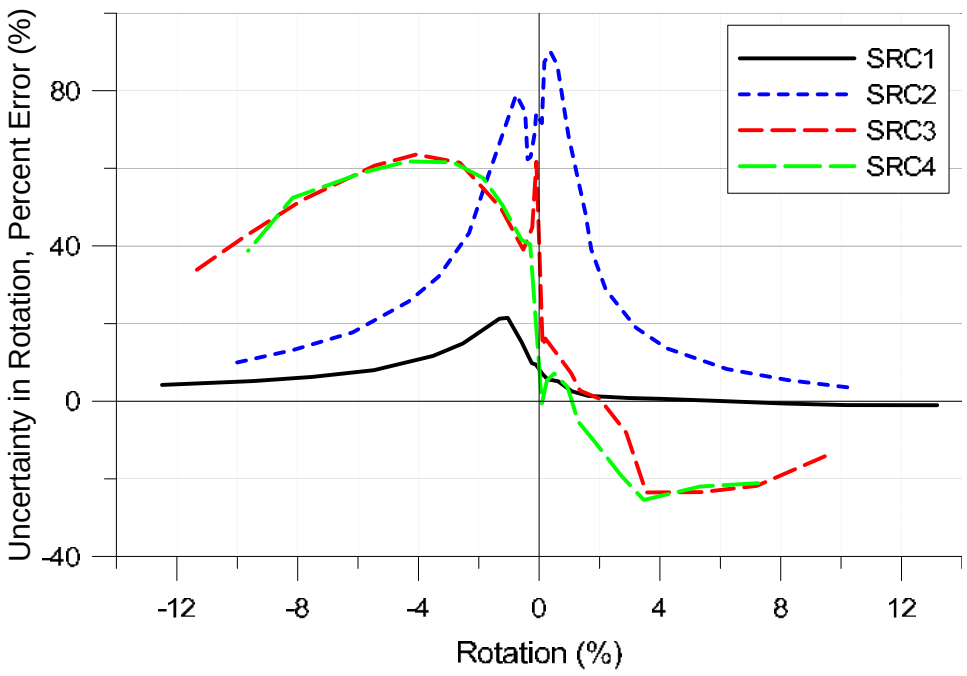

Figure 5.10: Comparison of Uncertainty in Measured Rotation for All Beams

5.4 DISSIPATED ENERGY

A plot of the total dissipated energy as a function of chord rotation is provided in Figure 5.11, while a plot of the average dissipated energy per cycle is provided in Figure 5.12, noting that average values of positive and negative peak rotations (absolute values) for all cycles at each load or displacement level applied were used to determine the chord rotations. It is evident from Figure 5.11 and Figure 5.12 that SRC1 and SRC2 dissipated about the same amount of energy through 3% rotation, at which point SRC1 provided improved energy dissipation over SRC2.

Since yielding occurred for SRC2 at a lower rotation than for SRC1, additional loading cycles were carried out for SRC2 between 1.0% and 3.0%, which slightly increased the total dissipated energy for SRC2 without affecting the average dissipated energy per cycle. Although the dissipated energy per cycle for SRC1 was noticeably larger than SRC2 between 3% and 6% rotation, the effect on the total dissipated energy was relatively minor at 6% rotation. Between 3% and 6% rotation the dissipated energy (per cycle and total) for SRC3 and SRC4 was similar and was ~50% less than for SRC2. The reduced energy dissipation of SRC3 and SRC4 compared to SRC1 and SRC2 is consistent with the relative amount of pinching observed in the load-deformation responses (Figure 5.4) and the observed damage in the embedment region (Figure 5.1).

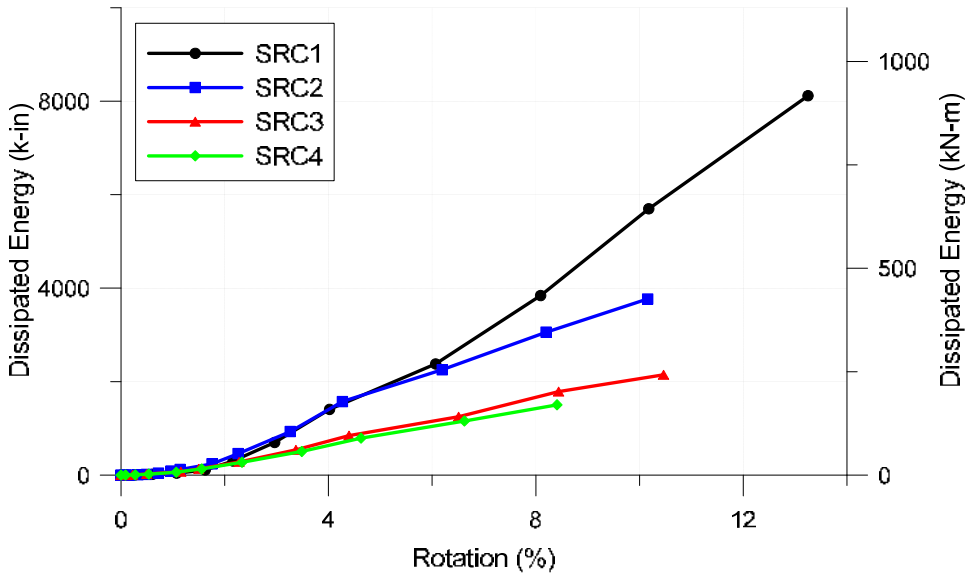

Figure 5.11: Cumulative Dissipated Energy

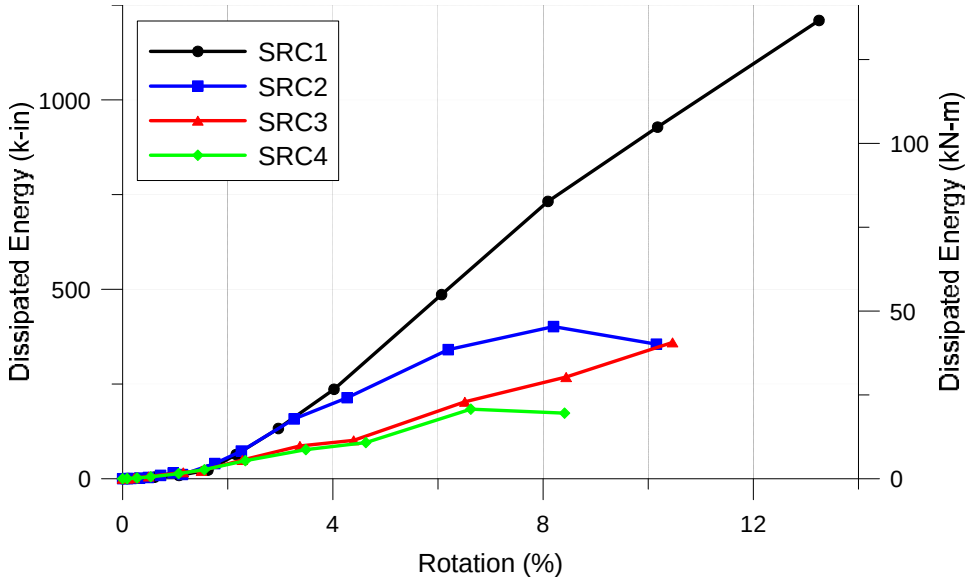

Figure 5.12: Average Dissipated Energy per Cycle

5.5 AXIAL DEFORMATION

Plots of the axial deformation versus applied coupling beam rotation for all test beams are provided in Figure 5.13. The axial deformation in Figure 5.13 was measured from the beam-wall interface to the point of coupling beam lateral load application (i.e. measured over the cantilever length) by taking an average of the sum of the displacements measured by the four longitudinal LVDTs along the top of the beam and the sum of the four longitudinal LVDTs along the bottom of the beam (Figure 4.14). Profiles of the axial deformation along the beam span are provided in Figure 5.14, noting that axial growth concentrated at the beam-wall interface with no appreciable growth occurring within the beam span for all four test beams. This suggested that axial growth occurred due to plastic deformation at the beam-wall interface or in the connection region as well as outward ratcheting of the steel section. Because the pair of LVDTs spanning across the beam-

wall interface (slip-extension sensors) for SRC1 and SRC2 had a +/- 1" stroke, the data became unreliable at around 1.0" to 1.2" of axial growth and the plots in Figure 5.13 and Figure 5.14 were terminated when this limit was exceeded. This occurred during cycles at ~10% rotation for SRC1 and during cycles at ~6% rotation for SRC2.

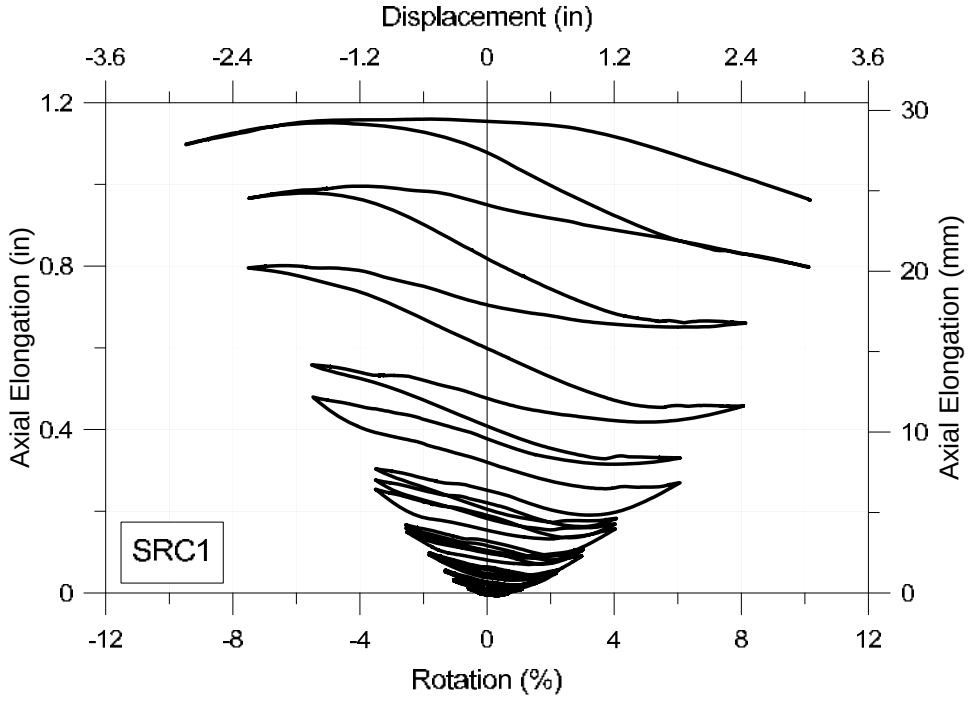

Figure 5.13: Axial Deformation: a) SRC1

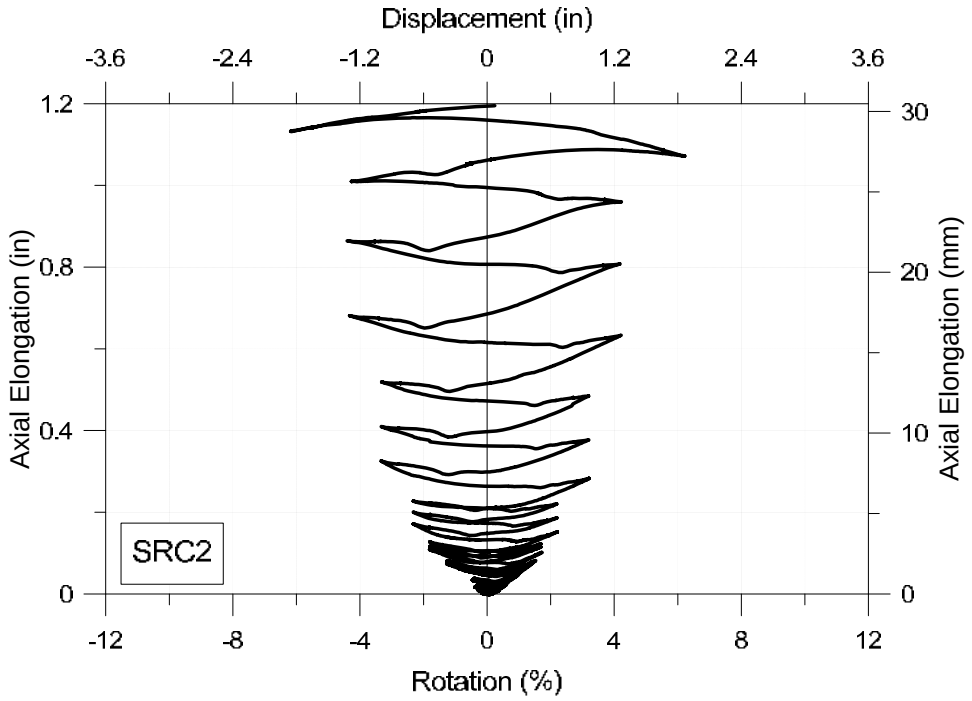

Figure 5.13: Axial Deformation: b) SRC2

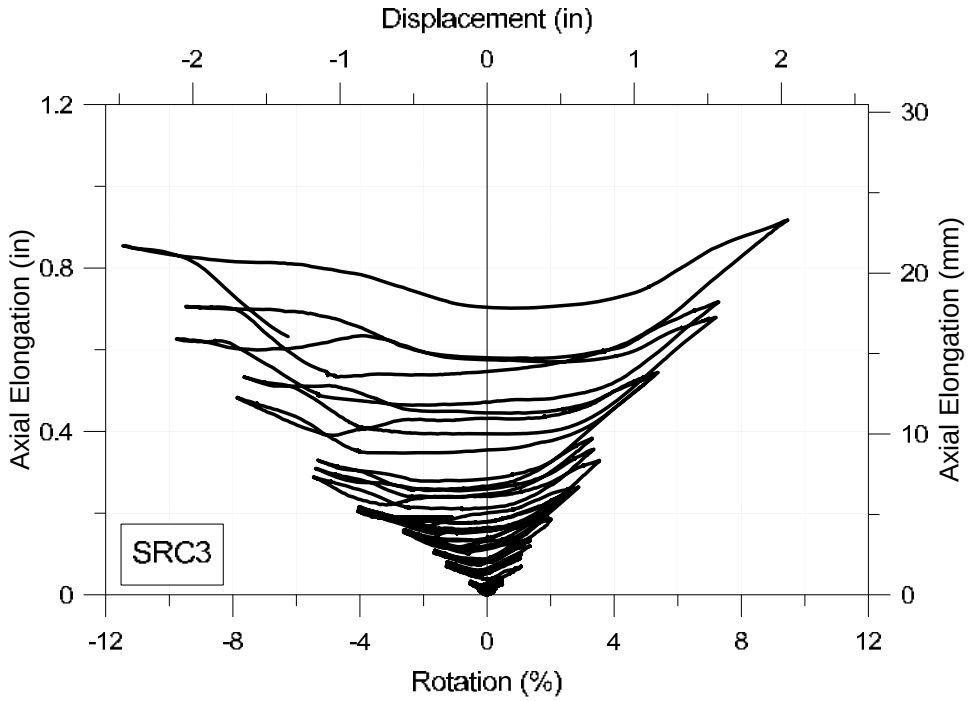

Figure 5.13: Axial Deformation: c) SRC3

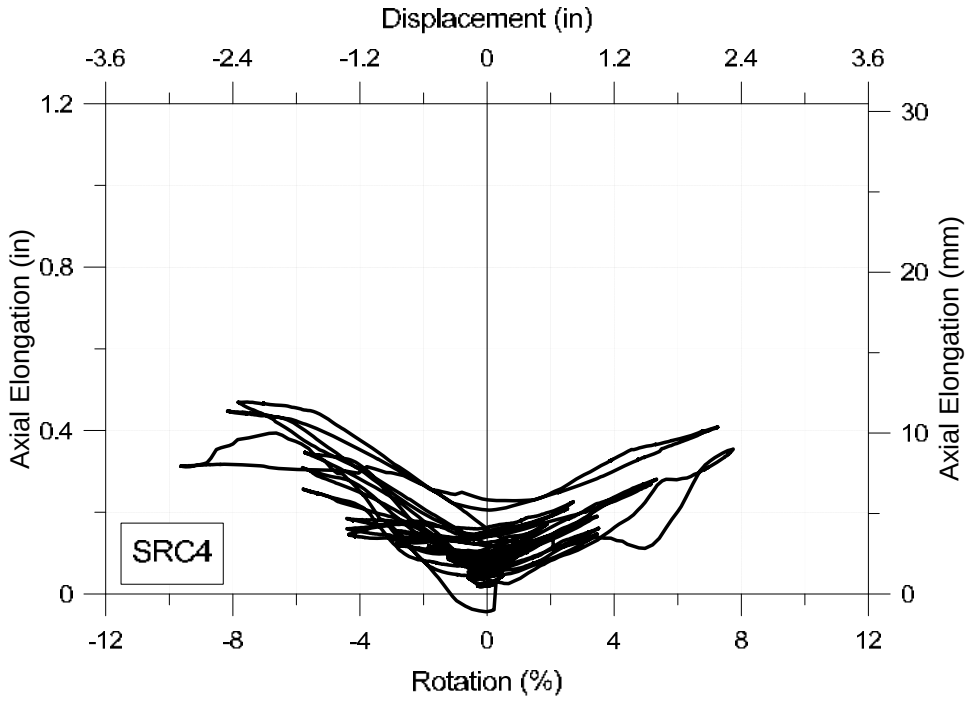

Figure 5.13: Axial Deformation: d) SRC4

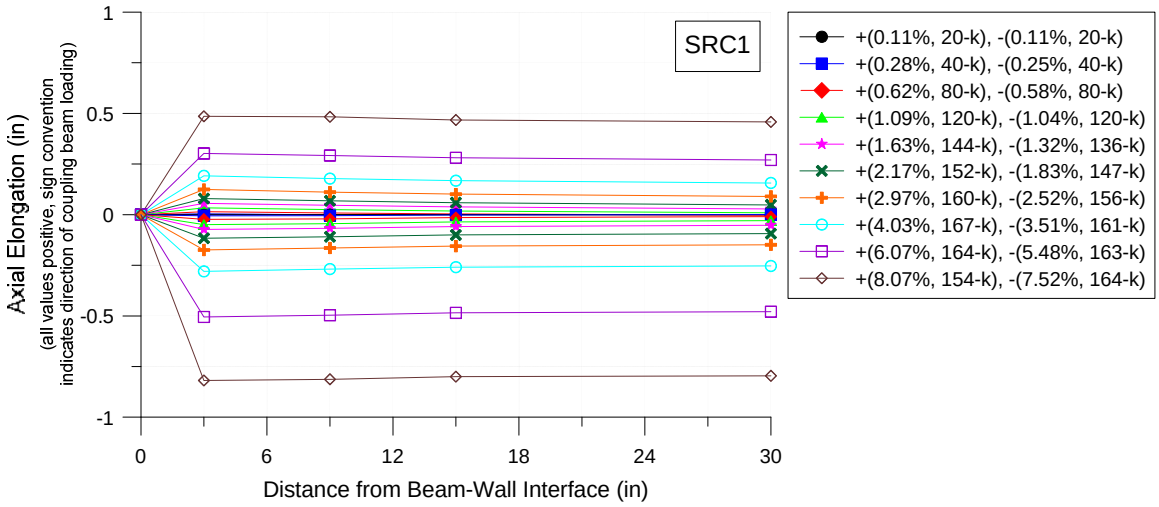

Figure 5.14: Axial Deformation Profile: a) SRC1

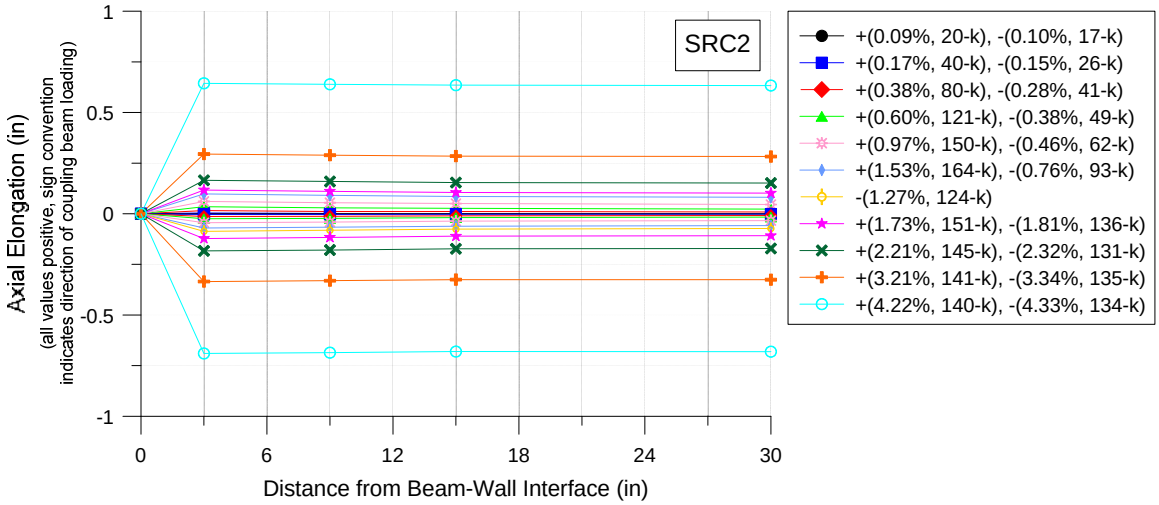

Figure 5.14: Axial Deformation Profile: a) SRC2

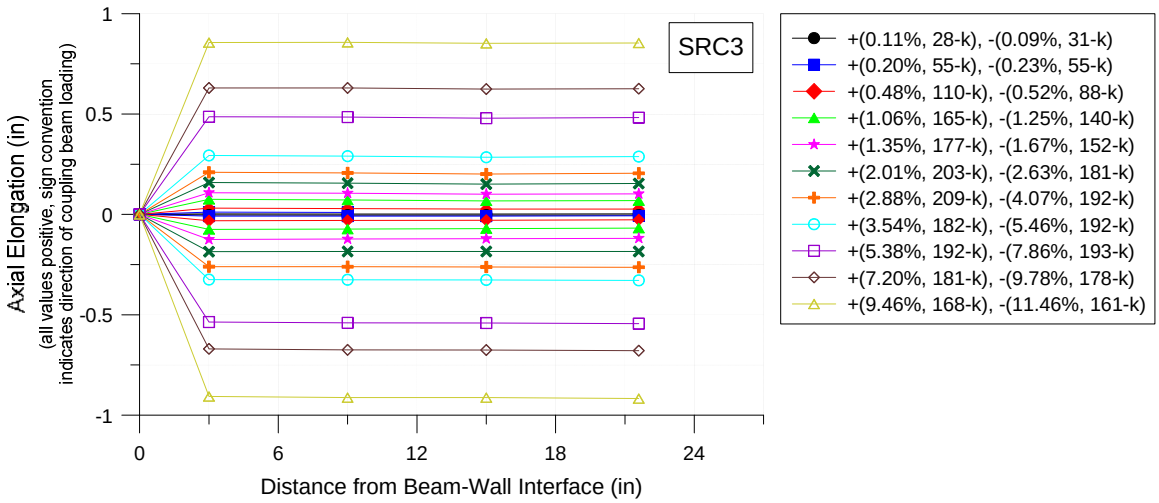

Figure 5.14: Axial Deformation Profile: a) SRC3

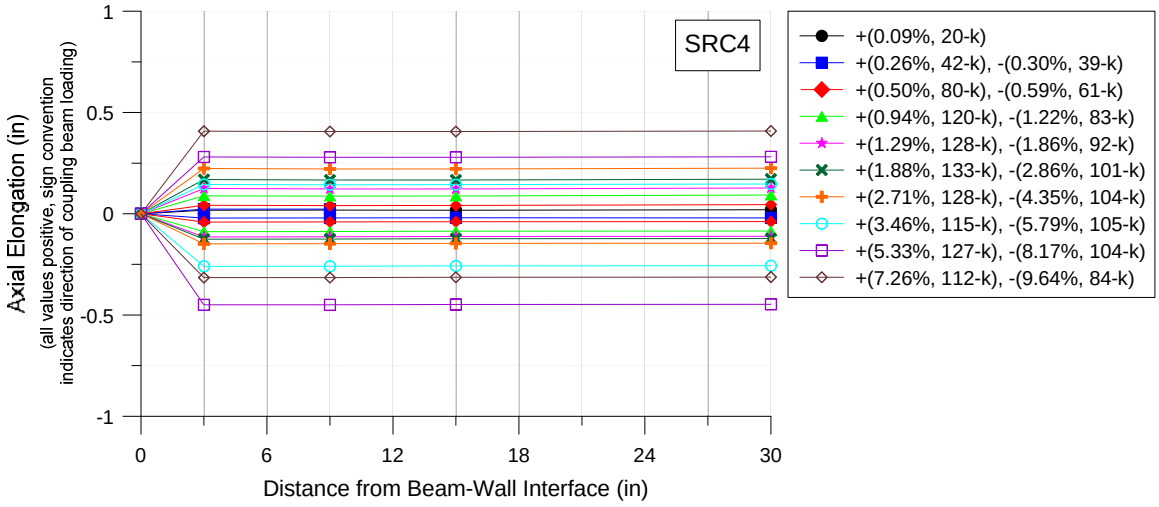

Figure 5.14: Axial Deformation Profile: a) SRC4

The gapping across the beam-wall interface was significant for SRC2 (Figure 5.13 and Figure 5.14), exceeding 1" on the third cycle at ~6% rotation, which led to the implementation of an axial restraining system for SRC3 and SRC4. This axial restraining system was designed to never provide greater than ~20-kips of total applied axial load. Plots of applied axial load versus coupling beam rotation, provided in Figure 5.15, indicate a measured peak load during testing of slightly less than 20-kips for SRC3 and SRC4. This axial restraining system was effective in limiting the axial growth of SRC3 and SRC4 relative to SCR1 and SRC2 (Figure 5.13 and Figure 5.14). Note that the reduced axial growth of SRC4 relative to SRC3 was potentially due to the extensive damage in the embedment zone and the associated reduction in plasticity of the steel section.

In actual structures with SRC coupling beams, outward slip of the steel section is restrained by a floor slab as well as embedment into an adjacent structural wall, which creates an axial compressive load on the coupling beam that would presumably be significantly larger than the

axial compressive load applied in this test set-up. It is evident from the axial deformation plots for SRC3 and SRC4 (Figure 5.13 and Figure 5.14) that the low level of axial restraint used in the test set-up was effective in preventing the beams from ratcheting outward. This suggests that the pull-out effect is not significant in actual structures, where the level of axial restraint would be larger. Including detailing in the embedment zone for the sole purpose of preventing pull-out is unnecessary.

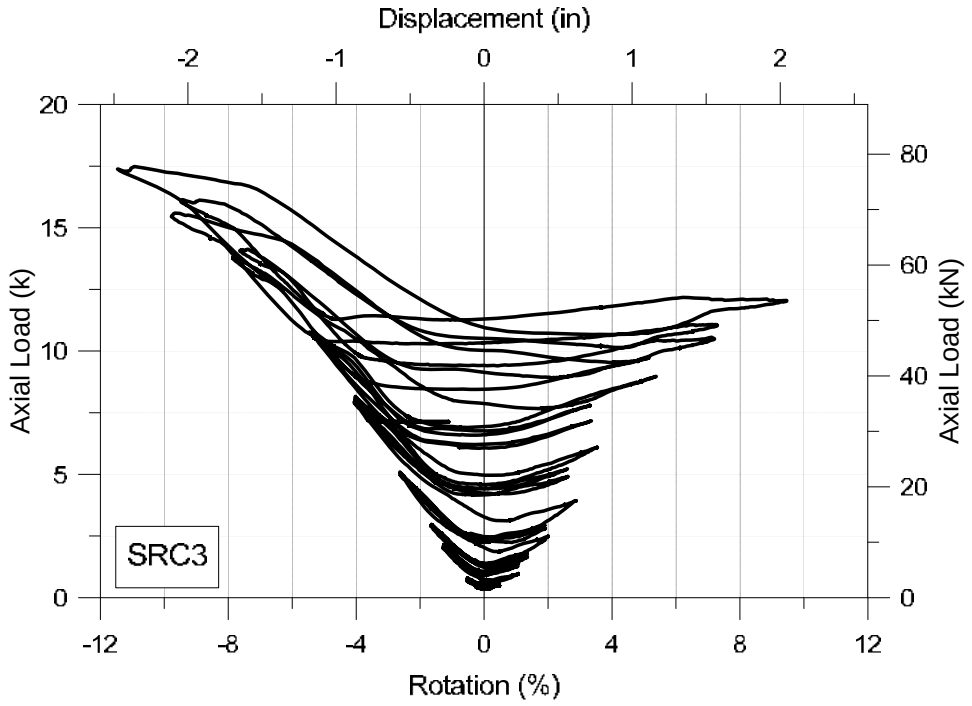

Figure 5.15: Coupling Beam Axial Load: a) SRC3

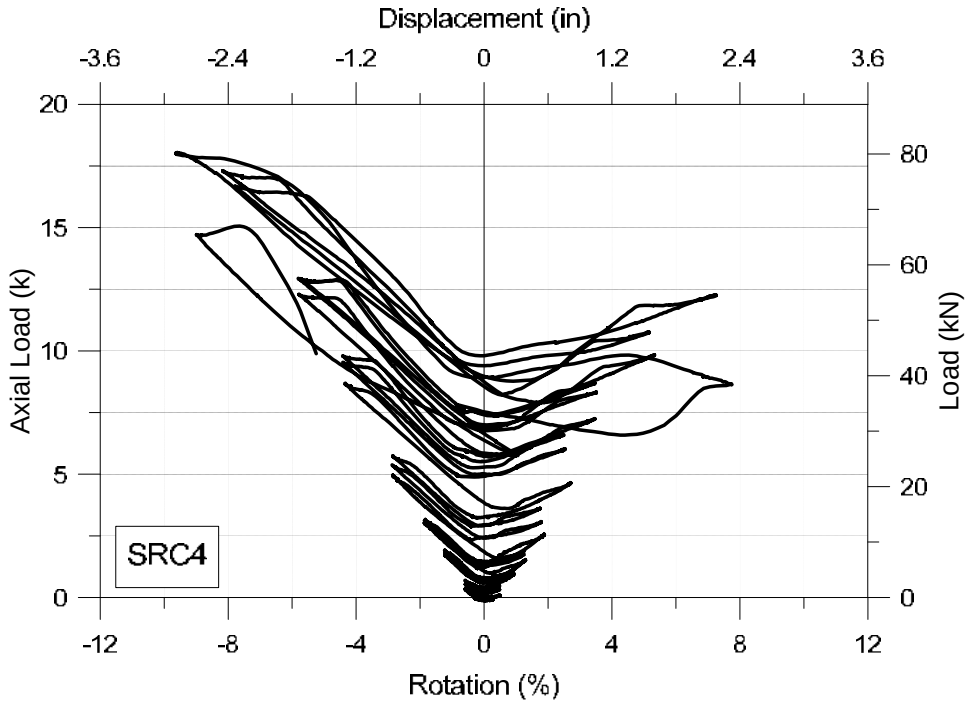

Figure 5.15: Coupling Beam Axial Load: b) SRC4

5.6 MOMENT-CURVATURE

Plots of moment versus curvature at the beam-wall interface are provided in Figure 5.16. The two LVDTs spanning across the beam-wall interface (Figure 4.14) were used to measure curvature. Test data were excluded from the plots in Figure 5.16 where test specimen damage at the locations of LVDT attachment points was observed that would likely impact LVDT measurements and where the stroke limits for LVDTs were exceeded (+/-). The stroke limits for LVDTs were exceeded for SRC1 and SRC2. Therefore, the plot for SRC1 terminates at zero curvature after the first positive cycle at 10% rotation (before reaching the first negative cycle at

10% rotation), and the plot for SRC2 terminates at zero curvature after the first positive cycle at 6% rotation (before reaching the first negative cycle at 6% rotation).

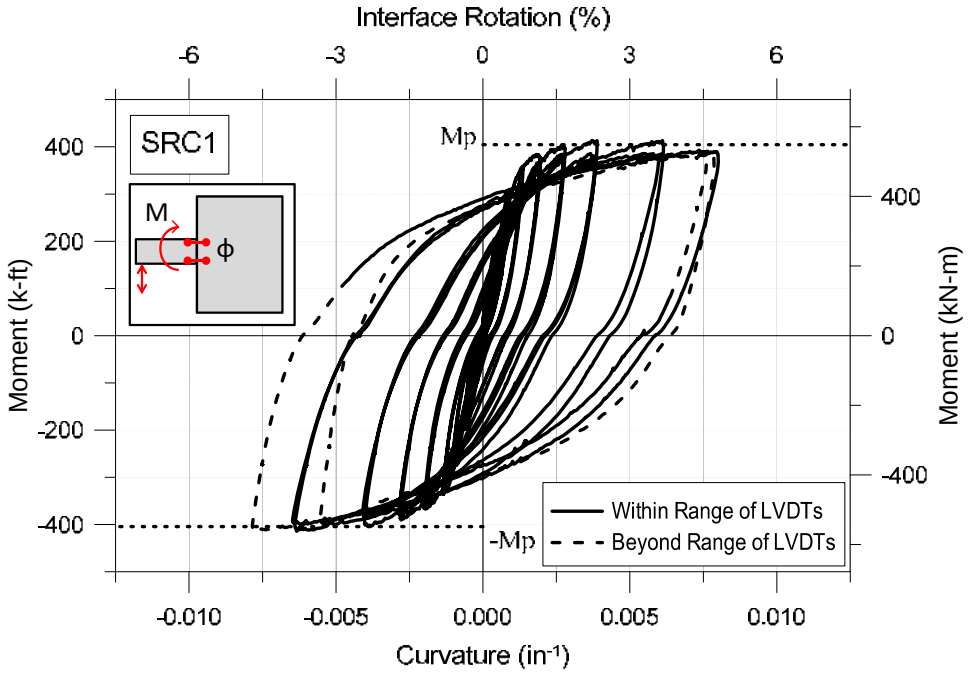

Figure 5.16: Moment-Curvature at Beam-Wall Interface: a) SRC1

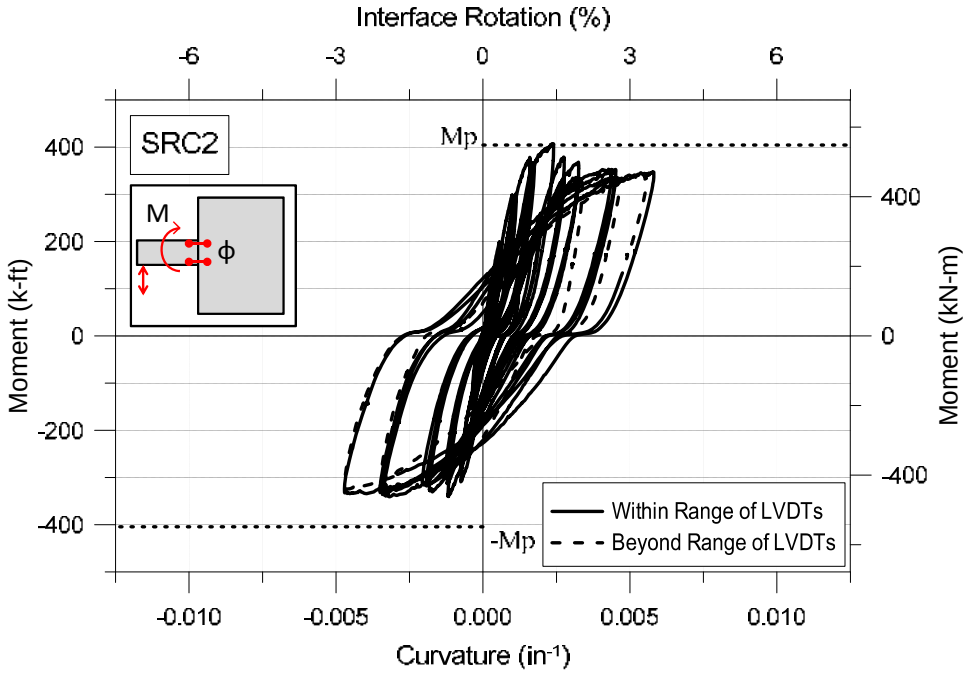

Figure 5.16: Moment-Curvature at Beam-Wall Interface: b) SRC2

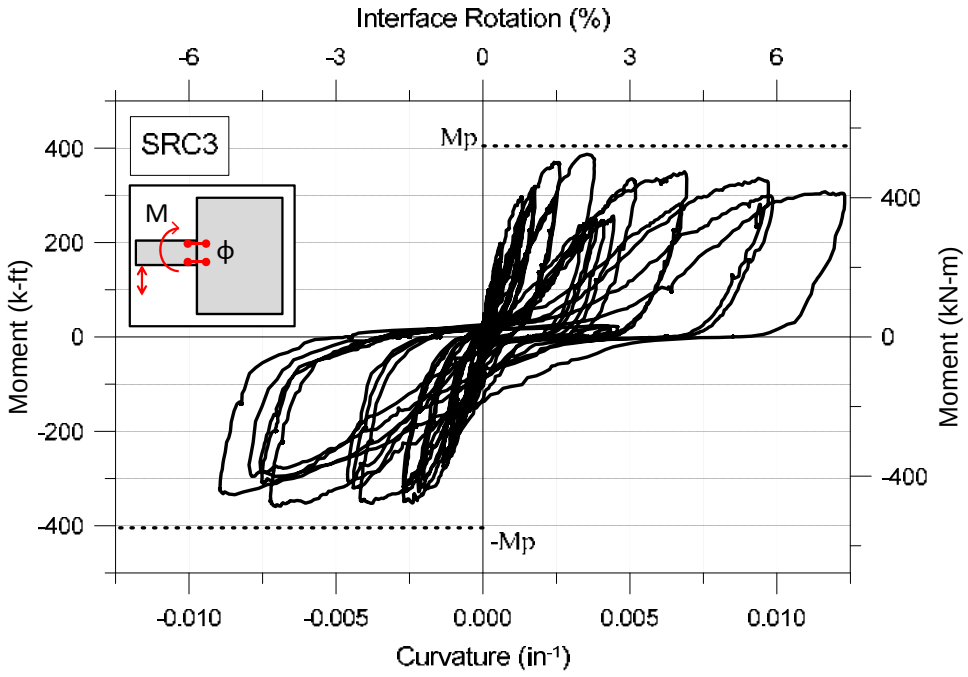

Figure 5.16: Moment-Curvature at Beam-Wall Interface: c) SRC3

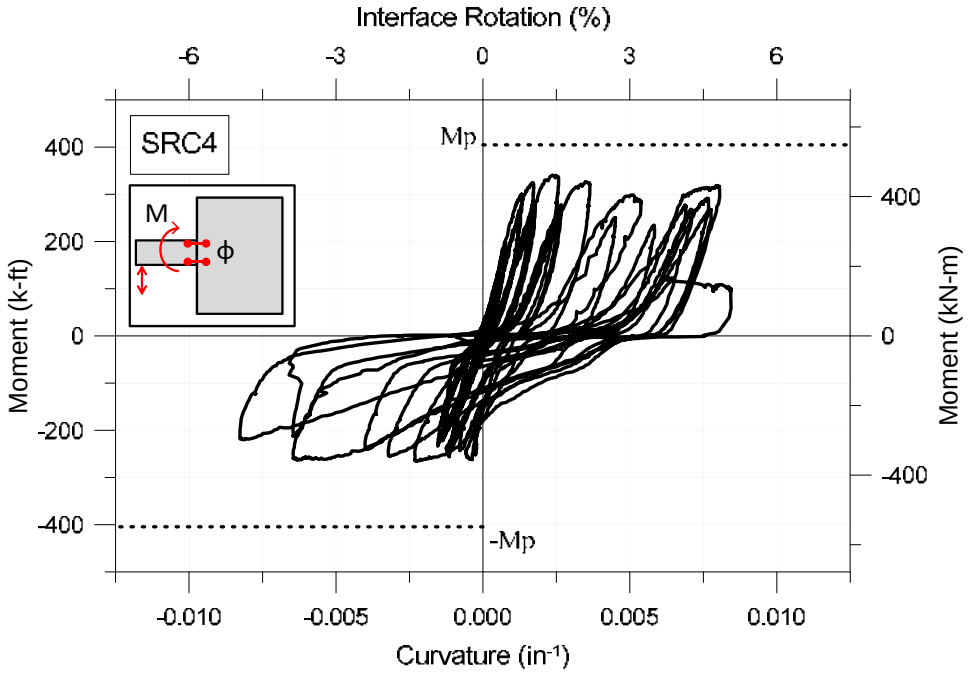

Figure 5.16: Moment-Curvature at Beam-Wall Interface: d) SRC4

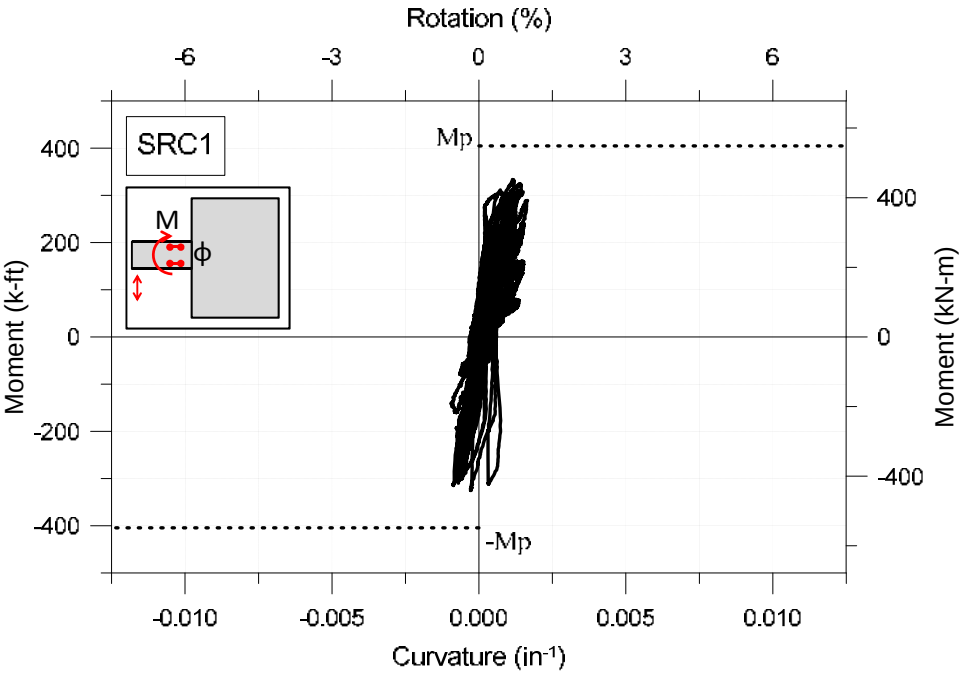

Figure 5.17: Moment-Curvature in Beam Span: a) SRC1

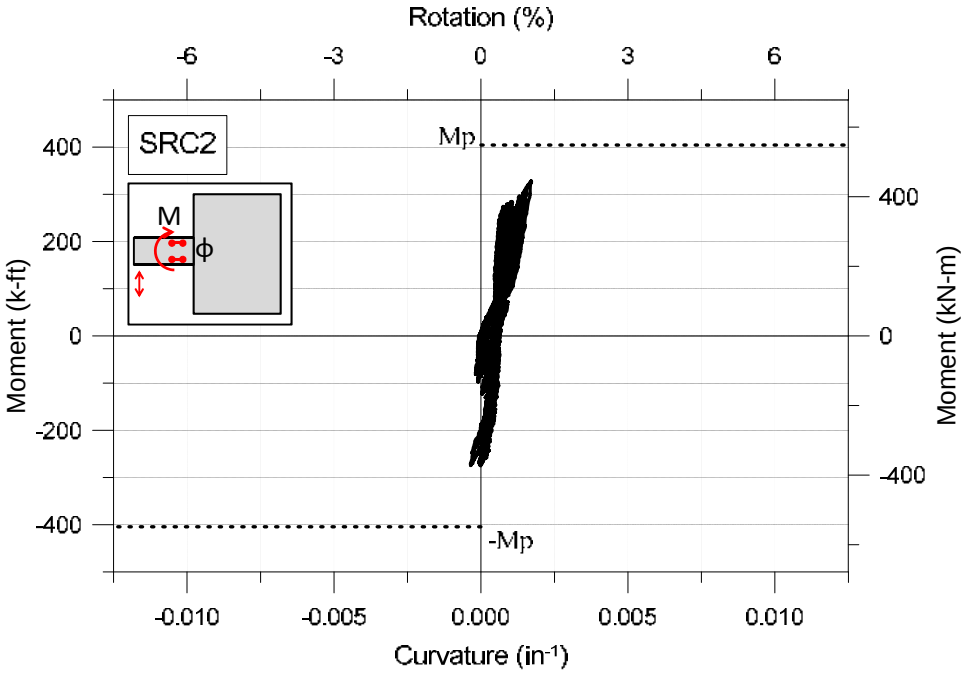

Figure 5.17: Moment-Curvature in Beam Span: b) SRC2

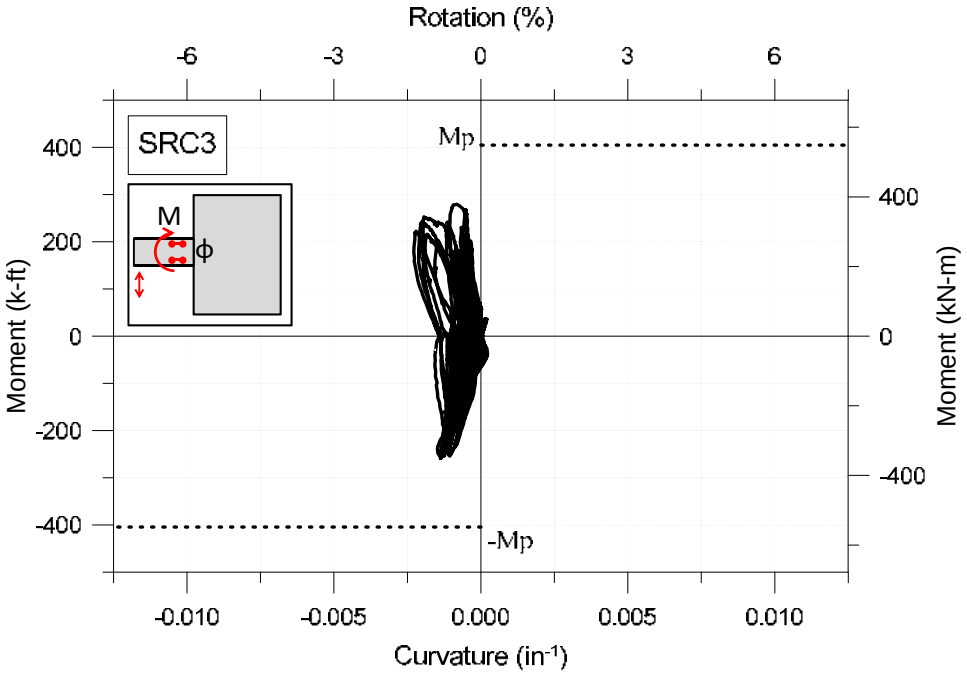

Figure 5.17: Moment-Curvature in Beam Span: c) SRC3

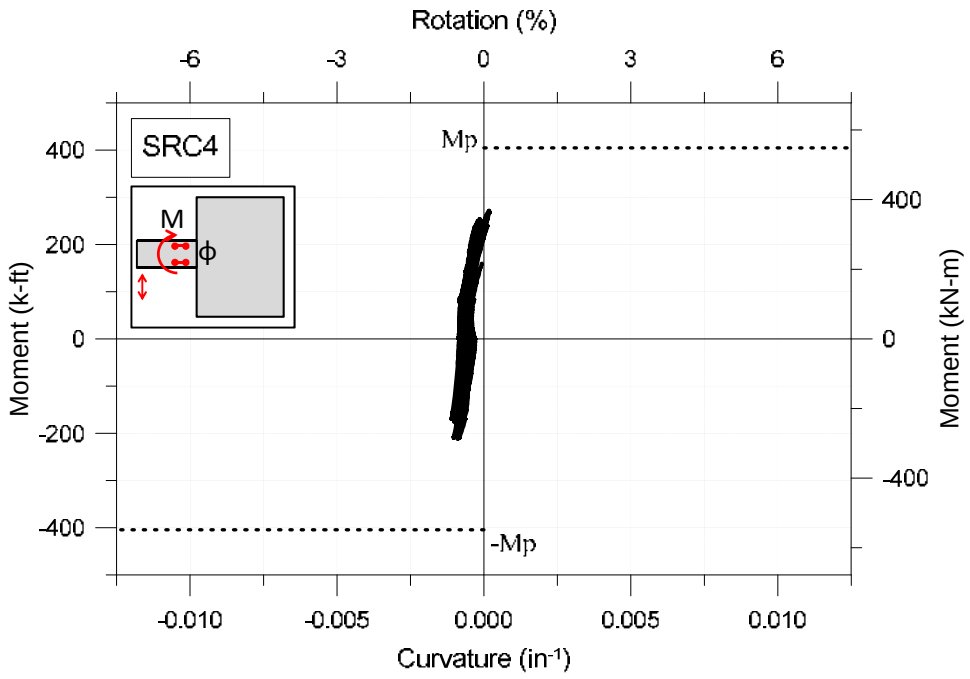

Figure 5.17: Moment-Curvature in Beam Span: d) SRC4

Although many of the same overall characteristics (i.e. pinching, strength degradation, etc.) of the load-deformation responses (Figure 5.4) are evident in the moment-curvature responses (Figure 5.16), more pinching during loading from a negative to a positive peak as opposed to loading from a positive to a negative peak is evident in the moment-curvature plots for SRC3 and SRC4 but is not evident in the load-deformation responses. This phenomenon occurred because wall tension was acting normal to the embedment length at the peak of negative loading (Figure 1.5), which caused gapping between the flange of the embedded steel section and the concrete (Figure 5.2). As the beam was displaced in the positive direction after reaching the peak of negative loading, significant positive curvature but minimal load was required to close the gap between the steel and concrete, and the beam did not display a significant increase in moment resistance until the gap was closed. Additionally, the compression demand at the wall boundary was initially resisted entirely by vertical reinforcement rather than concrete until the gap and the

tension cracks were closed, enabling concrete to participate in the resistance of the compression demand. Conversely, when loading from a positive to a negative peak, the compression at the wall boundary at the positive peak had already closed the tensile cracks and reduced the gapping, providing a more favorable initial condition that led to reduced pinching in this loading direction relative to the other loading direction.

The moment-curvature response within the beam span is provided in Figure 5.17 for all four test beams. The pair of LVDTs used to measure curvature (Figure 5.17) had attachment points roughly 3" and 9" from the beam-wall interface (Figure 4.14). Comparing Figure 5.17 to Figure 5.16, it is clear that yielding did not propagate into the beam span for any of the test specimens, noting that the moment-curvature response in the beam span (Figure 5.17) is nearly linear for each test specimen.

Profiles of the curvature measured along the beam span are provided in Figure 5.18 and were generated based on data at the positive and negative peak of the first loading cycle at each load or displacement level applied. The data were obtained from the eight coupling beam longitudinal LVDTs shown in Figure 5.19, with each of the four pairs of sensors used to calculate the measured curvature. The locations of the average curvature readings indicated in Figure 5.18 are consistent with the assumed center of rotation for each pair of sensors indicated in Figure 5.19, noting that the assumed center of rotation was at the midspan of the sensors. The lone exception was the outermost (as referenced from the beam-wall interface) pair of longitudinal sensors, i.e. the pair of sensors closest to the applied beam load, in which the center

of rotation was assumed to be 2/3 of the sensor length from the point of load application, consistent with the shape of the moment diagram in this very-nearly-elastic region (Figure 5.19).

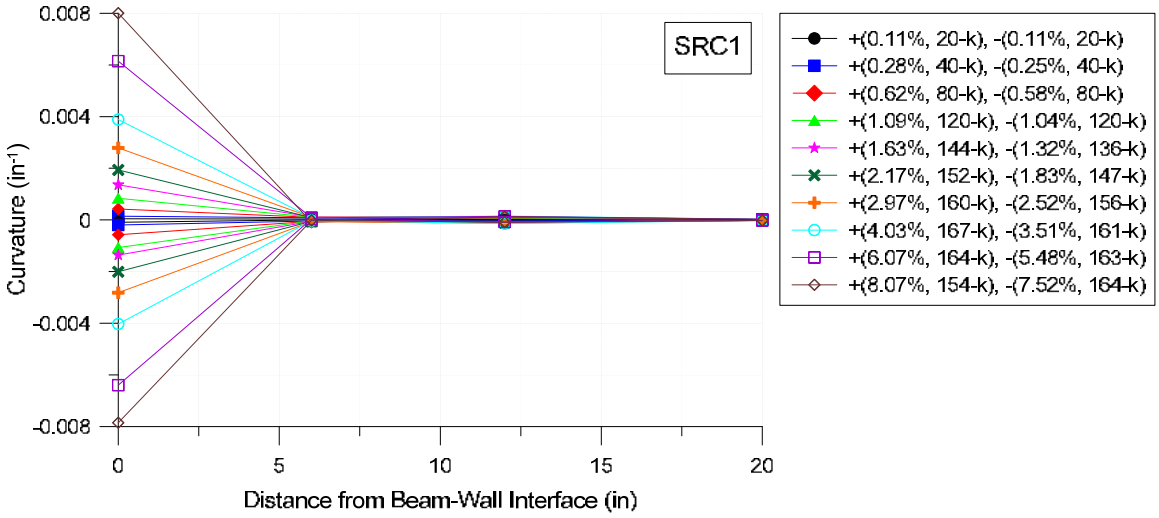

Figure 5.18: Coupling Beam Curvature Profile: a) SRC1

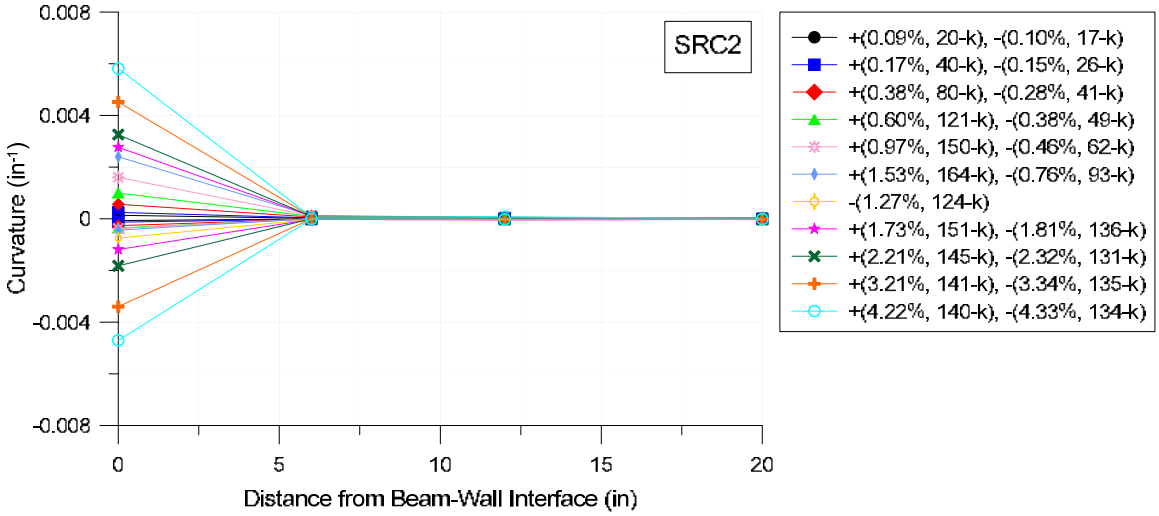

Figure 5.18: Coupling Beam Curvature Profile: b) SRC2

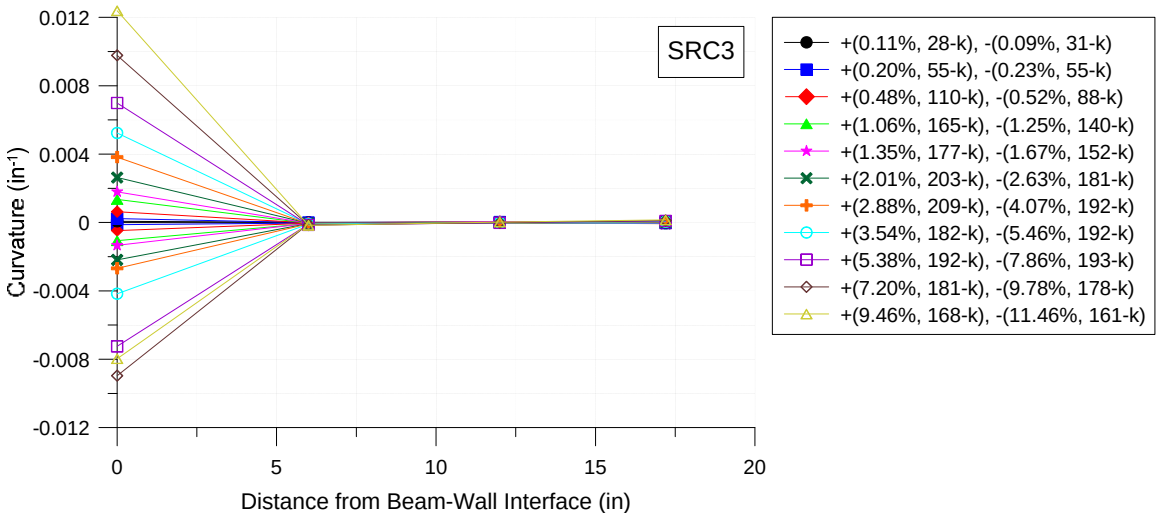

Figure 5.18: Coupling Beam Curvature Profile: c) SRC3

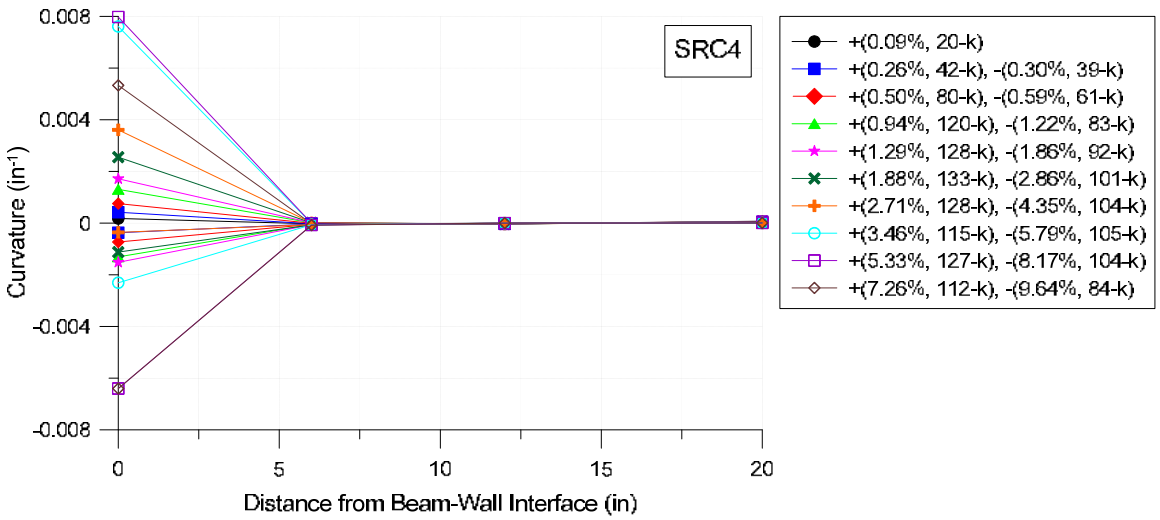

Figure 5.18: Coupling Beam Curvature Profile: d) SRC4

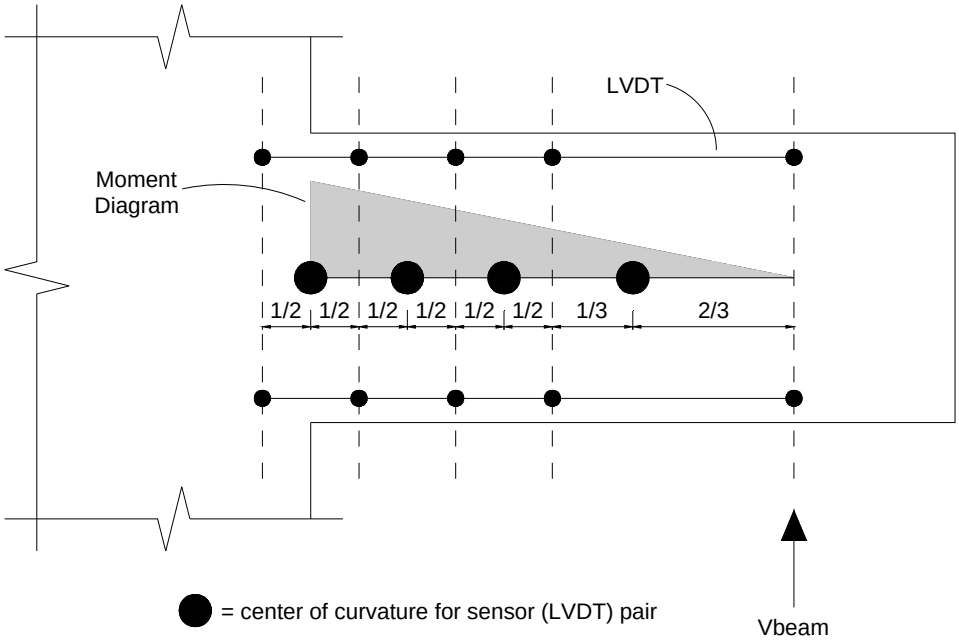

Figure 5.19: Assumed Center of Rotation for Flexural LVDTs

It is evident from Figure 5.18 that curvature concentrated at the beam-wall interface for all test beams, indicative of plastic hinge formation at this location, which is consistent with the observed damage (Figure 5.1). It is important to note that the curvature readings at the beam-wall interface included slip-extension deformations and rigid body or plastic flexural deformations of the steel section along the embedment length, which could have occurred due to the observed gapping of the steel section relative to concrete (Figure 5.2). The gapping between the steel flanges and the surrounding concrete corresponded to a loss of composite action and presumably enabled the formation of a plastic hinge in the embedment region. If this plastic hinge had formed beyond the extent of the interface sensors (i.e. at least 3" inside of the beam-wall interface), the interface sensors would have measured the plasticity of this hinge (since composite action was lost between the steel section and the surrounding concrete, and the LVDT attachment points were embedded into the surrounding concrete). Of the four test beams, SRC4

had the largest measured curvature at the beam-wall interface at the ~4% rotation level in both the positive and negative loading directions. This was likely due to rigid body or plastic flexural rotation along the embedment length rather than solely plasticity in the steel section at the beam-wall interface. The extensive connection damage for SRC4 (Figure 5.1) is consistent with this type of behavior.

5.7 SHEAR FORCE – SHEAR DISPLACEMENT

Shear deformations were determined using LVDTs in an "X" configuration in combination with longitudinal sensors. To obtain shear deformations, Massone and Wallace (2004) recommended making a correction to the measured relative lateral deformations (measured using the LVDTs in an "X" configuration) by removing the contribution of flexural deformations. In order to make this correction, an assumption must be made regarding the center of rotation for each pair of longitudinal sensors used to measure flexural deformations. The assumed center of rotation for each sensor pair is shown in Figure 5.19, discussed previously in Section 5.6. Given the concentration of measured curvature at the beam-wall interface (Figure 5.18), a more refined approach to locating the center of rotation for each sensor pairing was deemed unnecessary. Note that for each pair of longitudinal sensors, the curvature was multiplied by the average sensor length to obtain the flexural rotation.

As evident from the plots of the shear load versus shear displacement provided in Figure 5.20, the shear deformations for SRC1 and SRC2 were relatively small compared to the overall deformations (comparing to the plots in Figure 5.4). This is not surprising, as shear yielding was

not expected to occur for the flexure-controlled beams and relatively elastic shear stress versus shear strain behavior was anticipated. However, the shear load versus shear displacement responses for SRC3 and SRC4 were asymmetric, with significantly larger shear deformations observed in the negative loading direction. This is consistent with observations made during testing, in which shear sliding at the beam-wall interface appeared to be significant during negative loading. This shear sliding is believed to have occurred due to the large tension across the connection during loading in the negative direction, which increased gapping between the embedded steel section and the bearing concrete, leading to softening of the connection. It appears that shear stiffness, similar to flexural stiffness, was softening as deformation levels and damage increased, noting that shear deformations in the negative loading direction increased significantly over the final five to seven loading cycles for both SRC3 and SRC4 (Figure 5.20). In the negative loading direction relative to the positive loading direction for SRC3 and SRC4, the larger measured shear deformation (Figure 5.20) is consistent with the lower measured curvature during cycles at advanced yielding (Figure 5.18).

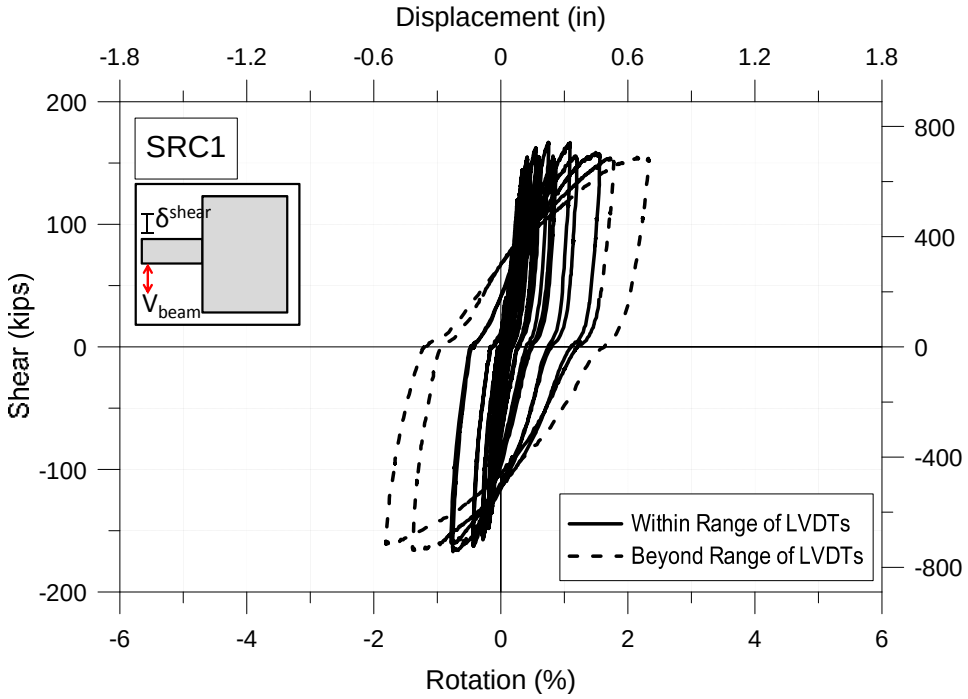

Figure 5.20: Shear Load-Displacement: a) SRC1

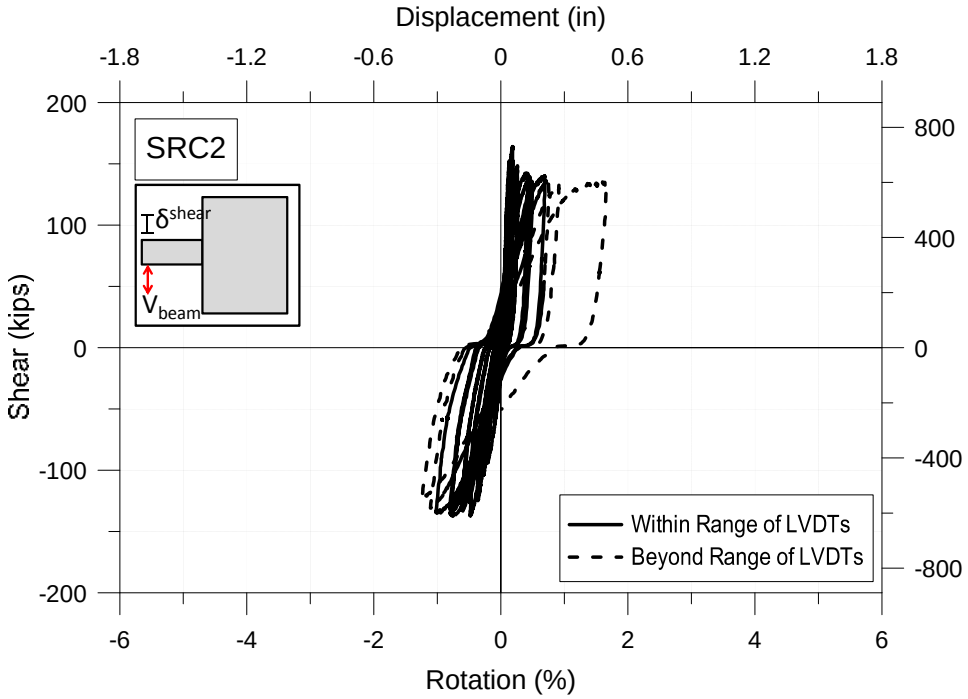

Figure 5.20: Shear Load-Displacement: b) SRC2

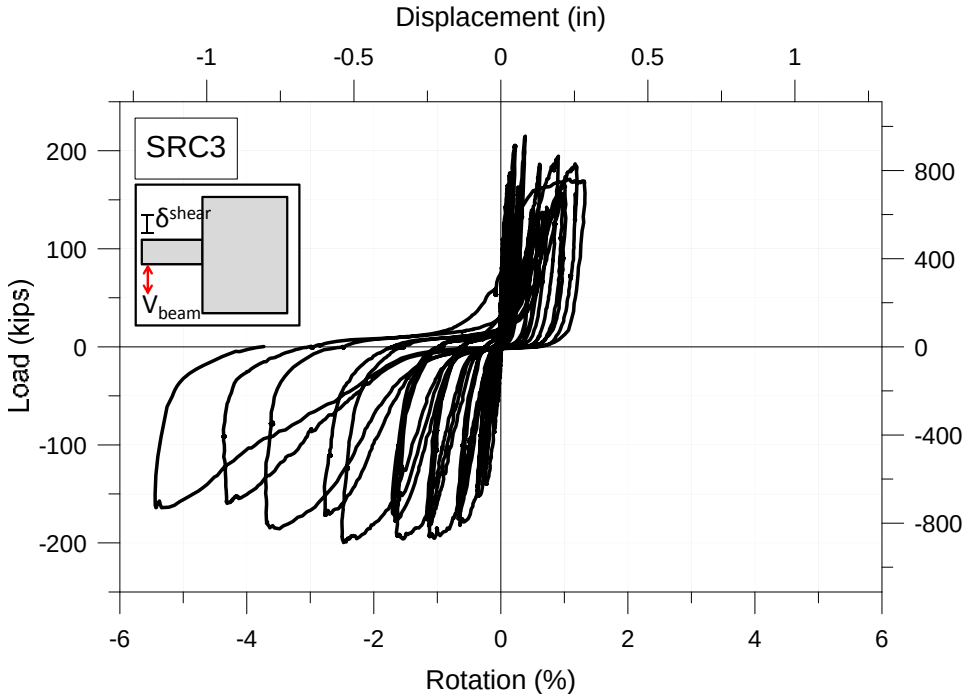

Figure 5.20: Shear Load-Displacement: c) SRC3

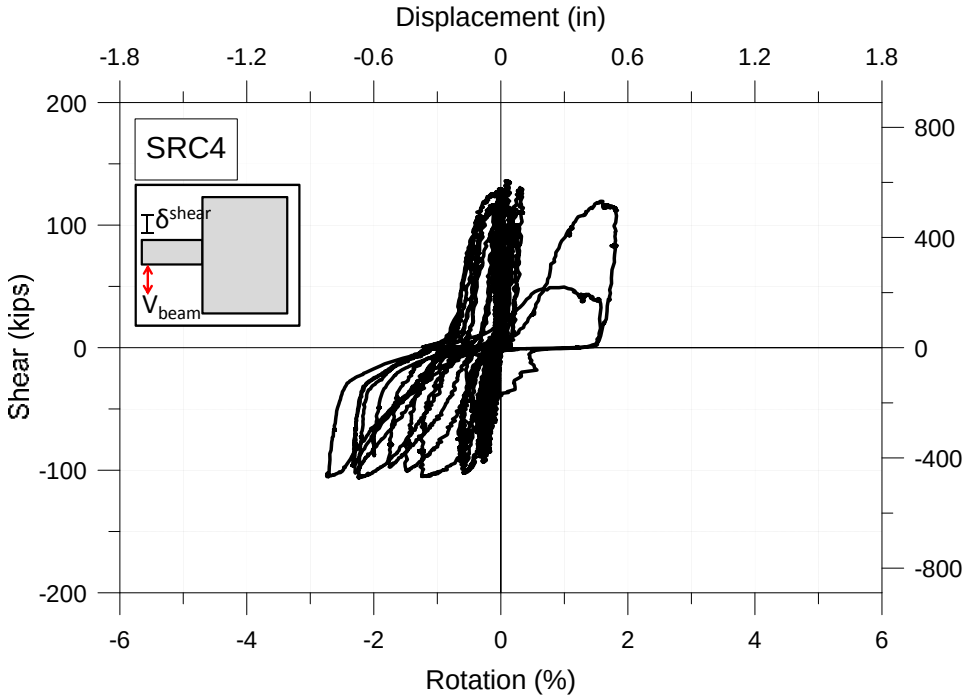

Figure 5.20: Shear Load-Displacement: d) SRC4

5.8 WALL ROTATION

Plots of the applied structural wall demand (lateral shear load and overturning moment) at the top of the wall versus full-height (clear span) rotation, provided in Figure 5.21, were based on data obtained from two LVDTs, one near each edge of the wall, spanning the clear height of the wall (footing to concrete top beam). It is evident from these wall load-deformation plots that the wall remained relatively elastic during testing of both SRC1 and SRC2, suggesting that the local bearing force effects did not cause local yielding (Figure 3.9). However, during testing of SRC3 and SRC4, it is evident from these wall load-deformation plots that significant wall yielding occurred in the negative loading direction due to the local bearing force effects, i.e. load path effects (Figure 3.9). It is also interesting to note that the elastic stiffness of the wall appears noticeably softer for SRC2 than for the other three tests.

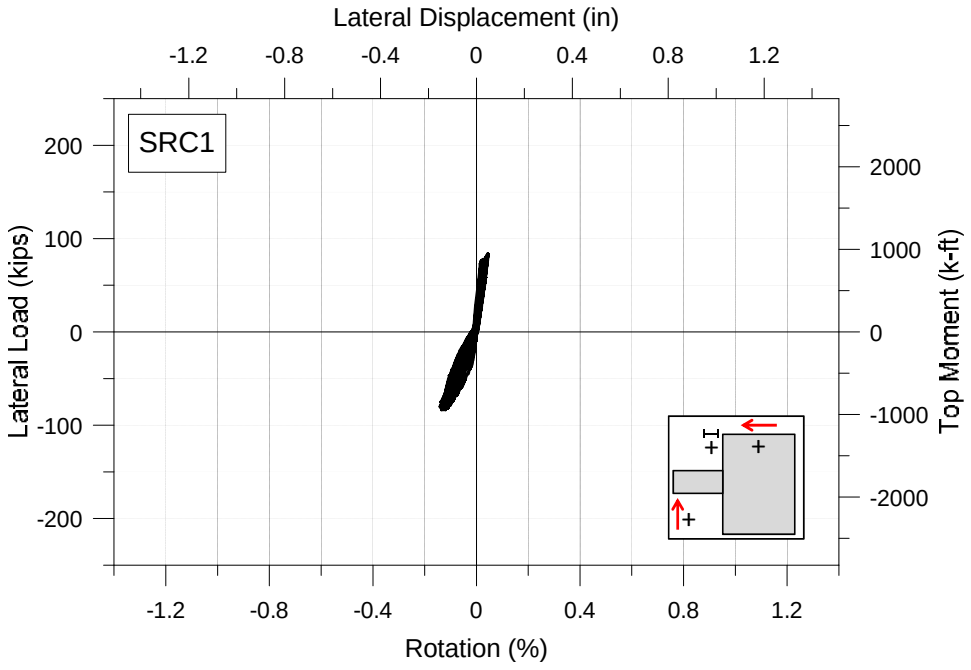

Figure 5.21: Wall Lateral Load-Displacement: a) SRC1

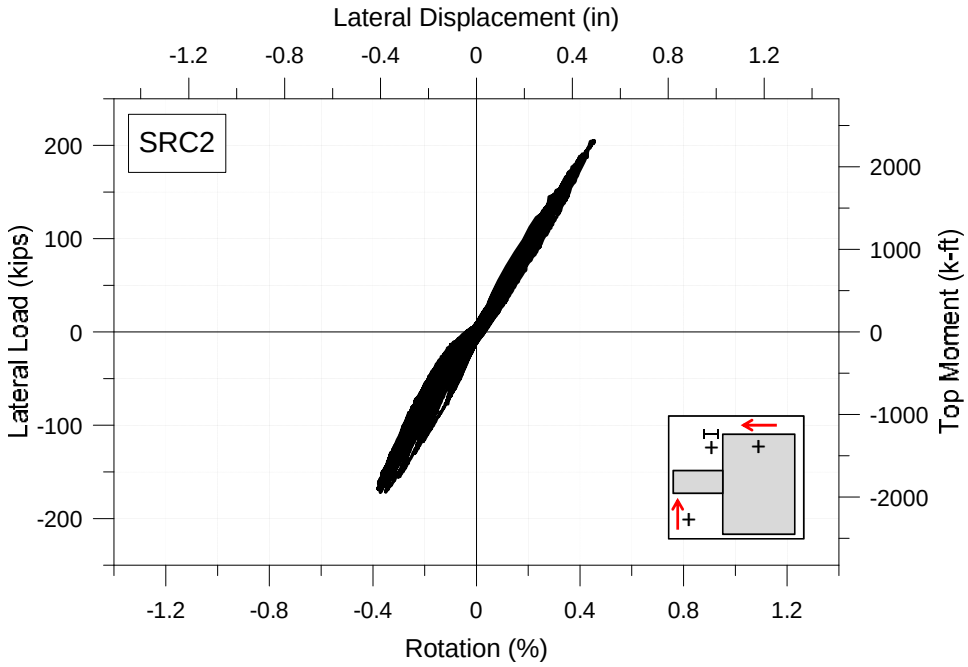

Figure 5.21: Wall Lateral Load-Displacement: b) SRC2

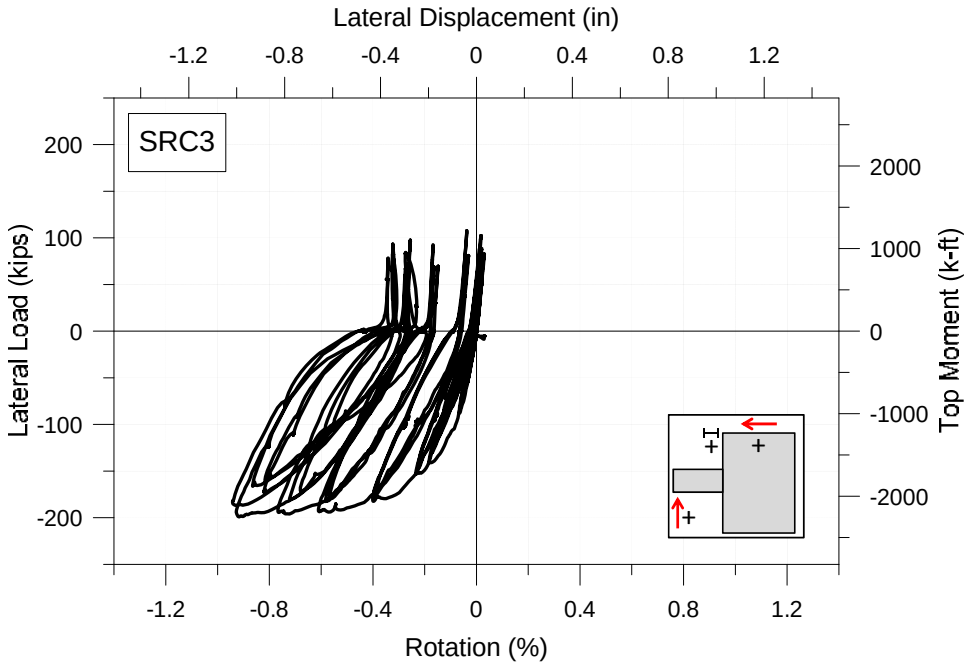

Figure 5.21: Wall Lateral Load-Displacement: c) SRC3

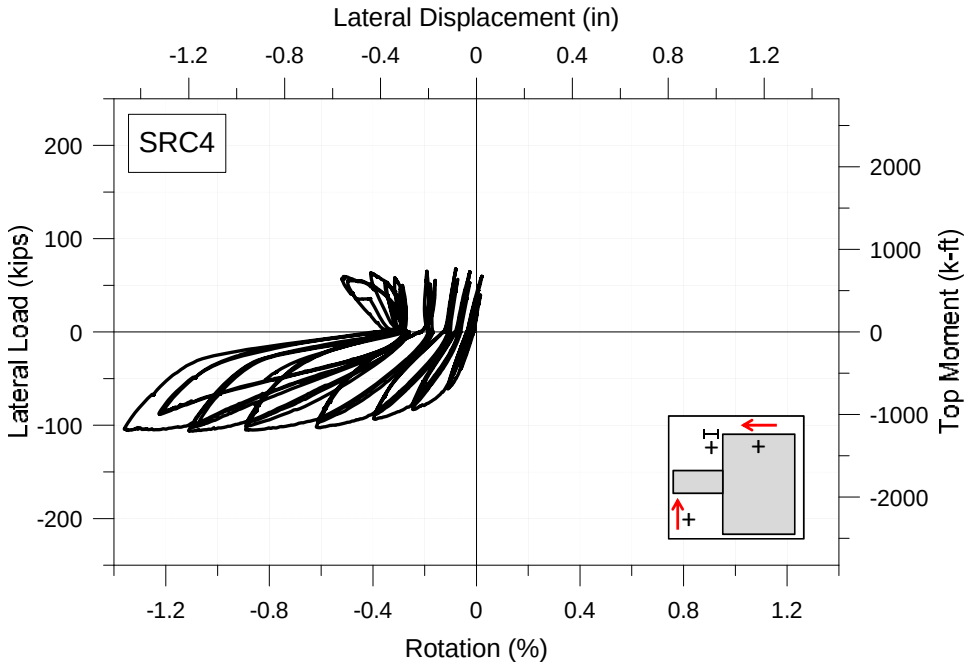

Figure 5.21: Wall Lateral Load-Displacement: d) SRC4

5.9 EMBEDMENT (CONCRETE) STRAIN

For each test specimen, a pair of embedment strain gages were placed at the back of the embedded steel section directly below the flange of the beam, with one gage aligned under the beam centerline (web) and the other aligned with the outside of the flange (Figure 4.20). The intent of using these strain gages was to study the effects of load spreading. When the coupling beam was loaded in the positive (upward) direction, compressive bearing strain is created at the back of the embedded member, consistent with the plane strain assumption shown in Figure 2.2. It is evident from the plots provided in Figure 5.22, which were based on data at the peak of initial cycles at each increment of load or displacement applied, that the compressive bearing strains are larger at the beam centerline than at the edge of the flange for all four tests, which

suggests that bearing strain reduces with an increase in out-of-plane distance from the beam centerline. This effect is not captured by the embedment model shown in Figure 2.2, as bearing strain is assumed to distribute uniformly in the out-of-plane orientation. However, modifications to the embedment model are not recommended based on the test data obtained, as the data display too much variation. For example, the difference between the magnitudes of the compressive bearing strains at the centerline versus the outside of the flange is relatively minor for SRC3 but more significant for the other three beams, and it is unclear as to why this is the case. For SRC3 and SRC4, the two members with inadequate embedment strength, the magnitude of the measured strain values beneath the beam centerline are large enough to correspond to concrete crushing. It is also interesting to note, that when loading in the opposite direction (i.e., the negative loading direction), the concrete tensile strains do not show a consistent trend (i.e. increase or decrease) with distance from the beam centerline. The magnitudes of the tensile strains suggest that yielding of reinforcement is occurring in this region, provided bond is maintained.

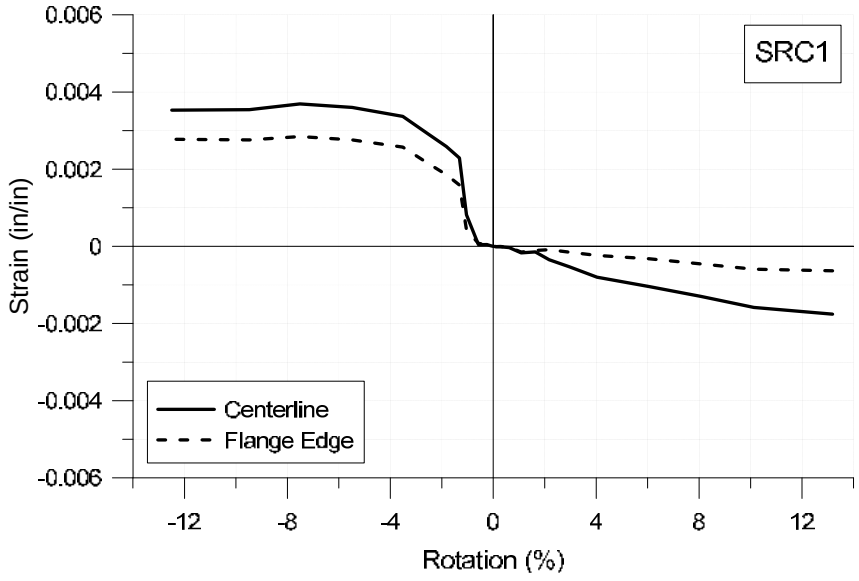

Figure 5.22: Concrete Bearing Strain at Back of Embedded Steel Section: a) SRC1

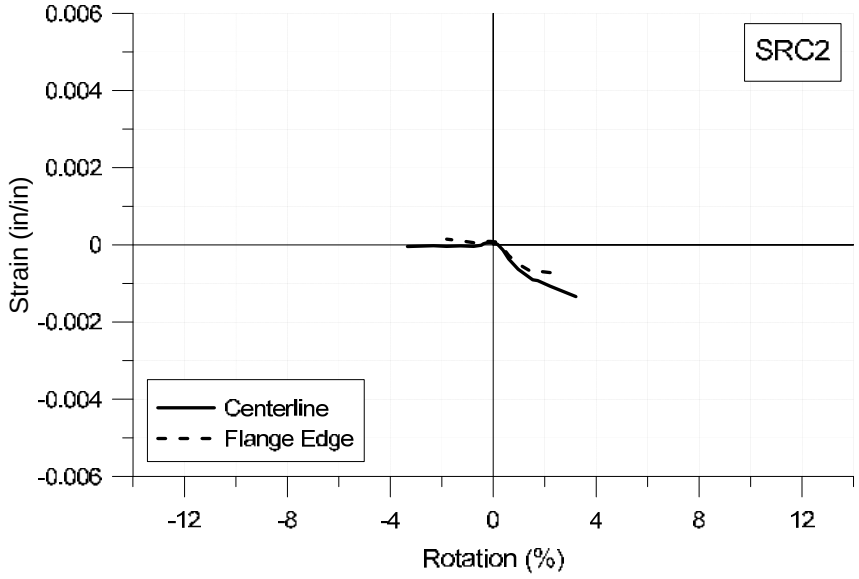

Figure 5.22: Concrete Bearing Strain at Back of Embedded Steel Section: b) SRC2

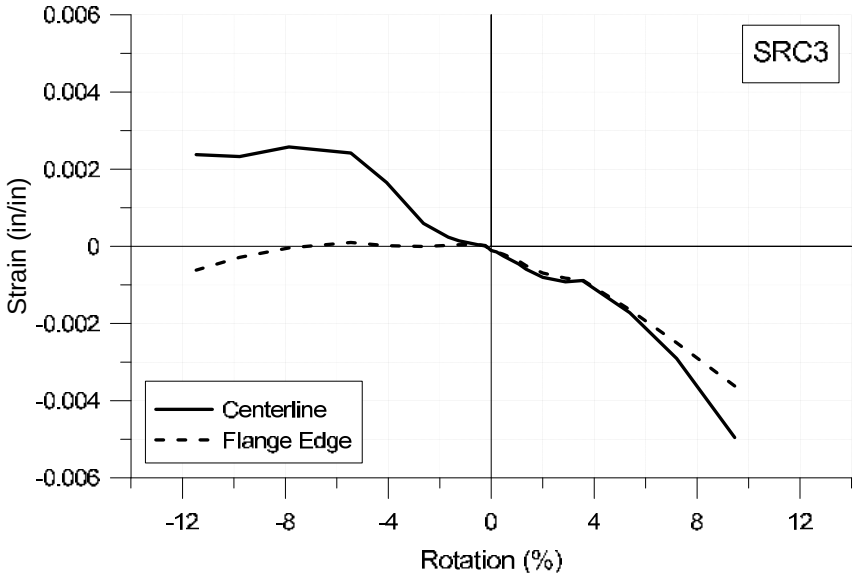

Figure 5.22: Concrete Bearing Strain at Back of Embedded Steel Section: c) SRC3

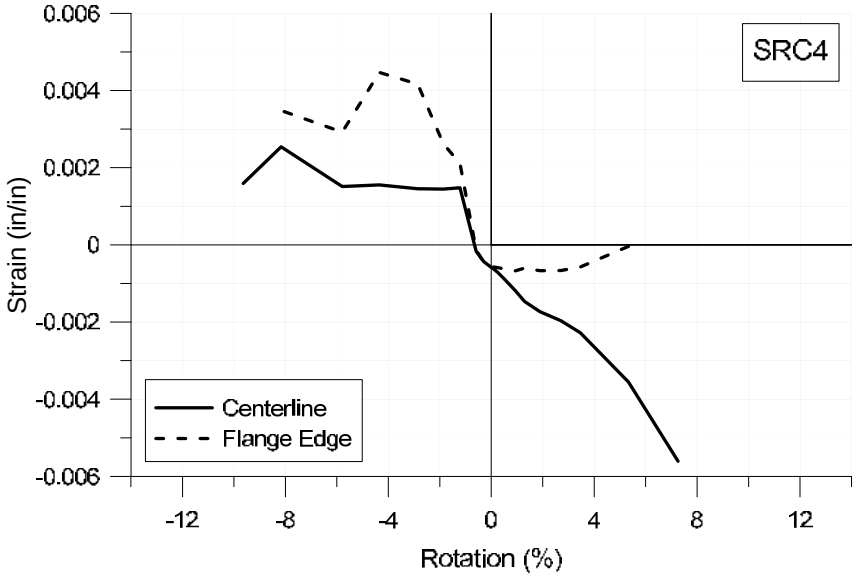

Figure 5.22: Concrete Bearing Strain at Back of Embedded Steel Section: d) SRC4

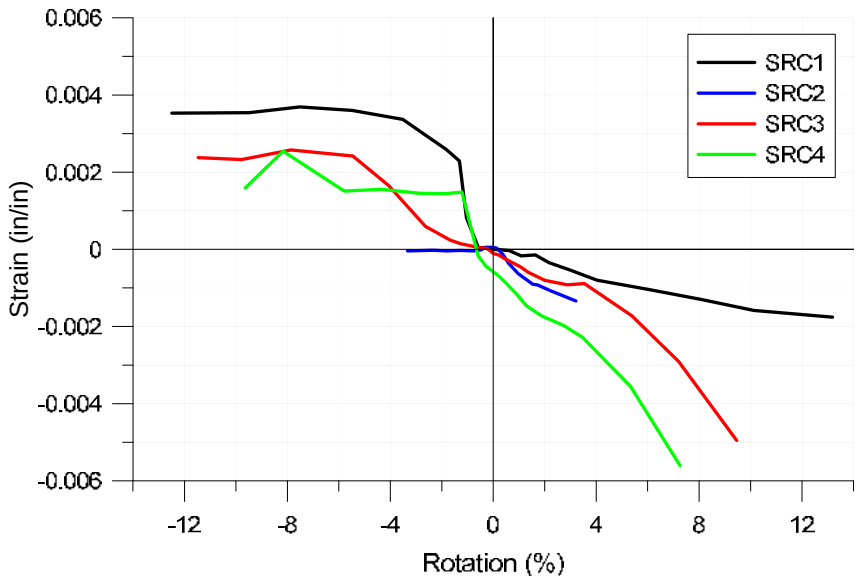

Figure 5.23: Concrete Bearing Strain at Back of Embedded Steel Section for All Beams

In comparing the bearing strain at the beam centerline versus coupling beam chord rotation for all test beams (Figure 5.23), the magnitudes of the compressive bearing strains are smallest for SRC1, the beam with the longest embedment length. The increased magnitude of the compressive bearing strains for SRC4 relative to SRC3 is interesting and may be due to the increased embedment damage (Figure 5.1) associated with the lower area of wall boundary longitudinal reinforcement (Table 3.1). It is surprising that the compressive bearing strains for SRC2 are larger than for SRC3, although the values differ only modestly, noting that data for SRC2 terminate prior to the end of testing (likely due to damage to the strain gage wire).

5.10 EMBEDMENT (STEEL) STRAIN

The profiles shown in Figure 5.24 were used to assess the bending strain in the embedded steel sections. As shown previously in Figure 4.17 and Figure 4.18, Cross-Section A was located in the beam span, 2" from the beam-wall interface, and Cross-Sections B, C, and D, were located along the embedment length at $¼L_e$, $½L_e$, and $¾L_e$ from the beam-wall interface, respectively. The embedment model (Figure 2.2) assumes plane strain behavior in the embedment zone, and thereby assumes that the embedded portion of the steel section rotates as a rigid body without bending. Based on the data provided in Figure 5.24, it is clear that bending occurs in the embedded portion of the steel member.

At Cross-Section A for all beams (Figure 5.24), strain magnitudes generally approach or slightly exceed the yield strain. Significant post-yield strain is not developed, which suggests that yielding is not spreading into the beam span. For SRC3, it appears that the magnitude of bending strain at Cross-Section B slightly exceeds that of Cross-Section A. Because only limited data for SRC1 and SRC2 are available at Cross-Section B, the degree of yielding at this location for these members cannot be determined. For SRC1 and SRC4, the magnitudes of the bending strains are largest at Cross-Section A and diminish with distance along the embedment length from the beam-wall interface. For SRC2, it is interesting to note that significant yielding occurs at Cross-Section C in the negative loading direction. This suggests that wall loading has a significant impact on the spread of yielding into the embedded portion of the member. Specifically, it appears that when wall loads create tension rather than compression normal to the embedment length, yielding propagates further along the embedment length from the beam-wall interface. For SRC4, significant yielding is not shown at any of the cross-section locations,

which may be due to significant connection rotation associated with the observed embedment damage for this member (Figure 5.1).

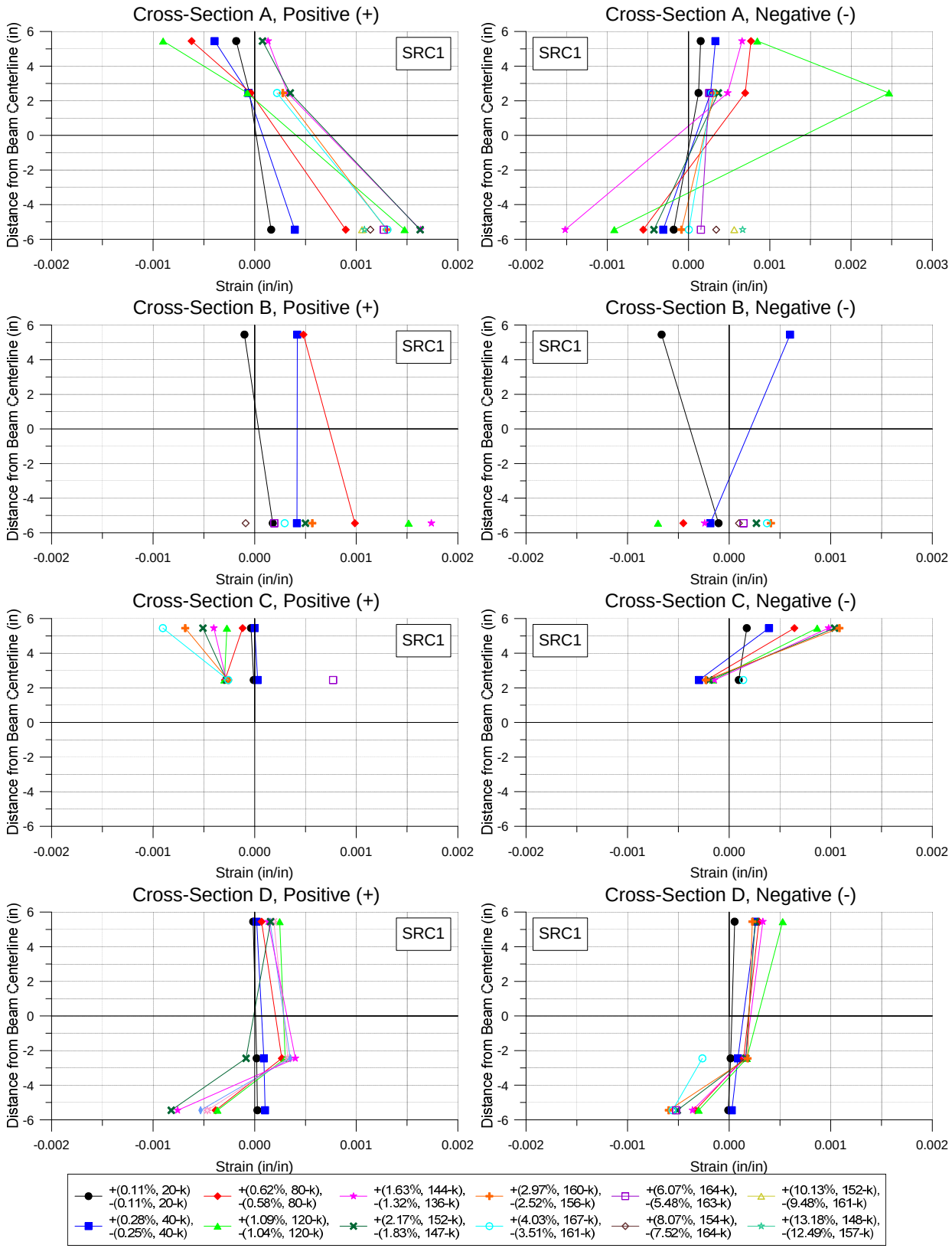

Figure 5.24: Embedded Steel Section Strain Profiles: a) SRC1

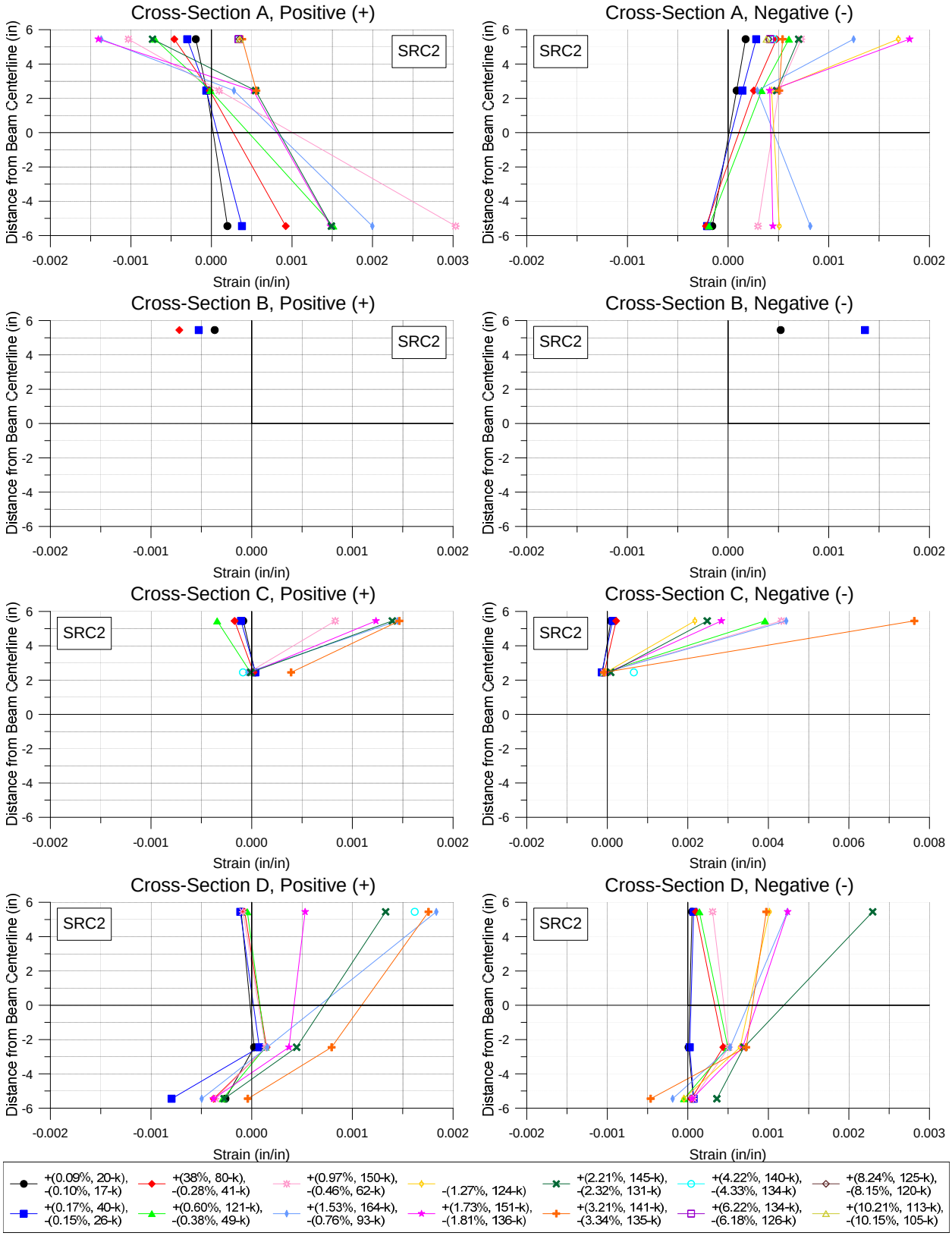

Figure 5.24: Embedded Steel Section Strain Profiles: b) SRC2

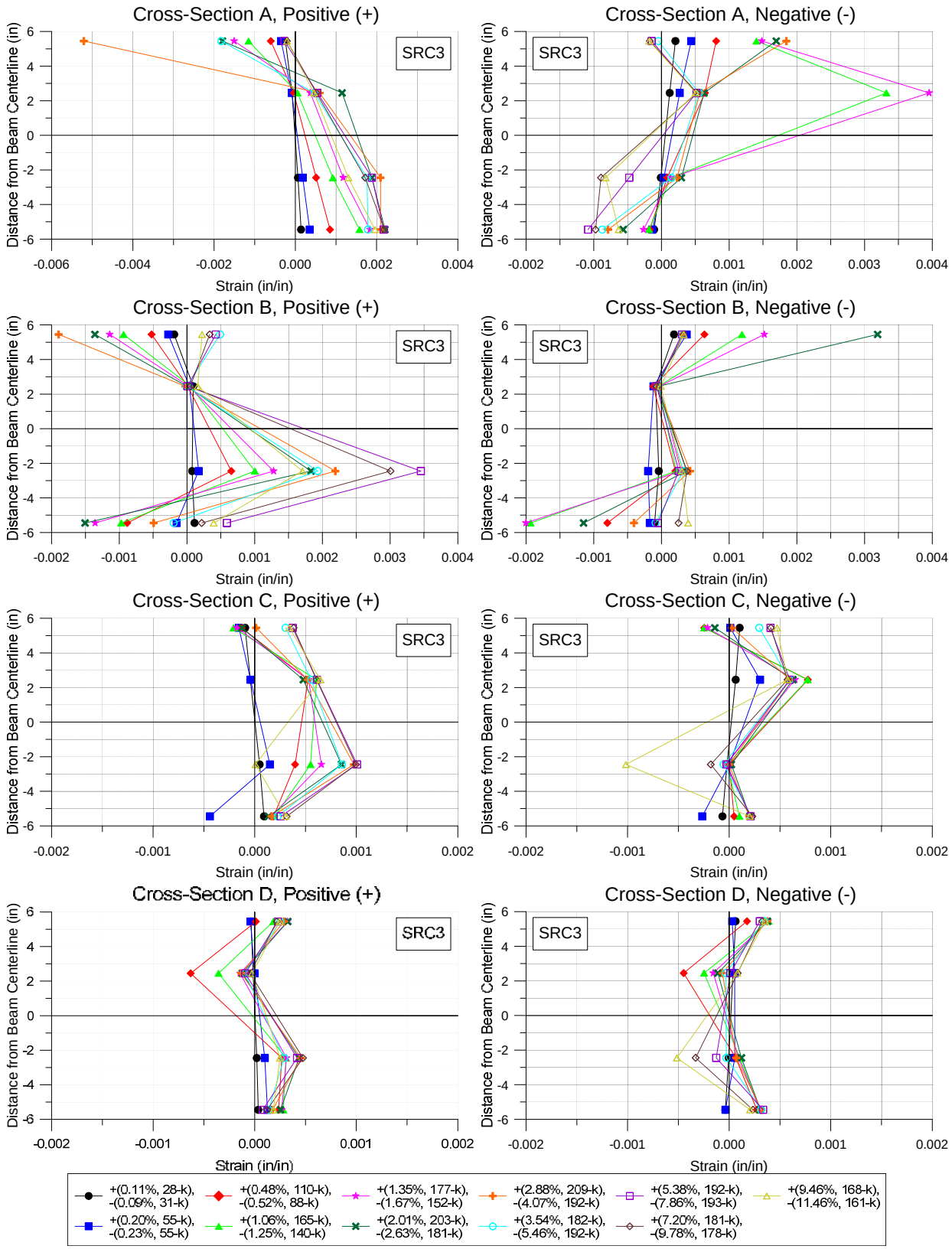

Figure 5.24: Embedded Steel Section Strain Profiles: c) SRC3

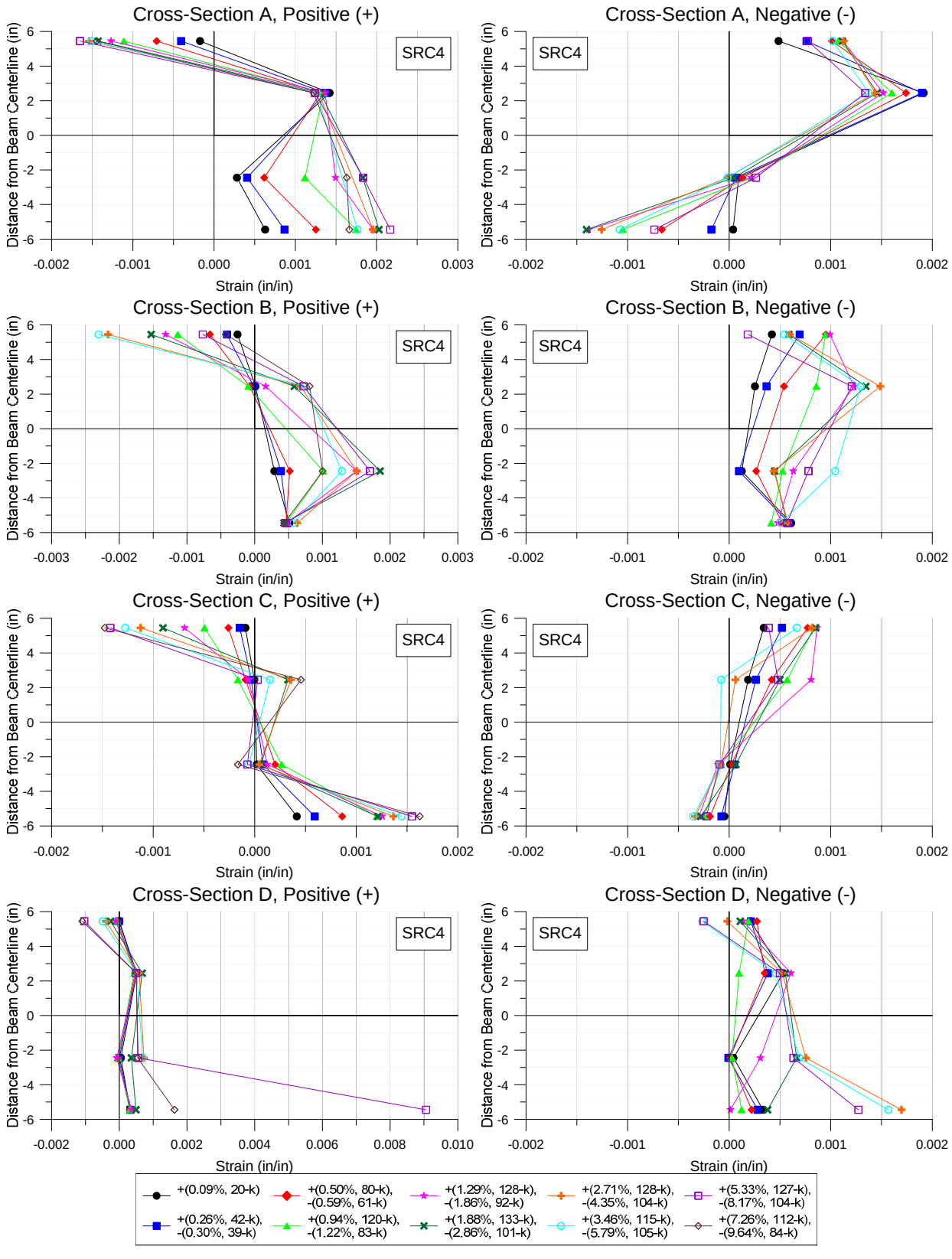

Figure 5.24: Embedded Steel Section Strain Profiles: d) SRC4

5.11 WALL STRAIN PROFILES

Wall strain profiles, generated based on data at the peak of each initial (first) cycle at each increment of load or displacement applied, for each of the four tests at each of the locations shown in Figure 5.25 are provided in Figure 5.26 for the wall cross-sections (Cross-Sections 1 through 10 in Figure 5.25) and in Figure 5.27 for the vertical locations (Locations A through E in Figure 5.25). It is noted that the plots for SRC2 and SRC4 include residual strain values remaining after the completion of testing of SRC1 and SRC3. Referring to Figure 5.26, plane-section behavior is generally observed at the cross-sections further away from the coupling beam, with noticeable lack of plane-section behavior observed at cross-sections 5, 6, 7, and 8 due to the influence of the beam. The measured strains are much larger at cross-sections 6, 7, and 8 than at the other cross-sections due to the local strain caused by the coupling beam (consistent with Figure 3.9). It is evident from Figure 5.27 that wall yielding for SRC3 and SRC4 occurred predominantly at the location of the coupling beam, consistent with the observed damage (Figure 5.1).

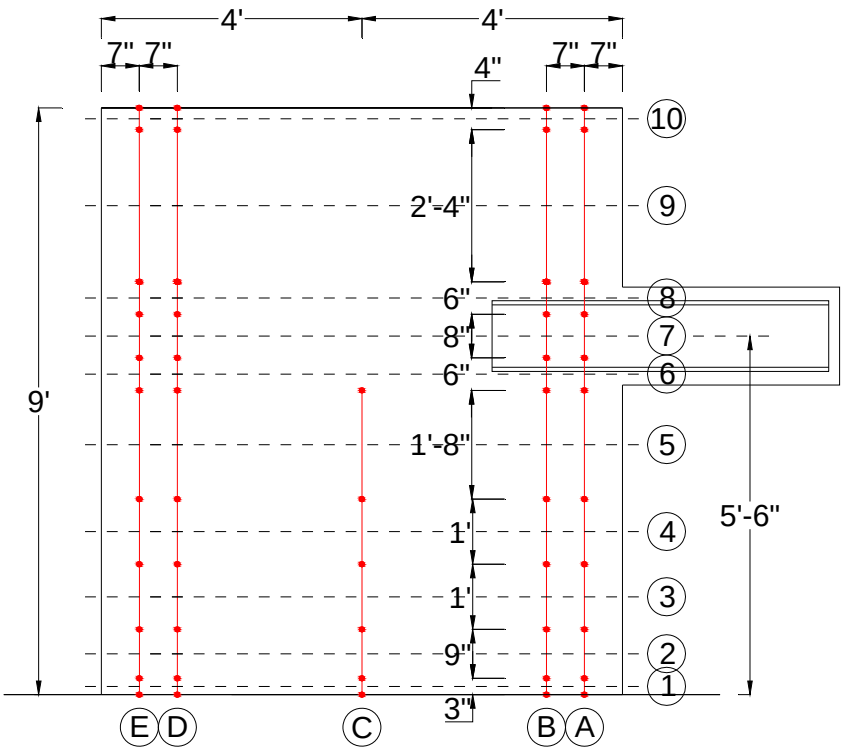

Figure 5.25: Designation of Wall Locations

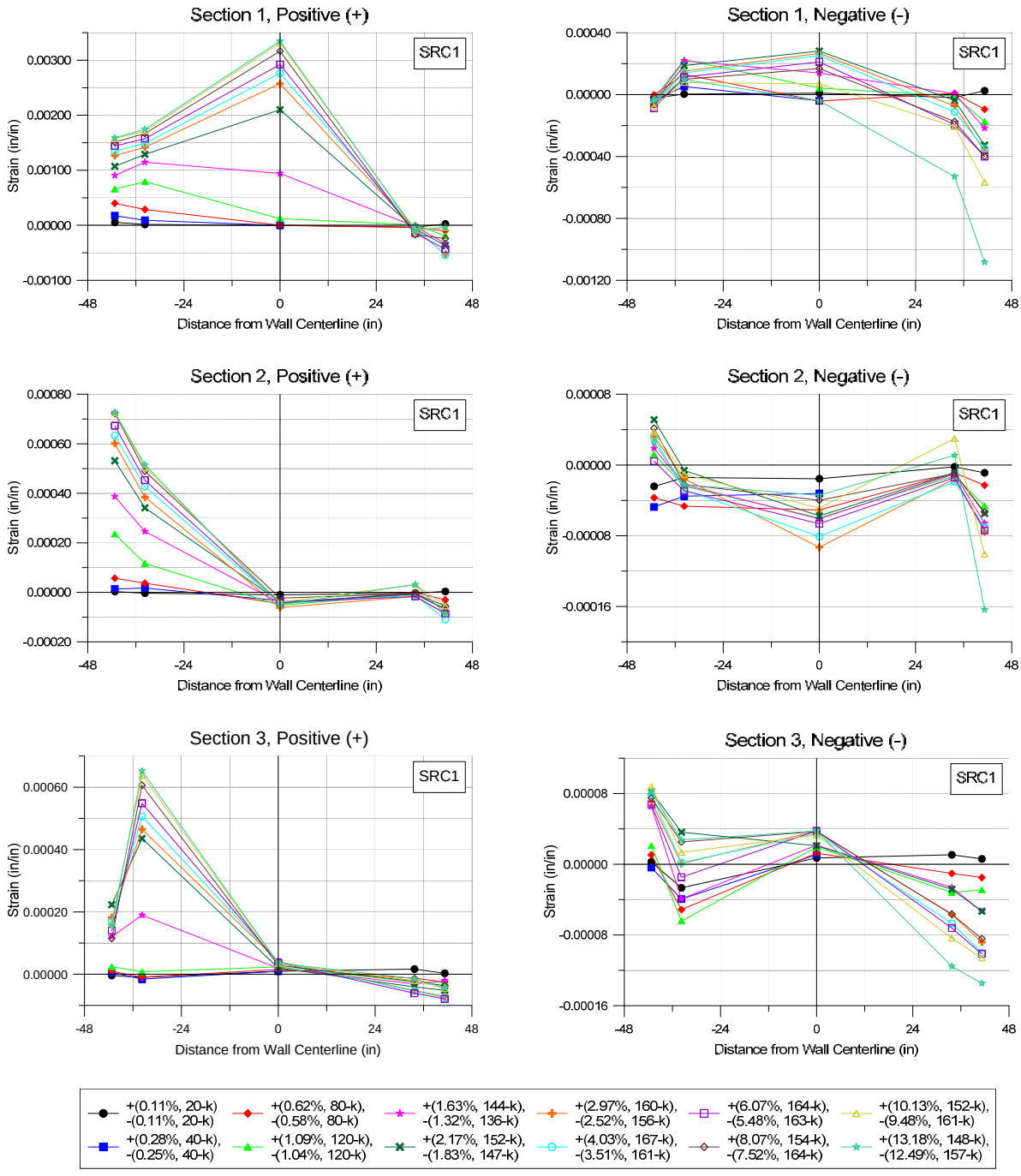

Figure 5.26: Wall Strain Profiles in Horizontal Direction: a) SRC1

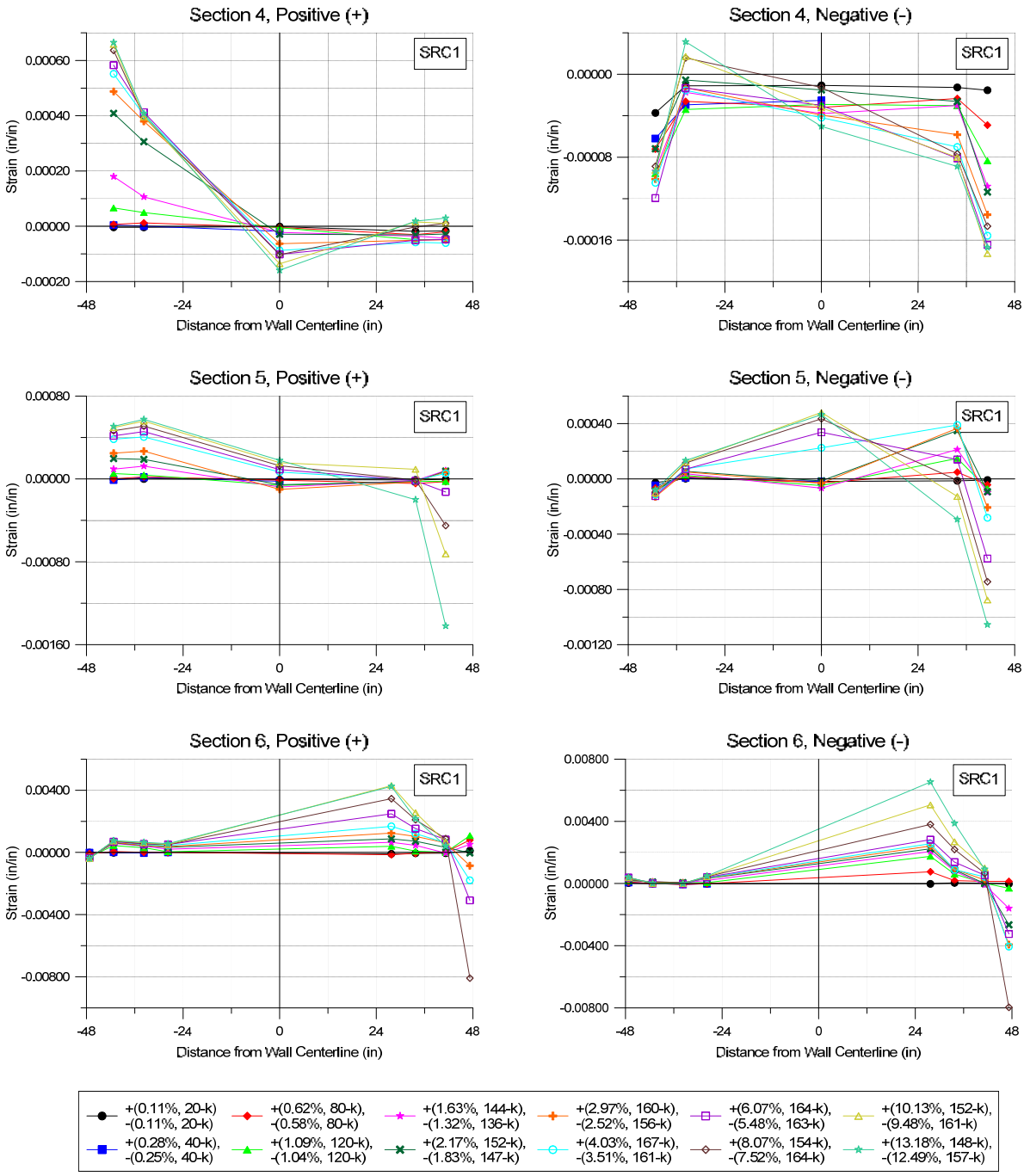

Figure 5.26: Wall Strain Profiles in Horizontal Direction: a) SRC1 (Continued)

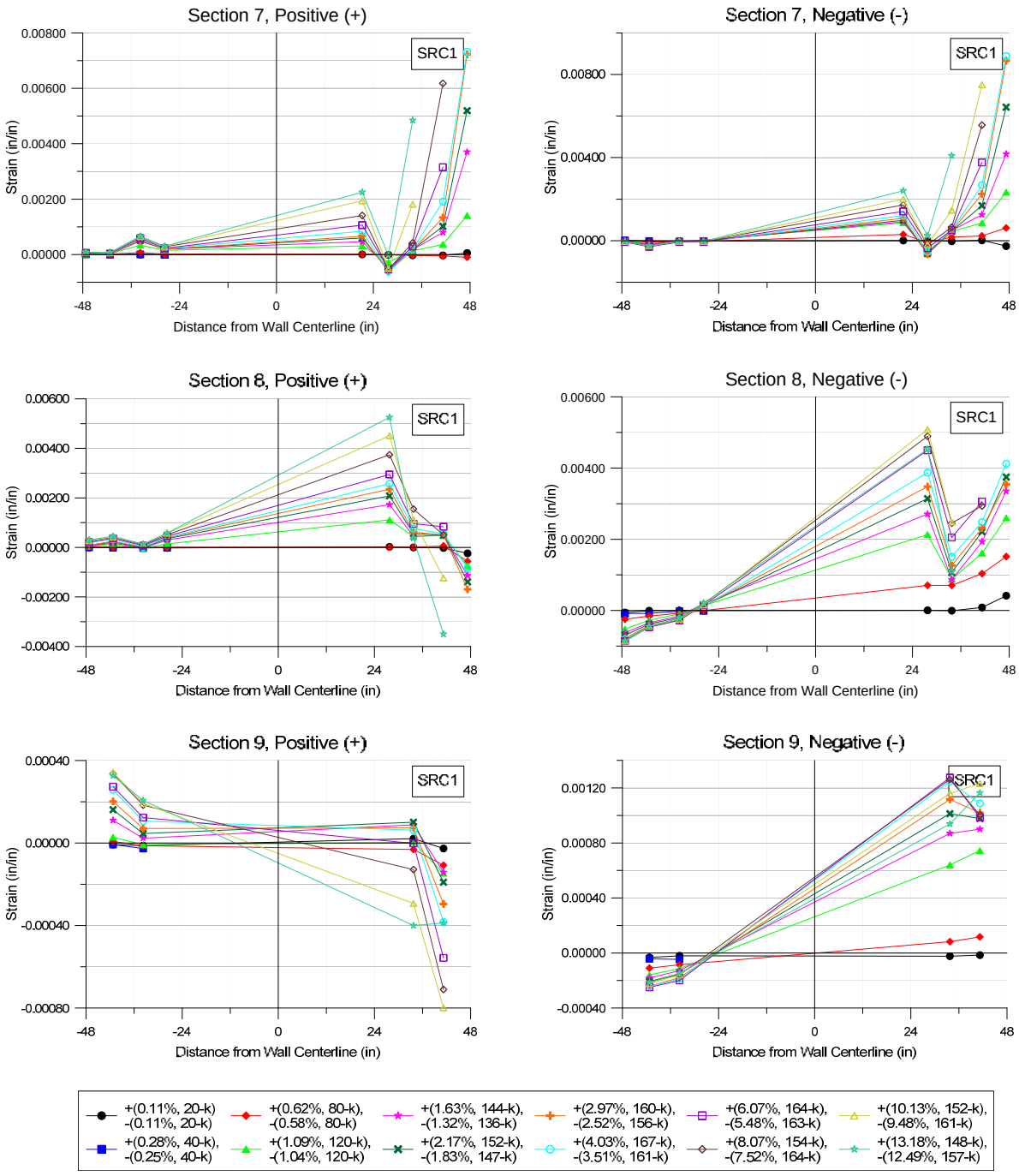

Figure 5.26: Wall Strain Profiles in Horizontal Direction: a) SRC1 (Continued)

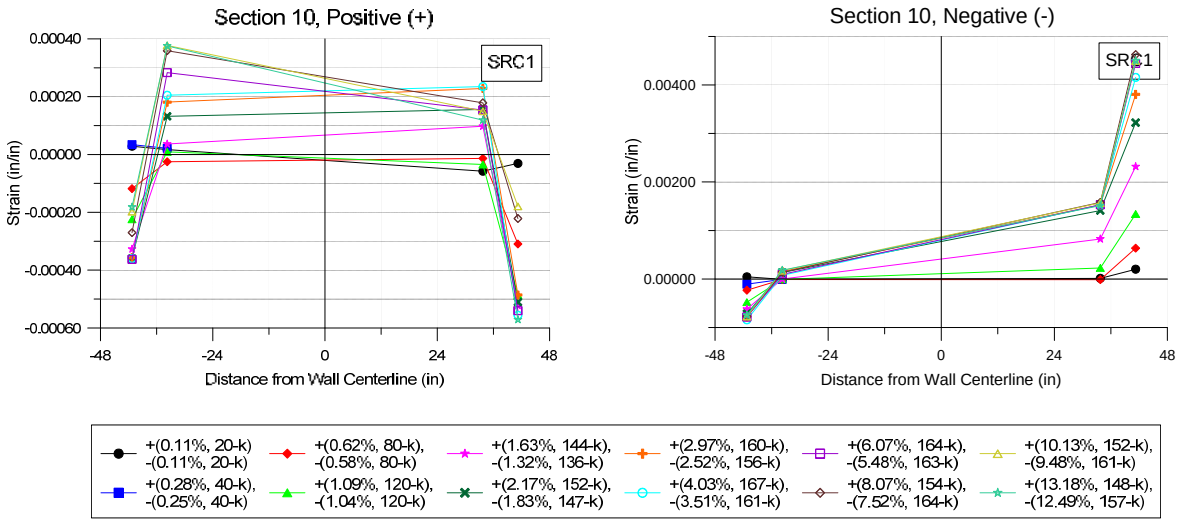

Figure 5.26: Wall Strain Profiles in Horizontal Direction: a) SRC1 (Continued)

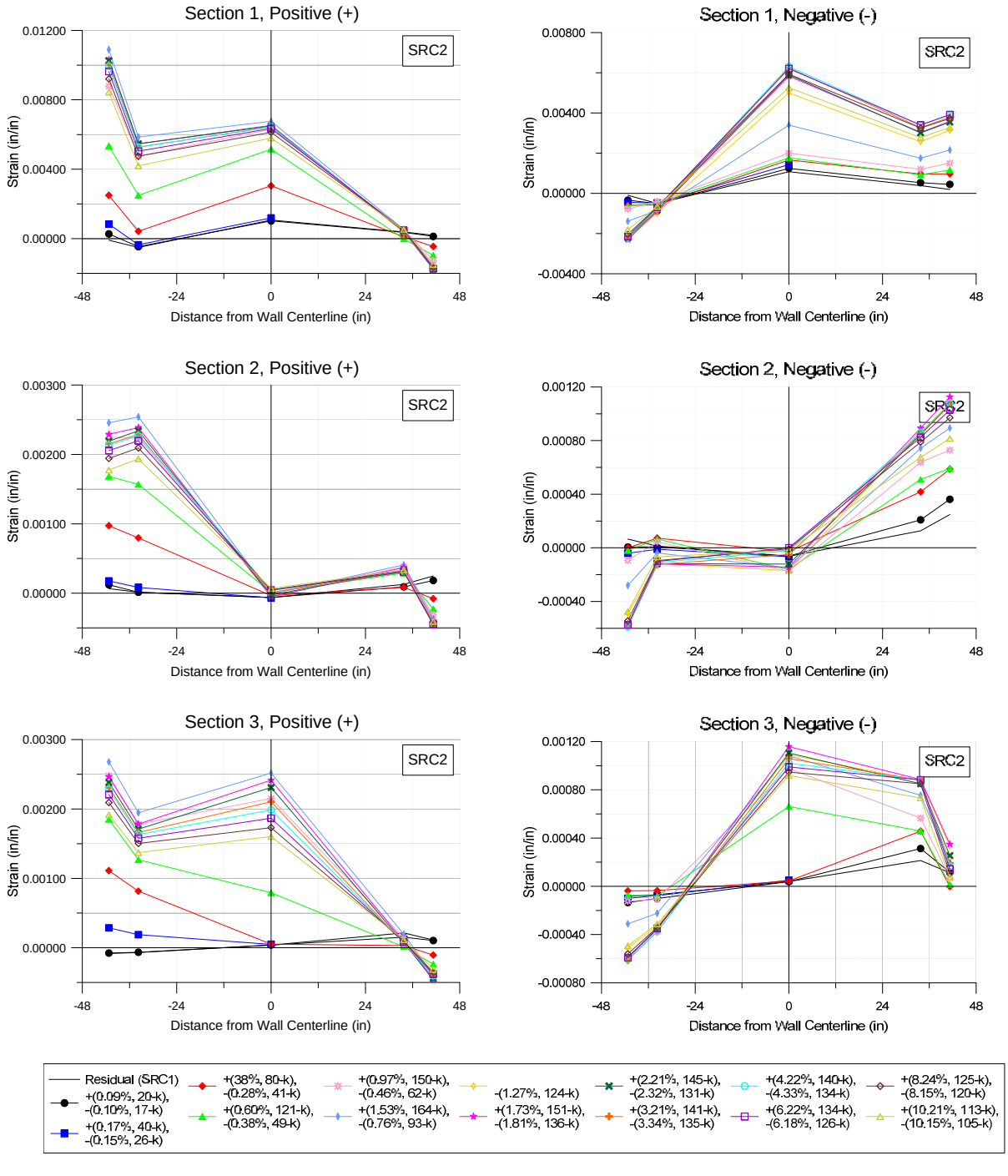

Figure 5.26: Wall Strain Profiles in Horizontal Direction: b) SRC2

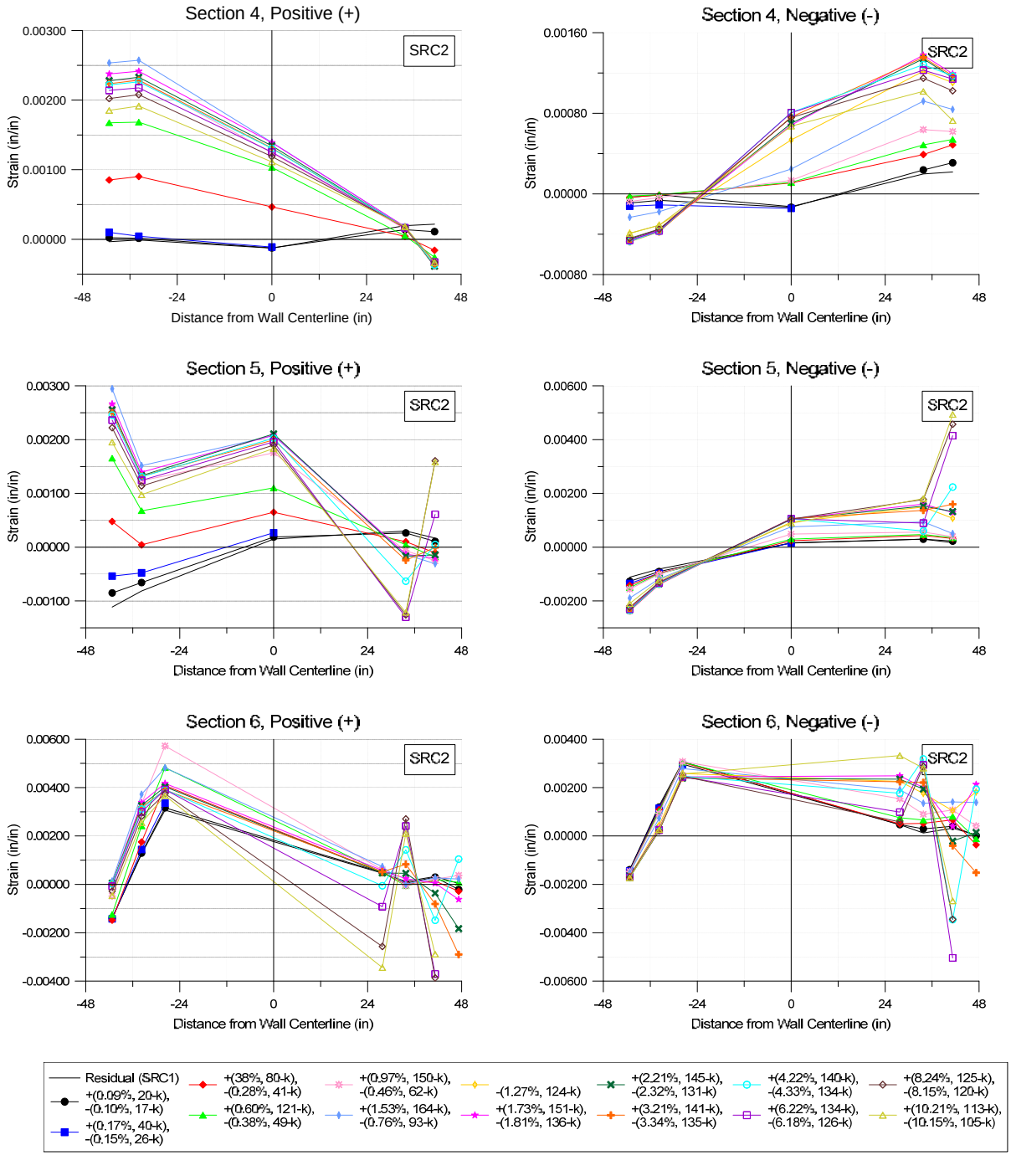

Figure 5.26: Wall Strain Profiles in Horizontal Direction: b) SRC2 (Continued)

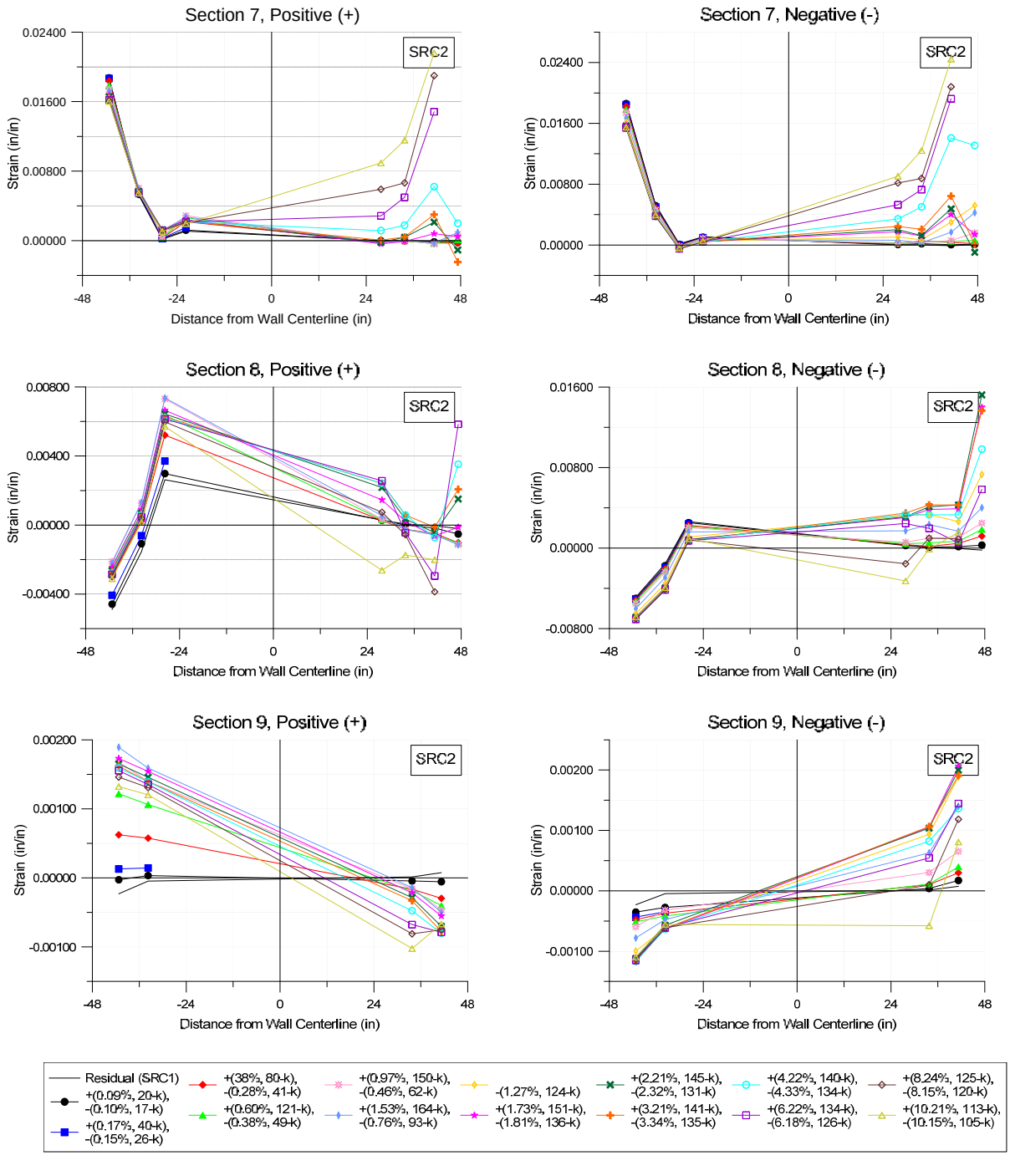

Figure 5.26: Wall Strain Profiles in Horizontal Direction: b) SRC2 (Continued)

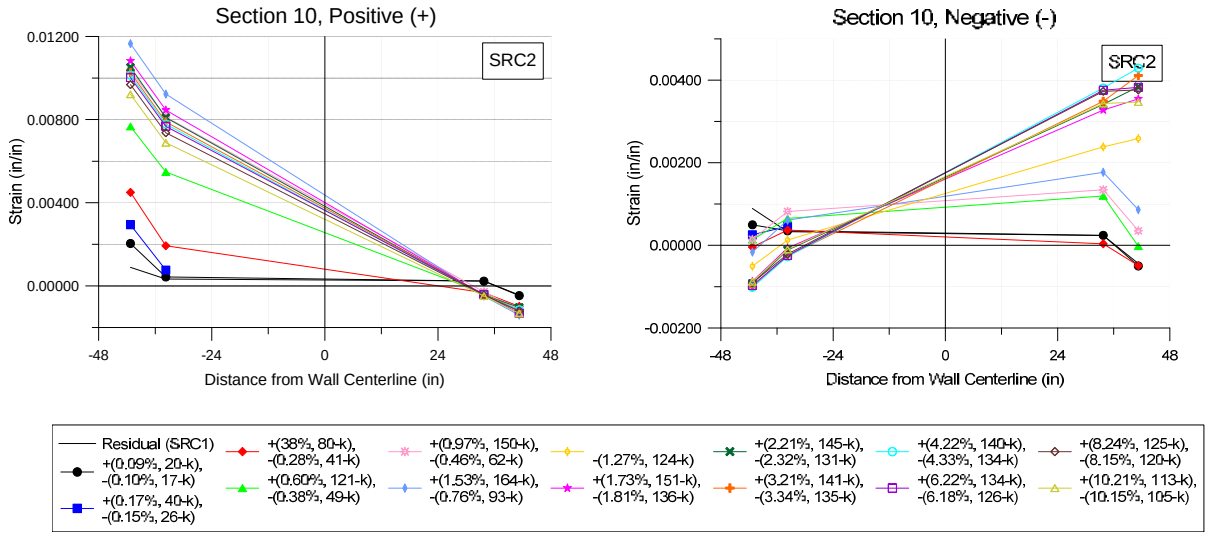

Figure 5.26: Wall Strain Profiles in Horizontal Direction: b) SRC2 (Continued)

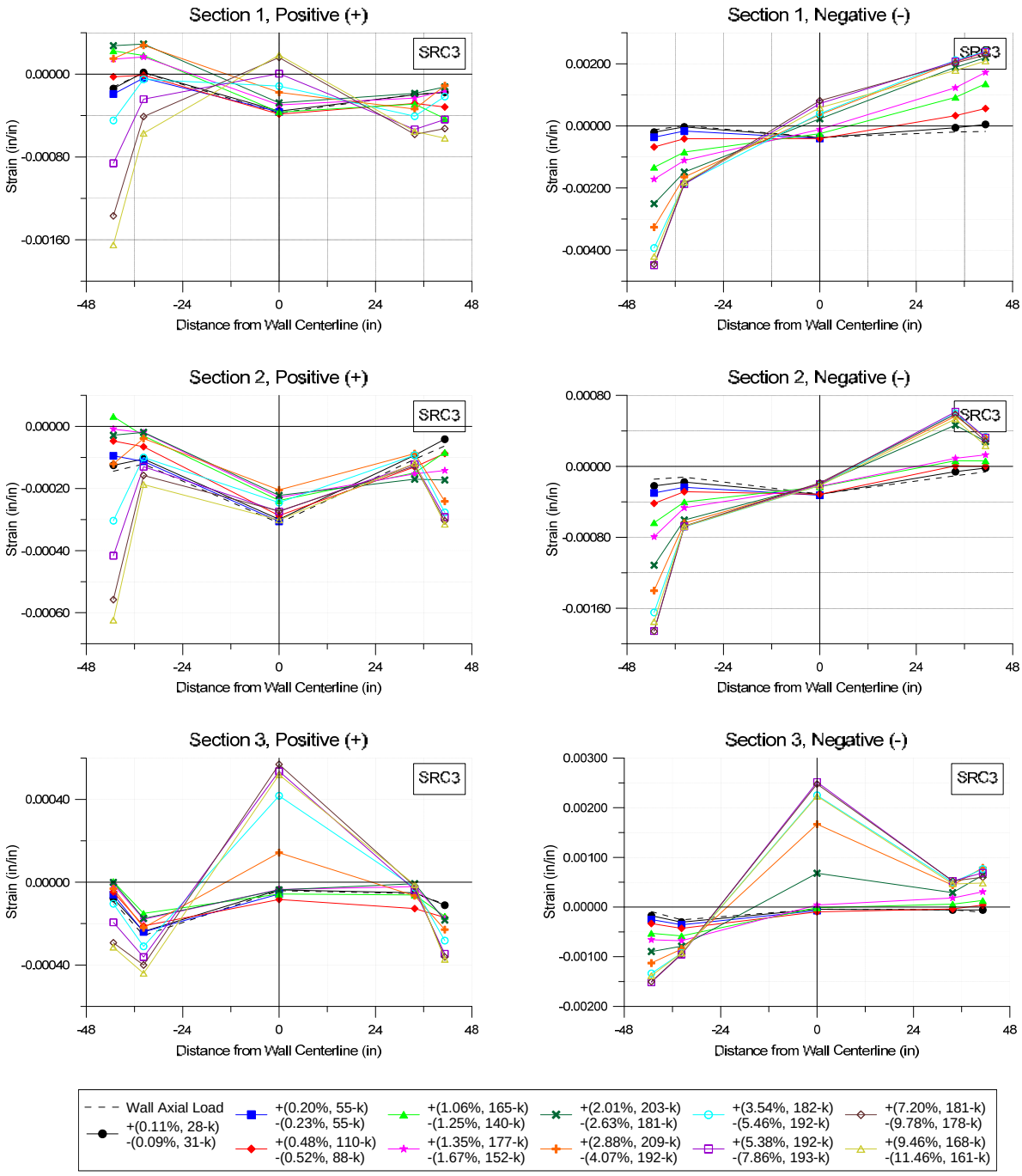

Figure 5.26: Wall Strain Profiles in Horizontal Direction: c) SRC3

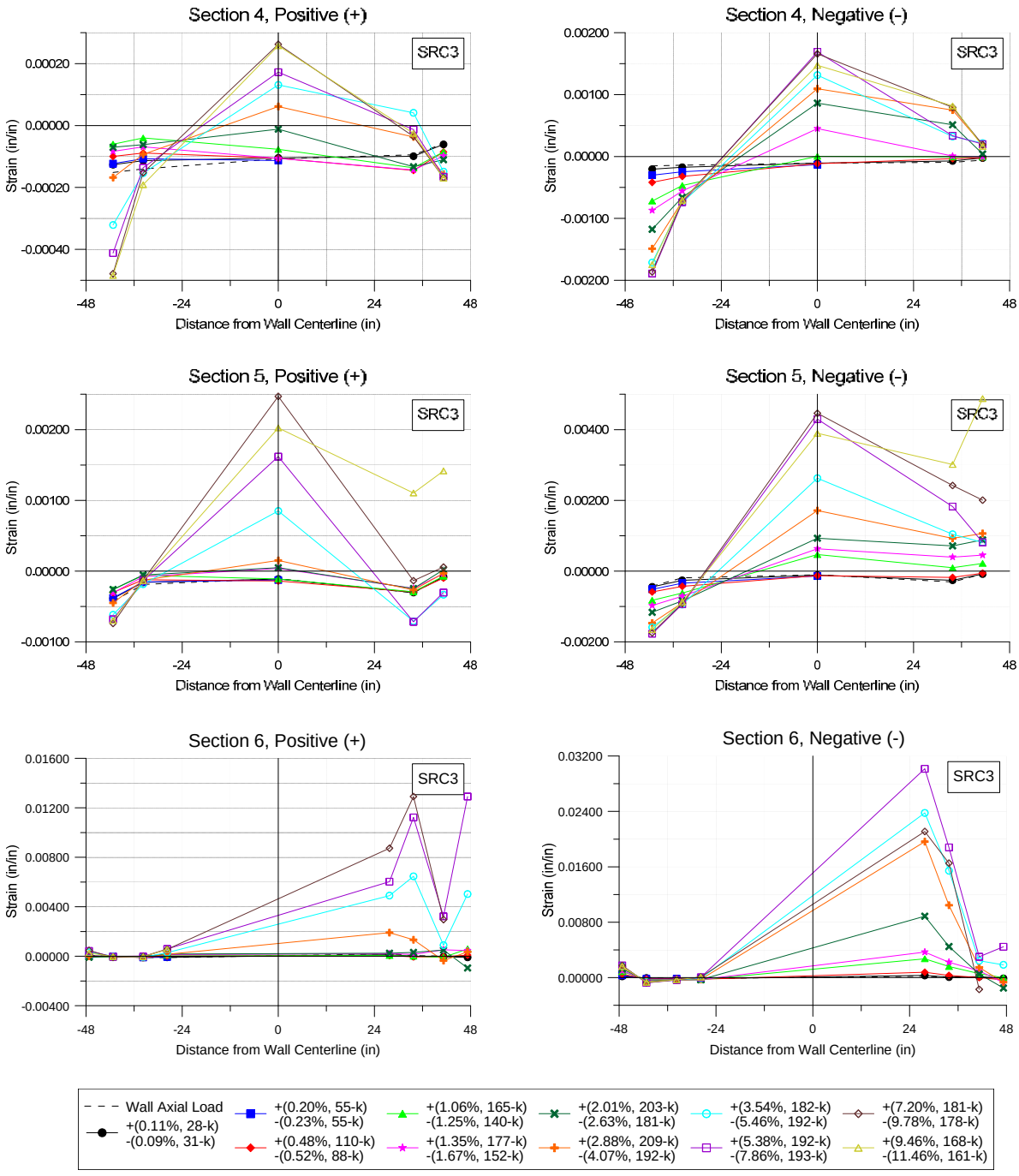

Figure 5.26: Wall Strain Profiles in Horizontal Direction: c) SRC3 (Continued)

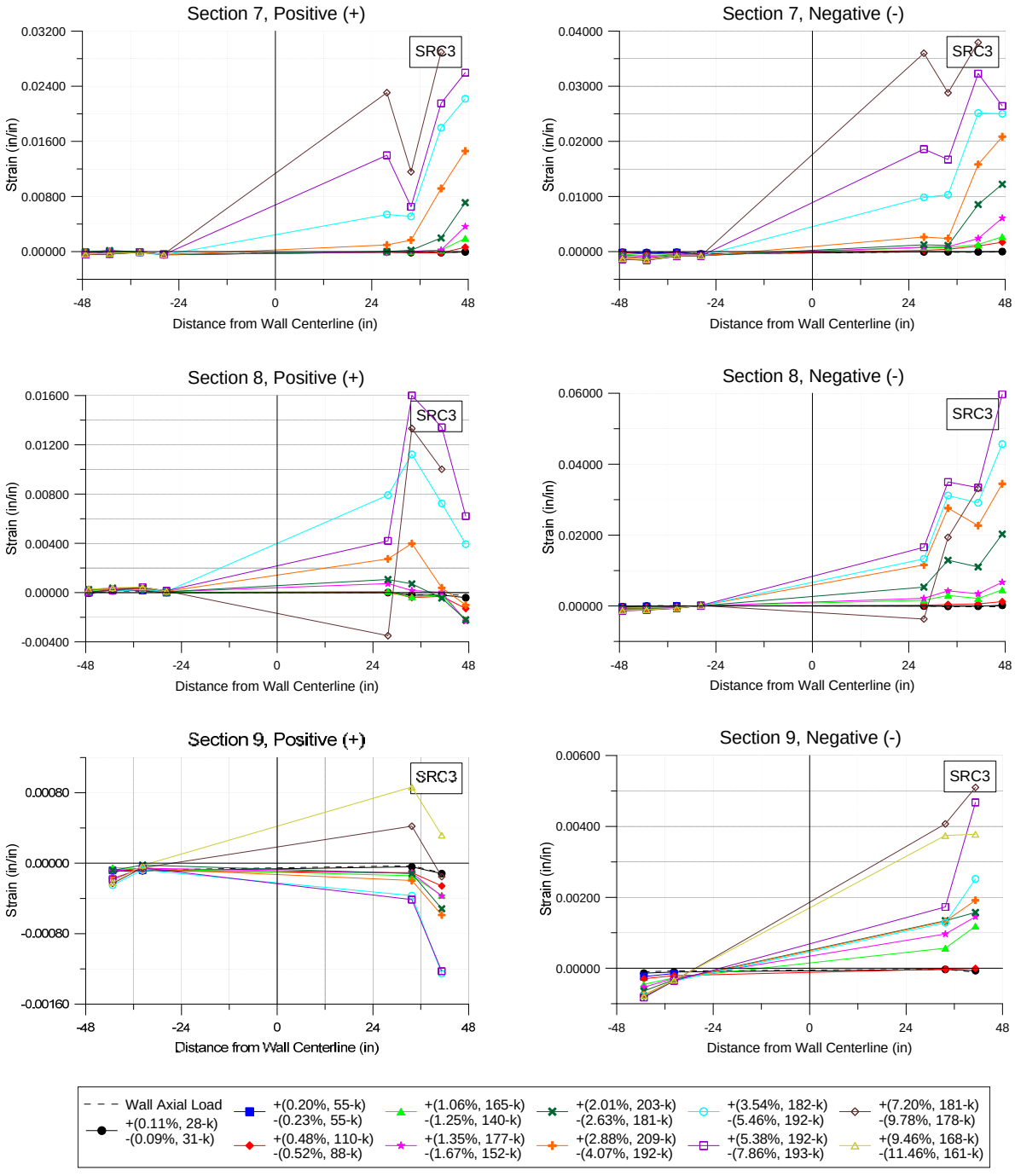

Figure 5.26: Wall Strain Profiles in Horizontal Direction: c) SRC3 (Continued)

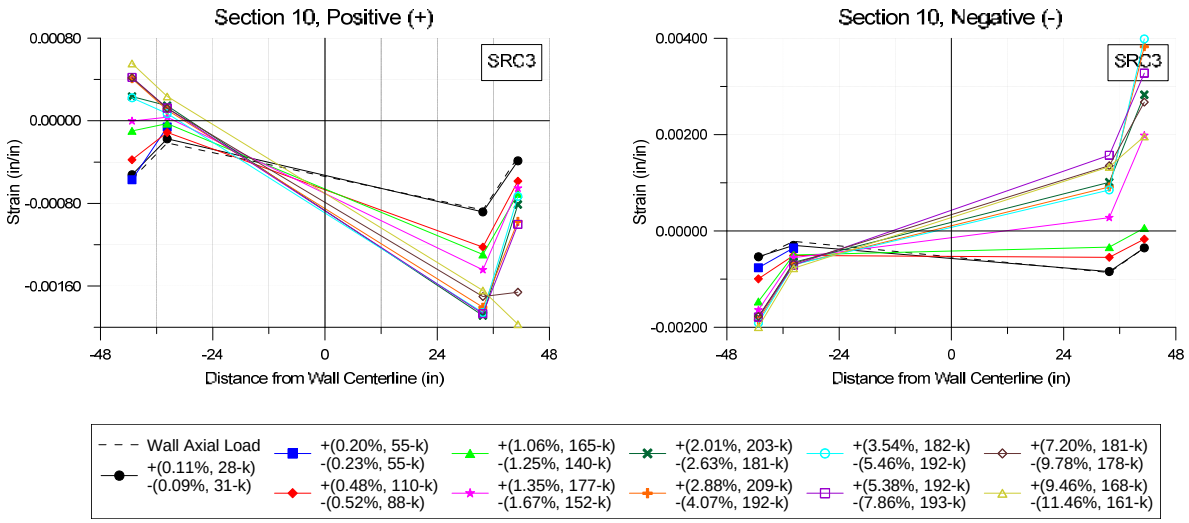

Figure 5.26: Wall Strain Profiles in Horizontal Direction: c) SRC3 (Continued)

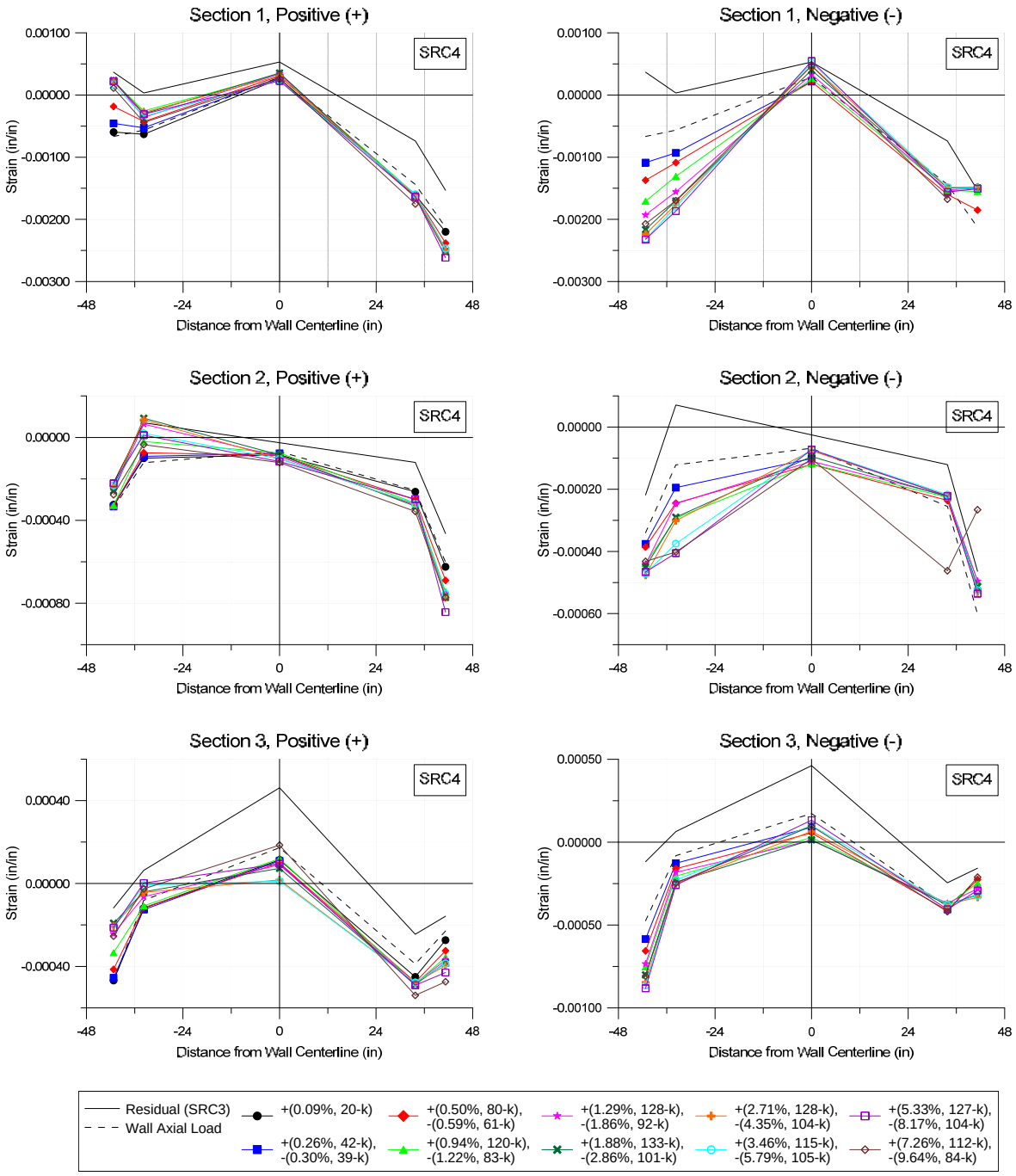

Figure 5.26: Wall Strain Profiles in Horizontal Direction: d) SRC4

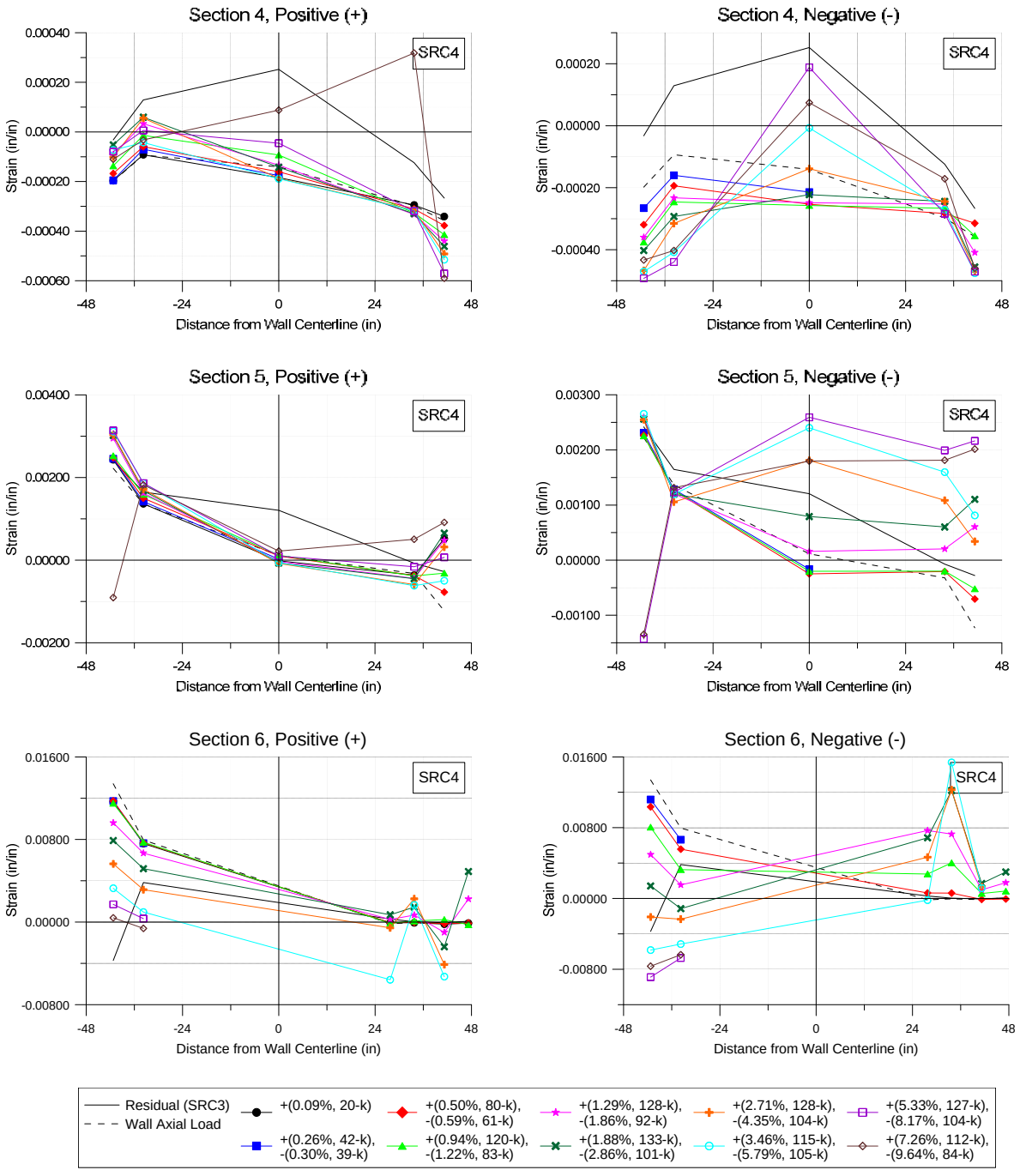

Figure 5.26: Wall Strain Profiles in Horizontal Direction: d) SRC4 (Continued)

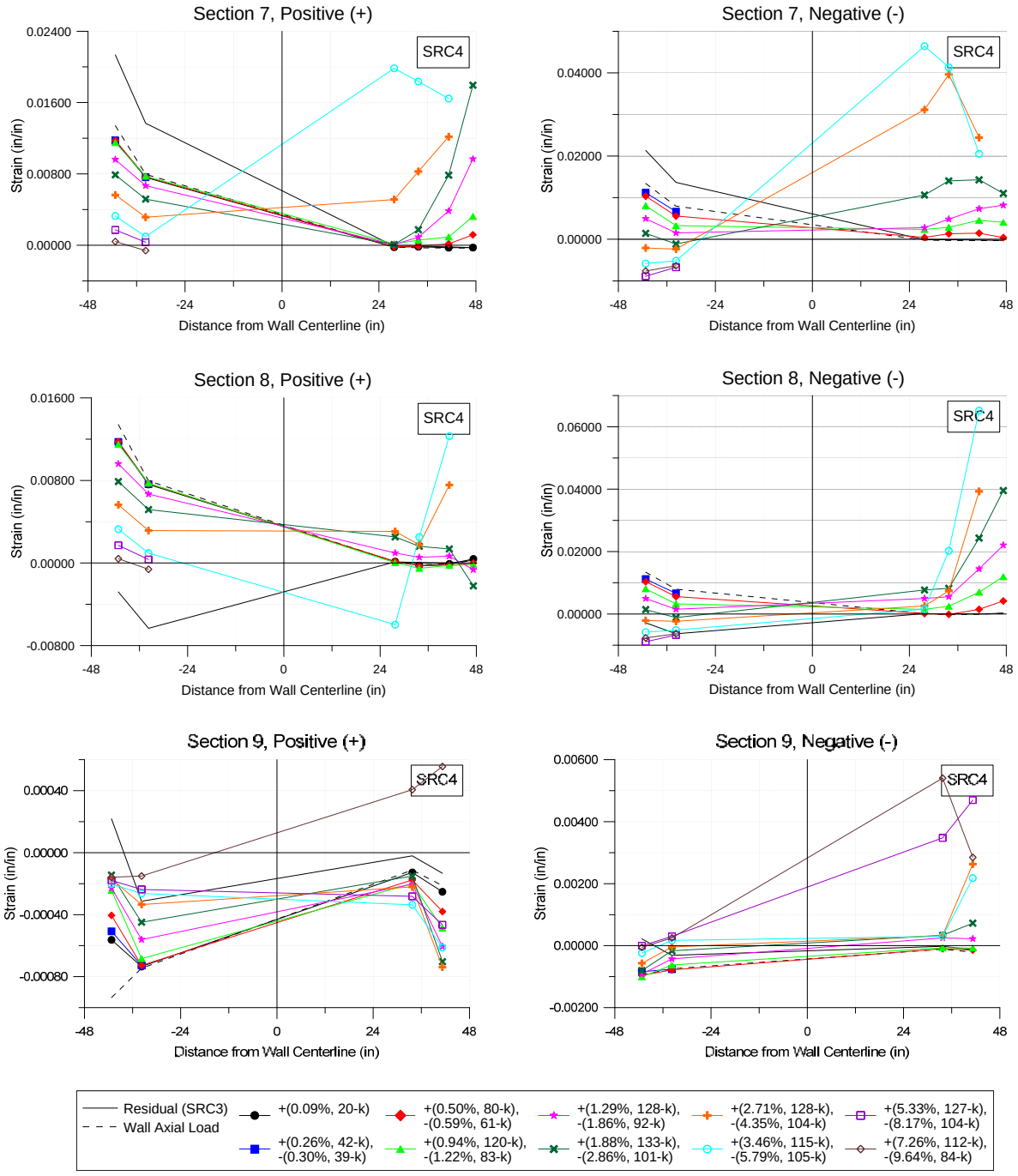

Figure 5.26: Wall Strain Profiles in Horizontal Direction: d) SRC4 (Continued)

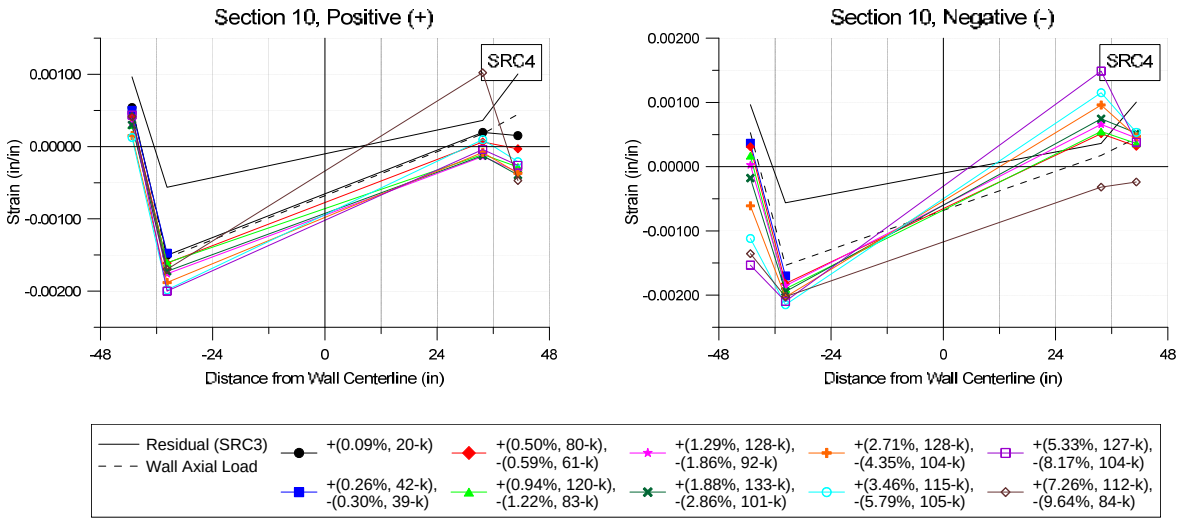

Figure 5.26: Wall Strain Profiles in Horizontal Direction: d) SRC4 (Continued)

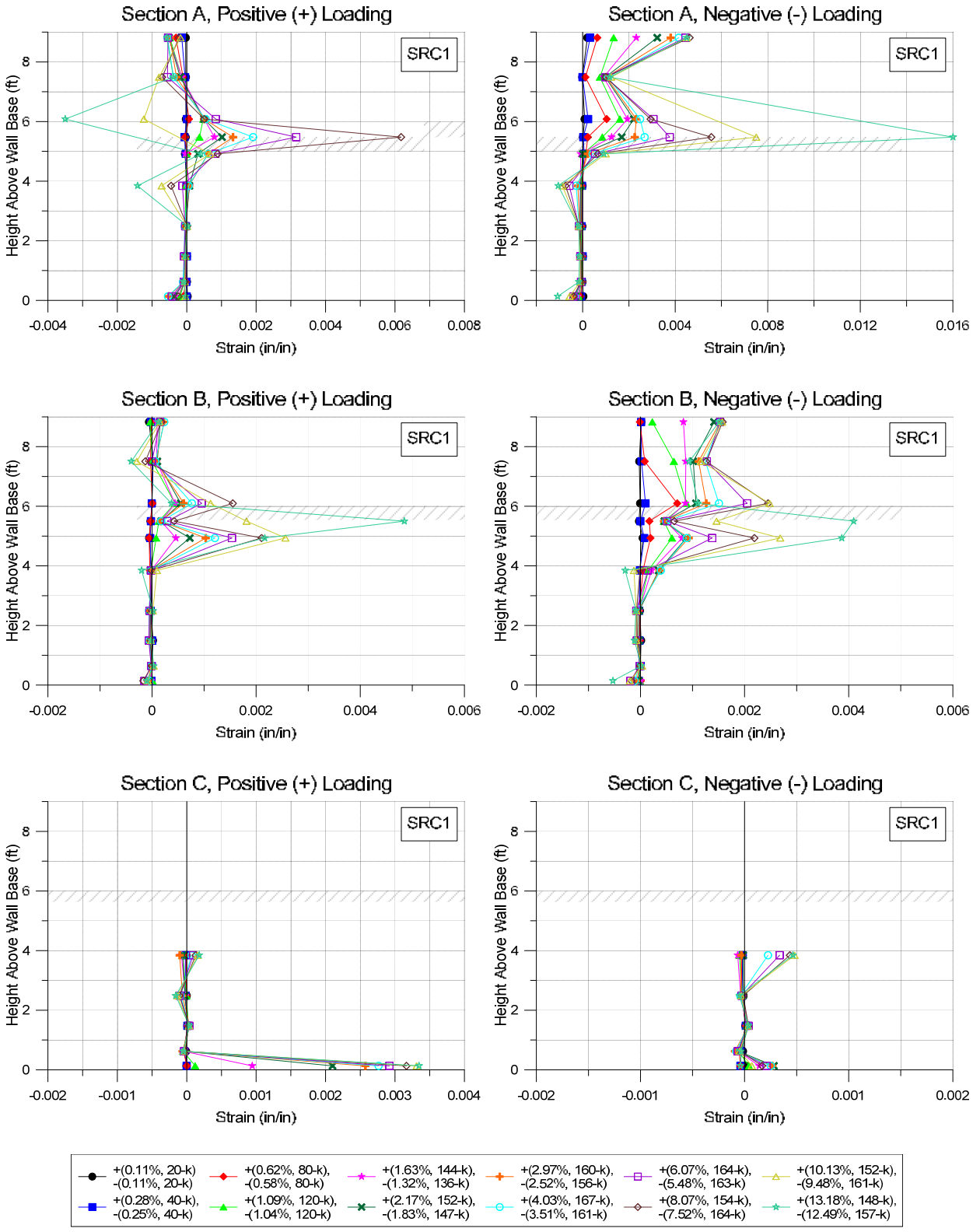

Figure 5.27: Wall Strain Profiles in Vertical Direction: a) SRC1

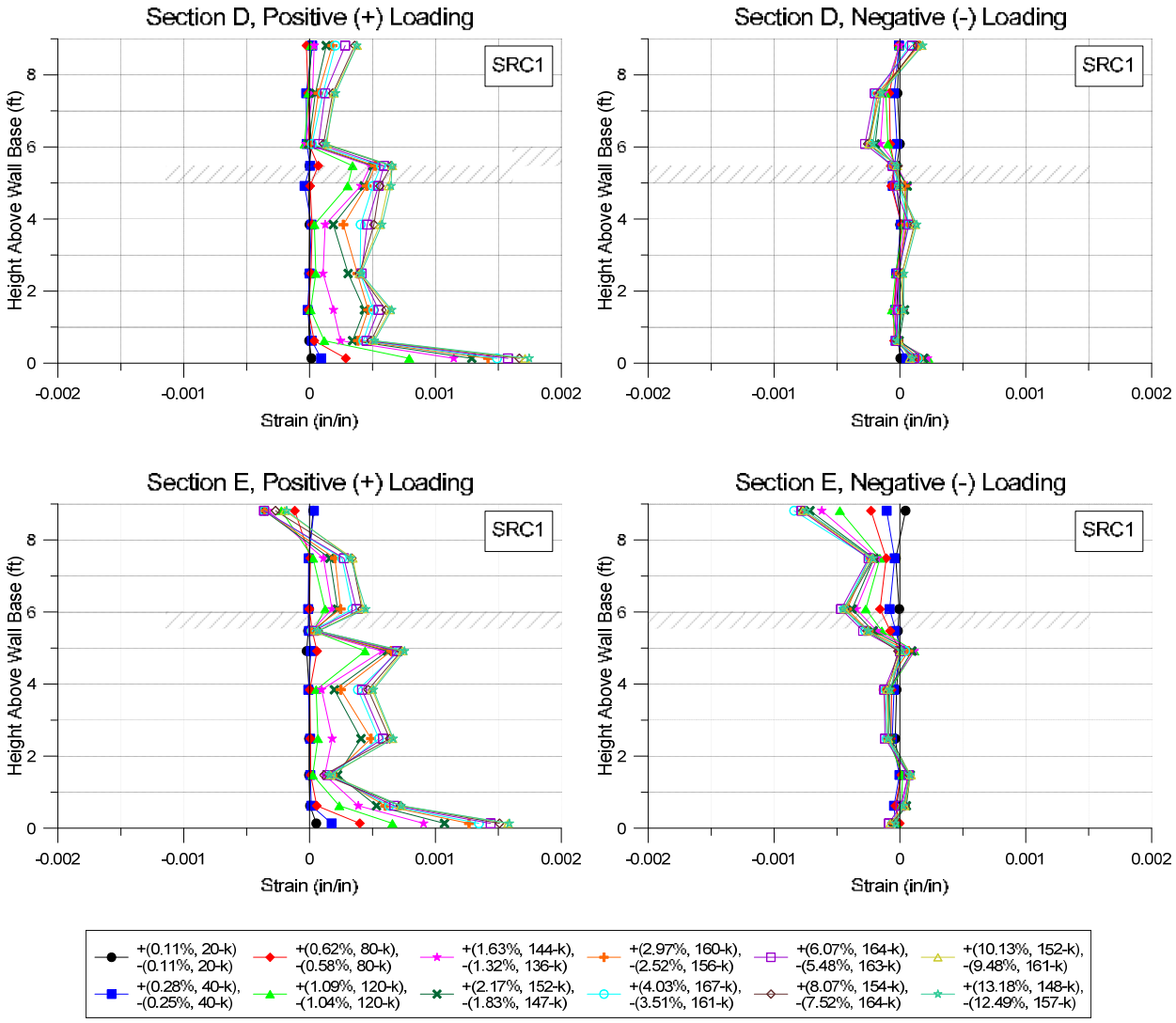

Figure 5.27: Wall Strain Profiles in Vertical Direction: a) SRC1 (Continued)

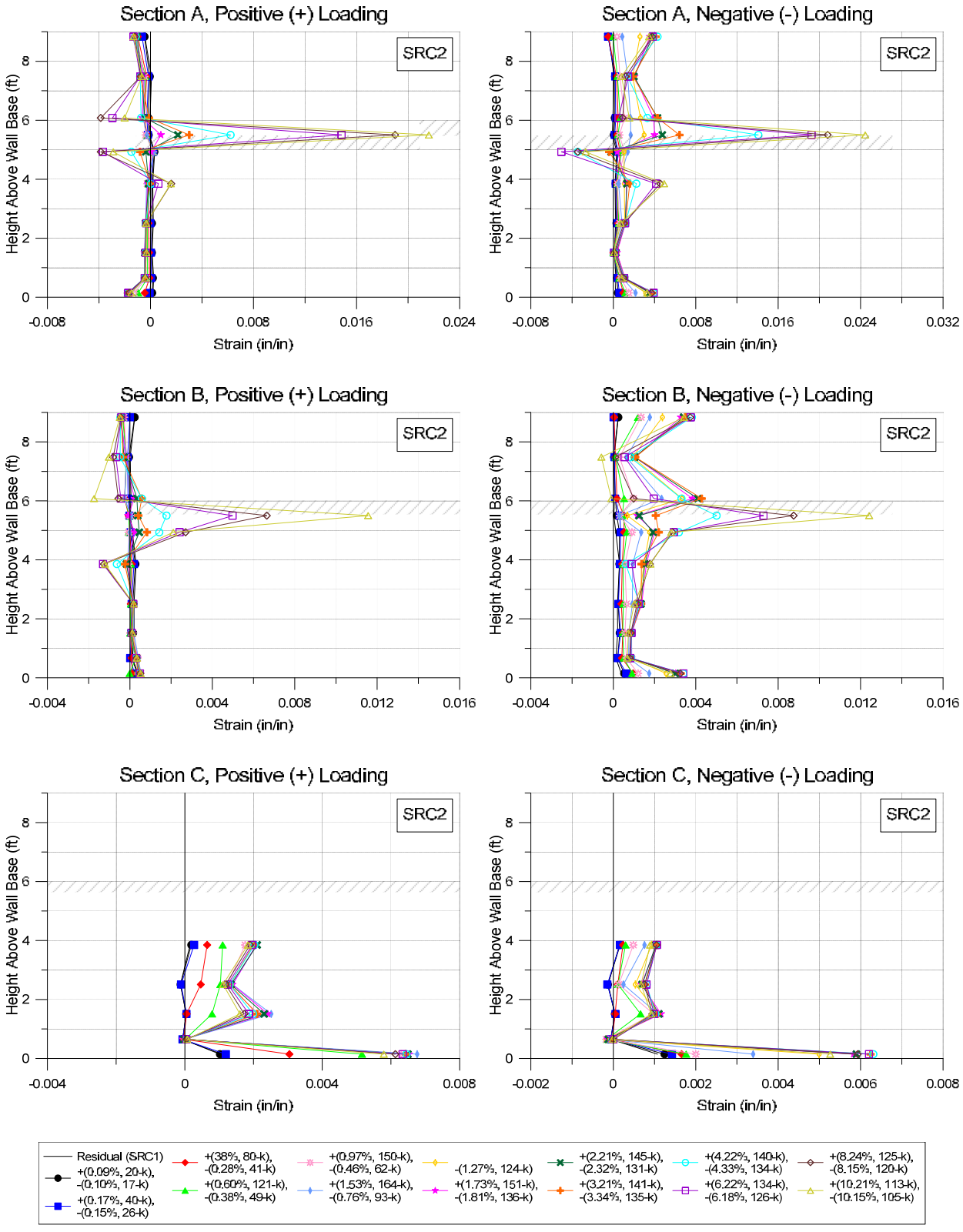

Figure 5.27: Wall Strain Profiles in Vertical Direction: b) SRC2

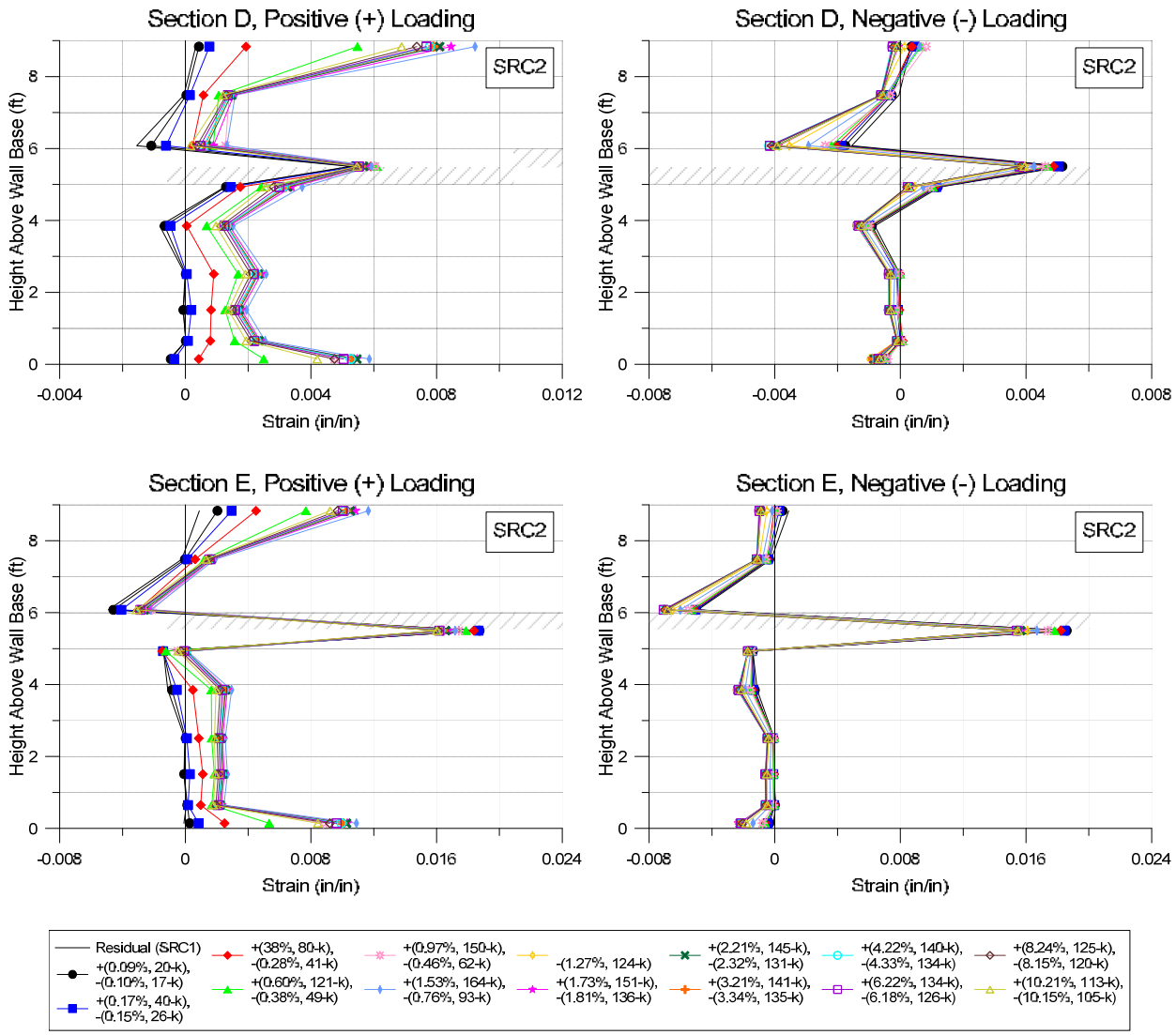

Figure 5.27: Wall Strain Profiles in Vertical Direction: b) SRC2 (Continued)

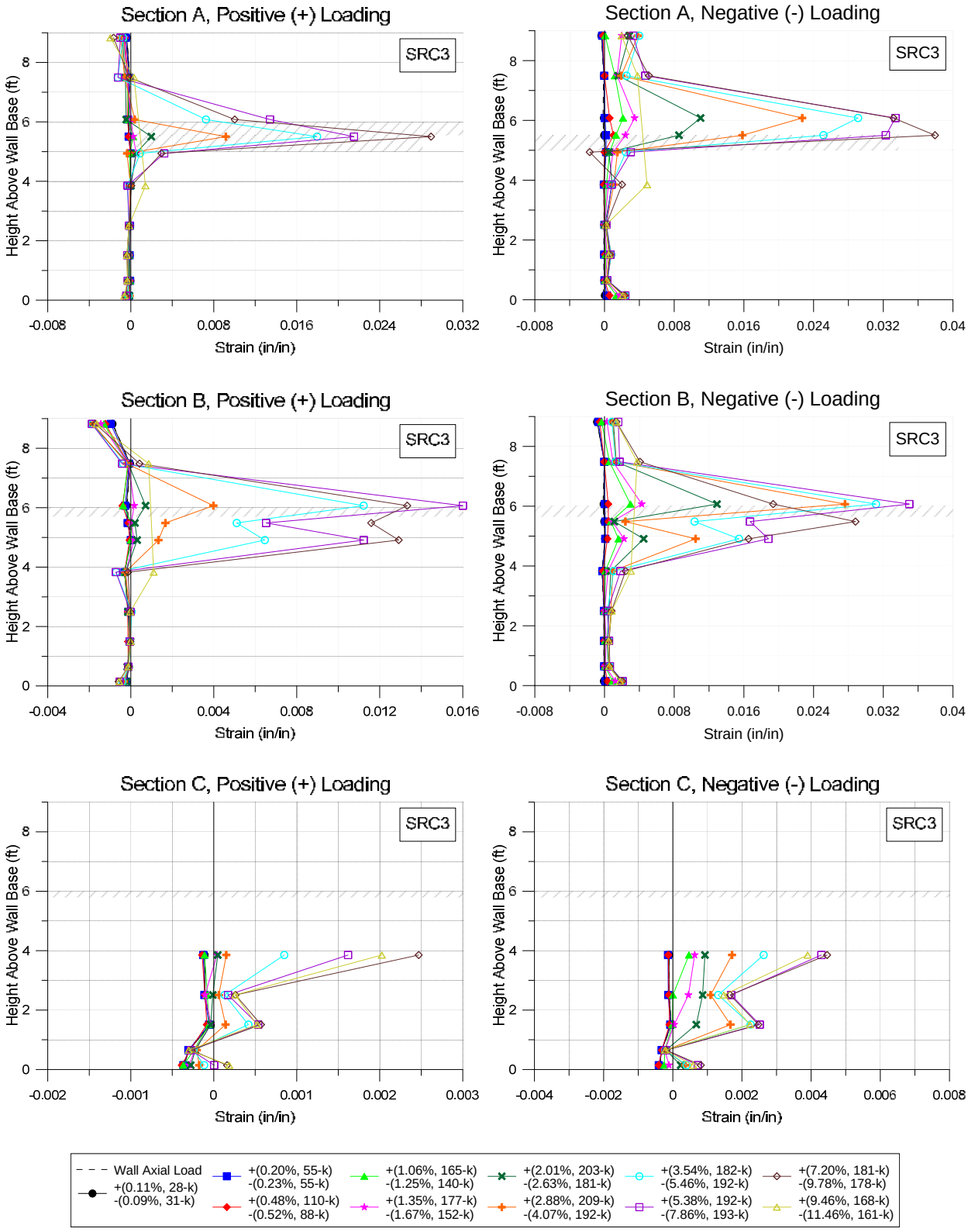

Figure 5.27: Wall Strain Profiles in Vertical Direction: c) SRC3

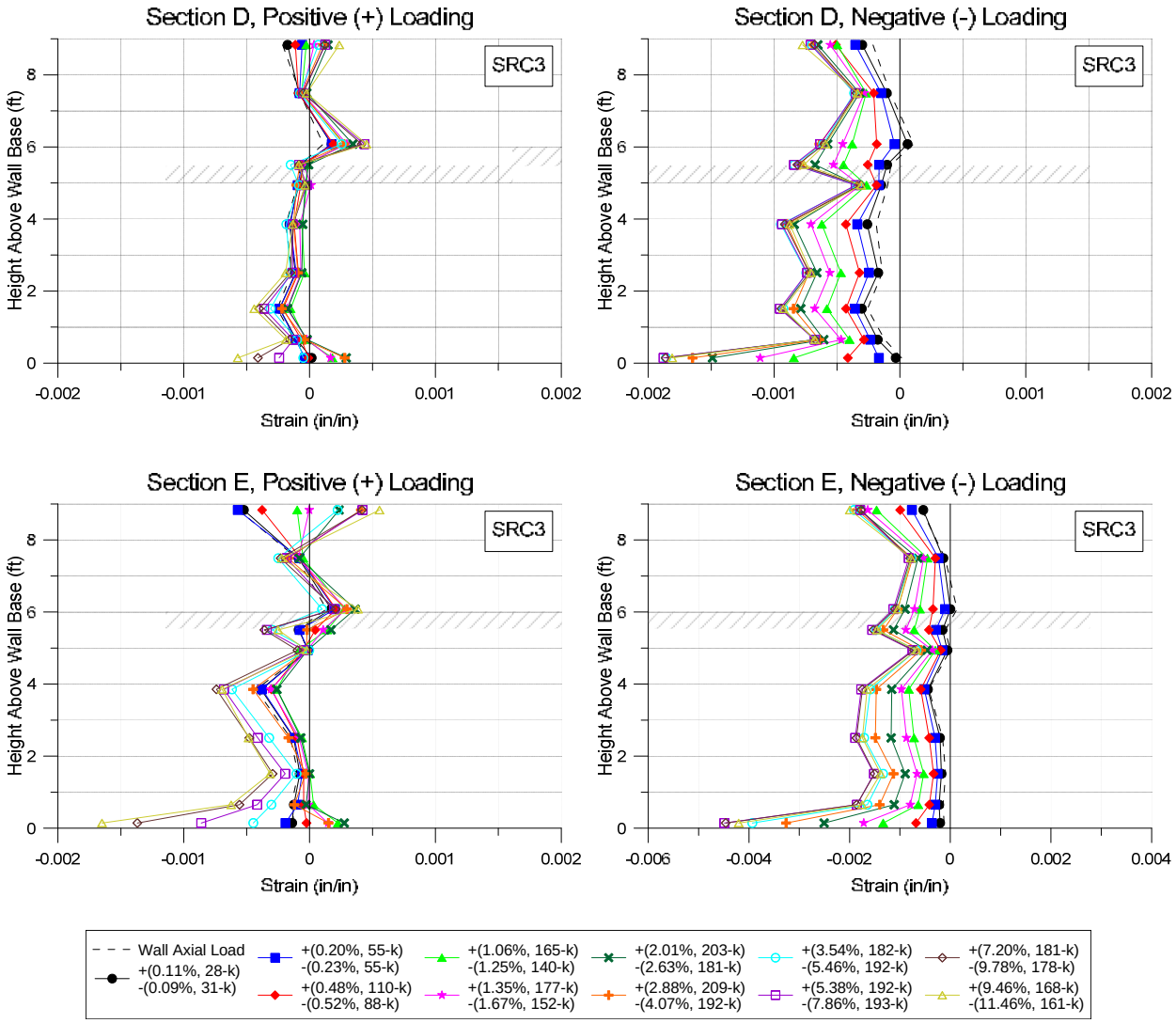

Figure 5.27: Wall Strain Profiles in Vertical Direction: c) SRC3 (Continued)

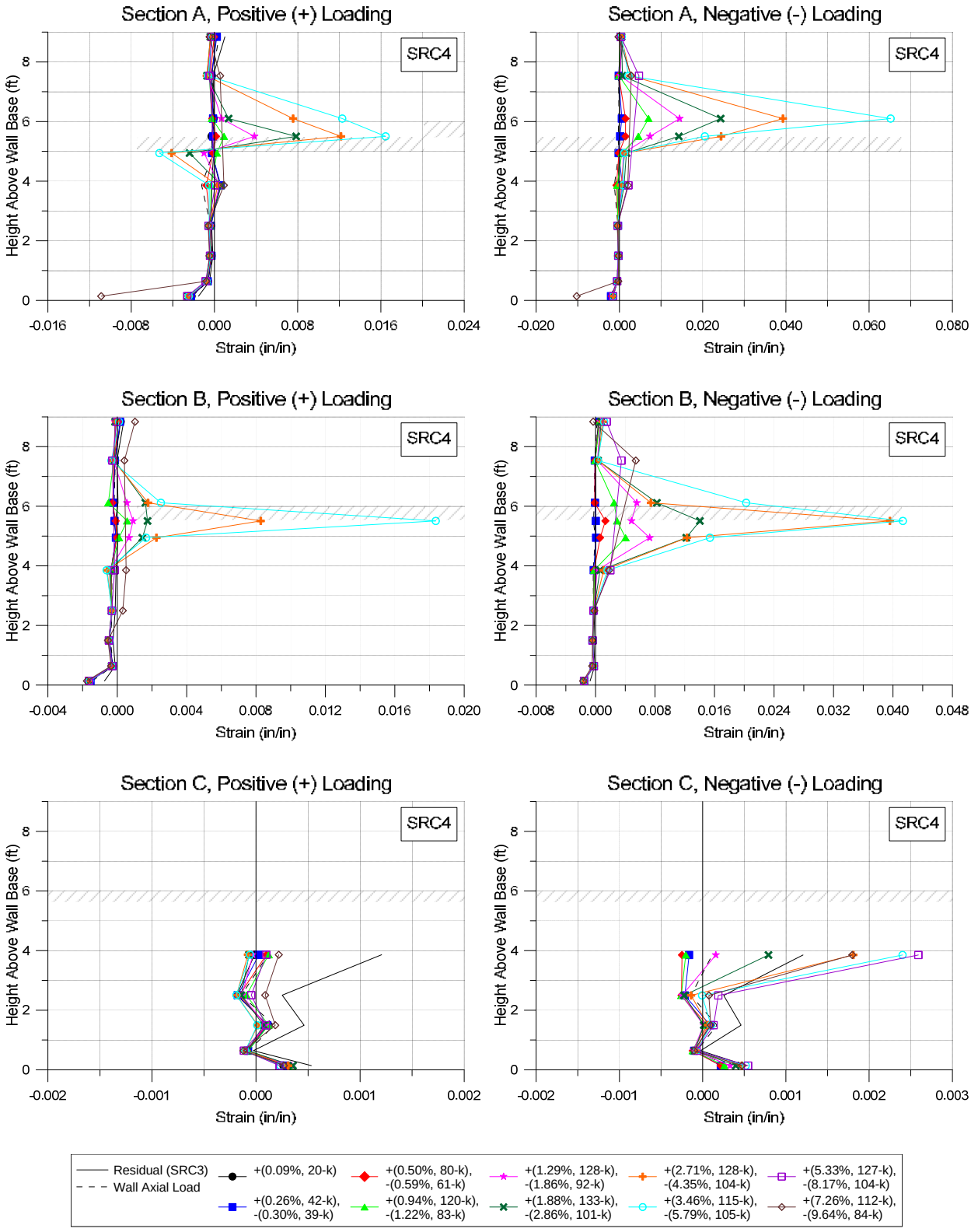

Figure 5.27: Wall Strain Profiles in Vertical Direction: d) SRC4

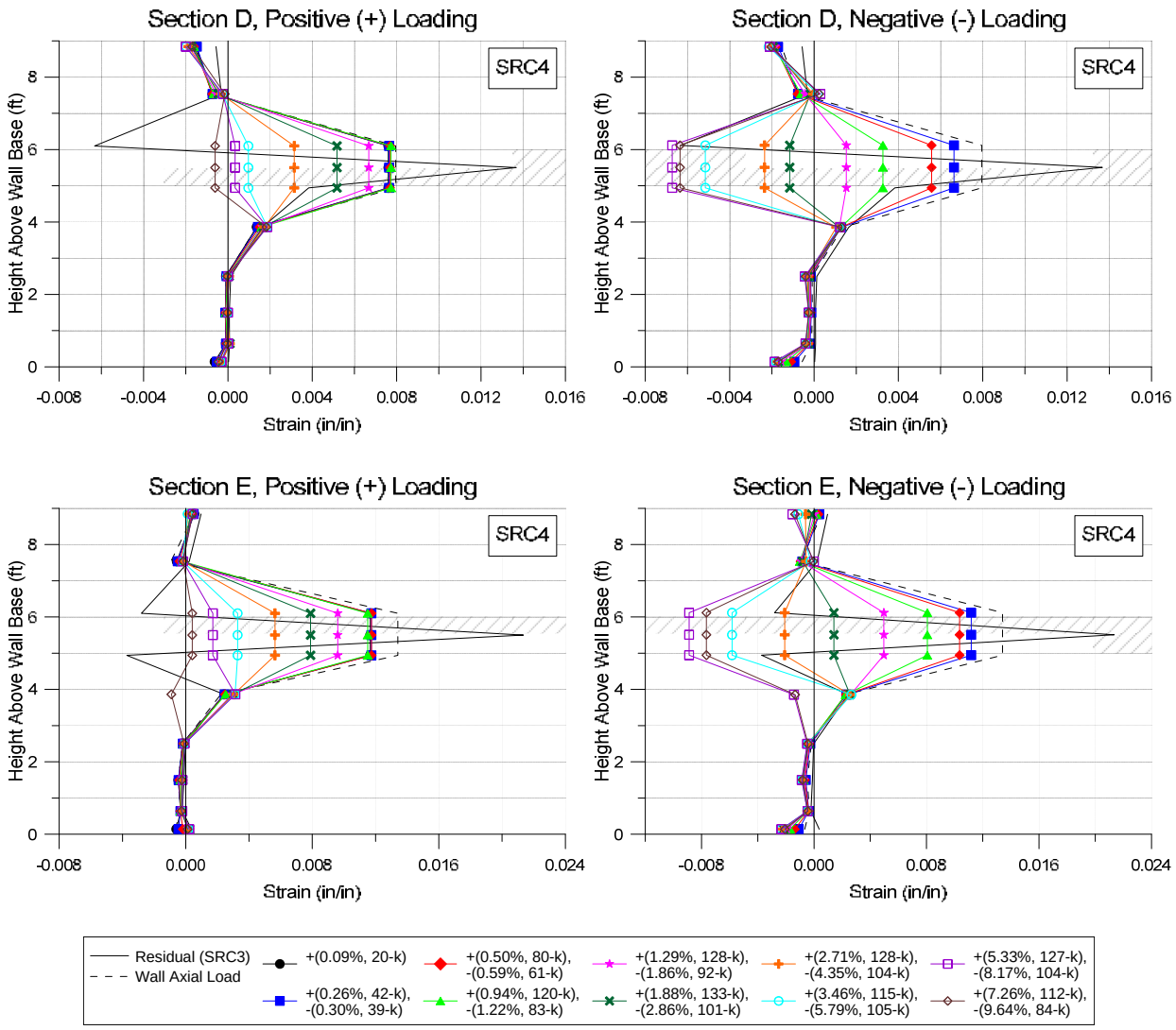

Figure 5.27: Wall Strain Profiles in Vertical Direction: d) SRC4 (Continued)

5.12 STRAIN IN WALL LONGITUDINAL REINFORCEMENT NEAR BEAMS

Figure 5.28 shows the location of the strain gages attached to wall longitudinal bars in the vicinity of the coupling beam, noting that additional gages were included for SRC3 and SRC4 that were not included for SRC1 and SRC2. For each of the four strain gages that were common to all four beams (referring to Figure 5.28), plots of the measured strain versus applied beam and wall shear loading are shown in Figure 5.29 with a comparison of the data obtained at the peak of each initial (first) cycle for each increment of load or displacement applied provided in Figure 5.30. It is evident from the data that localized wall yielding was minimal for SRC1 and SRC2 at these locations but was slightly larger for SRC3 and SRC4. However, the peak strain values in Figure 5.29 and Figure 5.30, which were less than three times the yield strain, do not indicate significant plasticity at these locations. As bar buckling and embedment damage was observed for SRC4 and, to a lesser extent, for SRC3 (Figure 5.1), the bar strains within the flanges of the embedded steel section are presumably much larger than those reflected by the plots in Figure 5.29 and Figure 5.30. It should also be noted, that many of the strain gages broke prior to the completion of testing. Therefore, strain levels could exceed the measured values in Figure 5.29 and Figure 5.30 in some instances, due to the absence of test data once strain gages had broken. The rotation levels at which the gages were broken are reflected in the plots of strain versus coupling beam chord rotation in Figure 5.30.

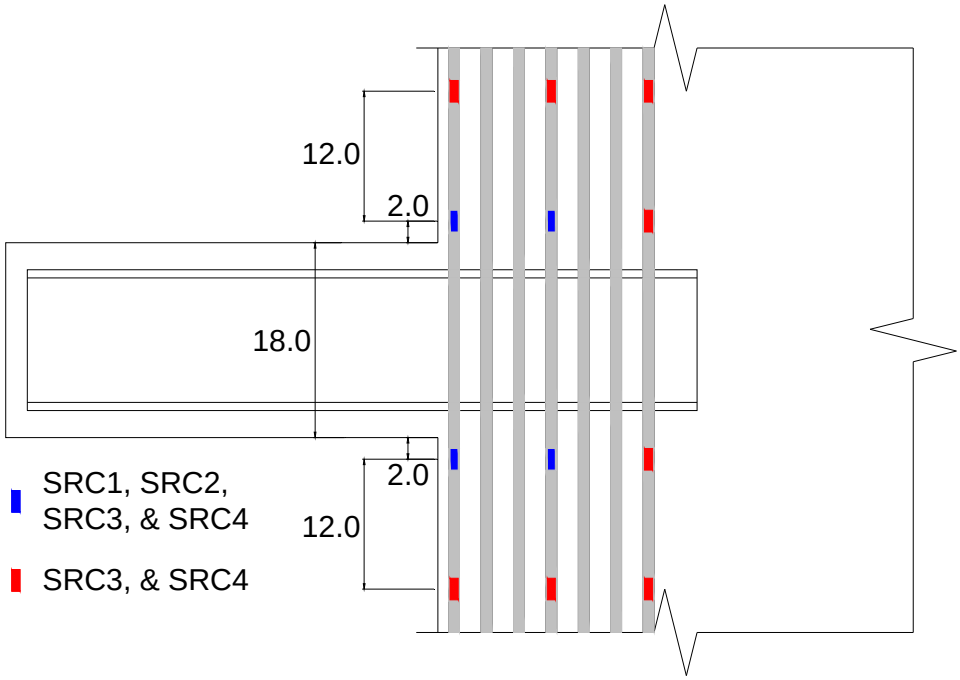

Figure 5.28: Location of Strain Gages on Wall Longitudinal Bars near Coupling Beam

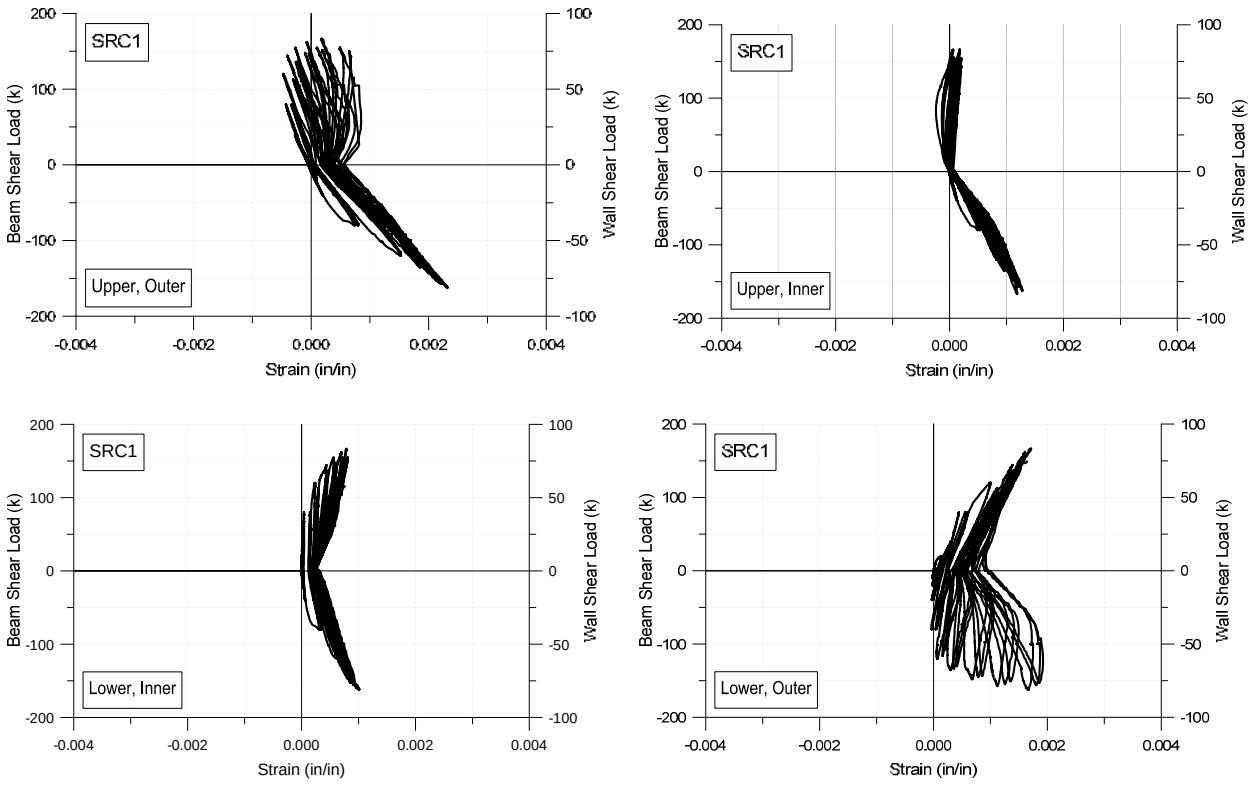

Figure 5.29: Strain in Wall Longitudinal Reinforcement near Coupling Beam: a) SRC1

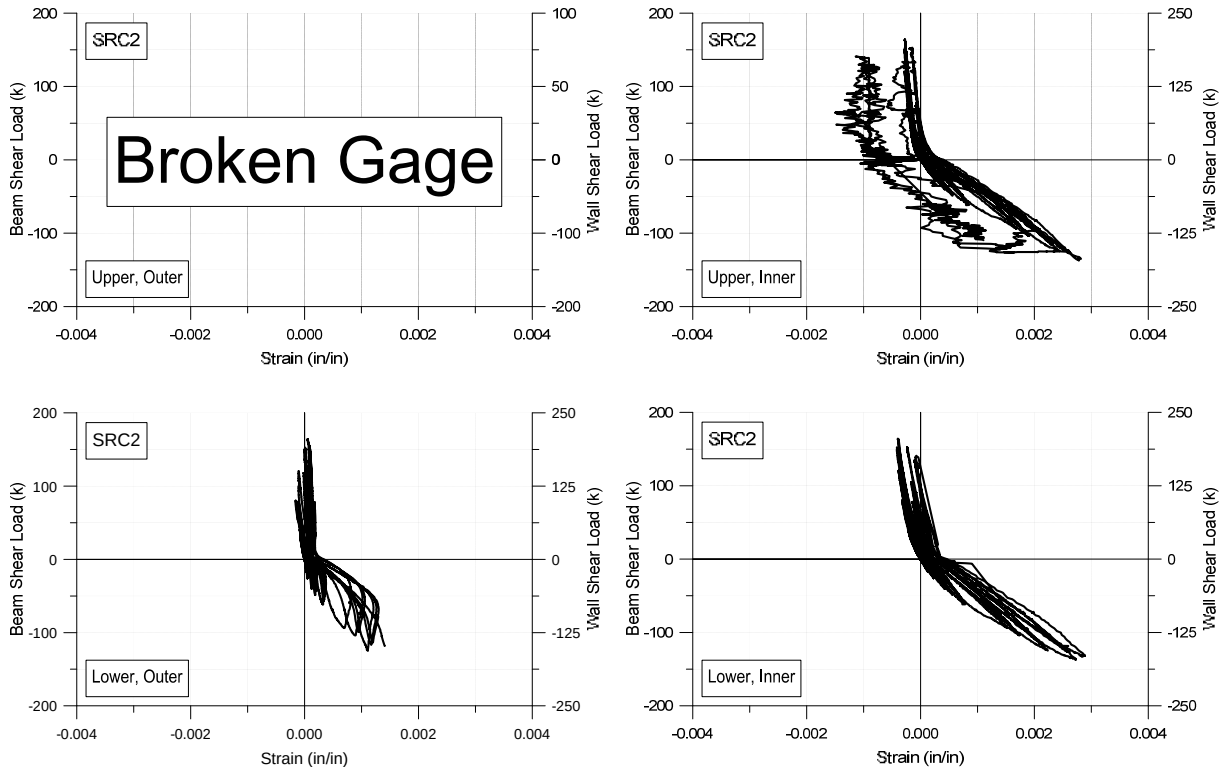

Figure 5.29: Strain in Wall Longitudinal Reinforcement near Coupling Beam: b) SRC2

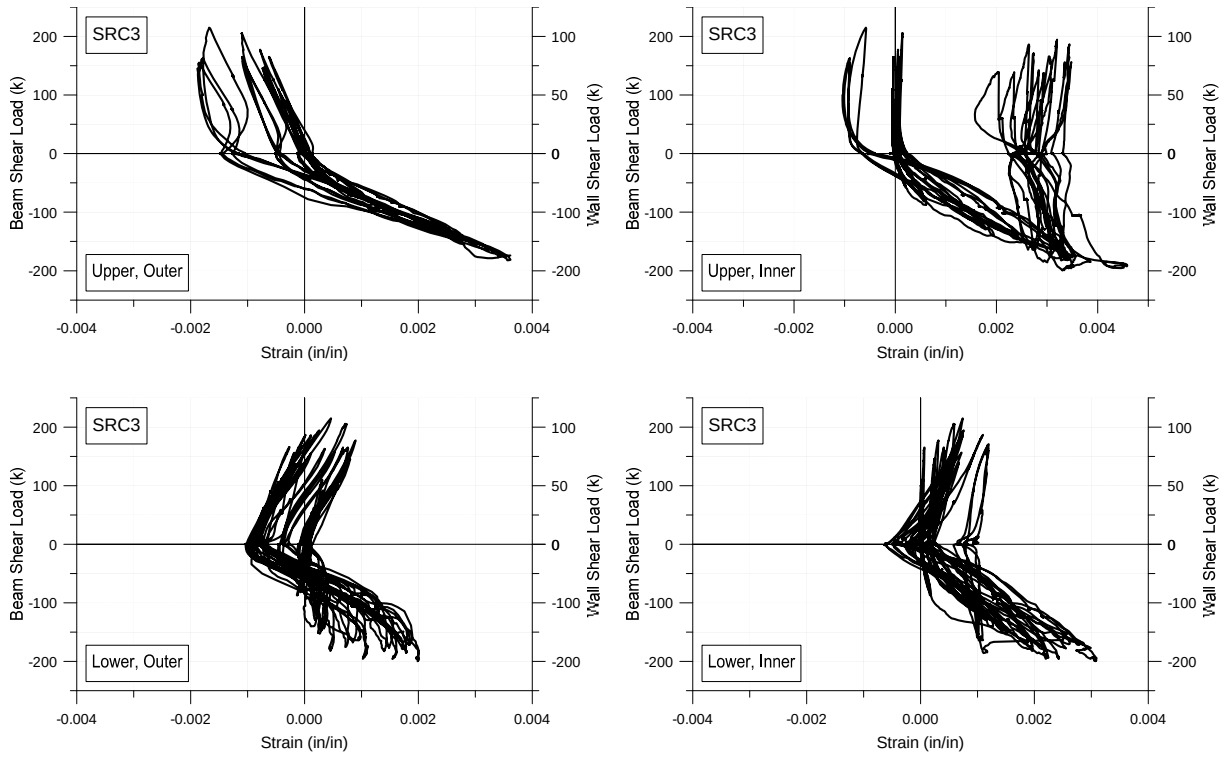

Figure 5.29: Strain in Wall Longitudinal Reinforcement near Coupling Beam: c) SRC3

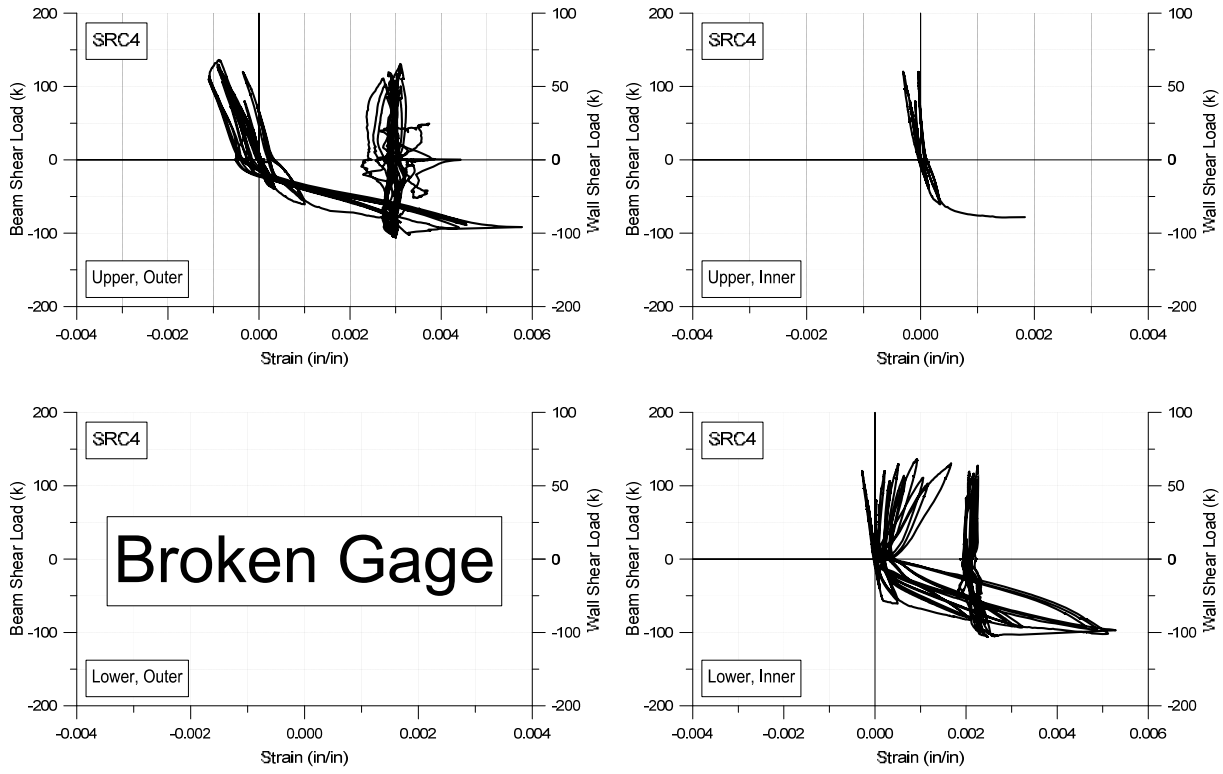

Figure 5.29: Strain in Wall Longitudinal Reinforcement near Coupling Beam: d) SRC4

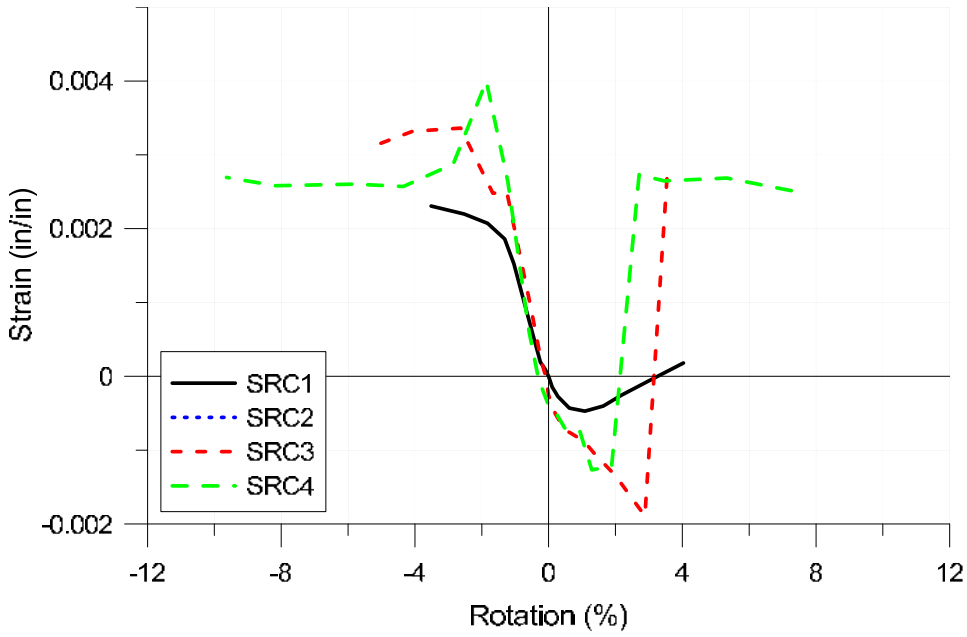

Figure 5.30: Comparison of Wall Strain for All Beams: a) Above Beam, Outer Bar

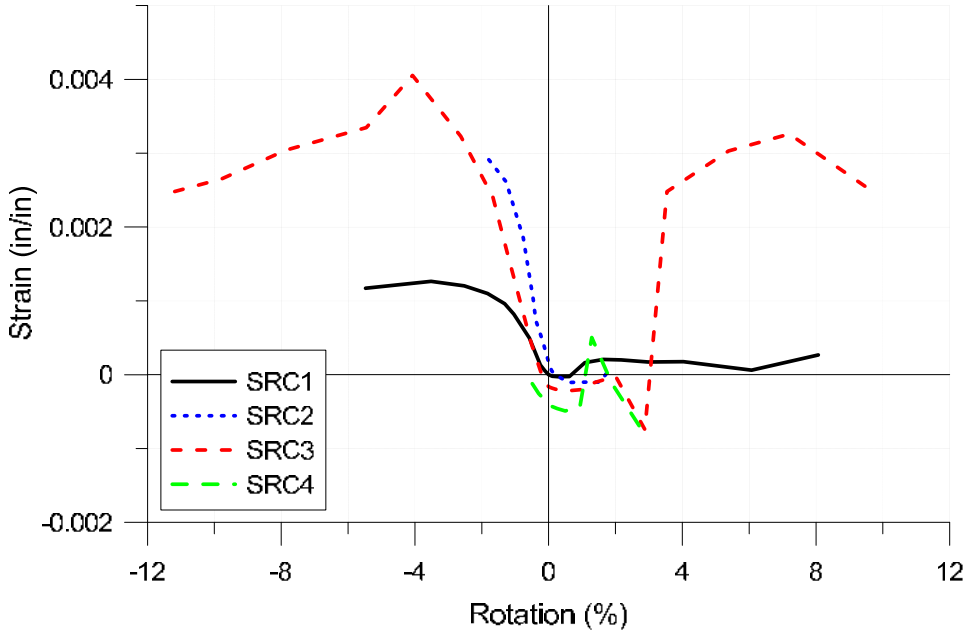

Figure 5.30: Comparison of Wall Strain for All Beams: b) Above Beam, Middle Bar

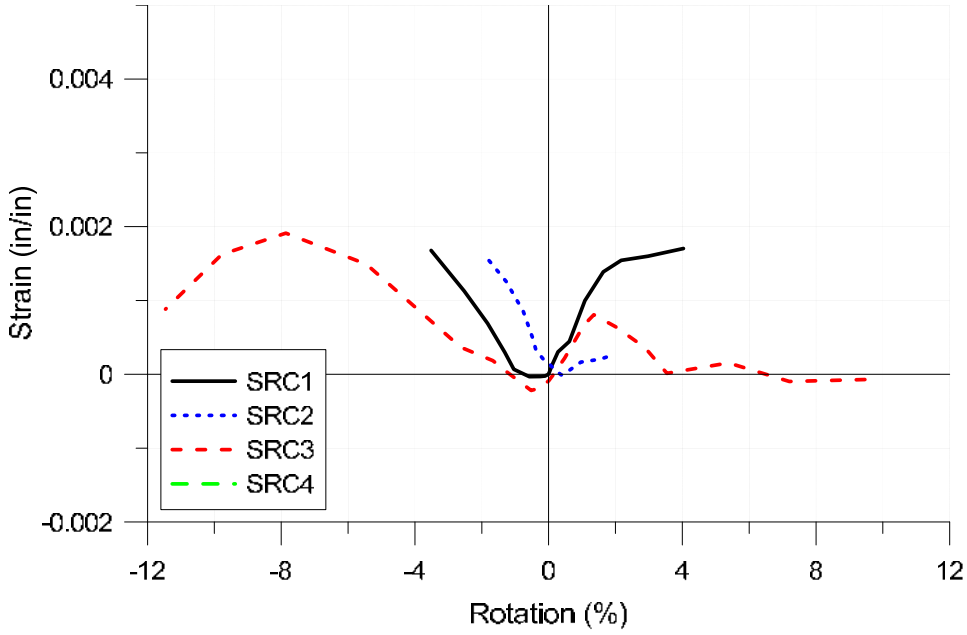

Figure 5.30: Comparison of Wall Strain for All Beams: c) Below Beam, Outer Bar

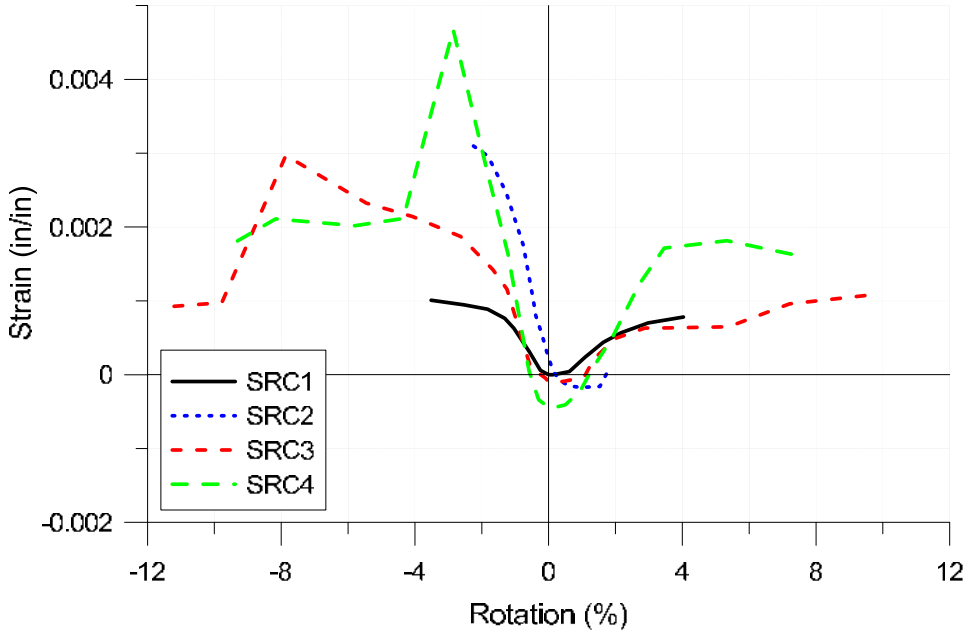

Figure 5.30: Comparison of Wall Strain for All Beams: d) Below Beam, Middle Bar

5.13 SUMMARY OF OVERALL PERFORMANCES

The performances of SRC1 and SRC2 were favorable, characterized by minimal strength degradation at large ductility demands and observed damage concentration (indicative of plastic hinge formation) at the beam-wall interface. SRC2 displayed reduced capacity in the negative loading direction due to large wall tensile demands acting normal to the embedment length. The load-displacement relationships for SRC3 and SRC4 displayed increased pinching relative to SRC1 and SRC2, and the performances of both members could likely have been improved by providing adequate embedment length. Yielding of the structural wall occurred under negative loading for both SRC3 and SRC4 due to the local demands imparted by the coupling beam bearing forces (consistent with the conceptual load path shown in Figure 3.9). The reduced capacity of SRC4 as compared to the other three test beams was the result of load path effects in combination with a significantly reduced quantity of longitudinal and transverse boundary reinforcement. It is important to note that the embedment damage observed during the latter stages of testing for SRC3 and SRC4 is undesirable, as it leads to increased pinching and reduced energy dissipation of the coupling beams and serves as an initiation point for plastic hinge formation in the structural wall.

The performance of SRC1 and SRC2 suggests that, in this particular instance, the embedment length was adequate to transfer the loads via bearing without the added benefit of additional force-transfer mechanisms. If adequate embedment length is provided and sufficient wall boundary longitudinal reinforcement is available to satisfy load paths and local tensile demands created by coupling beam bearing forces, changes to the 2010 AISC Seismic Provisions that would eliminate the need for face bearing plates and auxiliary transfer bars may be considered.

6 Recommendations for Code-Based Design

In this chapter, design and modeling recommendations for steel reinforced concrete (SRC) coupling beams, developed based on test results, are provided for code-based (prescriptive) design (i.e. for use with ASCE 7-10, ACI 318-11, and the 2010 AISC Seismic Provisions) accomplished using linear approaches such as the equivalent static procedure, response history analysis, and response spectrum analysis. Recommendations for alternative (non-prescriptive) design (i.e. for use with the LATBSDC (2014) document, SEAONC AB-083 (2007), and the PEER TBI (2010)) accomplished using linear response spectrum analysis (for either service-level or code-level design) and nonlinear response history analysis (for service-level or MCE-level design) are provided in Chapter 7. In the 2010 AISC Seismic Provisions, recommendations for steel and SRC coupling beams differ depending on whether the coupling beams are used with ordinary shear walls (satisfying ACI 318-11, excluding Chapter 21) or special shear walls (satisfying ACI 318-11, including Chapter 21). The recommendations in this chapter and Chapter 7 were developed specifically for special shear wall systems and specifically for steel reinforced concrete (SRC) coupling beams, although many of the recommendations may also apply to the design of steel coupling beams without concrete encasement. The test results of Gong and Shahrooz (2001a,b,c) were used in this chapter to aid in the development of the recommendations, noting that this experimental study was summarized in greater detail in Section 2.2.

Recommendations are provided for determining expected material properties (Section 6.1) as well as SRC coupling beam nominal and expected flexural and shear strengths (Section 6.2). Recommendations for determining embedment strength and embedment length (Section 6.3) and embedment detailing (Section 6.4) are presented, including a procedure to determine the required quantity of wall longitudinal reinforcement crossing the coupling beam embedment length. Based on the various sources of deformation measured during testing (e.g., flexure, shear, etc.), stiffness modeling recommendations were developed and compared to other testing programs (Gong and Shahrooz, 2001a,b,c) and to existing recommendations in Section 6.5.

6.1 EXPECTED MATERIAL PROPERTIES

For the code-based design recommendations provided in this chapter, expected material properties are needed to apply capacity design procedures. For alternative design recommendations in Chapter 7, expected material properties are used for all calculations. In this section, recommendations for determining the expected material properties of structural steel, reinforcement, and concrete are provided.

R_y is the ratio of the expected yield strength of structural steel, F_{ye}, to the specified minimum yield strength of structural steel, F_y. Table A3.1 in Section A3.2 of the 2010 AISC Seismic Provisions specifies R_y values for hot-rolled structural shapes as 1.1 for A992 and A572 and 1.5 for A36, which is consistent with Table 2 of the LATBSDC (2014) document and Table 7.1 of the PEER TBI (2010). It is recommended to permit the use of project-specific F_{ye} values if

material test results are available to justify the values used. Values for F_{ye} may differ for the web and the flanges of the steel section.

Table 2 of the LATBSDC (2014) document and Table 7.1 of the PEER TBI (2010) recommend determining f_{ye}, the expected yield strength of steel reinforcement, as $f_{ye} = 1.17f_y$, where f_y is the specified yield strength of steel reinforcement. Nowak et al (2008) reported mean f_{ye} / f_y values for Grade 60 reinforcement as a function of bar size. Specifically, for #4 through #14 reinforcement, the mean values for f_{ye} / f_y were between 1.12 and 1.14, and for #3 reinforcement, the mean value was 1.18. Given the lack of significant variation in these values, the use of $f_{ye} = 1.17f_y$ (and $f_{yte} = 1.17f_{yt}$ for transverse reinforcement) appears reasonable.

Table 2 of the LATBSDC (2014) document and Table 7.1 of the PEER TBI (2010) recommend determining f'_{ce}, the expected compressive strength of concrete, as $f'_{ce} = 1.3f'_c$, where f'_c is the specified compressive strength of concrete. Use of the relationships provided in Table 6.1 and Figure 6.1 (which correspond to Table 5-6 and Figure 5-7, respectively, in Nowak et al, 2008) is recommended for the determination of f'_{ce}, as Table 6.1 and Figure 6.1 indicate that the use of $f'_{ce} = 1.3f'_c$ overestimates f'_{ce}, particularly for high strength concrete. Although regional differences exist in concrete materials (e.g. aggregate), which affects the ratio of f'_{ce} to f'_c, the recommended values provided in Table 6.1 and Figure 6.1 are intended to represent average values, and the use of a larger value for f'_{ce} is only permitted if it can be demonstrated to be reliable based on project-specific material test information.

Table 6.1: Recommended Values for Expected Compressive Strength of Concrete (Nowak et al, 2008)

f'_c (ksi)	3.0	3.5	4.0	4.5	5.0	5.5	6.0	6.5	7.0	8.0	9.0	10.0	12.0
f'_{ce} / f'_c	1.31	1.27	1.24	1.21	1.19	1.17	1.15	1.14	1.13	1.11	1.1	1.09	1.08

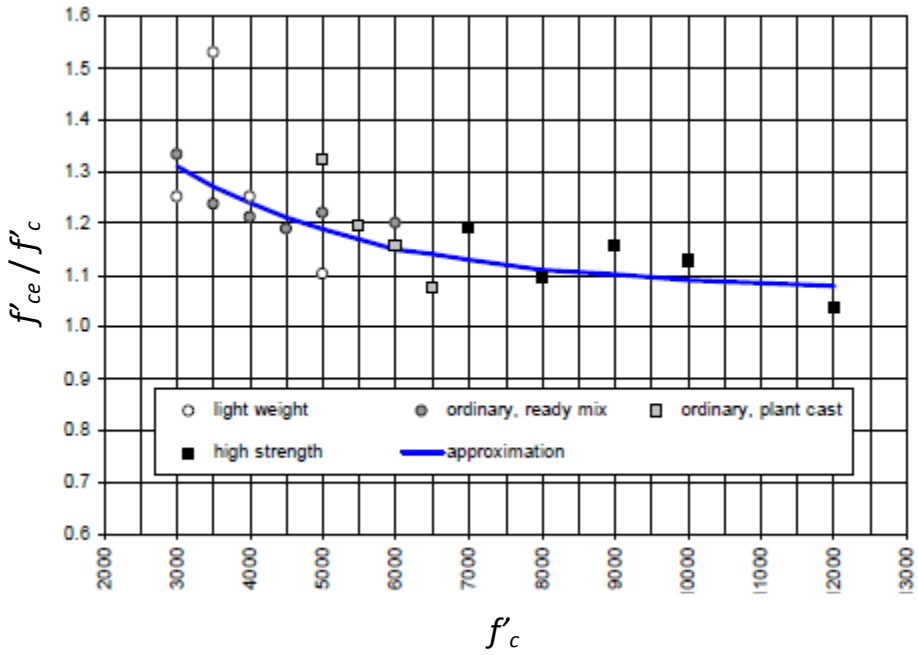

Figure 6.1: Expected Compressive Strength of Concrete (Nowak et al, 2008)

6.2 BEAM STRENGTH

The limiting shear strength, $V_{ne,limit}$, represents the expected shear force that the SRC coupling beam will develop, determined as the minimum value based on the expected shear strength, V_{ne}, and expected plastic flexural strength, M_{pe}, of the beam. The 2010 AISC Seismic Provisions provide a design equation (Equation H5-3) to compute V_{ne} of an SRC coupling beam, developed based on calibration to test results (Gong and Shahrooz, 2001a,b). The 2010 AISC Seismic

Provisions (Section H5.5d and Section H4.5b(2)(1)) require that the expected plastic flexural strength of an SRC coupling beam be determined using the plastic stress distribution or strain compatibility method, with appropriate R_y factors used for various elements of the cross-section (i.e. web, flanges). It is noted that different values will be computed using the two approaches (plastic stress distribution and strain compatibility method), and that neither method was calibrated to test results in the 2010 AISC Seismic Provisions. No recommendations for nominal shear strength, V_n, and nominal flexural strength, M_n, are provided in the 2010 AISC Seismic Provisions. A designer may be inclined to use the expected strengths (for flexure and shear) provided in the 2010 AISC Seismic Provisions as nominal values, but this approach is not recommended. Specific recommendations for nominal strengths are developed in this section.

Based on calibration to test results, recommendations for computing M_n and M_{pe} are provided in Section 6.2.1 with recommendations for computing V_{ne} and V_n provided in Section 6.2.2. When designing SRC coupling beams, expected strength is intended for use in capacity design calculations, such as embedment length (designed to exceed the peak strength of the coupling beam), whereas nominal strength is intended to provide a reliable strength over the range of chord rotations typically expected for coupling beam (i.e., up to roughly 6% chord rotation, see Equation (4.1) and discussion in Section 4.5.2).

6.2.1 Flexural Strength

Figure 6.2 provides a comparison between first-, second-, and third-cycle load-displacement backbone data and the beam shear corresponding to expected and nominal beam flexural

strengths, $V@M_{pe}$ and $V@M_n$, respectively, for all four test beams. The expected plastic flexural strength of the SRC coupling beam, M_{pe}, was computed using both a plastic analysis and a plane-strain moment-curvature analysis neglecting strain hardening of reinforcement, as the two approaches produced similar results for the cross-sections in this study. For the plastic analysis approach, the plastic steel stress was taken equal to the expected yield strength of structural steel, $F_{ye} = R_y * F_y$ (with R_y for hot-rolled structural shapes taken as 1.1 for A992 and A572 and 1.5 for A36) and a uniform magnitude (Whitney) stress block with compressive stress equal to the expected compressive strength of concrete, f'_{ce}, was used to model concrete resistance in compression. For the plane-strain moment-curvature approach, the Hognestaad (1955) stress-strain relationship was used with f'_{ce} and ϵ_0 = 0.002 (or slightly higher than 0.002, based on concrete strength exceeding 6-ksi, see Wee et al, 1996) to model concrete in compression, and an elastic-perfectly-plastic bilinear stress-strain relationship was used with F_{ye} and E_s = 29000-ksi to model structural steel. In both analytical approaches, the contribution of concrete in tension to flexural strength was neglected, and the beam longitudinal reinforcement was not included in the analysis, since this reinforcement was not developed into the wall. A sample computation for M_p is provided in Appendix B, noting that the only difference between the computation of M_{pe} and M_p is in the use of expected rather than specified material properties, i.e. $F_{ye} = R_y * F_y$ instead of F_y and f'_{ce} instead of f'_c. The $V@M_{pe}$ values shown in Figure 6.2 were computed using the plastic analysis approach rather than the strain compatibility approach, with the expected material properties based on the as-tested material properties (Section 4.1), i.e. $F_{y,test}$ instead of $F_{ye} = R_y * F_y$ and $f'_{c,test}$ instead of f'_{ce}. The relationship between M_{pe} and $V@M_{pe}$ is based on the cantilever length for the test beams and the clear span for full-length coupling beams (Figure 6.3).

Referring to Figure 6.2, the backbone curves for the test data did not exceed $V@M_{pe}$, although SRC1 approaches this value in both the positive and negative directions. Because SRC1 tested a favorable condition, characterized by low wall demands and long embedment length, which resulted in very minimal embedment damage and overall excellent performance, the capacity developed by SRC1 is a reasonable upper-bound estimate of the flexural capacity for SRC coupling beams, although it should be noted that members with larger as-tested yield strength of structural steel could develop slightly larger strength than SRC1. Computing the minimum required embedment length for flexure-yielding SRC coupling beams using $V@M_{pe}$, is recommended (i.e. providing $V_{n,embed} \geq V@M_{pe}$), as it is modestly conservative; more detailed recommendations for embedment length are provided in Section 6.3. Computing M_{pe} using a plastic analysis approach is recommended (noting that plane-strain moment-curvature approach that neglects strain hardening produced a similar result for the sections in this study). The use of a plane-strain moment-curvature approach that considers strain hardening leads to a larger computed value for expected plastic flexural strength than using a plastic analysis approach (Table 3.4), which, based on Figure 6.2, would lead to overly conservative values for determining the required embedment length. For diagonally-reinforced concrete coupling beams, it is recommended in ACI 318-11 Figure R21.9.7 that longitudinal reinforcement at the perimeter of the beam not be developed into the wall. Adhering to this guideline is recommended for SRC coupling beams in order to avoid increasing M_{pe}. Although extension of beam longitudinal reinforcement into the wall avoids discontinuity at the beam-wall interface, it is suggested here that this extension be limited to 6".

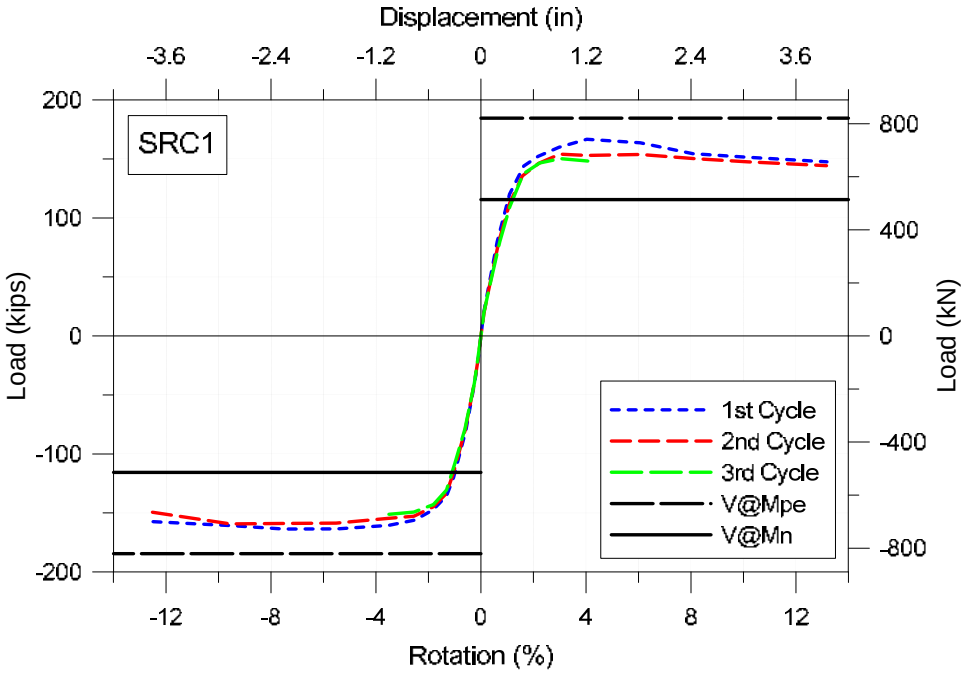

Figure 6.2: Expected and Nominal Flexural Strength: a) SRC1

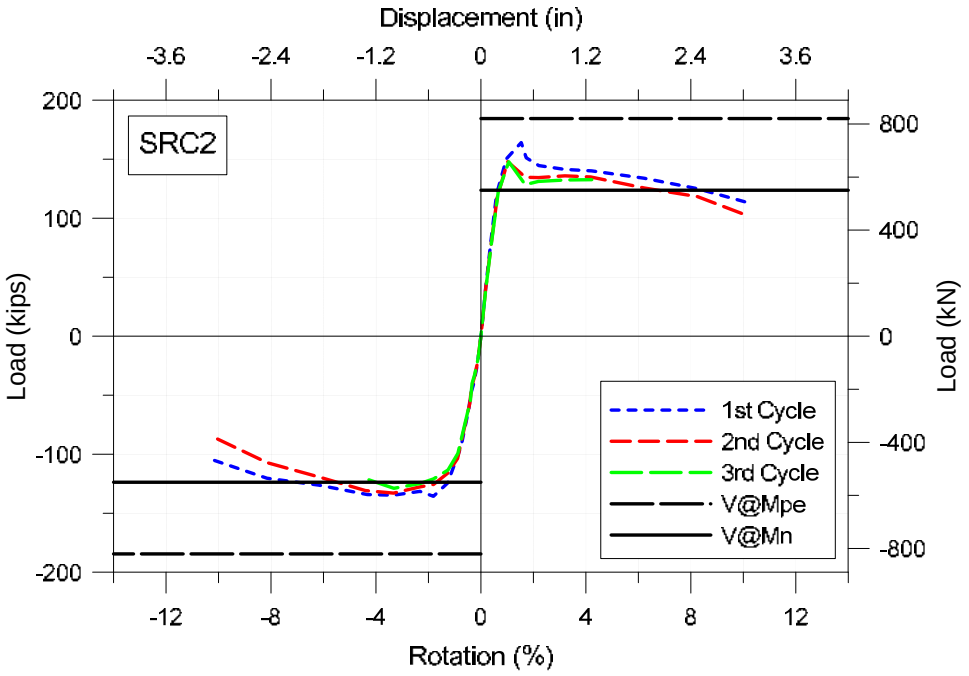

Figure 6.2: Expected and Nominal Flexural Strength to Test Data: b) SRC2

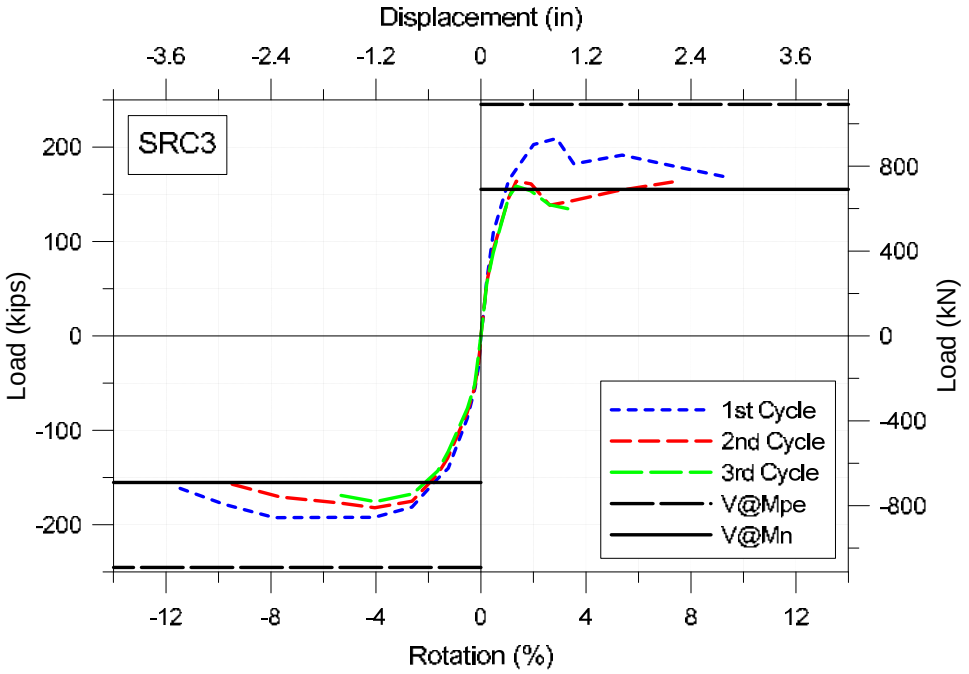

Figure 6.2: Expected and Nominal Flexural Strength: c) SRC3

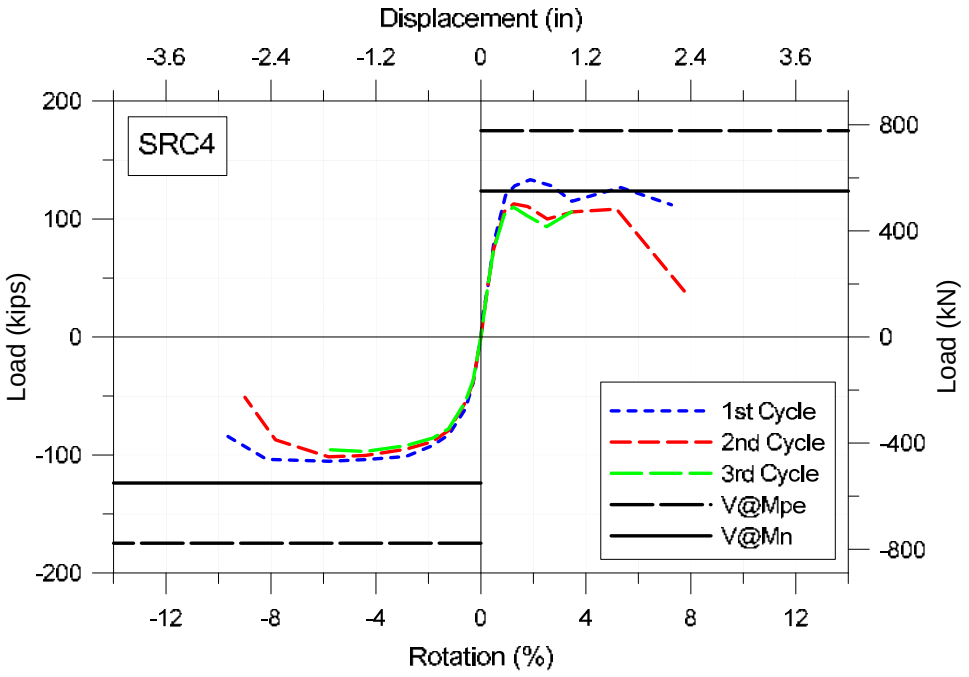

Figure 6.2: Expected and Nominal Flexural Strength: d) SRC4

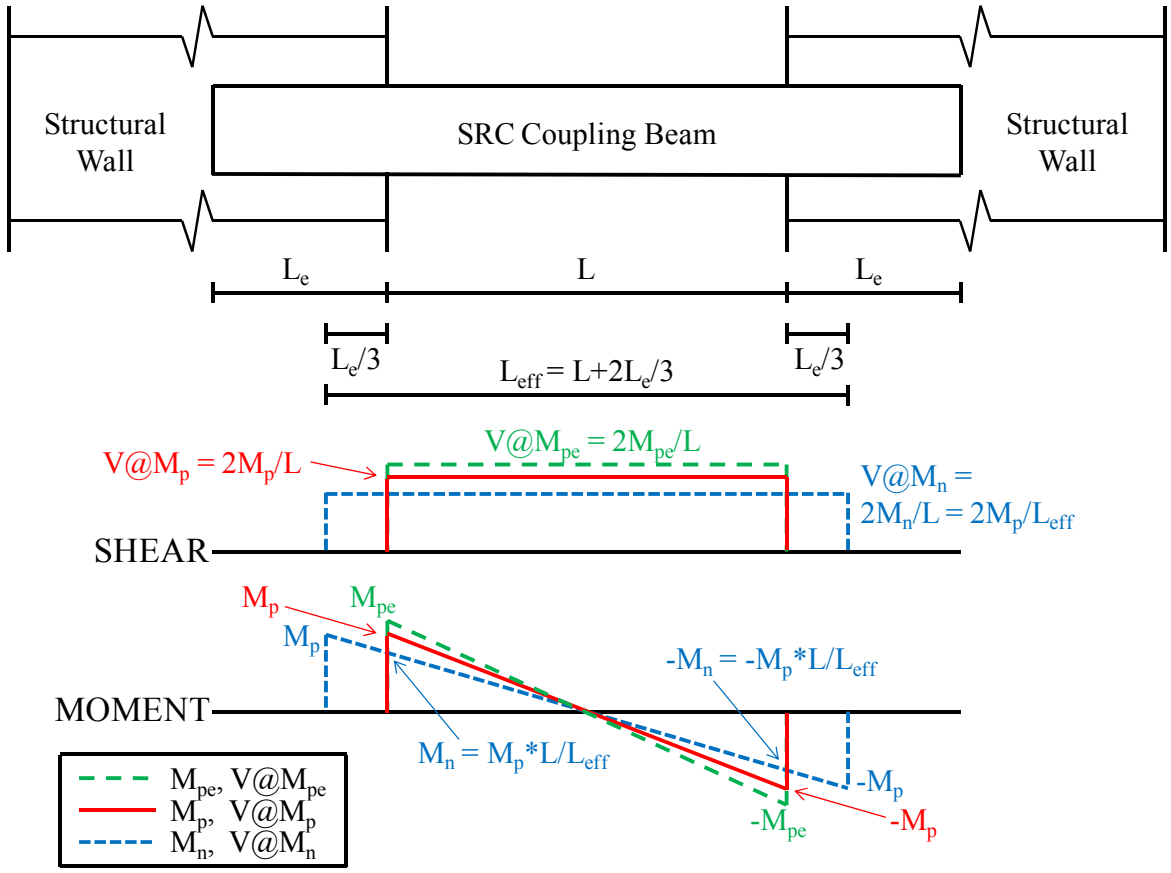

Figure 6.3: Flexural Capacities and Shear Demands

In Figure 6.2, the nominal flexural strength of the SRC coupling beam, M_n, was computed based on the modeling recommendation of Shahrooz et al (1993), in which the effective fixity for an SRC coupling beam is taken at $L_e/3$ inside the beam-wall interface. This concept was mentioned in Section 5.2 and represents the added flexibility due to the gapping between the embedded steel flange and the wall concrete in the embedment region (e.g., see Figure 5.2 and Figure 5.3). Specifically, the nominal flexural strength, M_n, is the moment value developed at the beam-wall interface when developing M_p at $L_e/3$ inside the beam-wall interface (Figure 6.3). Rather than modeling an increased coupling beam clear span (which would be cumbersome in computer programs), it is recommended here that the interface moment and corresponding beam shear be

adjusted to account for fixity at $L_e/3$ inside the interface to allow use of the actual coupling beam clear span, L. Therefore, it is recommended to compute M_n and $V@M_n$ as:

$$M_n = \left(\frac{a}{a + L_e/3} \right) * M_p = \left(\frac{L}{L_{eff} = L + 2L_e/3} \right) * M_p \quad (6.1)$$

$$V@M_n = \frac{M_n}{a} = \left(\frac{a}{a + L_e/3} \right) * V@M_p = \frac{2M_n}{L} = \left(\frac{L}{L_{eff} = L + 2L_e/3} \right) * V@M_p \quad (6.2)$$

respectively, where $a = L/2$ for one-half length cantilever test beams and L_{eff} is the effective span length.

Referring to Figure 6.2, M_n appears to reasonably estimate the strength developed over the range of rotations typically expected for coupling beams (i.e. up to roughly 6% chord rotation, as discussed in Section 4.5.2), noting that providing a full embedment length for SRC3 and SRC4, based on satisfying $V_{n,embed} \geq V@M_{pe}$, is expected to result in improved performance of these members, as the embedment limit states were exceeded during testing (Figure 5.4 and Table 5.3). The strength of SRC4, which is below the lower bound limit, was significantly limited by the reduced quantity of wall boundary longitudinal reinforcement relative to the other three beams (Table 3.1). The strength of SRC4 would be expected to exceed M_n over the range of post-yield rotations had a sufficient quantity of wall longitudinal reinforcement been provided across the embedment length; further discussion and a specific design recommendation is provided in Section 6.4.1.

Although the tests of Gong and Shahrooz (2001a,b,c) were reported to be conducted on shear-controlled specimens, comparison of the load-deformation results to the $V@M_{pe}$ recommendation developed in this section is of interest. The three beams with adequate embedment strength tested by Gong and Shahrooz (2001b) developed larger strengths than the four beams with inadequate embedment strength (2001a). All three specimens with adequate embedment strength included auxiliary transfer bars and two included face-bearing plates, one of which included a floor slab. Focusing on the two beams without the floor slab, WB1 and WB2 (WB2 with face-bearing plates), it is interesting to note that the $V@M_{pe}$ limit was exceeded by both WB1 and WB2 in the positive loading direction (Figure 6.4), noting that Gong and Shahrooz (1998) reported that some flexural yielding was observed for these shear-controlled members. It appears that the use of auxiliary transfer bars increases the strength of SRC coupling beams beyond the $V@M_{pe}$ limit defined here. The transfer bars and bearing plates likely increase the flexural strength by improving composite action of the beam, which increases the participation of concrete; therefore, use of $V@M_{pe}$ to design SRC coupling beams with auxiliary transfer bars and/or bearing plates is not recommended. It was previously shown (Table 3.4) that computing the expected plastic flexural strength using plane-strain moment-curvature analysis with inclusion of strain hardening produces a value larger than M_{pe}. Although this approach could be used to compute the expected plastic flexural strength for SRC coupling beams with transfer bars and bearing plates, there are potential issues. For example, the capacity of flexure-controlled SRC coupling beams with bearing plates and transfer bars might exceed that of shear-controlled members such as WB1 and WB2. Therefore, use of tests WB1 and WB2 to calibrate the expected plastic flexural strength might not be appropriate; additional testing of flexure-

controlled SRC coupling beams with transfer bars and bearing plates is probably needed to address this issue.

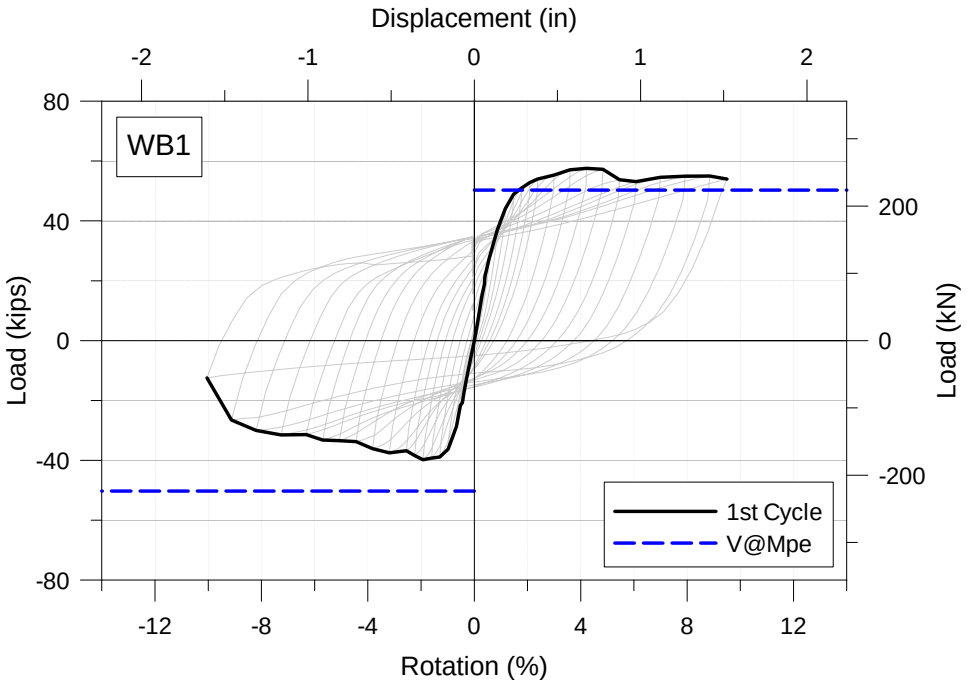

Figure 6.4: Expected plastic flexural Strength: a) WB1

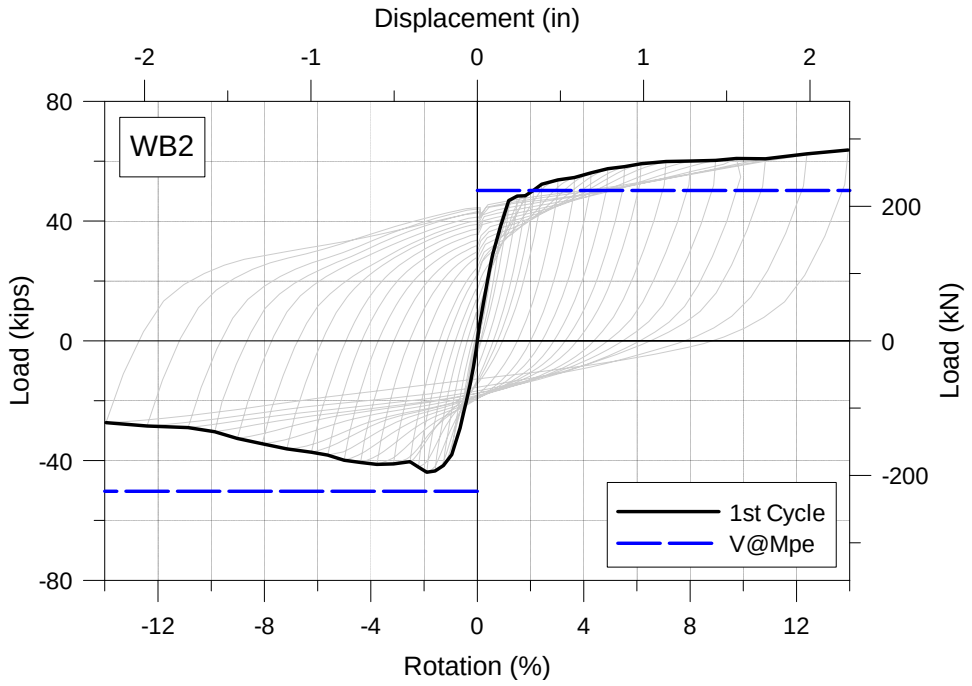

Figure 6.4: Expected plastic flexural Strength: b) WB2

6.2.2 Shear Strength

Based on an equation developed and calibrated to test results by Gong and Shahrooz (2001b), the 2010 AISC Seismic Provisions (Equation H5-3) recommend computing the expected shear strength, V_{ne}, of an SRC coupling beam as:

$$V_{ne} = 1.1 R_y V_p + 1.56\left(2\sqrt{f_c'}\, b_c d_c + \frac{A_{st} f_{yt} d_c}{s}\right) \tag{6.3}$$

where f'_c is the specified compressive strength of concrete, b_c is the beam width, i.e. the width of concrete encasement, d_c is the effective depth of concrete encasement, A_{st} is the area of

transverse reinforcement, f_{yt} is the specified yield strength of transverse reinforcement, s is the spacing of transverse reinforcement, and V_p is the nominal shear strength of the steel section, computed as $0.6F_yA_w$, where F_y is the specified minimum yield strength and A_w is the web area, taken as the product of the overall depth, d, and the web thickness, t_w. Equation (6.3) uses a combination of expected and specified material properties, which is inconsistent with common capacity design approaches used in building codes, in which expected material properties are used to determine demand and nominal material properties are used to determine capacity (e.g., ACI 318-11 for design of beam shear (Section 21.5.4.1) and joint shear (Section 21.7.2.1) for special moment frames). Therefore, it is recommended to modify Equation (6.3) as:

$$V_{ne} = 1.1R_yV_p + 1.42\left(2\sqrt{f'_{ce}}b_cd_c\right) + 1.33\left(\frac{A_{st}f_{yte}d_c}{s}\right) \quad (6.4)$$

where R_y is the ratio of the expected to specified minimum yield strength of structural steel, f'_{ce} is the expected compressive strength of concrete, and f_{yte} is the expected yield strength of transverse reinforcement. Recommendations for determining R_y, f'_{ce}, and f_{yte} were provided in Section 6.1.

The coefficient for concrete shear strength was changed from 1.56 in Equation (6.3) to 1.42 in Equation (6.4) in order to remove concrete overstrength from the coefficient, and f'_c was changed to f'_{ce} to consider overstrength for a broader range of specified concrete compressive strengths than considered in the development of Equation (6.3). The 1.56 coefficient in Equation (6.3) was developed based on a parametric study that considered f'_c = 4.0-ksi for 19 of the 24 cases analyzed and an average f'_c of 4.4-ksi (Gong and Shahrooz, 2001b); therefore, a

representative ratio of $f'_{ce} / f'_c = 1.21$ was obtained from Table 6.1 (Nowak et al, 2008) to develop Equation (6.4), i.e., $1.56/\sqrt{1.21} = 1.42$. This modification was made to address the potential overprediction of V_{ne} for higher f'_c values, which are commonly used for high-rise construction. For example, for specified concrete strength exceeding 6-ksi, the ratio f'_{ce} / f'_c is less than 1.21, and typically in the range of 1.1 to 1.2 (Table 6.1 and Figure 6.1, which correspond to Table 5-6 and Figure 5-7 in Nowak et al, 2008).

Similarly, the coefficient applied to the shear strength associated with shear reinforcement was modified from 1.56 in Equation (6.3) to 1.33 in Equation (6.4) to account for the reinforcement overstrength based on recommendations in the LATBSDC (2014) document and the PEER TBI (2010), i.e., $f_{ye} / f_y = 1.17$ (1.56/1.17 = 1.33). It should be noted that Nowak et al (2008) reported mean f_{ye} / f_y values of 1.18, 1.13, and 1.12 for #3, #4, and #5 Grade 60 reinforcement, respectively, indicating that it might be appropriate to use a slightly lower overstrength ratio for smaller bar sizes commonly used for shear reinforcement (i.e., to use $f_{yte} / f_{yt} < 1.17$). However, this refinement does not result in significant variation of V_{ne} and, thus, was not adopted here (i.e., the use of $f_{yte} / f_{yt} = 1.17$ was deemed appropriate).

Figure 6.5 provides a comparison between first-cycle load-displacement backbone data and the expected and nominal beam shear strengths for specimens WB1 and WB2, tested by Gong and Shahrooz (2001b), noting that only one loading cycle was carried out at each loading increment for these tests. In Figure 6.5, V_{ne}, which was computed using Equation (6.4) with values for R_y, f_{ye}, and f'_{ce} based on as-tested material properties, provides a reasonable estimate of the expected capacity for WB1, while slightly underestimating capacity for WB2. As the limit for V_{ne} was not

exceeded by WB2 until the imposed chord rotation in the positive loading direction exceeded 4%, this slight underestimate in strength was deemed acceptable. Additionally, it is noted that for both WB1 and WB2, the ratio V_{ne} / $V_{n,embed}$ was computed to be 0.94 based on the as-tested material properties and the provided embedment lengths. Although the embedment strength did not exceed the expected shear strength, both beams displayed excellent energy dissipation, suggesting that this method for computing V_{ne} is sufficient for computing embedment strength based on capacity design. When designing shear-controlled SRC coupling beams, providing $V_{n,embed} > V_{ne}$ is recommended; more detailed recommendations for embedment length are provided in Section 6.3.

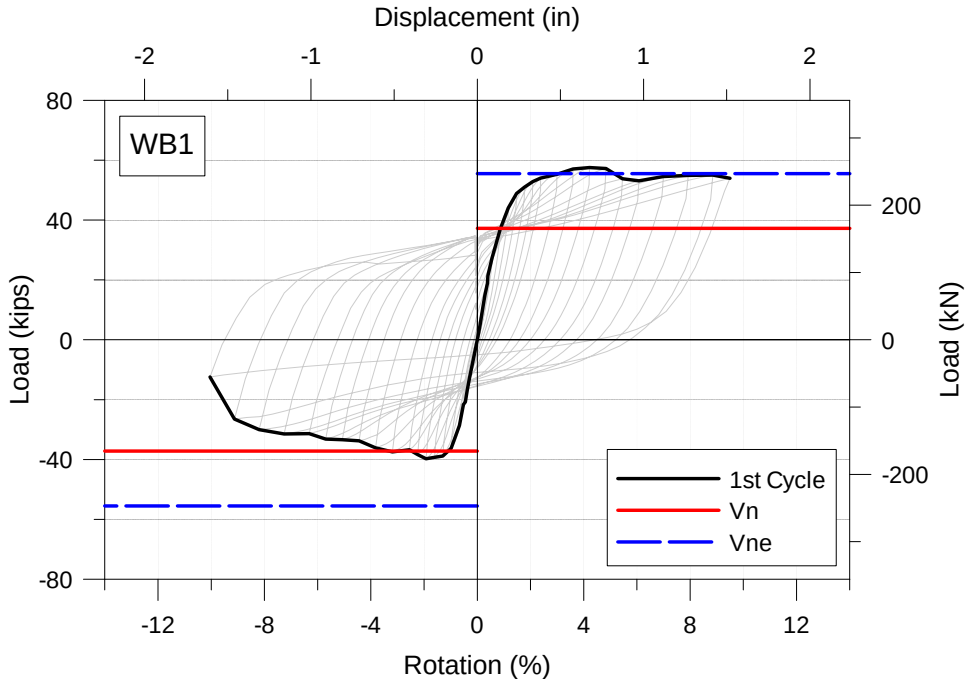

Figure 6.5: Expected and Nominal Shear Strength: a) WB1

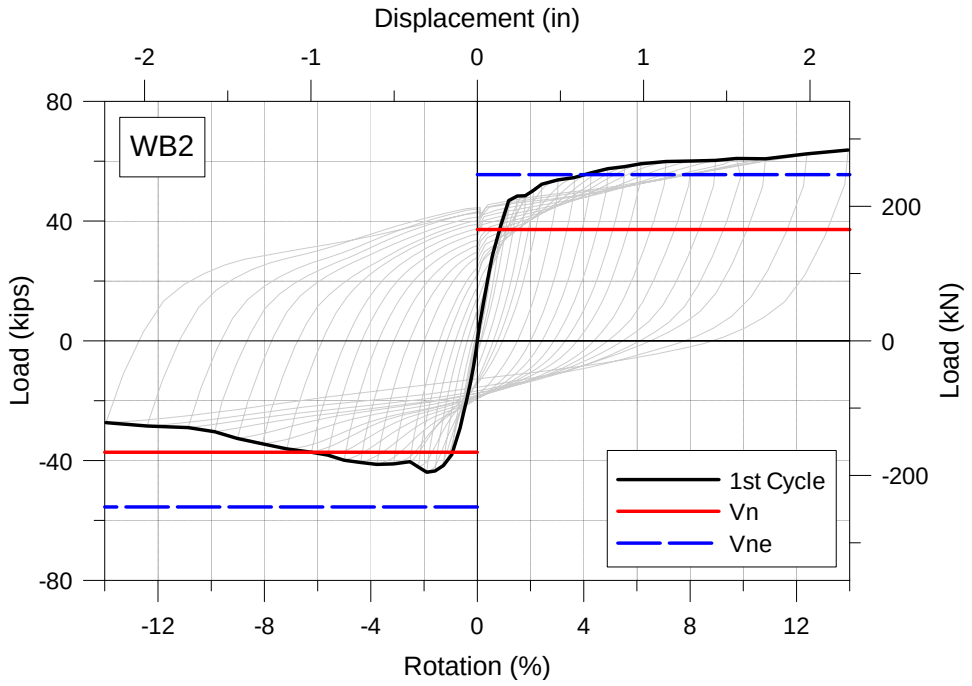

Figure 6.5: Expected and Nominal Shear Strength: a) WB2

In Figure 6.5, the nominal shear strength, V_n, was computed based on the contribution of structural steel, concrete, and transverse reinforcement to shear strength as:

$$V_n = V_p + 2\sqrt{f_c'}\,b_c d_c + \frac{A_{st} f_{yt} d_c}{s} \tag{6.5}$$

For WB2, V_n provides a reasonable estimate of reliable strength over the range of rotations typically expected for coupling beams (i.e. up to about 6% chord rotation, as discussed in Section 4.5.2). For WB1, V_n provides a slight overestimate of reliable strength for negative loading (Figure 6.5), which was deemed acceptable.

ACI 318-11 Section 21.9.7.4 describes two confinement options for diagonally-reinforced concrete coupling beams. One option is to provide transverse reinforcement enclosing each group of diagonal bars (Section 21.9.7.4(c)), and the other option is to provide transverse reinforcement for the entire beam cross-section (Section 21.9.7.4(d)). For the first confinement option, ACI 318-11 Section 21.9.7.4(c) requires that longitudinal and transverse reinforcement be distributed around the beam perimeter with total area in each direction not less than $0.002b_c s$ and spacing, s, not exceeding 12". Satisfying this requirement, which typically requires providing more than the minimum shear reinforcement required by ACI 318-11 Section 11.4.6.3, is recommended for SRC coupling beams in order to be consistent with code provisions for diagonally-reinforced coupling beams. Referring to ACI 318-11 Figure R21.9.7(a), the confined diagonal bars are essentially replaced with a steel section for SRC coupling beams without altering the detailing around the perimeter of the beam. Additionally, it is recommended that each beam longitudinal bar be of equal or larger diameter relative to the bar diameter of the transverse reinforcement (similar to a requirement in Section 21.9.7.4(d)). Developing beam longitudinal reinforcement into the wall is not recommended, consistent with ACI 318-11 Figure R21.9.7(a). It was suggested in Section 6.2.1 of this document that the extension of the beam longitudinal reinforcement into the wall be limited to 6".

6.3 EMBEDMENT LENGTH

Based on test results (Section 5.3), the embedment strength appears to be reasonably estimated using the modified Marcakis and Mitchell (1980) or modified Mattock and Gaafar (1982) embedment equations (Equation (2.22) or Equation (2.23), respectively), consistent with the

embedment model shown in Figure 2.2. It is recommended that Equation H4-2 in the 2010 AISC Seismic Provisions, which is consistent with the modified Mattock and Gaafar (1982) embedment equation (Equation (2.23)) but is more conservative due to the use of a strength reduction factor of 0.9, be used to compute the embedment strength for design purposes. This equation was presented previously as Equation (2.35), but is repeated here for convenience:

$$V_{n,embed} = 1.54\sqrt{f_c'}\left(\frac{b_w}{b_f}\right)^{0.66} \beta_1 b_f (L_e - c)\left[\frac{0.58 - 0.22\beta_1}{0.88 + \frac{L + 2c}{2(L_e - c)}}\right] \tag{6.6}$$

where $V_{n,embed}$ is the embedment strength, which is the peak beam shear load that the embedment can resist, b_w is the wall thickness, b_f is the beam flange width, L_e is the provided embedment length of the steel section into the reinforced concrete structural wall (measured from the beam-wall interface), L is the clear span, c is the wall clear cover measured from the edge of the wall to the outside of the transverse boundary reinforcement if a boundary element is present or to the outside of the outermost longitudinal reinforcement if a boundary element is not present, and β_1 is the depth factor, relating the depth of the equivalent uniform (Whitney) stress block, a_1, to the neutral axis depth, x. It is noted that f'_c is input in units of ksi to produce an output, $\sqrt{f_c'}$, in units of ksi.

Consistent with the methodology presented in the 2010 AISC Seismic Provisions (Section H5.5d and H4.5b(2)(1)), the use of a capacity design approach, in which the embedment strength ($V_{n,embed}$) is designed to meet or exceed the limiting coupling beam shear strength ($V_{ne,limit}$), is

recommended, i.e. $V_{n,embed} \geq V_{ne,limit}$. It is noted that $V_{ne,limit}$ is taken as the smaller of $V@M_{pe}$ and V_{ne} (Section 6.2). $V_{n,embed}$ is set equal to $V_{ne,limit}$ in Equation (6.6) in order to solve for the minimum required L_e, noting that iteration may be used to determine L_e. This approach, to use expected material properties to determine demand and nominal material properties to determine capacity, is consistent with the capacity design approach used in ACI 318-11 for beam shear (Section 21.5.4.1) and joint shear (Section 21.7.2.1) for special moment frames.

6.4 EMBEDMENT DETAILING

6.4.1 Wall Longitudinal Reinforcement

As discussed in Chapter 2, Section H4.5b(1)(4) of the 2010 AISC Seismic Provisions recommends providing wall vertical reinforcement across the embedment length such that $A_s f_y$ of the wall reinforcement meets or exceeds the expected peak shear demand on the coupling beam. This requirement seems inconsistent with the load path illustrated previously in Figure 3.9 (developed based on strut-and-tie modeling), which indicates that the coupling beam bearing forces (C_f and C_b in Figure 2.2) act in opposite directions. An alternative approach is suggested, where the required $A_s f_y$ is based on the coupling beam bearing forces instead of the beam shear strength. It is noted that for SRC4, and to a lesser extent for SRC3, the added local tensile demand due to the bearing forces caused yielding of longitudinal boundary reinforcement when global demands were not large enough to produce yielding (Section 5.8). This local yielding of longitudinal reinforcement crossing the embedment length led to lower beam strength and

significant pinching, strength degradation, and cyclic degradation in the force-deformation response for SRC4 and, to a lesser extent, for SRC3 (Figure 5.4).

The local increase in wall tension due to the coupling beam bearing forces (see Figure 3.9) is proportional to the smaller of the two bearing forces (see Figure 4.24 and Figure 4.25), which is always the back bearing force, C_b. Using the Mattock and Gaafar (1982) formulation of the embedment equation (i.e. assuming $x/L_e = 0.66$), the back bearing force, C_b, can be computed as (based on modification of Equation (2.16b) to account for spalling):

$$C_b = \left(\frac{\frac{(L+2c)}{2(L_e - c)} + 0.33\beta_1}{0.88 - 0.33\beta_1} \right) V_{ne,limit} \tag{6.7}$$

where β_1 is determined based on the expected compressive strength of concrete, f'_{ce}.

For SRC1, SRC2, SRC3, and SRC4, the ratio of the provided strength of wall longitudinal reinforcement crossing the embedment length to the back bearing force, $A_s f_{ye}/C_b$, was determined to be 1.49, 1.40, 0.62, and 0.26, respectively, where f_{ye} is the expected yield strength of reinforcement determined from material testing information provided in Appendix A (i.e. mill certificates). The significant pinching, strength degradation, and cyclic degradation observed in the load-deformation responses of SRC3 and SRC4 (Figure 5.4 and Figure 5.5), which were due to both inadequate embedment strength and inadequate strength of wall longitudinal reinforcement crossing the embedment length, may be greater than implied by the R-factor used for design of the lateral force-resisting system; this is probably not the case for SRC1 and SRC2.

Based on the preceding information, to ensure satisfactory performance of SRC coupling beams, it is recommended that a quantity of wall longitudinal reinforcement equal to $A_s f_y \geq C_b$ be provided across the embedment length of flexure-controlled SRC coupling beams. Note that $A_s f_y$ is based on specified material properties, while C_b is based on expected material properties, as it is typical for capacity design recommendations to require the nominal strength $A_s f_y$ to exceed a demand based on expected strengths. It is interesting to note that for SRC3, the performance of which was deemed unsatisfactory, this recommendation ($A_s f_y \geq C_b$) was not satisfied; however, the provided $A_s f_y$ does satisfy the AISC provision ($A_s f_y \geq V_{ne,limit}$). It is noted that, at upper-level stories of coupled walls, satisfying $A_s f_y \geq C_b$ may require more wall boundary longitudinal reinforcement than is required to resist design actions (P_u and M_u).

To satisfy $A_s f_y \geq C_b$, the required $A_s f_y$ may be decreased by increasing the provided embedment length, as this decreases C_b in Equation (6.7). Although longer embedment length is associated with better performance, providing additional embedment length well in excess of the required embedment length is unlikely to improve performance. Therefore, for determination of C_b using Equation (6.7), the value of L_e should not be taken greater than 1.25 times the minimum required embedment length computed using $V_{n,embed} = V_{ne,limit}$ in Equation (6.6).

The AISC provision regarding $A_s f_y$ (Section H4.5b(1)(4)) also states that at least two-thirds of the longitudinal wall reinforcement crossing the embedment length should be located between the beam-wall interface and one-half of the embedment length. This provision was not satisfied for SRC2, SRC3, or SRC4, and satisfying this provision appears unnecessary for the members tested in this study so long as the required $A_s f_y$ is provided. The 2010 AISC Seismic Provisions also

require that wall longitudinal reinforcement used to provide $A_s f_y$ extend at least one development length for f_y in tension above the top flange and below the bottom flange of the structural steel beam. It is recommended that wall longitudinal reinforcement used to satisfy $A_s f_y \geq C_b$ meet this requirement, as the intent of this requirement is to ensure that the reinforcement may develop the yield force beyond the critical sections, located at the bearing surfaces between structural steel and the surrounding concrete. It is noted that satisfying this recommendation may influence the location of bar cut-offs.

A parametric study was conducted based on 48 different beams, by varying beam cross section, beam aspect ratio, and concrete strength, in order to assess the difference in wall longitudinal reinforcement required by the new recommendation ($A_s f_y \geq C_b$) and that required by AISC ($A_s f_y \geq V_{ne,limit}$). The parameter $M@V_{ne,limit}$, which is the moment at the beam-wall interface corresponding to the development of $V_{ne,limit}$, was of interest in this study, as this parameter is a better indicator of the strength of flexure-controlled sections than $V_{ne,limit}$. The cross-sections selected for the parametric study were intended to be representative of sections typically used in practice and both normal-strength and high-strength concrete were considered. The results of the parametric study (Table 6.2) indicate that C_b / $V_{ne,limit}$ and C_b / $M@V_{ne,limit}$ are both only modestly sensitive to changes in cross-section or concrete strength, while C_b / $V_{ne,limit}$ is very sensitive to changes in aspect ratio but C_b / $M@V_{ne,limit}$ is not. A summary of the results (Table 6.3) indicates (based on comparing the ratio of C_b / $V_{ne,limit}$) that the new recommendation requires more longitudinal reinforcement on average than that required by AISC, noting that the difference increases with increasing aspect ratio. It is noted that, because most of the beams considered in formulating Table 6.2 and Table 6.3 are flexure-controlled, the ratio C_b / $V_{ne,limit}$ increases with

increasing aspect ratio, while the ratio $M@V_{ne,limit}$ / C_b is nearly constant. This nearly-constant relationship between C_b and $M@V_{ne,limit}$ suggests that using C_b rather than $V_{ne,limit}$ to determine the required strength of wall longitudinal reinforcement crossing the embedment length is appropriate for flexure-controlled beams, which are controlled by $M@V_{ne,limit}$ rather than $V_{ne,\ limit}$.

Table 6.2: Results of Parametric Study on Wall Longitudinal Reinforcement

Cross-Section	f'_c (ksi)	M_{pe} (k-ft)	V_{ne} (k)	α	$V@M_{pe}$ (k)	$V_{ne,limit}$ (k)	L_e (in.)	C_b (k)	C_b / $V_{ne,limit}$	C_b / $M@V_{ne,limit}$
24.0 x 33.0 (c = 1.5) with W24x250 with #4 hoops at 6" spacing	4	3951	1330	1.75	1642	1330	84	1440	1.08	0.45
				2.40	1197	1197	84	1561	1.30	0.39
				3.33	863	863	73	1540	1.78	0.39
				4.00	718	718	69	1540	2.14	0.39
	8	4124	1379	1.75	1714	1379	75	1300	0.94	0.39
				2.40	1250	1250	76	1445	1.16	0.35
				3.33	901	901	66	1466	1.63	0.36
				4.00	750	750	63	1482	1.98	0.36
21.0 x 30.0 (c = 1.5) with W21x182 with #4 hoops at 6" spacing	4	2562	972	1.75	1171	972	70	1108	1.14	0.52
				2.40	854	854	69	1189	1.39	0.46
				3.33	615	615	61	1178	1.91	0.46
				4.00	512	512	57	1179	2.30	0.46
	8	2680	1010	1.75	1225	1010	63	1009	1.00	0.46
				2.40	893	893	63	1110	1.24	0.41
				3.33	644	644	56	1127	1.75	0.42
				4.00	536	536	53	1140	2.13	0.43
18.0 x 28.0 (c = 1.5) with W21x93 with #4 hoops at 6" spacing	4	1272	706	1.75	623	623	59	758	1.22	0.60
				2.40	454	454	52	743	1.63	0.58
				3.33	327	327	46	740	2.26	0.58
				4.00	273	273	44	742	2.72	0.58
	8	1342	737	1.75	657	657	54	701	1.07	0.52
				2.40	479	479	47	706	1.47	0.53
				3.33	346	346	43	718	2.08	0.54
				4.00	288	288	41	726	2.52	0.54
20.0 x 27.0 (c = 1.5) with W18x175 with #4 hoops at 6" spacing	4	2136	898	1.75	1085	898	68	986	1.10	0.56
				2.40	791	791	67	1056	1.34	0.49
				3.33	570	570	58	1043	1.83	0.49
				4.00	475	475	55	1043	2.20	0.49
	8	2240	931	1.75	1138	931	61	892	0.96	0.49
				2.40	830	830	61	983	1.19	0.44
				3.33	598	598	53	997	1.67	0.44
				4.00	498	498	51	1008	2.02	0.45

Table 6.2: Results of Parametric Study on Wall Longitudinal Reinforcement (Continued)

Cross-Section	f'_c (ksi)	M_{pe} (k-ft)	V_{ne} (k)	α	$V@M_{pe}$ (k)	$V_{ne,limit}$ (k)	L_e (in.)	C_b (k)	C_b / $V_{ne,limit}$	C_b / $M@V_{ne,limit}$
16.0 x 26.0 (c = 1.5) with W18x71 with #4 hoops at 6" spacing	4	869	555	1.75	459	459	51	592	1.29	0.68
				2.40	334	334	44	582	1.74	0.67
				3.33	241	241	40	581	2.41	0.67
				4.00	201	201	38	582	2.90	0.67
	8	923	581	1.75	487	487	46	552	1.13	0.60
				2.40	355	355	41	557	1.57	0.60
				3.33	256	256	37	567	2.21	0.61
				4.00	213	213	35	573	2.69	0.62
12.0 x 18.0 (c = 0.75) with W12x96 * with #2 hoops at 3" spacing	4	431	331	1.75	328	328	44	361	1.10	0.84
				2.40	239	239	38	351	1.47	0.81
				3.33	172	172	34	349	2.02	0.81
				4.00	144	144	32	349	2.43	0.81
	8	460	345	1.75	350	345	40	328	0.95	0.73
				2.40	255	255	35	332	1.30	0.72
				3.33	184	184	31	338	1.84	0.73
				4.00	153	153	30	342	2.23	0.74

* flanges trimmed to 5.5" width

Table 6.3: Summary of Results of Parametric Study on Wall Longitudinal Reinforcement

Aspect Ratio, α	C_b / $V_{ne,limit}$					C_b / $M@V_{ne,limit}$ (ft^{-1})				
	Min.	Max.	Mean	Standard Deviation	Coefficient of Variation	Min.	Max.	Mean	Standard Deviation	Coefficient of Variation
1.75	0.94	1.29	1.08	0.11	0.10	0.39	0.84	0.57	0.13	0.23
2.40	1.16	1.74	1.40	0.18	0.13	0.35	0.81	0.54	0.15	0.27
3.33	1.63	2.41	1.95	0.25	0.13	0.36	0.81	0.54	0.15	0.27
4.00	1.98	2.90	2.36	0.30	0.13	0.36	0.81	0.55	0.15	0.27

It should be noted that the tests in this study (SRC1, SRC2, SRC3, and SRC4), which were the basis for the development of the new recommendation ($A_s f_y \geq C_b$), considered a more critical wall-loading condition (i.e. with cyclic wall loading) than the tests of Harries et al (1993) and Harries et al (1997), which were the basis for the development of the AISC recommendation ($A_s f_y \geq V_{ne,limit}$). Harries (1995) developed the recommendation for $A_s f_y \geq V_{ne,limit}$ based on the results of four laboratory tests (Harries et al, 1993, and Harries et al, 1997) conducted on steel coupling beams without concrete encasement embedded into wall segments that were post-tensioned to loading beams. The post-tensioning of the wall segments created compression normal to the length of the embedded steel section, improving load-transfer between the beam and the wall. The testing procedure used for the specimens in this study included the application of reversed-cyclic loading to a wall panel with embedded SRC beams. This loading approach created alternating (cyclic) tension and compression normal to the embedment length (Figure 1.5). Because the transfer of coupling beam bearing forces into wall reinforcement creates local tensile demands, the more critical loading condition occurs when the wall demands create tension normal to the connection (Figure 3.9). As the tests conducted by Harries et al (1993) and Harries et al (1997) did not include a cyclically-loaded wall, the development of the $A_s f_y > V_{ne,limit}$ recommendation was based on tests that did not consider this critical load-transfer condition.

It is interesting to consider the results of carrying out a code-based design for the beams tested in this study, following the recommendations provided in Section 6.1 through Section 6.4.1 and assuming that the as-tested material properties were not reliably known (i.e. following recommendations in Section 6.1). Using the cross-section of the four beams tested in this study with f'_c = 4.5-ksi and F_y = 50-ksi leads to M_{pe} = 435.1 k-ft ($V_{ne,limit} = V@M_{pe}$ since all members

are flexure-controlled), leading to minimum required embedment lengths of 33.7" and 38.1" for members with aspect ratios of 3.33 and 2.4, respectively ($V_{n,embed} = V_{ne,limit} = V@M_{pe}$ = 174.1-k and 241.7-k, respectively). Based on the configuration of wall longitudinal reinforcement and the size of the web bars (Figure 3.5 and Figure 3.6), i.e., 14 boundary bars with 3" center-to-center spacing and #3 web bars with 6" center-to-center spacing, the longitudinal boundary bars must be #6 or larger (which was satisfied for SRC1 and SRC2, but not SRC3 and SRC4) to satisfy $A_s f_y \geq C_b$, noting that C_b = 332.2-k and C_b = 331.5-k for aspect ratios of 3.33 and 2.4, respectively.

6.4.2 Wall Boundary Transverse Reinforcement

For taller buildings that utilize Special Structural Walls per ACI 318-11, boundary transverse reinforcement satisfying Section 21.9.6.4 (where special boundary elements, or SBEs, are required), is typically provided only near the wall base where moment and axial load demands on the wall tend to produce the highest stresses and strains. Above this region, wall boundary transverse boundary reinforcement need only satisfy Section 21.9.6.5 (or OBEs). Per Section 21.9.6.5, if the wall boundary longitudinal reinforcement ratio, $\rho_{bound} > 400/f_y$, where f_y is the specified yield strength of this reinforcement in units of psi, then modest detailing must be provided with vertical spacing of hoops and crossties limited to a maximum of 8 in. (200 mm) on center. For ACI 318-14, Section 18.10.6.5 (equivalent to 21.9.6.5 in ACI 318-11), the 8 in. limit will be modified to be the smaller of 8 in. and $8d_b$, except at yielding sections above the well-detailed (plastic hinge) region near the wall base, where the limit will be reduced to 6 in. and $6d_b$. It is recommended that these new limits be satisfied. Where the wall boundary longitudinal

reinforcement ratio, $\rho_{bound} \leq 400/f_y$, hoops and crossties need not be provided, and horizontal web reinforcement is typically lapped with U-bars at the wall boundary.

For SRC coupling beams, it is recommended that wall boundary transverse reinforcement in the embedment region be provided in accordance with ACI 318-11 Section 21.9.6.4 (SBE) or Section 21.9.6.5(a), as modified by (b). Until further testing indicates that doing so is unnecessary, it is recommended that the detailing requirements of Section 21.9.6.5(a) be satisfied for cases in which $\rho_{bound} \leq 400/f_y$. In other words, the use of OBEs or SBEs in the embedment region is recommended for all SRC coupling beams. For cases in which OBEs are not required in the wall ($\rho_{bound} \leq 400/f_y$), it is recommended that the OBEs or SBEs used in the embedment region extend at least one coupling beam embedment length (L_e) above and below the top and bottom flanges, respectively, of the embedded steel section. For constructability, providing OBEs or SBEs over the full story height where SRC coupling beams are used is suggested.

As noted in Section 3.5, the use of conventional wall boundary transverse reinforcement at the location of an embedded steel section is not practical due to the construction-related difficulties associated with passing hoops and cross-ties (with seismic hooks) through the web of the steel section. The detail shown previously in Figure 3.10, in which holes were pre-drilled through the web of the steel section to allow the use of threaded rods and steel plates to provide an equivalent $A_{st}f_{yt}$ and spacing of transverse boundary reinforcement through the embedment region (for the specified yield strength values of the plate and rods), was used for the test specimens in this study.

Detailing requirements for conventional rebar hoops and cross-ties require the use of 135-degree hooks, which engage both sides of wall boundary longitudinal bars in the plane of the wall. As the threaded rods used for boundary transverse reinforcement in this study (Figure 3.10) engage only one side of the wall boundary longitudinal bars in the plane of the wall, conventional rebar hoops and cross-ties offer potentially better restraint against buckling of wall boundary longitudinal bars in the plane of the wall. To provide roughly equivalent restraint against buckling of wall boundary longitudinal bars in the plane of the wall, use of a detail such as that shown in Figure 6.6a, where short-length threaded rods are used to provide additional restraint against bar buckling, is suggested as one option. Use of the detail shown in Figure 6.6b further improves restraint against bar buckling by engaging every longitudinal bar rather than every other longitudinal bar (Figure 6.6a). Note that adding a plate along the inside of the wall boundary longitudinal bars (Figure 6.6c) could improve the stability of the short-length threaded rods. As an alternative to using side plates and threaded rods, pre-drilled holes through the embedded flanges of the steel section enable the installation of short-length threaded rods which span between the flanges and allow the use of conventional rebar hoop and cross-tie detailing (Figure 6.6d). Note that any alternative detailing approach that provides concrete confinement and restraint against rebar buckling that is equivalent to, or better than, that provided by conventional rebar hoops and crossties is acceptable for design purposes.

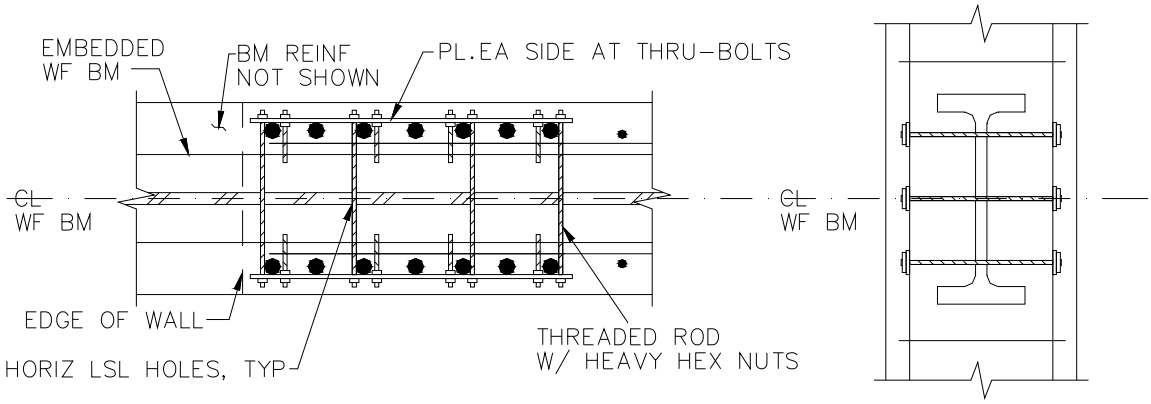

Figure 6.6: Alternative Embedment Detailing: a) Buckling Restraint of Every Wall Boundary Longitudinal Bar

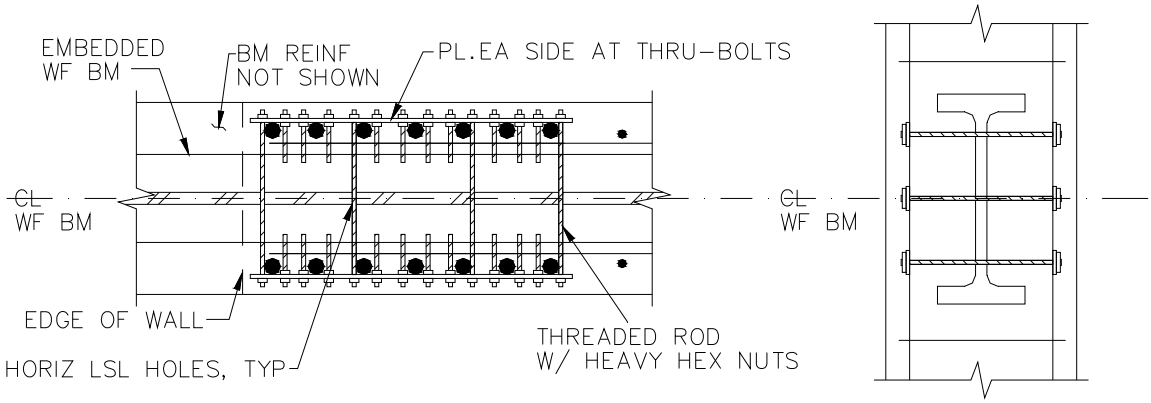

Figure 6.6: Alternative Embedment Detailing: b) Buckling Restraint of Every Wall Boundary Longitudinal Bar

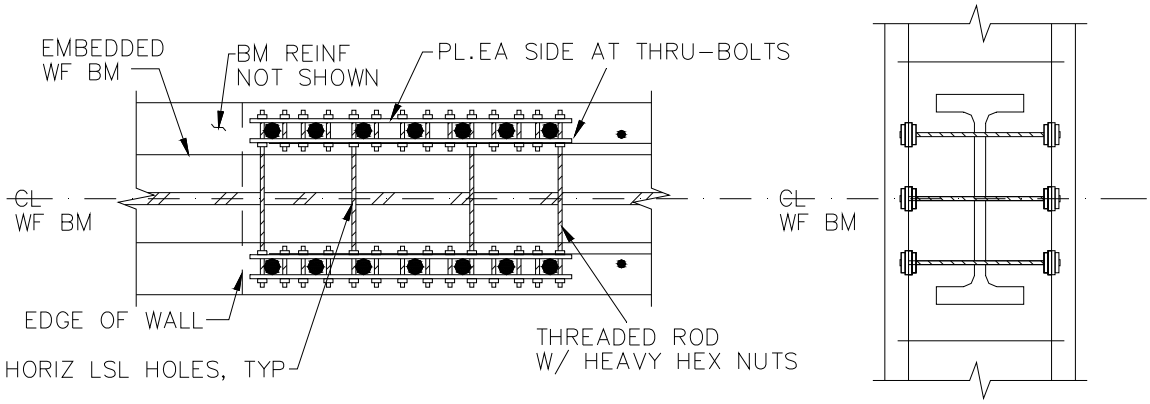

Figure 6.6: Alternative Embedment Detailing: c) Buckling Restraint of Every Wall Boundary Longitudinal Bar with Added Stability

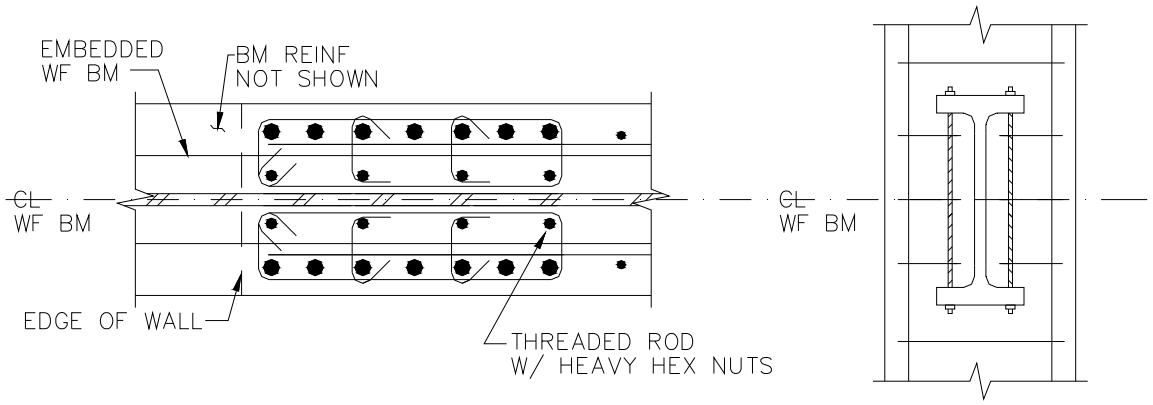

Figure 6.6: Alternative Embedment Detailing: d) Hoops and Cross-Ties

The embedment detail used for the specimens in this study (Figure 3.10) included threaded rods that were fit through pre-drilled holes in the web of the steel section during installation. Presumably, these through rods could act in a manner similar to shear studs when used in SRC coupling beams. In addition to improving composite action between steel and concrete, consideration was given to the influence of the stud strength of the threaded rods on the embedment strength. For SRC1 and SRC2, the threaded rod was A307 grade A (F_u = 60-ksi), 5/16"-diameter (0.24" minor diameter), and the total stud strength, Q_{total}, in single shear is as follows:

$$
\begin{aligned}
Q_n &= 0.5 A_{sc} \sqrt{f'_c E_c} \le A_{sc} F_{uc} \\
&= 0.5 * (0.045 in^2) \sqrt{4.5 ksi * 3824 ksi} \le (0.045 in^2)(60 ksi) \\
&= 2.95k \le 2.71k \\
&= 2.71k
\end{aligned}
$$

$$Q_{total} = 12 * 2.71k = 32.5k \text{ (single shear)}$$

where Q_n is the nominal strength of one stud shear connector embedded in solid concrete, E_c is the modulus of elasticity of concrete, A_{sc} is the cross-sectional area of a stud shear connector, and F_{uc} is the specified minimum tensile strength of a stud shear connector. Given that the total stud strength, Q_{total}, is small relative to the magnitude of the resultant embedment bearing forces (C_f and C_b), the stud-like action of the threaded rods was not expected to significantly influence the embedment strength. It is noted that for SRC3, the strength of the threaded rod was lower than for SRC1 and SRC2 (see Section 3.5 and Appendix A).

6.4.3 Auxiliary Transfer Bars and Face Bearing Plates

The 2010 AISC Seismic Provisions (Section H5.5d for SRC coupling beams, which references provisions in Section H5.5c for steel coupling beams) require the use of auxiliary transfer bars attached to both the top and bottom flange of the embedded steel section, at both the front and back of the embedment zone, and bearing plates at the location of the back transfer bars and at the beam-wall interface (Figure 1.4). The use of the auxiliary transfer bars and bearing plates has been shown to improve the performance of SRC coupling beams, i.e., increasing shear strength modestly and reducing the degree of pinching that occurs in the load-deformation response (Shahrooz et al, 1993). However, the test results in this study indicate that the use of auxiliary transfer bars and bearing plates, which complicates construction, is not necessary when providing adequate embedment length (Section 6.3), sufficient boundary vertical reinforcement (Section 6.4.1) and adequate transverse boundary reinforcement (Section 6.4.2).

6.5 EFFECTIVE STIFFNESS

This section is organized into six subsections. Based on the observed sources of deformation in Section 6.5.1, effective stiffness recommendations are developed in Section 6.5.2 based on test data. The influence of loading cycles and wall rotation, respectively, on effective stiffness is examined in Section 6.5.3 and Section 6.5.4, respectively. The effective stiffness determined for the beams in this study are compared to other testing programs in Section 6.5.5, while the stiffness recommendations developed in Section 6.5.2 are compared to existing recommendations in Section 6.5.6.

6.5.1 Sources of Deformation

Examining the contribution of various sources of deformation to the total coupling beam deformation (e.g., rotation) was required to develop the effective stiffness recommendations presented in Section 6.5.2. The plots in Figure 6.7, which show the relative contributions of various sources of deformation to the total measured beam displacement at the point of load application for each of the four coupling beams tested, were developed based on measurements at the peak of the initial cycle for each load or displacement level applied. The flexure and shear displacements were determined using the LVDTs attached to the coupling beams, with the slip/extension contribution determined using the LVDTs spanning across the beam-wall interface (Figure 4.14 and Figure 5.19). The slip/extension deformation includes flexural deformations; however, given the small contribution provided by flexure along the beam span, the flexural component included in the slip/extension data was presumably small in the elastic range. The "other" category was determined as the difference in the total measured beam displacement and the sum of the flexure, shear, and slip/extension displacements (ensuring that the percentages added to 100%). The other category includes additional sources of deformation such as connection rotation, wall rotation, and accounts for data errors. The plot for SRC2 terminates at 4% rotation because stroke limits of the LVDTs measuring slip/extension were exceeded, and the plot for SRC4 terminates at 3% because data beyond 3% appeared unreliable due to embedment damage at sensor attachment locations.

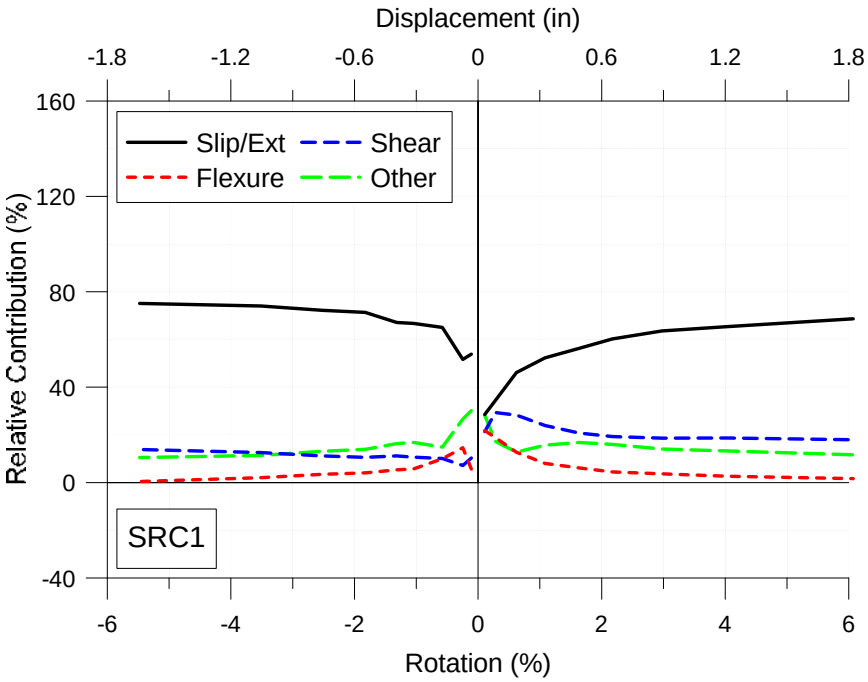

Figure 6.7: Components of Deformation: a) SRC1

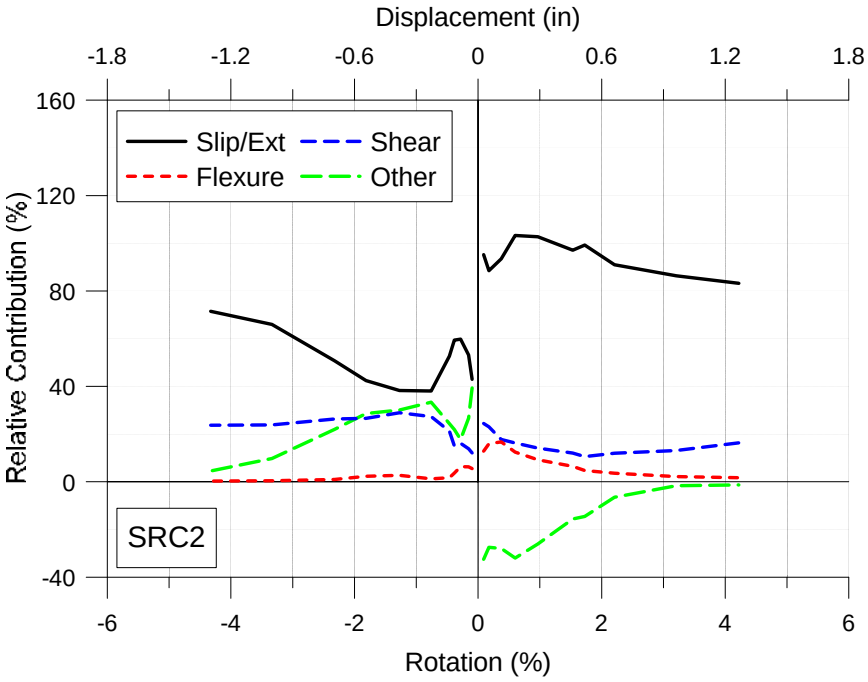

Figure 6.7: Components of Deformation: b) SRC2

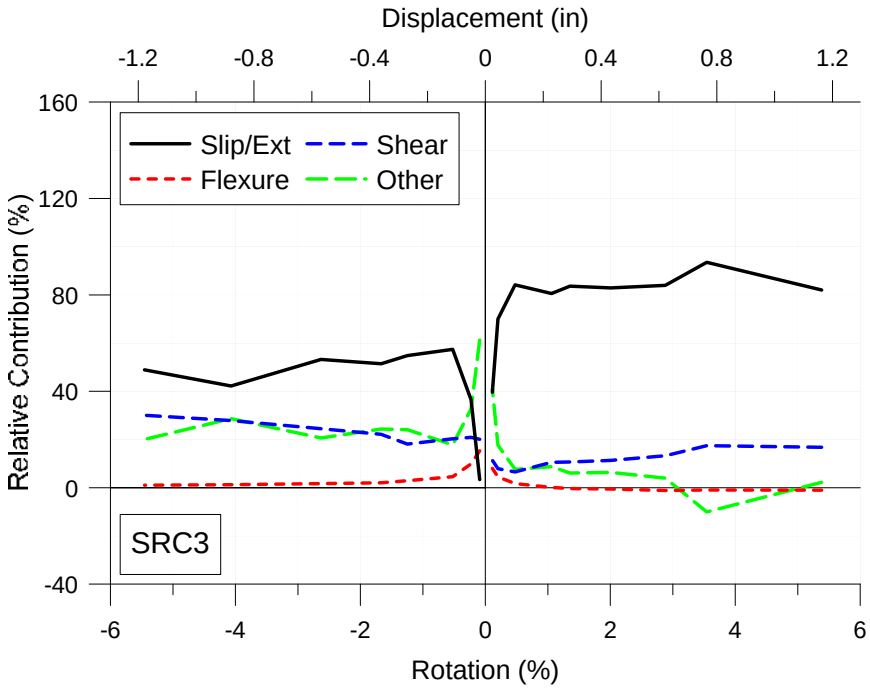

Figure 6.7: Components of Deformation: c) SRC3

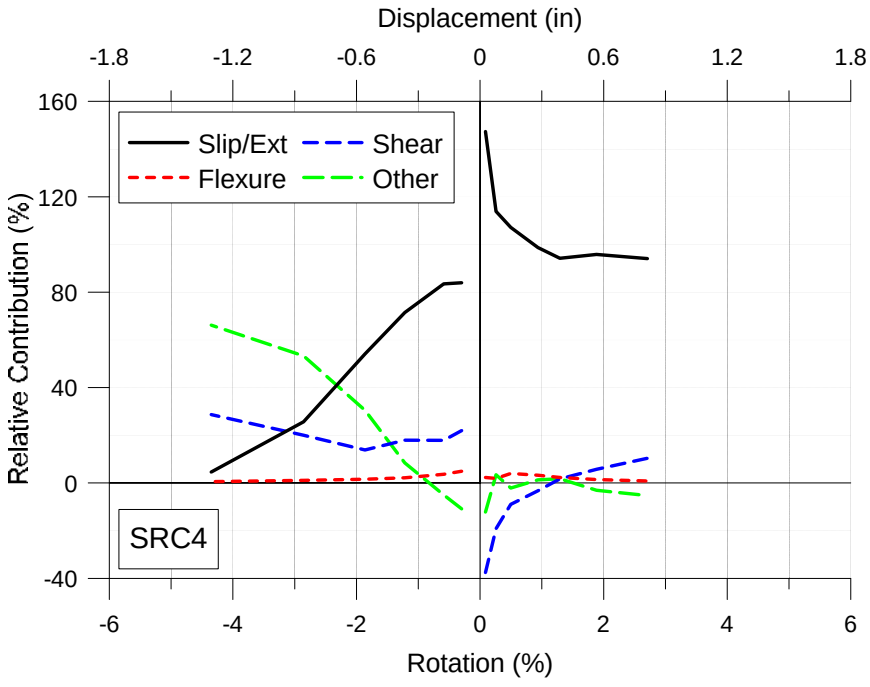

Figure 6.7: Components of Deformation: d) SRC4

According to Figure 6.7, slip/extension deformations accounted for the majority of the beam deformation (35-100% for rotation values between 1.0% and 4.0% for SRC1, SRC2, and SRC3, and between 1.0% and 2.5% for SRC4), whereas flexure and shear deformations were relatively small. This finding is consistent with test results for diagonally-reinforced and conventionally-reinforced coupling beams reported by Naish et al (2013a,b). Referring to Figure 6.7 for the SRC coupling beams tested in this study, the contribution of flexure within the SRC coupling beam span (i.e., neglecting slip/extension) to the total beam lateral displacement at the point of load application was generally close to zero and never greater than ~25%, while shear deformations, although larger, typically contributed about 10-30%. For rotation values less than 1.0%, some inconsistencies in data trends are observed (e.g., the contribution of shear deformations for SRC4 in the positive loading direction); however, the trends reported in Figure 6.7 help determine the primary sources of deformation. It should be noted that the measured shear deformations included shear slip across the beam-wall interface, which occurred for SRC3 and SRC4 due to connection softening, as noted in Section 5.7. Although the relative contribution of shear deformations for SRC3 was expected to be larger than the other three beams due to the lower aspect ratio, the data do not show this trend definitively, noting that in the positive loading direction, the shear contributions for SRC3 were smaller than SRC1 and SRC2.

It is evident from Figure 6.7 that the influence of wall rotations is particularly significant for SRC2 in the elastic range, as the contribution of the "other" category for this case is larger than for the other test beams, while the contribution of flexure and shear appears fairly consistent with the other test beams. In the positive loading direction, the wall rotation causes the coupling

beam to rotate in the opposite direction of the imposed beam rotation, which is represented by the negative contribution of the "other" category for SRC2 in Figure 6.7, noting that this negative contribution to beam rotation was offset by an increase in the slip/extension contribution. As explained in Section 5.1, the wall rotation at the location of the coupling beam was based on the average of the rotation at the top and bottom of the wall. For SRC2, the large contribution of the "other" category in Figure 6.7 suggests that the actual wall rotations may have differed significantly from this average value, with actual wall rotations in the positive loading direction exceeding the average value. Relative to the other three test beams, the influence of wall rotations was particularly significant for SRC2 in the elastic range. This was noted previously in Section 5.8 with specific reference to Figure 5.21, in which the wall rotation in the positive loading direction is noticeably larger for SRC2 than for the other three beams, and is also noted in Section 6.5.4.

For SRC4 in the negative loading direction, the contribution of flexure and shear to the total deformation appears consistent with the other three tests beams, while the contribution of slip/extension and the "other" category do not. Specifically, the contribution of the "other" category increases with applied coupling beam rotation, as the slip/extension contribution decreases. The increased contribution of the "other" category is likely due to increased rotation in the connection region, consistent with the extensive embedment damage observed for this test (Section 5.2).

6.5.2 Development of Effective Stiffness Recommendations

The effective stiffness plots presented in this section were determined based on the load-displacement pairs at the peak of each positive and negative value for the first loading cycle at each level of applied load or displacement. Rather than plotting the peak-to-peak stiffness, which is an average of the positive and negative stiffness, origin-to-peak stiffness is plotted in order to capture asymmetry between positive and negative stiffness values.

It is common when modeling component elastic stiffness to use a lumped-deformation approach, in which all of the deformations are lumped into one component of deformation. It follows that the use of a lumped deformation approach is most reliable for cases in which one type of deformation is responsible for the majority of the total observed deformation. For the coupling beams tested in this study, slip and extension (or pullout) of the steel section from the embedment region (at the beam-wall interface) was the primary source of coupling beam chord rotation, while the relative contributions of shear and flexure deformations to the overall deformations were small, as noted in the previous section. This suggested the use of a lumped deformation modeling approach for stiffness, in which all of the coupling beam deformations were attributed to interface slip/extension.

To model all of the coupling beam deformation as slip/extension, an elastic rotational spring with stiffness, K, in terms of moment per unit rotation is placed at the beam-wall interface, and the coupling beam is modeled as a rigid body, i.e. with infinite flexural and shear stiffness values. Using this approach, a plot of the measured effective stiffness of the rotational spring as a function of the beam chord rotation is shown in Figure 6.8, which includes a normalization of the

rotational stiffness by the expected plastic flexural strength, M_{pe}, of the SRC coupling beam. For this approach, M_{pe} was computed based on the as-tested material properties presented in Section 4.1 and differed for each of the four tests. The variables in this study, including embedment length, aspect ratio, wall demands, and the quantities of longitudinal and transverse wall boundary reinforcement, do not appear to have a significant impact on the effective elastic stiffness based on the relations shown in Figure 6.8. It appears that the wall stresses normal to the embedment may have a modest impact, as the stiffness values appear slightly larger in the positive direction, with compressive stresses normal to the connection, than in the negative direction, with tensile stresses normal to the connection. Attempts to quantify a relationship between wall strain/stress and effective stiffness did not produce a reliable correlation.

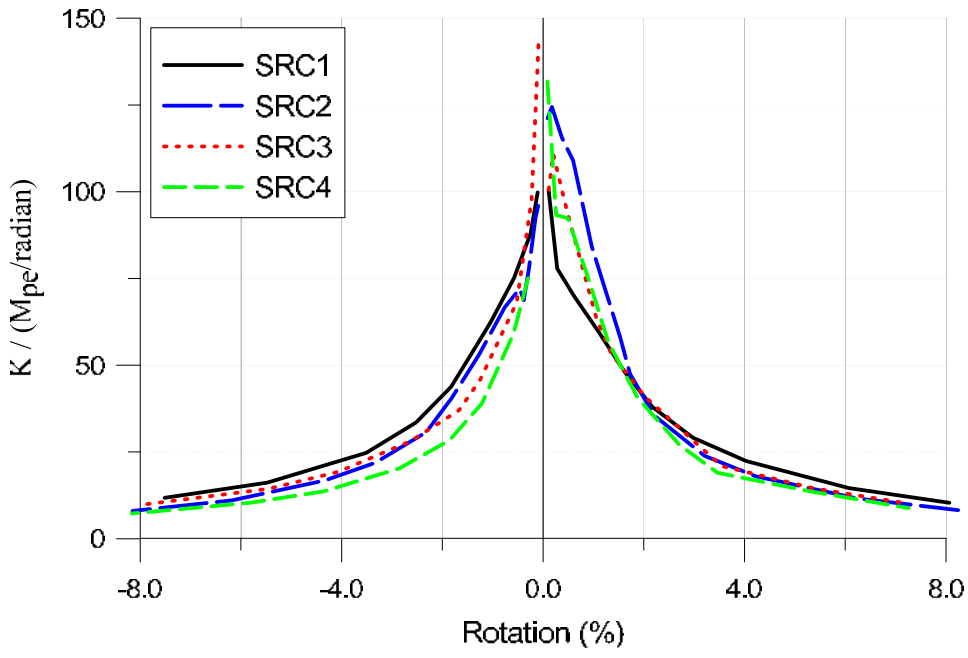

Figure 6.8: Effective Interface Spring Rotational Stiffness

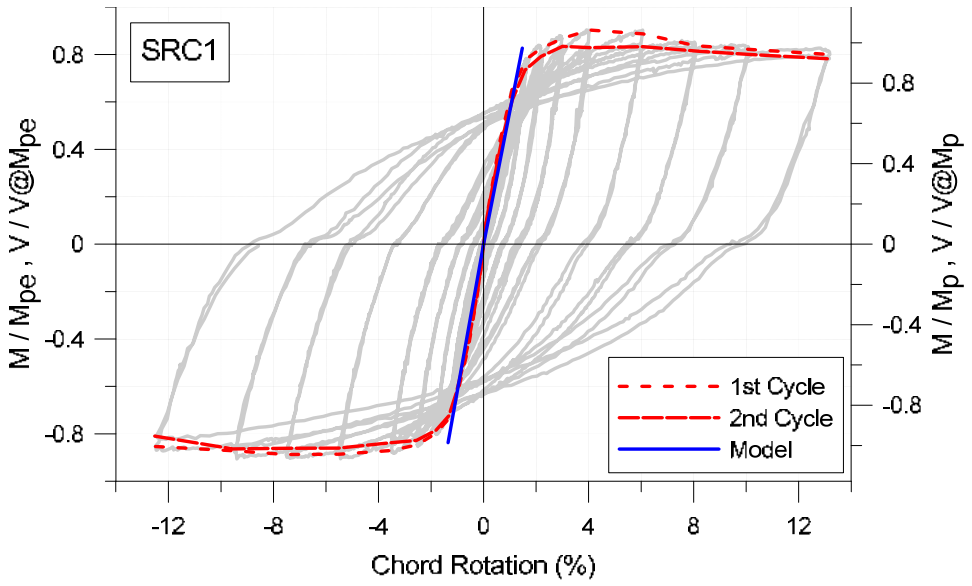

Figure 6.9: Effective Elastic Stiffness Modeling: a) SRC1

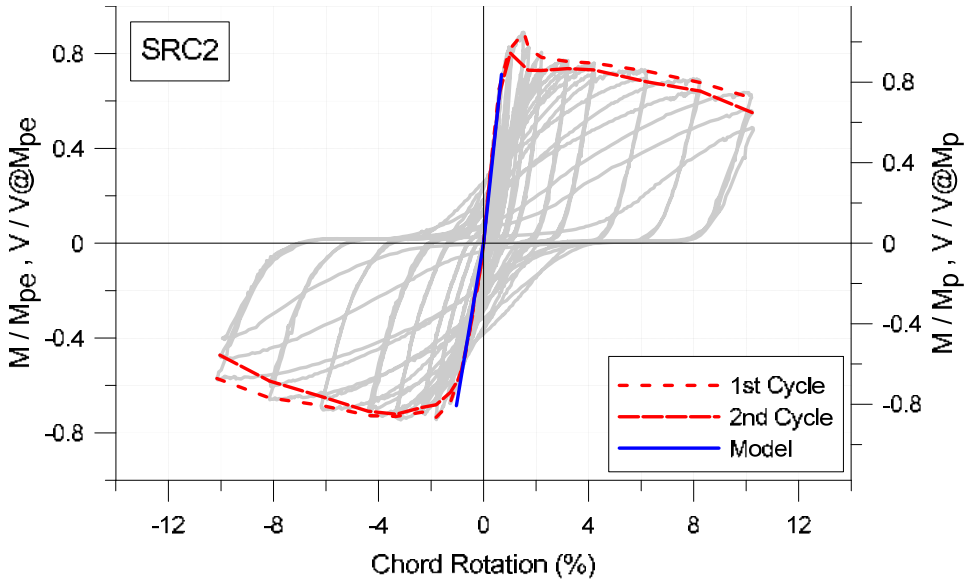

Figure 6.9: Effective Elastic Stiffness Modeling: b) SRC2

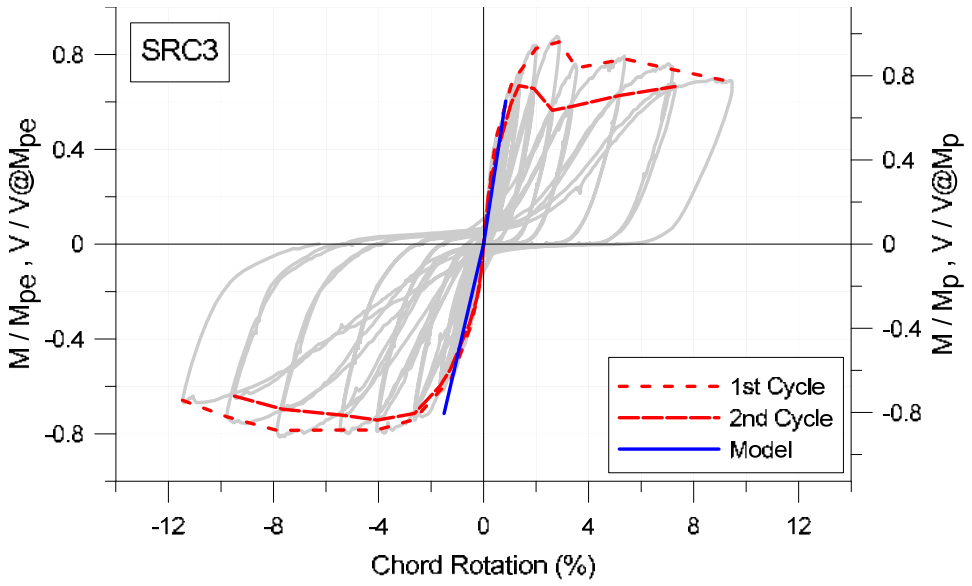

Figure 6.9: Effective Elastic Stiffness Modeling: c) SRC3

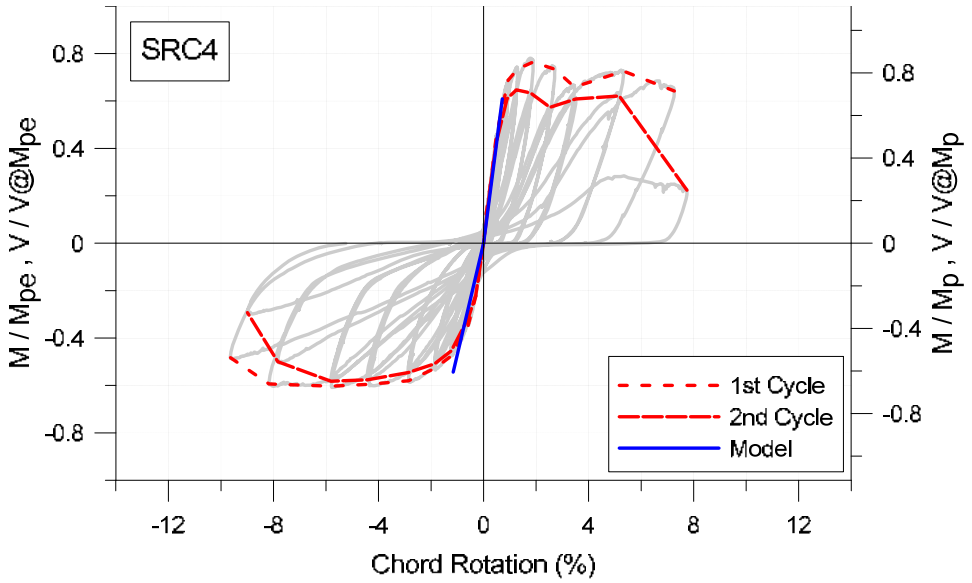

Figure 6.9: Effective Elastic Stiffness Modeling: d) SRC4

Table 6.4: Effective Elastic Stiffness Parameters

	SRC1		SRC2		SRC3		SRC4	
	(+)	(-)	(+)	(-)	(+)	(-)	(+)	(-)
K / M_{pe} (rad^{-1})	58	63	107	66	73	44	88	45
$(EI)_{eff}$ / $\alpha E_s I_{trans}$	0.048	0.053	0.090	0.055	0.062	0.038	0.075	0.038

Because K decreases with increasing chord rotation (Figure 6.8) in the elastic range, a more refined modeling procedure (Figure 6.9) was used to aid in the determination of an average value for K based on test data that could be used to model elastic stiffness; more details on the procedure used to model stiffness (Figure 6.9) are provided in Section 7.2 (nonlinear backbone modeling). The effective stiffness parameters provided in Table 6.4 correspond to the elastic stiffness shown in Figure 6.9, and, based on an average value from Table 6.4, the use of an elastic rotational spring stiffness of

$$K = \frac{0.75M_p}{\theta(\%)} = \frac{75M_p}{rad.} = \frac{M_p}{\theta_y \approx 1.33\%} \tag{6.8}$$

is recommended for modeling purposes, where θ(%) is the percent chord rotation and θ_y is the chord rotation at yield.

In terms of modeling coupling beam stiffness using computer software, designers are accustomed to modeling coupling beam stiffness as either effective shear and/or bending stiffness. Rather than modeling an interface spring, the beam-to-wall connection may be

modeled as rigid if the spring stiffness is converted into an equivalent effective shear stiffness, $(EA)_{eff}$, with a rigid flexural stiffness as:

$$\left(EA\right)_{eff} = \frac{2K}{L} = \frac{2M_p}{\theta_y L} \tag{6.9}$$

or converted into an equivalent effective bending stiffness, $(EI)_{eff}$, with a rigid shear stiffness as:

$$\left(EI\right)_{eff} = \frac{KL}{6} = \frac{M_p L}{6\theta_y} \tag{6.10}$$

These relationships were developed based on the stiffness relationships for elastic beams (Figure 6.10), noting that modeling interface slip/extension as shear or flexure in the beam span requires consideration of the coupling beam span length, L, or span-to-depth aspect ratio, α, to achieve equivalent beam stiffness.

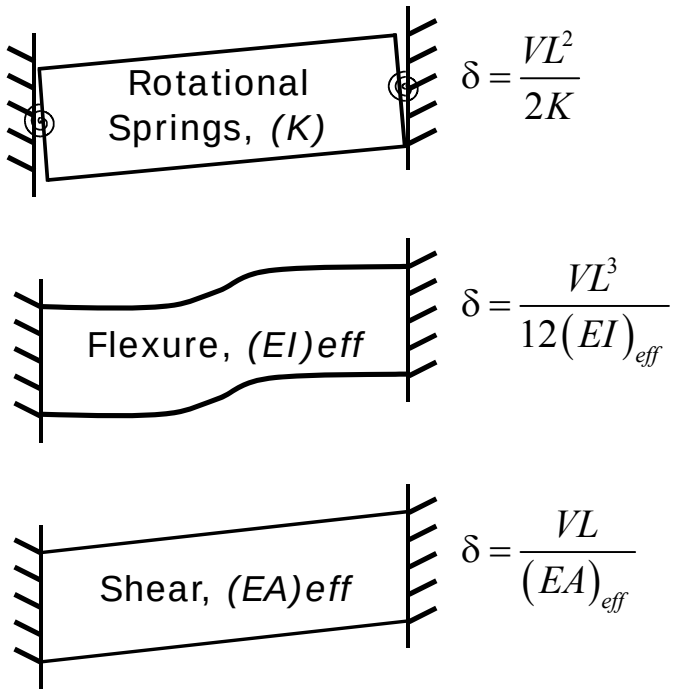

Figure 6.10: Stiffness Relationships for Elastic Beam

Consideration was also given to expressing the effective bending stiffness $(EI)_{eff}$ in terms of the transformed moment of inertia, I_{trans}, of the SRC coupling beam rather than M_{pe}. Using this approach, a plot of the measured effective bending stiffness as a function of the beam chord rotation is shown in Figure 6.11, which includes a normalization of the effective bending stiffness by $\alpha E_s I_{trans}$, where α is the span-to-depth aspect ratio of the SRC coupling beam, E_s is the modulus of elasticity of steel, and I_{trans} is determined based on transforming concrete to steel based on the modular ratio and neglecting cracked concrete, i.e. I_{trans} is computed for a cracked section. The elastic modulus of concrete, E_c, used in the determination of I_{trans}, was determined using ACI 318-11 Section 8.5.1 based on $f'_{c,test}$ (Section 4.1.1), meaning that the modular ratio, E_s/E_c, differed for the four tests.

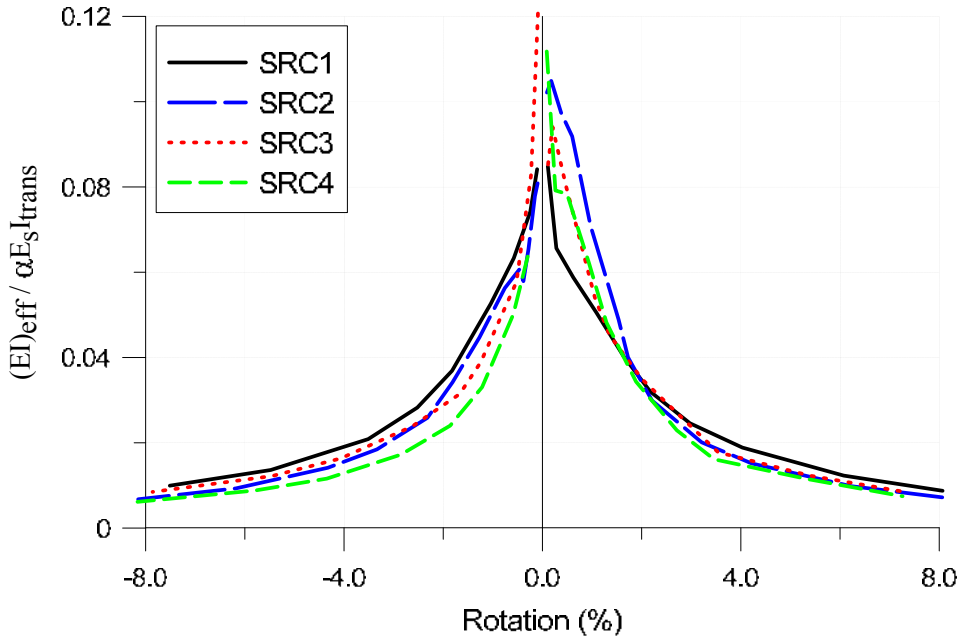

Figure 6.11: Effective Bending Stiffness

The same trends observed for the effective rotational spring stiffness plot in Figure 6.8 are evident in the effective bending stiffness plot in Figure 6.11, noting that stiffness discrepancies between tests do not appear to depend on normalization by $\alpha E_s I_{trans}$ versus M_{pe}. Based on an average of the values provided in Table 6.4, which are based on the stiffness models fit to test data in Figure 6.9, the use of an elastic effective bending stiffness of

$$\left(EI\right)_{eff} = 0.06\alpha E_s I_{trans} \tag{6.11}$$

is recommended for modeling purposes with a rigid shear stiffness and rigid beam-wall interface connections.

Although the recommendations for computing elastic stiffness (Equations (6.8) through (6.11)) were developed based on calibration to parameters that were computed based on as-tested material properties, i.e. M_{pe} and I_{trans}, it is recommended that specified material properties be used for prescriptive design. This is reflected in the use of M_p in Equations (6.8) through (6.10) and will affect the computation of E_c, which is used in the computation of I_{trans} in Equation (6.11). For alternative design, expected material properties should be used (discussed in Section 7.1). The use of prescriptive recommendations versus alternative recommendations typically leads to slightly lower calculated stiffness values.

The coupling beams tested in this study did not include the presence of a floor slab or significant axial load. Previous studies, one that included a reinforced concrete floor slab (Shahrooz et al, 2001b) and one that included a post-tensioned (axially loaded) floor slab (Naish et al, 2013b), indicate that the presence of a floor slab has a relatively minor impact on the effective stiffness (primarily in the elastic range), suggesting that the inclusion of a floor slab in this study would not significantly impact the effective elastic stiffness values recommended.

The effective stiffness recommendations presented in this section were all based on lumped-displacement modeling approaches. Theoretically, a more refined modeling approach that includes modeling of slip/extension, flexure, and shear deformations individually should lead to a better match with test results. However, given that the majority of the deformations were attributed to slip/extension and the contribution from shear and flexure shows dispersion among tests without following expected trends (e.g., shear deformations did not provide a greater

contribution for the shorter aspect ratio beam, as expected), this added level of detail is not justified with the current information available.

A summary of the four effective stiffness modeling approaches for SRC coupling beams presented in this section is provided in Table 6.5. As these modeling approaches were developed based on tests of flexure-yielding specimens with aspect ratios of 3.33 and 2.4, modest extrapolation of test results to include flexure-yielding SRC coupling beams between aspect ratios of two and four is recommended.

Table 6.5: *Stiffness Modeling Approaches for Flexure-Controlled Beams with* $2 \leq (\alpha = L/h) \leq 4$

Stiffness Modeling Approach	Interface Slip/Extension Spring Stiffness	Effective Shear Stiffness	Effective Bending Stiffness
(1)	Equation (6.8)	Rigid	Rigid
(2)	Rigid	Equation (6.9)	Rigid
(3)	Rigid	Rigid	Equation (6.10)
(4)	Rigid	Rigid	Equation (6.11)

6.5.3 Influence of Loading Cycles

The plots presented in Figure 6.12 are a means to assess cyclic stiffness degradation. Cyclic stiffness degradation appears largest in the positive loading direction, between the first cycle and the two subsequent cycles. This suggests that loading in the negative direction was causing softening in the positive direction upon load reversal, noting that loading in the positive direction

occurred prior to loading in the negative direction for each cycle. This cyclic degradation appears largest for SRC3 and SRC4, members in which embedment damage was observed.

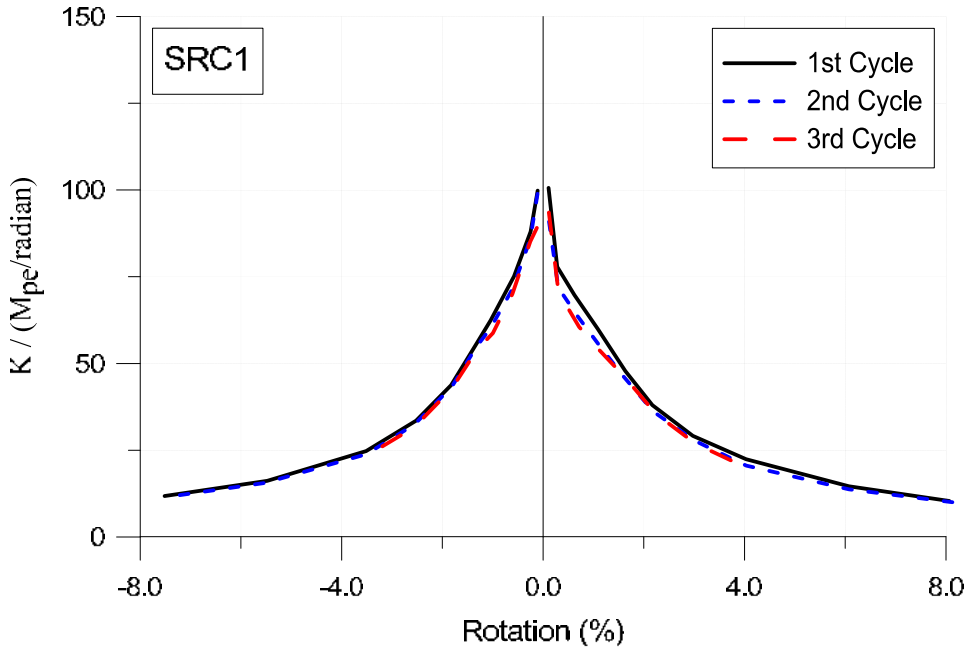

Figure 6.12: Effective Stiffness Cyclic Degradation: a) SRC1

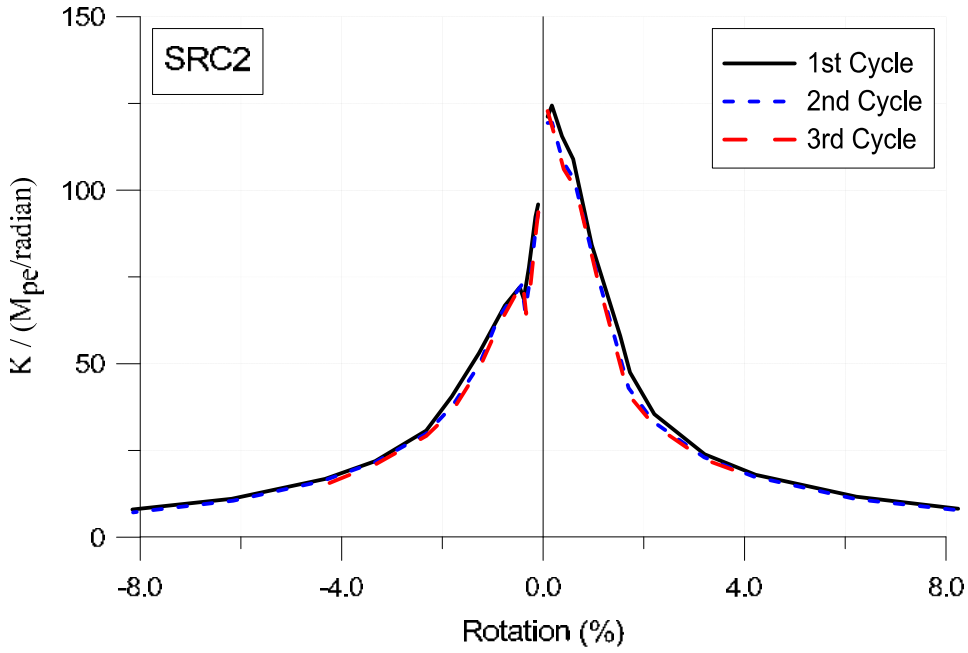

Figure 6.12: Effective Stiffness Cyclic Degradation: b) SRC2

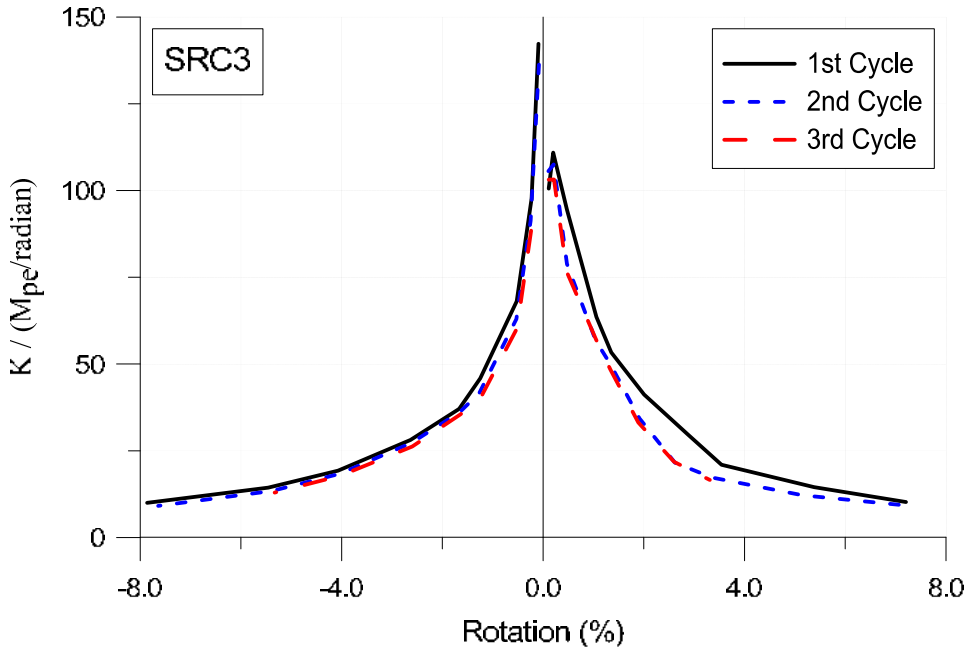

Figure 6.12: Effective Stiffness Cyclic Degradation: c) SRC3

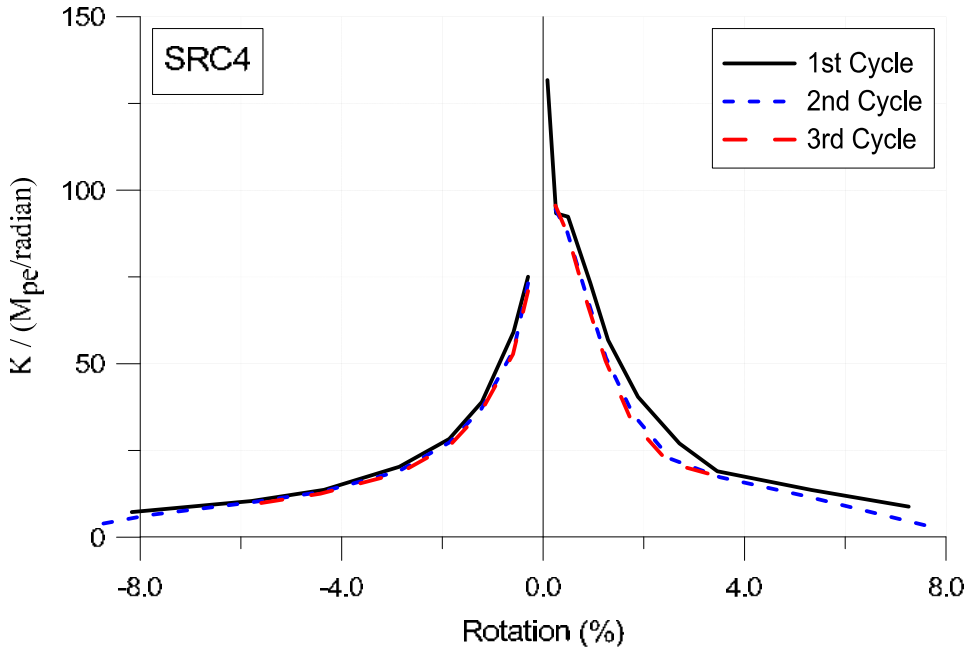

Figure 6.12: Effective Stiffness Cyclic Degradation: d) SRC4

6.5.4 Influence of Wall Deformation

As explained in Section 5.1, the wall rotation at the location of the coupling beam was estimated as the average value of the rotation measured at the top and bottom of the wall. The plots shown in Figure 6.13 are presented as a means to assess the sensitivity of stiffness to wall rotation, based on the difference in beam stiffness measured relative to the top and bottom of the wall. Referring to Figure 6.13, the influence of wall rotation on measured stiffness is relatively minor for SRC1, SRC3, and SRC4. However, wall rotation has a more significant impact for SRC2, indicating a higher degree of uncertainty in the stiffness data for SRC2 relative to the other three test beams. The same procedure used in Section 6.5.2 to estimate the observed effective elastic stiffness of the test beams (Figure 6.9 and Table 6.4) was used again here to estimate lower- and

upper- bound values for observed stiffness values, which are provided in Table 6.6 and Table 6.7, respectively (noting that figures comparing model stiffness to test data are not provided, due to the visual similarity with Figure 6.9). Note that the lower-bound values (Table 6.6) correspond to coupling beam chord rotations measured relative to the base of the wall, while the upper-bound values (Table 6.7) correspond to chord rotations measured relative to the top of the wall. The lower-bound stiffness values in Table 6.6 are roughly 15-20% lower on average than the values in Table 6.4. To address this uncertainty, lateral drift limits could be checked for a lower-bound stiffness, e.g., using 80% of the stiffness value recommended in Section 6.5.2.

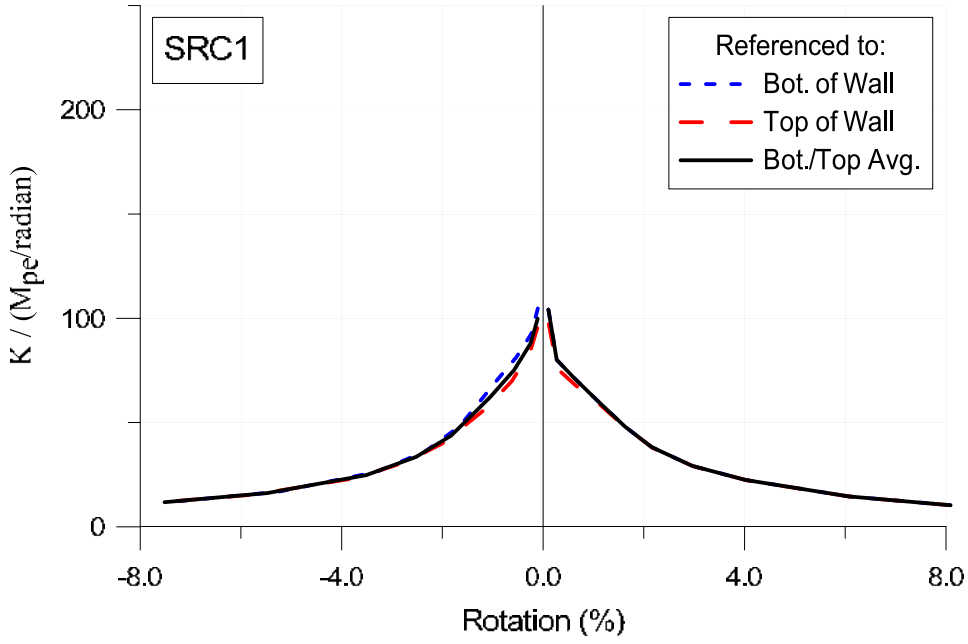

Figure 6.13: Sensitivity of Effective Stiffness Measurements to Wall Rotation: a) SRC1

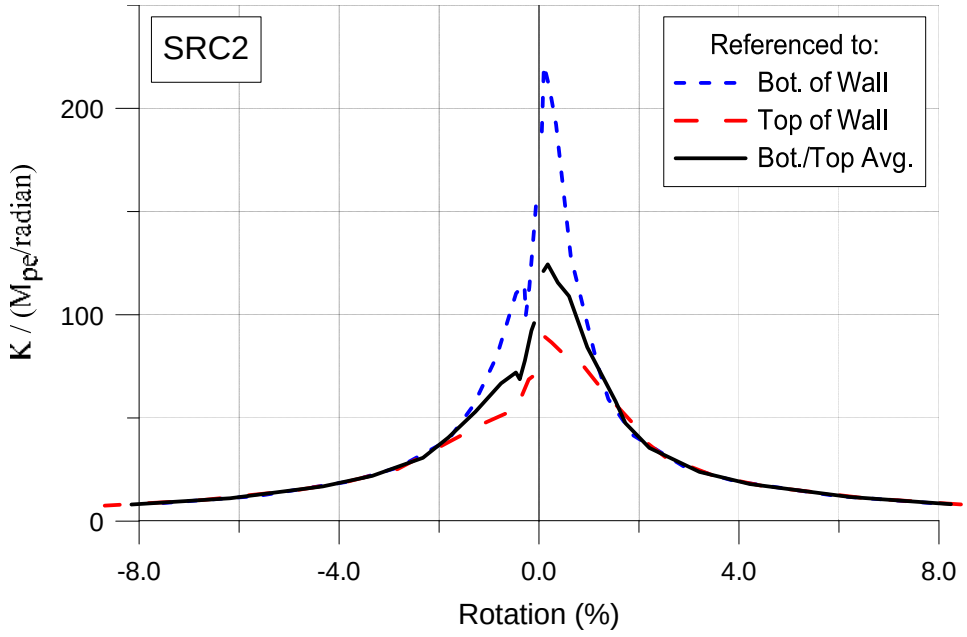

Figure 6.13: Sensitivity of Effective Stiffness Measurements to Wall Rotation: b) SRC2

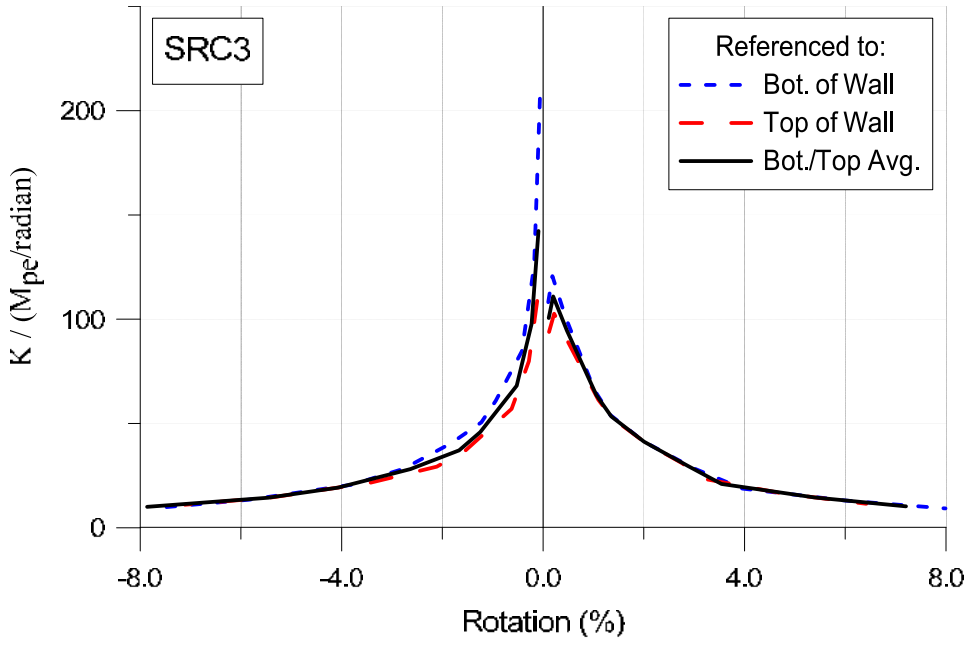

Figure 6.13: Sensitivity of Effective Stiffness Measurements to Wall Rotation: c) SRC3

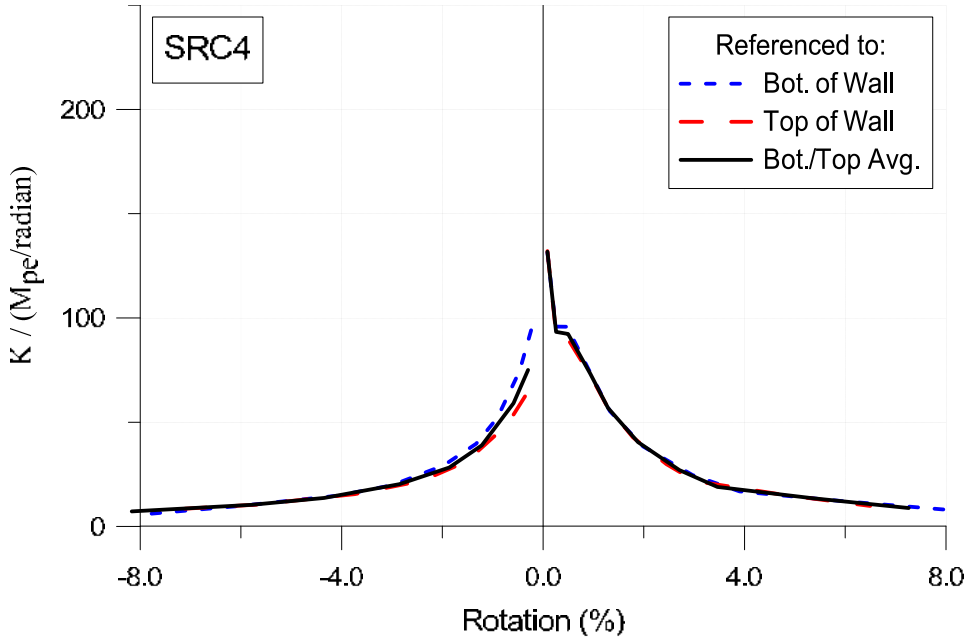

Figure 6.13: Sensitivity of Effective Stiffness Measurements to Wall Rotation: d) SRC4

Table 6.6: Lower Bound Effective Elastic Stiffness Parameters

	SRC1		SRC2		SRC3		SRC4	
	(+)	(-)	(+)	(-)	(+)	(-)	(+)	(-)
K / M_{pe} (rad^{-1})	57	57	75	48	70	36	88	37
$(EI)_{eff} / \alpha E_s I_{trans}$	0.048	0.048	0.063	0.040	0.060	0.030	0.074	0.031

Table 6.7: Upper Bound Effective Elastic Stiffness Parameters

	SRC1		SRC2		SRC3		SRC4	
	(+)	(-)	(+)	(-)	(+)	(-)	(+)	(-)
K / M_{pe} (rad^{-1})	58	70	184	106	77	58	89	58
$(EI)_{eff} / \alpha E_s I_{trans}$	0.049	0.059	0.155	0.090	0.065	0.049	0.075	0.049

6.5.5 Comparison to Other Testing Programs

As mentioned previously, Gong and Shahrooz (2001a,b) tested a total of seven steel coupling beams, six with reinforced-concrete encasement (SRC coupling beams) and one without. Based on Figure 6.14, which shows a comparison of the measured effective stiffness versus chord rotation for two of the beams with adequate embedment strength (WB1 and WB2) and two without (CB4 and CB1), one of which did not include concrete encasement (CB1), it appears that there is minimal variation in effective stiffness for the beams with encasement and a minor reduction in stiffness for the beam without encasement. Based on Figure 6.15, which shows a comparison of the measured effective stiffness versus chord rotation for two concrete-encased beams tested by Gong and Shahrooz (2001a,b), one with adequate embedment strength (WB2) and one without (CB4), with two of the beams tested in this study (SRC1 and SRC3), it appears that there is relatively minor variation in effective stiffness between the beams from the different test programs. It is observed that there is less variation in effective stiffness when normalizing stiffness to $\alpha E_s I_{trans}$ (consistent with Equation (6.11)) rather than M_{pe} (consistent with Equation (6.8), Equation (6.9), and Equation (6.10)). This result is evident in Table 6.8, which provides effective elastic stiffness values for positive and negative loading estimated using secant stiffness values to two-thirds of the peak loads (Figure 6.16). The lack of variation in the effective elastic stiffness presented in Figure 6.15 and Table 6.8, compared with the values recommended per the approach presented in Section 6.5.2, suggests that the stiffness recommendations developed in Section 6.5.2 could be applied to the shear-yielding beams tested by Gong and Shahrooz (2001a,b,c). It is noted that use of Equation (6.11) (with $\alpha E_s I_{trans}$) rather than Equation (6.8), Equation (6.9), or Equation (6.10) (with M_{pe}) appears slightly more accurate.

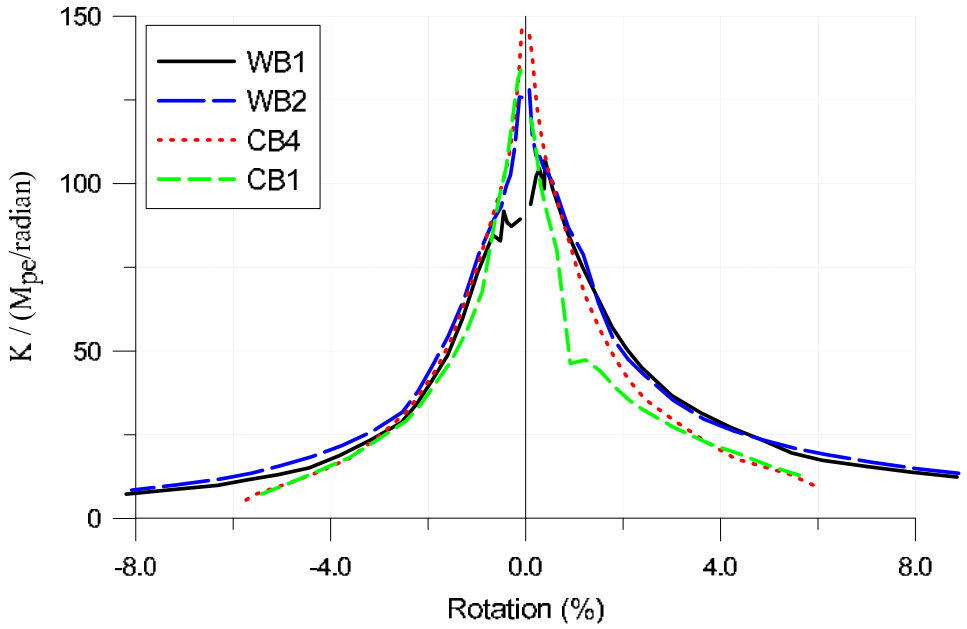

Figure 6.14: Effective Stiffness for Gong and Shahrooz (2001 a,b,c) Test Specimens: a) Rotational Hinge

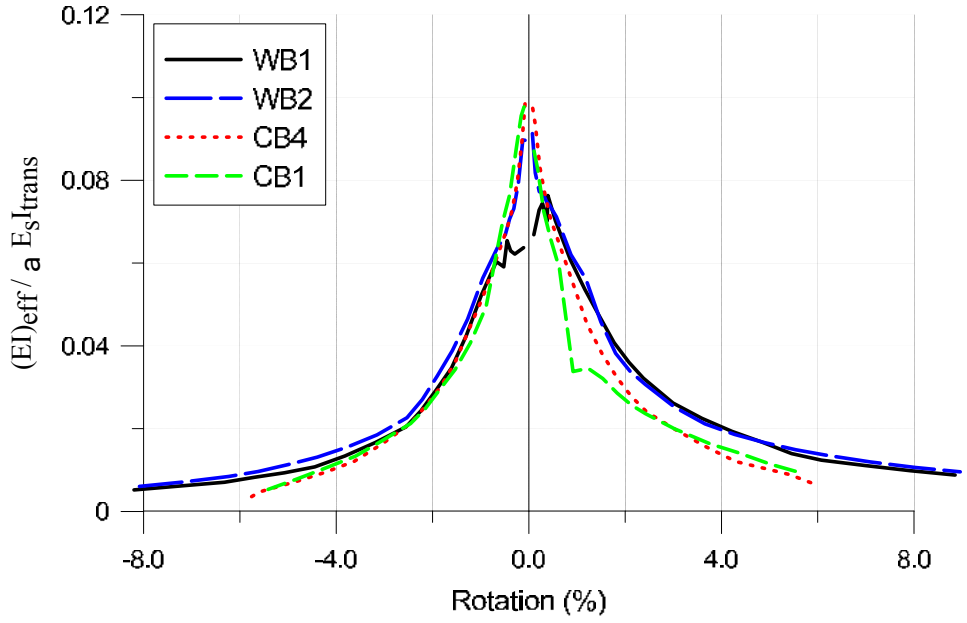

Figure 6.14: Effective Stiffness for Gong and Shahrooz (2001 a,b,c) Test Specimens: b) Bending

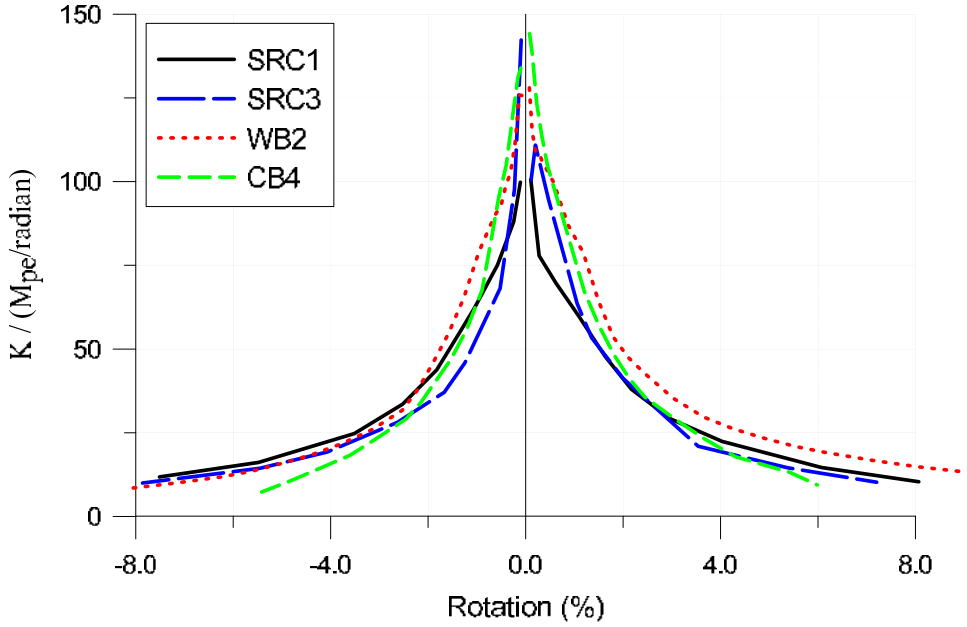

Figure 6.15: Effective Stiffness Comparison: a) Rotational Hinge

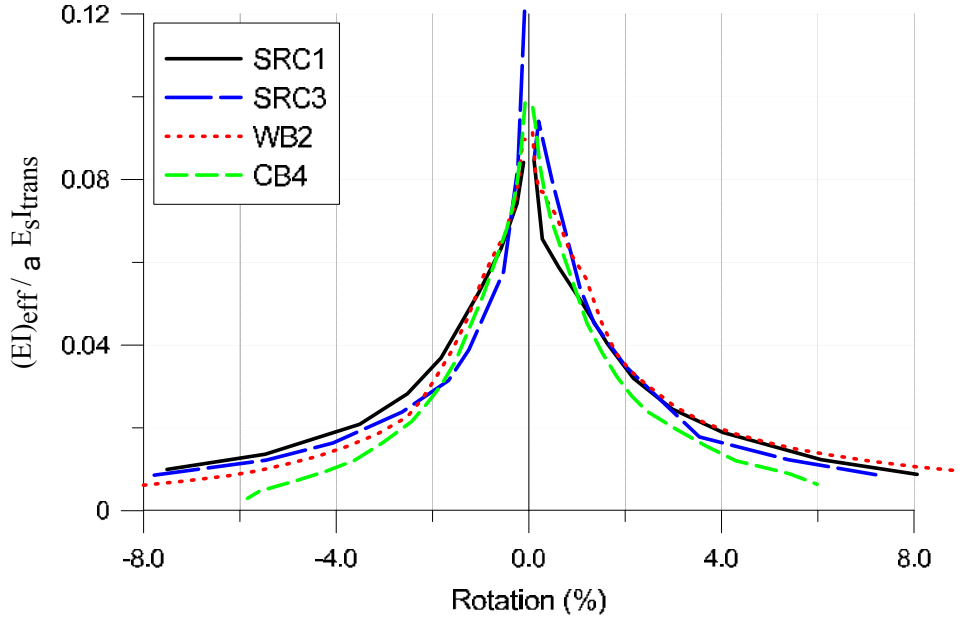

Figure 6.15: Effective Stiffness Comparison: b) Bending

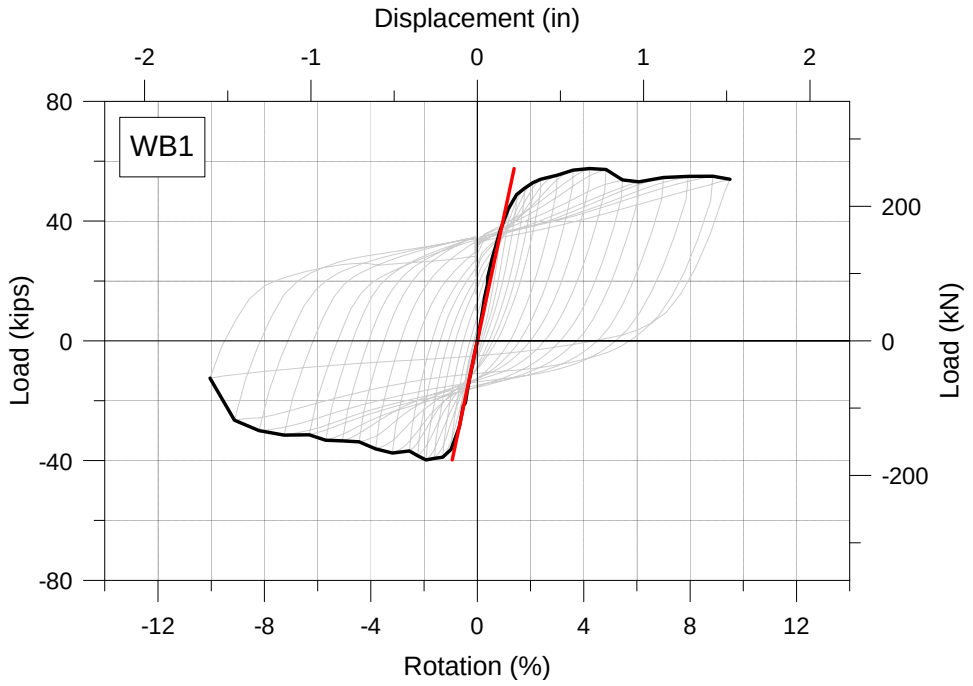

Figure 6.16: Effective Elastic Stiffness Modeling: a) WB1

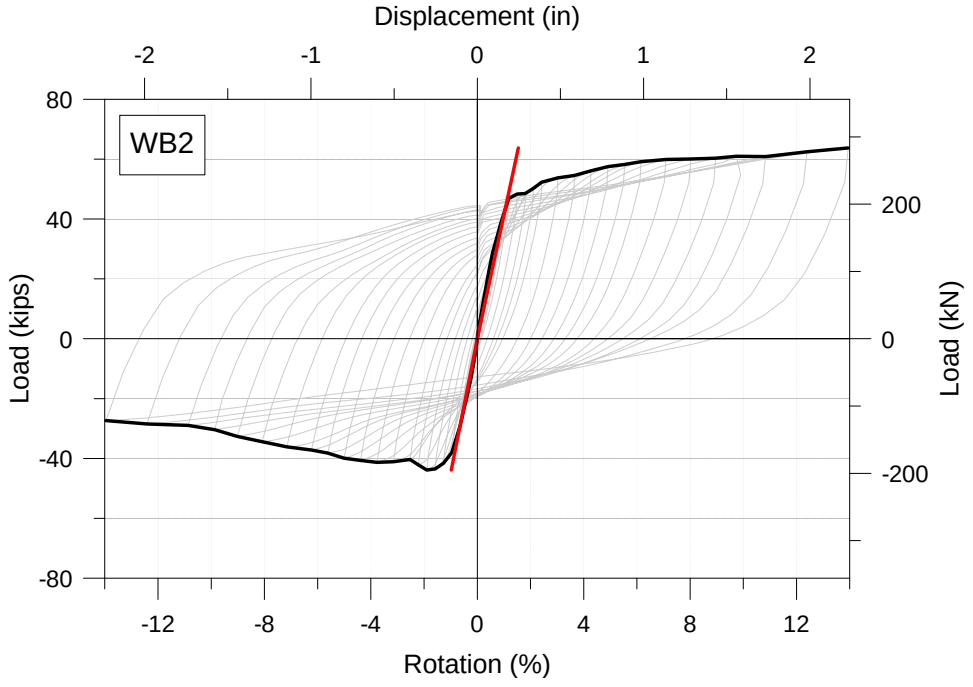

Figure 6.16: Effective Elastic Stiffness Modeling: b) WB2

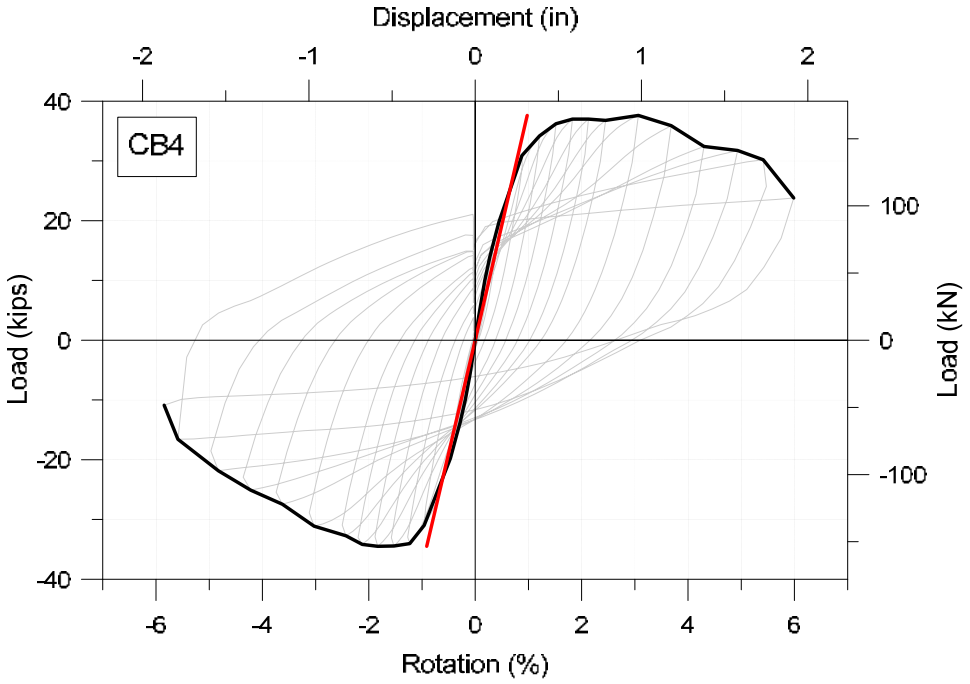

Figure 6.16: Effective Elastic Stiffness Modeling: c) CB4

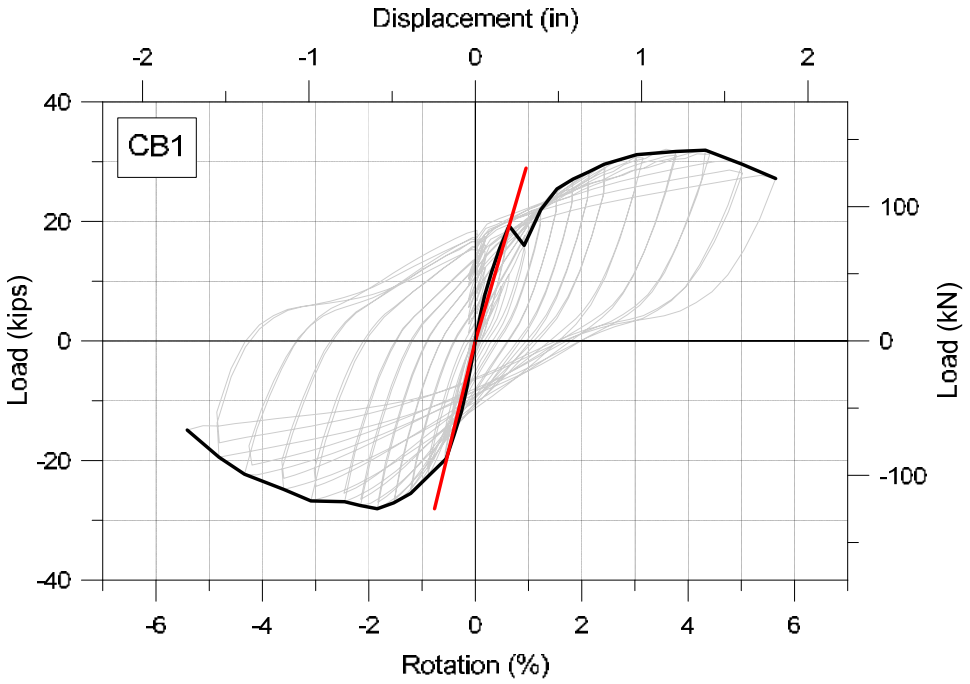

Figure 6.16: Effective Elastic Stiffness Modeling: d) CB1

Table 6.8: Effective Elastic Stiffness Parameters for Gong and Shahrooz (2001a,b) Tests

	WB1		WB2		CB4		CB1	
	(+)	(-)	(+)	(-)	(+)	(-)	(+)	(-)
K / M_{pe} (rad^{-1})	83	84	82	89	91	90	80	97
$(EI)_{eff} / \alpha E_s I_{trans}$	0.059	0.060	0.059	0.064	0.062	0.061	0.059	0.071

6.5.6 Comparison to Previous Recommendations

Sections H4.3 and H5.3 of the 2010 AISC Seismic Provisions refer to ACI 318 Chapter 10 for the determination of the effective bending stiffness of SRC coupling beams for elastic analysis and note that shear deformations and connection flexibility should also be considered (but provide limited details as to how this shall be accomplished). ACI 318-11 Section 10.10.4.1 specifies an effective moment of inertia of $0.35I_{g,c}$ for beams, where $I_{g,c}$ is the moment of inertia of the gross concrete section neglecting the impact of reinforcement (a transformed section analysis is not required). Use of the ACI 318 Chapter 10 provisions is not recommended, as the expressions developed in this section provide more guidance and were developed based on test data.

The expression for the effective bending stiffness, $(EI)_{eff}$, of embedded steel coupling beams without concrete encasement, developed by Harries (1995) and included in Harries et al (2000) and the Commentary of the 2010 AISC Seismic Provisions, is duplicated here (see Equation (2.26) in Section 2.2) as:

$$\left(EI\right)_{eff} = 0.6k'E_s I_{g,s} = 0.6E_s I_{g,s}\left(1+\frac{12E_s I_{g,s}\lambda}{L_c{}^2 G_s A_w}\right)^{-1} \tag{6.12}$$

where *k'* represents the reduction in flexural stiffness due to shear deformations, $I_{g,s}$ is the moment of inertia of the gross steel section (neglecting reinforced concrete encasement, where applicable), E_s is the modulus of elasticity of steel, G_s is the shear modulus of steel, A_w is the area of the steel section resisting shear (taken as the product of the steel section depth, *d*, and web thickness, t_w), λ is the cross-section shape factor for shear (1.5 for W-shapes), L_c is the effective clear span of the coupling beam, computed as $L_c = L + 2c$ to account for spalling of the wall clear cover, *c*. Given that the effective bending stiffness is reduced to account for shear deformations using *k'*, the beam shear stiffness should be modeled as rigid, unless shear deformations are modeled separately, in which case *k'* = 1. When using *k'* = 1, modeling an effective shear stiffness of $0.6G_sA_w/\lambda$ is consistent with Equation (6.12). It is noted that the -1 coefficient is erroneously omitted in the expression provided in the commentary of the 2010 AISC Seismic Provisions but is included in Equation (6.12) to be consistent with Harries (1995) and Harries et al (2000).

Noting that the effective coupling beam stiffness is identical when using Equation (6.8), Equation (6.9), or Equation (6.10), a parametric study was conducted based on the same 48 variations of beam cross-section, beam aspect ratio, and concrete strength considered in the parametric study in Section 6.4.1 in order to compare the variation in stiffness between Equation (6.10), Equation (6.11), and Equation (6.12). Results of the parametric study, provided in Table 6.9 with a statistical summary provided in Table 6.10, indicate that there is minimal difference in stiffness values obtained with Equation (6.10) and Equation (6.11), and only a modest difference

in stiffness between Equation (6.12) and either Equation (6.10) or Equation (6.11). On average (i.e. using the statistical results), relative to the effective stiffness obtained using Equation (6.10), the effective stiffness obtained using Equation (6.11) is roughly 10% larger with a coefficient of variation of 3%, whereas the effective stiffness obtained using Equation (6.12) is roughly 20% larger with a coefficient of variation of roughly 15%.

The results presented in Table 6.9, may be used to assess the sensitivity of discrepancies in stiffness values computed with the various equations to the variables used in the study. The ratio of computed effective stiffness between Equation (6.10) and Equation (6.11) does not appear sensitive to changes in concrete strength and is only minimally sensitive to changes in member cross-section; changes in aspect ratio have no effect, since both expressions incorporate aspect ratio in the same way. The ratio of computed effective stiffness between Equation (6.12) and either Equation (6.10) or Equation (6.11) is minimally sensitive to changes in concrete strength and modestly influenced by changes in member cross-section and aspect ratio.

The sensitivity of differences between stiffness values computed using Equation (6.12) and Equation (6.10) or Equation (6.11) to changes in member cross-section is likely because concrete encasement is not considered in Equation (6.12), whereas concrete encasement is considered in Equation (6.10) and Equation (6.11). The test results of Gong and Shahrooz (2001a) suggest that effective stiffness is only modestly impacted by concrete encasement. It should be noted that the use of I_{trans} assumes fully-composite action between concrete and steel, which is not likely developed for SRC coupling beams without shear studs or some other means to improve composite action.

As mentioned previously, the inclusion of an aspect ratio or beam length term in Equation (6.10) and Equation (6.11) was deemed necessary when modeling interface slip/extension (pullout) using a shear or bending stiffness term. Using the concept of dimensional similitude, the load-displacement stiffness of a beam is a function of L^3 for bending stiffness, L^2 for rotational interface spring stiffness, L^1 for shear stiffness, and L^0 for shear spring stiffness. Therefore, modeling slip/extension rotations using flexural stiffness or shear stiffness introduces error into the stiffness data for coupling beams if aspect ratio is not considered. It is noted that applying Equation (6.12) to the beam cross-section tested in this study produces *k'*-values of less than 0.25, suggesting that shear deformations were responsible for over 75% of the total deformations, which is not supported by the test data in this study (Figure 6.7).

Table 6.9: Results of Parametric Study on Stiffness

Cross-Section	f'_c (ksi)	M_p (k-ft)	I_{trans} / $I_{g,s}$	α	$(EI)_{eff}$ / $E_sI_{g,s}$			Eq. 6.4 / Eq. 6.3	Eq. 6.5 / Eq. 6.3	Eq. 6.5 / Eq. 6.4
					Eq. 6.5	Eq. 6.3	Eq. 6.4			
24.0 x 33.0 (c = 1.5) with W24x250	4	3561	1.33	1.75	0.12	0.13	0.14	1.11	0.97	0.87
				2.40	0.19	0.17	0.19	1.11	1.11	1.00
				3.33	0.28	0.24	0.26	1.11	1.18	1.06
				4.00	0.33	0.29	0.32	1.11	1.17	1.05
	8	3746	1.42	1.75	0.12	0.13	0.15	1.13	0.92	0.82
				2.40	0.19	0.18	0.20	1.13	1.05	0.93
				3.33	0.28	0.25	0.28	1.13	1.12	0.99
				4.00	0.33	0.30	0.34	1.13	1.11	0.98
21.0 x 30.0 (c = 1.5) with W21x182	4	2308	1.38	1.75	0.12	0.13	0.15	1.10	0.94	0.86
				2.40	0.19	0.18	0.20	1.10	1.07	0.98
				3.33	0.28	0.25	0.28	1.10	1.13	1.03
				4.00	0.34	0.30	0.33	1.10	1.12	1.02
	8	2435	1.49	1.75	0.12	0.14	0.16	1.12	0.89	0.80
				2.40	0.19	0.19	0.21	1.12	1.01	0.91
				3.33	0.28	0.27	0.30	1.12	1.07	0.96
				4.00	0.34	0.32	0.36	1.12	1.06	0.95
18.0 x 28.0 (c = 1.5) with W21x93	4	1143	1.54	1.75	0.16	0.14	0.16	1.15	1.11	0.96
				2.40	0.23	0.19	0.22	1.15	1.22	1.06
				3.33	0.33	0.27	0.31	1.15	1.23	1.07
				4.00	0.38	0.32	0.37	1.15	1.18	1.03
	8	1219	1.66	1.75	0.16	0.15	0.17	1.17	1.04	0.89
				2.40	0.23	0.20	0.24	1.17	1.14	0.97
				3.33	0.33	0.28	0.33	1.17	1.15	0.98
				4.00	0.38	0.34	0.40	1.17	1.11	0.95
20.0 x 27.0 (c = 1.5) with W18x175	4	1923	1.38	1.75	0.18	0.14	0.14	1.06	1.32	1.24
				2.40	0.26	0.19	0.20	1.06	1.41	1.33
				3.33	0.36	0.26	0.27	1.06	1.37	1.30
				4.00	0.41	0.31	0.33	1.06	1.30	1.23
	8	2035	1.48	1.75	0.18	0.14	0.16	1.08	1.25	1.15
				2.40	0.26	0.20	0.21	1.08	1.33	1.23
				3.33	0.36	0.27	0.30	1.08	1.30	1.20
				4.00	0.41	0.33	0.36	1.08	1.23	1.14

Table 6.9: Results of Parametric Study on Stiffness (Continued)

Cross-Section	f'_c (ksi)	M_p (k-ft)	I_{trans} / $I_{g,s}$	α	$(EI)_{eff}$ / $E_sI_{g,s}$			Eq. 6.4 / Eq. 6.3	Eq. 6.5 / Section	Eq. 6.5 / (ksi)
					Eq. 6.5	Eq. 6.3	Eq. 6.4			
16.0 x 26.0 (c = 1.5) with W18x71	4	780	1.68	1.75	0.26	0.16	0.18	1.12	1.66	1.48
				2.40	0.35	0.22	0.24	1.12	1.62	1.45
				3.33	0.43	0.30	0.33	1.12	1.45	1.29
				4.00	0.47	0.36	0.40	1.12	1.32	1.18
	8	839	1.83	1.75	0.26	0.17	0.19	1.14	1.54	1.35
				2.40	0.35	0.23	0.26	1.14	1.51	1.32
				3.33	0.43	0.32	0.37	1.14	1.35	1.19
				4.00	0.47	0.39	0.44	1.14	1.23	1.08
12.0 x 18.0 (c = 0.75) with W12x96 *	4	387	1.52	1.75	0.17	0.15	0.16	1.05	1.11	1.06
				2.40	0.25	0.21	0.22	1.05	1.20	1.15
				3.33	0.35	0.29	0.30	1.05	1.19	1.14
				4.00	0.40	0.35	0.37	1.05	1.14	1.09
	8	417	1.66	1.75	0.17	0.16	0.17	1.06	1.03	0.97
				2.40	0.25	0.23	0.24	1.06	1.11	1.05
				3.33	0.35	0.31	0.33	1.06	1.10	1.04
				4.00	0.40	0.38	0.40	1.06	1.05	0.99

* flanges trimmed to 5.5" width

Table 6.10: Statistical Summary of Results of Parametric Study on Stiffness

	$(EI)_{eff}$ / $E_sI_{g,s}$			Eq. 6.4 / Eq. 6.3	Eq. 6.5 / Eq. 6.3	Eq. 6.5 / Eq. 6.4
	Eq. 6.5	Eq. 6.3	Eq. 6.4			
Minimum	0.12	0.13	0.14	1.05	0.89	0.80
Maximum	0.47	0.39	0.44	1.17	1.66	1.48
Mean	0.29	0.24	0.26	1.11	1.19	1.08
Standard Deviation	0.10	0.08	0.08	0.04	0.17	0.16
Coefficient of Variation	0.35	0.32	0.32	0.03	0.14	0.15

7 Recommendations for Alternative Design

The recommendations provided in the previous chapter were prescriptive in nature, i.e. the type of recommendations that would be used in building codes, whereas the recommendations developed in this chapter are useful for alternative (non-prescriptive) design. In this chapter, it is assumed that alternative (non-prescriptive) analysis procedures are accomplished using both linear response spectrum analysis (e.g., for service level earthquake (SLE) and wind design, and design level earthquake (DE)) and nonlinear response history analysis (e.g., for maximum considered earthquake (MCE) level shaking), which is consistent with existing consensus documents for alternative design procedures for tall buildings, such as the Los Angeles Tall Buildings Structural Design Council document (LATBSDC, 2014), the Structural Engineers Association of Northern California (SEAONC) AB-083 Tall Buildings Task Group Recommended Administrative Bulletin for San Francisco (SEAONC AB-083, 2007), and the Pacific Earthquake Engineering Research (PEER) Center Tall Buildings Initiative (PEER TBI, 2010). The recommendations provided in this chapter are intended to be used in conjunction with these existing consensus documents.

In this chapter, the applicability of the code-based recommendations developed in Chapter 6 to alternative analysis is summarized (Section 7.1), and nonlinear load-displacement backbone models, which define the deformation capacity and address cyclic behavior, are fit to test data for

each of the four beams tested (Section 7.2). Three behavior categories are developed (Section 7.3), and recommendations regarding the wall demands are provided (Section 7.4).

7.1 APPLICABILITY OF CODE-BASED RECOMMENDATIONS

This section addresses the applicability of the code-based recommendations developed in Chapter 6 to alternative analysis procedures. Expected material properties, determined in accordance with Section 6.1, should be used for all calculations for alternative analysis, consistent with alternative analysis approaches presented in consensus documents (LATBSDC, 2014; SEAONC AB-083, 2007; and PEER TBI, 2010). Calculation of strength parameters (Section 6.2) that do not utilize expected material properties (e.g., M_p and $V@M_p$, M_n and $V@M_n$, and V_n) is unnecessary for alternative analysis where backbone relations are used (Section 7.2).

The recommendations of Section 6.3 are applicable, except that the expected compressive strength of concrete, f'_{ce}, shall be used in place of the specified compressive strength of concrete, f'_c, in Equation (6.6) to compute the embedment strength. Because the embedment strength is dependent on the compressive strength of concrete, a reliable estimate of the embedment strength depends on an accurate estimate of f'_{ce}; overestimating f'_{ce} corresponds to an overestimate of the embedment strength, which should be avoided in order to satisfy capacity design, i.e. to ensure $V_{n,embed} \geq V_{ne,limit}$. Therefore, f'_{ce} should be determined in accordance with Section 6.1.

The recommendation developed in Section 6.4.1 for providing wall longitudinal reinforcement across the embedment length satisfying $A_s f_{ye} \geq C_b$ need not be satisfied for alternative design, as

the ratio of the expected strength of reinforcement crossing the embedment length to the coupling beam back bearing force, $A_s f_{ye}$ / C_b, is instead used to categorize the level of wall boundary reinforcement provided. For alternative design, the recommendation in Section 6.4.2 to provide an OBE or SBE in the embedment region (extending at least one embedment length above and below the top and bottom flange, respectively, of the embedded steel section) for cases in which $\rho_{bound} \leq 400/f_y$ need not be satisfied. Other recommendations in Section 6.4.2 and recommendations in Section 6.4.3 are applicable for alternative analysis, noting that if auxiliary transfer bars and bearing plates are used, the use of any of the behavior categories developed in Section 7.3 for alternative analysis is no longer applicable, as these categories were developed for the tests in this study, which did not include transfer bars and bearing plates. Using the test results of Gong and Shahrooz (2001b), it was demonstrated in Section 6.2.1 that the use of transfer bars and bearing plates increase flexural strength. Using the test results of Gong and Shahrooz (2001b) to develop additional behavior categories for flexure-controlled beams requires accurately quantifying the increase in flexural strength due to transfer bars and bearing plates, which may not be appropriate, as these test specimens were shear-controlled.

Consistent with consensus design documents (LATBSDC, 2014; SEAONC AB-083, 2007; and PEER TBI, 2010), the determination of effective stiffness is based on expected material properties. For design-level and MCE-level alternative analysis, determining the effective stiffness in accordance with Section 6.5.2 is recommended, except that M_{pe} shall be used in place of M_p and I_{trans} shall be determined based on f'_{ce} rather than f'_c (which influences the calculation of the elastic modulus of concrete, E_c).

The LATBSDC (2014) document, which outlines a procedure for conducting alternative analysis, differentiates between reinforced concrete component stiffness values used for service- and wind-level analysis versus values used for MCE-level analysis. For reinforced concrete coupling beams, the effective bending stiffness for service- and wind-level analysis is defined as 1.5 times larger than that for MCE-level analysis ($0.3EI_{g,c}$ versus $0.2EI_{g,c}$). The use of a larger coupling beam effective stiffness value for service- and wind-level analysis requires greater member strengths to limit Demand-to-Capacity (D/C) ratios to acceptable values (typically 1.5). A similar approach is recommended here, i.e. use of a service-level effective stiffness value for SRC coupling beams that is 1.5 times the value used for MCE-level design.

7.2 NONLINEAR BACKBONE MODELING

The plots in Figure 7.1 show the load-displacement response, the corresponding first- and second-cycle backbone curves (from test data), and a backbone model for each of the four test beams. First- and second-cycle backbone curves were included as a means to assess cyclic degradation. The first-cycle backbone is indicative of peak responses, whereas the second-cycle backbone is more indicative of reliable strength conditions. The model backbones were based on curve-fitting to the second-cycle backbone relation. Specifically, in each (positive and negative) direction, the strength along the yield plateau was computed as the average value between 2% and 6% rotation, and the elastic stiffness was computed based on interpolating a displacement from the backbone curve at a load equal to two-thirds of the load associated with the yield plateau. Post-peak strength degradation was modeled to be linear after 6% rotation, and the final point on each backbone model corresponds to the final point on the second-cycle backbone curve

for each test. Note that a minor variation to this curve-fitting procedure was made for SRC3 in the positive loading direction. Due to the strength increase for SRC3 beyond 6% rotation in the positive loading direction, the strength along the yield plateau was computed as the average value between 2% and the final point on the second-cycle backbone curve. Note that alternative bilinear backbone curves could be developed to avoid modeling strength degradation.

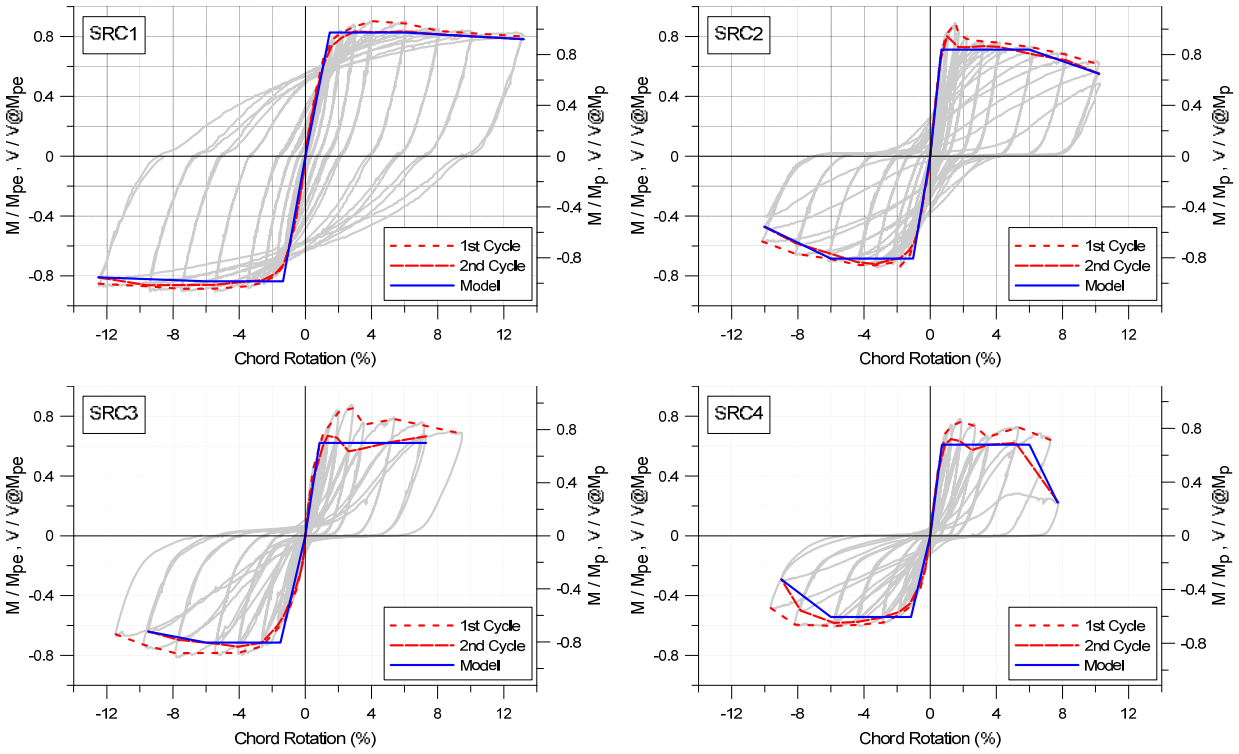

Figure 7.1. Backbone Modeling of Load-Displacement Response

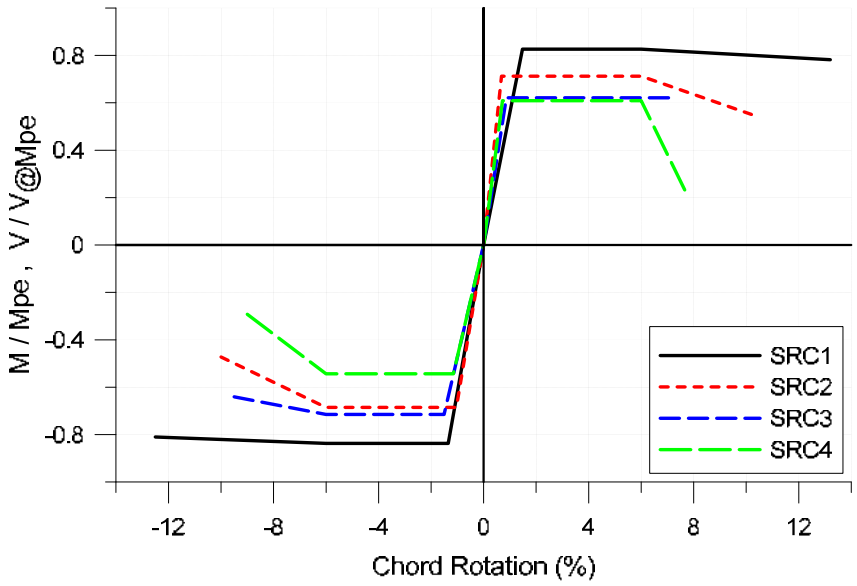

Figure 7.2. Comparison of Backbone Models for All Test Beams

Figure 7.2 shows the backbone models for all test beams, in order to highlight the differences in beam performance. Figure 7.3 illustrates five variables, namely A_1, A_2, B_1, C_1, and D_1, used to define the backbone models in Figure 7.1 and Figure 7.2. A_1 is the effective rotational stiffness, expressed as a fraction of M_{pe}/rad or $V@M_{pe}$/rad, when modeling a rigid beam span with rotational springs at the beam-wall interfaces (a concept discussed in Section 6.5.2, where the spring stiffness K represents the stiffness term A_1). Alternatively, A_2 is the equivalent effective bending stiffness, expressed as a fraction of $\alpha E_s I_{trans}$ (noting that α was 3.33 for SRC1, SRC2, and SRC4 and 2.4 for SRC3, where I_{trans} is based on E_c, computed using the as-tested compressive strength of concrete, $f'_{c,test}$), when using a lumped deformation approach in which all deformations are modeled as flexure within the beam span (i.e. when modeling a rigid shear stiffness with no rotational springs at the beam-wall interfaces). B_1 is the strength along the backbone yield plateau, expressed as a fraction of M_{pe} or $V@M_{pe}$ (with M_{pe} and $V@M_{pe}$ computed in accordance with Section 6.2.1). C_1 indicates the strength drop (also expressed as a

fraction M_{pe} or $V@M_{pe}$) occurring after a chord rotation of 0.06 radians, and D_1 (in radians) indicates the rotation beyond 0.06 radians over which this linear strength drop occurs.

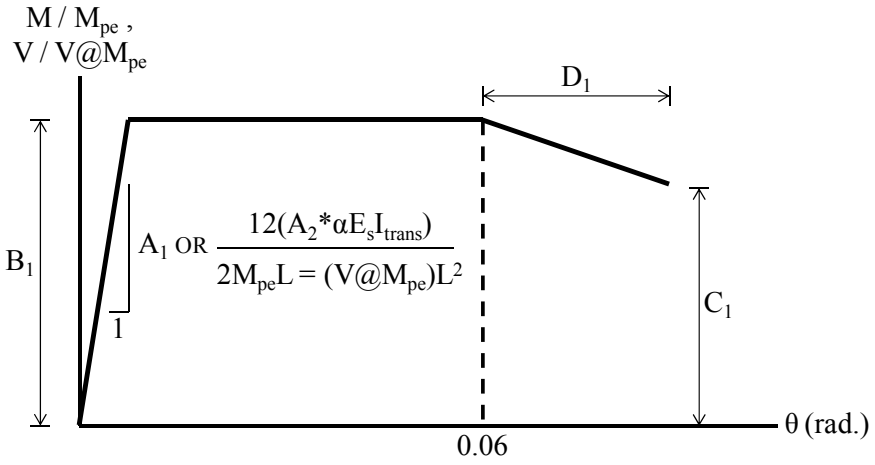

Figure 7.3*:* Parameters Used to Define Backbone Models

Table 7.1: Backbone Modeling Parameters for All Test Beams

Test Beam	Sign	A_1	A_2	B_1	C_1	D_1
SRC1	(+)	58	0.048	0.83	0.78	0.072
	(-)	63	0.053	0.84	0.81	0.065
SRC2	(+)	107	0.090	0.71	0.55	0.042
	(-)	66	0.055	0.69	0.47	0.040
SRC3	(+)	74	0.063	0.62	0.62	0.013
	(-)	47	0.040	0.71	0.64	0.035
SRC4	(+)	88	0.075	0.61	0.22	0.017
	(-)	47	0.040	0.54	0.29	0.030

Similar to the tables found in ASCE Standard 41-06 for conventional and diagonally-reinforced coupling beams, Table 7.1 summarizes the values of A_1, A_2, B_1, C_1, and D_1 for each of the backbone models shown in Figure 7.1 and Figure 7.2. Although the values of A_1, A_2, B_1, C_1, and

D_1 in Table 7.1 differ in the positive and negative loading directions due to asymmetry in the observed load-displacement responses, the backbone models used for alternative analysis may be based on average values (Figure 7.4 and Table 7.2). Specifically, values of A_1 = 75 and A_2 = 0.06 in Table 7.2, which were used to formulate the stiffness recommendations provided in Section 6.5.2, were based on the average of all values shown in Table 7.1, while the values for B_1, C_1, and D_1 in Table 7.2 were based on the average of the positive and negative values shown in Table 7.1 for each beam. Further discussion on the use of average values is provided in the following paragraph.

While stiffness parameters could be selected for the various behavior categories based on Table 7.1, stiffness values depend modestly on wall loading (Section 6.5.2). Because the wall demands will vary over the wall height at locations where coupling beams exist (due to structural geometry, spatial layout of lateral force resisting elements, etc.), the use of an average stiffness is recommended. Given that the load-displacement asymmetry was relatively modest (Figure 7.2 and Table 7.1) and that beam shear in full-length coupling beams (as opposed to one-half-length cantilever test beams) would be based on the average of the positive and negative moments that develop at each end of the beam (i.e. the inflection point is not at the center of the clear span if the magnitude of the member end moments differ), use of average values is recommended and should be used when modeling is performed with a shear force - displacement/rotation backbone (as opposed to a moment-rotation backbone).

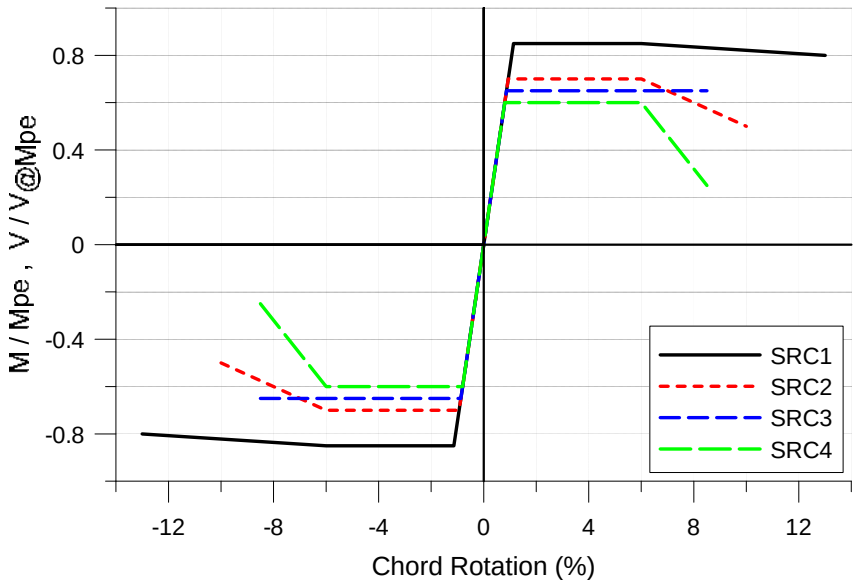

Figure 7.4: Backbone Models for Alternative Analysis

Table 7.2: Backbone Modeling Parameters for Alternative Analysis

Test Beam	A_1	A_2	B_1	C_1	D_1
SRC1	75	0.06	0.85	0.80	0.070
SRC2			0.70	0.50	0.040
SRC3			0.65	0.65	0.025
SRC4			0.60	0.25	0.025

Nonlinear modeling of buildings using alternative analysis is typically conducted with the assistance of computer software, such as CSI Perform 3D (2011). In Perform 3D, using shear-displacement hinges or moment-rotation hinges, which include the optional use of cyclic degradation energy factors (which range between zero and one, with larger values corresponding to broader hysteretic loops, i.e., less pinching) to specify the degree of pinching in the load-deformation relations, is appropriate for modeling the nonlinear response of coupling beams. For each test beam, the cyclic degradation energy factors provided in Table 7.3 and the backbone

parameters in Table 7.2 were used in Perform 3D (Figure 7.5) to produce the modeling results in Figure 7.6. To better match the shape of the hysteretic loops, the backbone models shown in Figure 7.4 were modified slightly in Perform 3D. Specifically, a trilinear rather than bilinear (elastic-perfectly-plastic) relationship was used in Perform 3D (Figure 7.5), consistent with the modeling approached used by Naish et al (2009). In this trilinear relationship, the yield strength was taken as 95% of the ultimate strength (DY/DU = 0.95 in Figure 7.5, with ultimate strength indicated by parameter B_1 in Table 7.2) and the rotation at which peak strength is reached was taken as 0.055 radians (DU = 0.055 in Figure 7.5). The cyclic degradation energy factors (Table 7.3 and Figure 7.5) were selected in order to achieve roughly equivalent energy dissipation (Figure 7.7 and Figure 7.8) between the model relations and the test beam relations over the range of rotations typically expected for coupling beams (i.e., up to about 6% chord rotation, as discussed in Section 4.5.2). Due to the limitations of the cyclic degradation modeling parameters in Perform 3D, accurate modeling of energy dissipation over this range of rotations led to an underestimate of energy dissipation at rotations beyond this range in certain instances (Figure 7.7 and Figure 7.8). In comparing the shear-displacement hinge (V-Hinge) versus moment-rotation hinge (M-Hinge) modeling results for each specific test beam (Figure 7.6), it is noted that use of the Unloading Stiffness Factor, which is available with a moment-rotation hinge but not with a shear-displacement hinge in Perform 3D, improves the shape of the hysteretic loops (Figure 7.6). Despite the difference in the shape of the hysteretic loops, the difference in energy dissipation between the M-Hinge model (Figure 7.7) and V-hinge model (Figure 7.8) is negligible.

Table 7.3: Perform 3D Cyclic Degradation Parameters for Alternative Analysis

Test Beam	Y	U	L	R	X	Unloading Stiffness Factor *
SRC1	0.40	0.40	0.40	0.40	0.40	1.0
SRC2	0.40	0.40	0.40	0.20	0.20	1.0
SRC3	0.20	0.20	0.20	0.20	0.20	1.0
SRC4	0.20	0.15	0.15	0.15	0.15	1.0

* available with moment-rotation hinge, unavailable with shear-displacement hinge

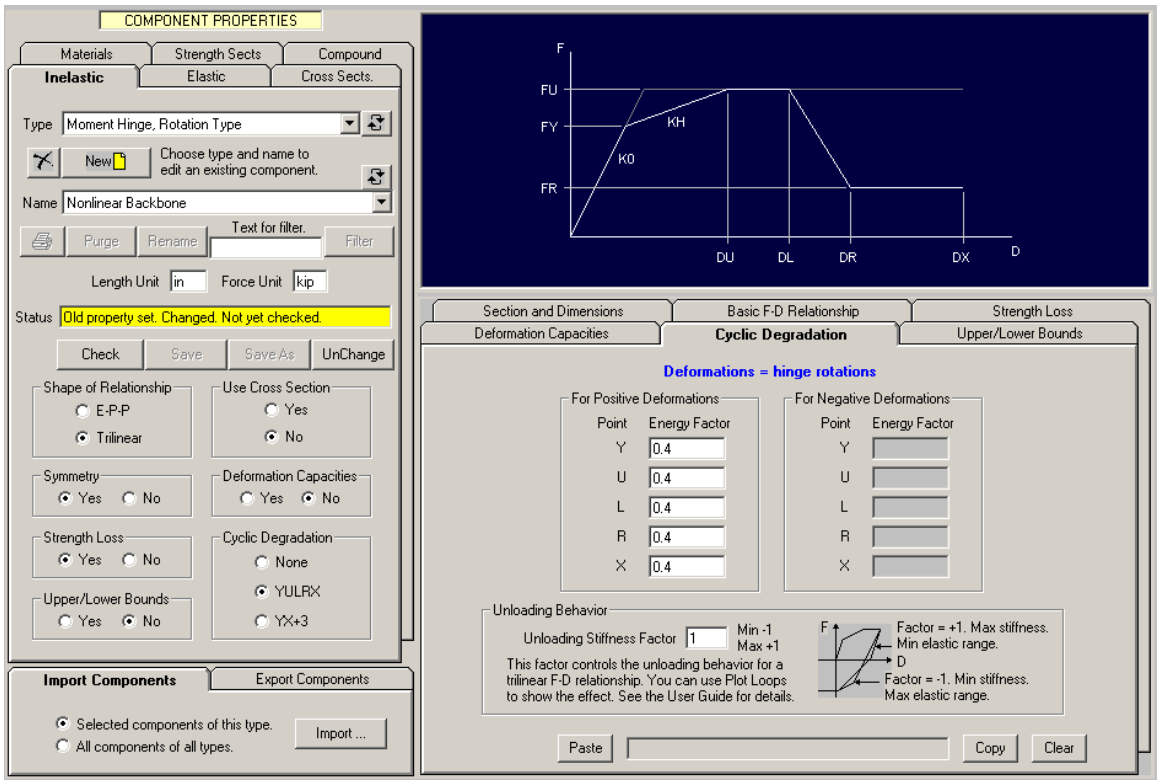

Figure 7.5: Screenshot of Perform3D Modeling Input (for SRC1)

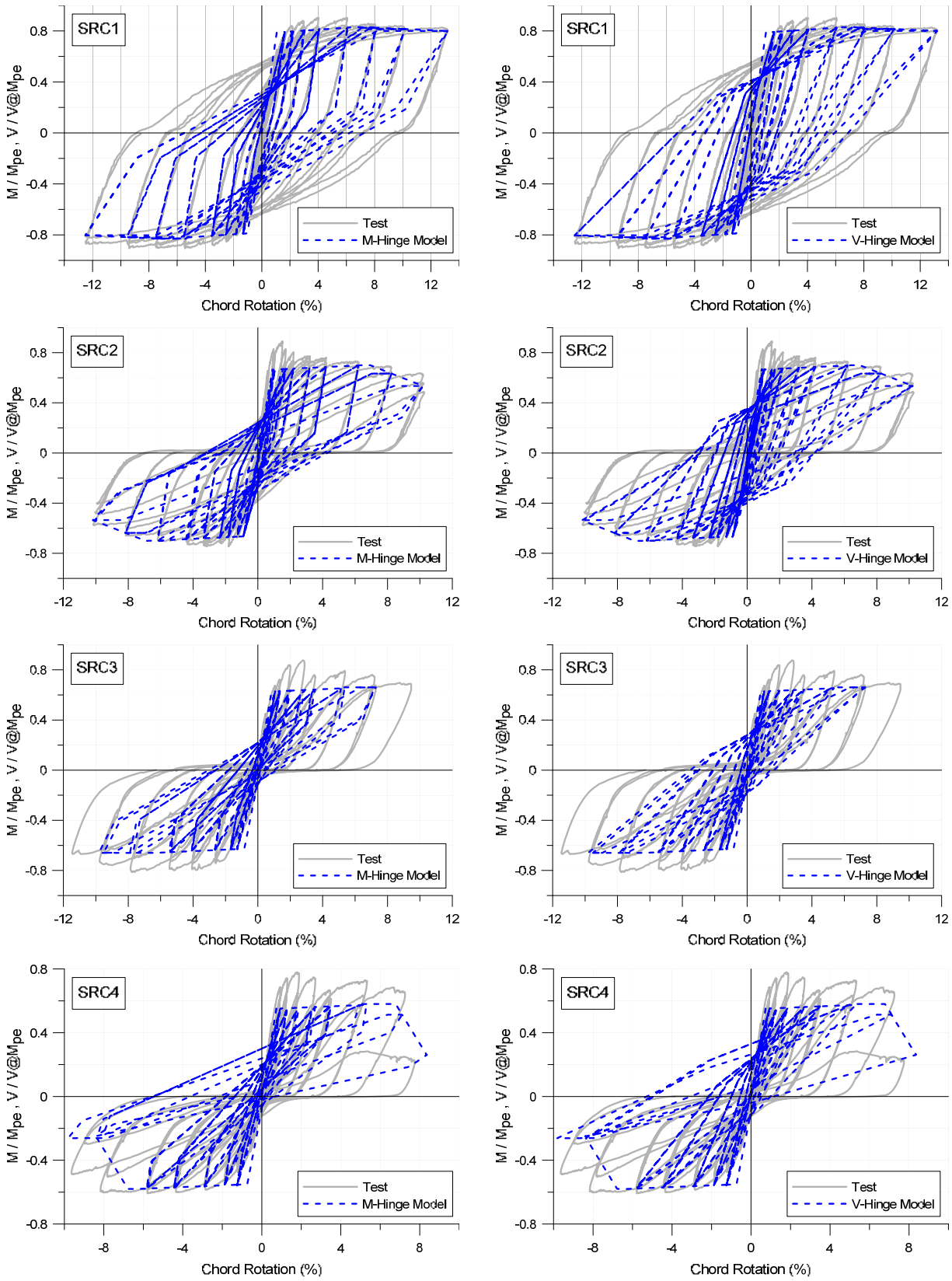

Figure 7.6: Perform 3D Modeling of Load-Displacement Response for Each Test Beam

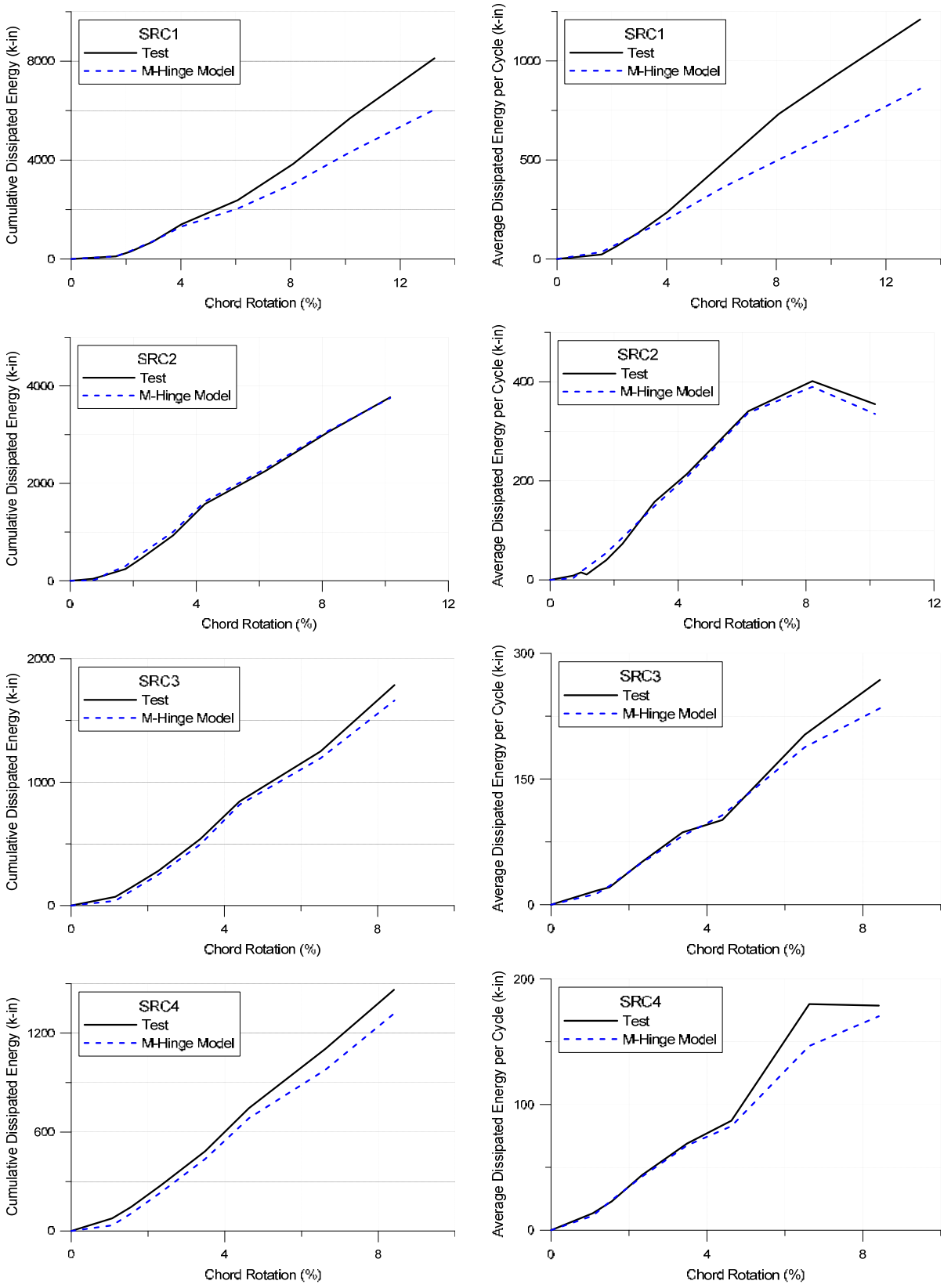

Figure 7.7: Dissipated Energy for Test Beams and Perform 3D M-Hinge Models

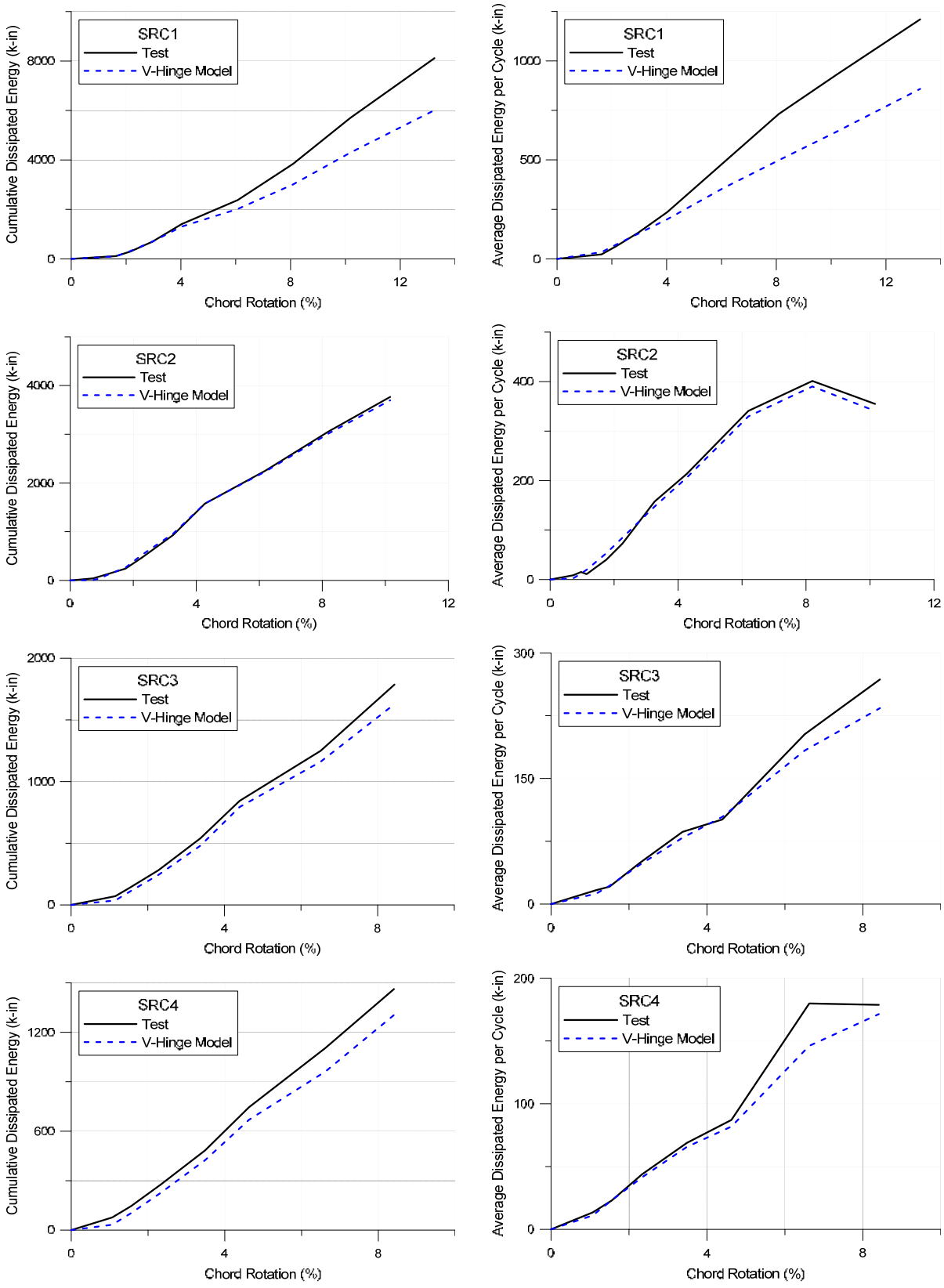

Figure 7.8: Dissipated Energy for Test Beams and Perform 3D V-Hinge Models

7.3 BEHAVIOR CATEGORIES

Table 7.4 provides a summary of some important test parameters for the four flexure-yielding beams, SRC1 to SRC4. All parameters in Table 7.4 were computed based on as-tested material properties with $V_{n,embed}$ and C_b computed based on the provided embedment length (and $V_{ne,limit}$ taken as $V@M_{pe}$ in the computation of C_b). $\varepsilon_{s,max}$ is the analytically-determined maximum tensile strain on the outermost wall boundary longitudinal reinforcement at the location of the coupling beam centerline. $\varepsilon_{s,max}$ was determined based on plane-section analysis of the structural wall section for the observed maximum applied wall demands during testing; the effect of the local coupling beam bearing forces was not considered in this analysis (i.e., the impact of the bearing forces on the plane section assumption is neglected). ε_y is the yield strain of the wall boundary longitudinal bars based on the as-tested material properties.

Table 7.4: Test Parameters Used to Determine Behavior Categories

Test Beam	$V@M_{pe}$ (kips)	$V_{n,embed}$ (kips)	C_b (kips)	$V_{n,embed}$ / $V@M_{pe}$	$A_s f_{ye}$ / C_b	Wall $\varepsilon_{s,max}$ / ε_y	Wall Bound. Trans. Reinf.
SRC1	184.5	189.2	340.3	1.03	1.49	0.41	OBE[1]
SRC2	184.5	119.1	435.6	0.65	1.40	0.70	OBE[1]
SRC3	245.2	146.5	457.6	0.60	0.62	1.06	OBE[1]
SRC4	174.8	105.2	457.2	0.60	0.26	0.50	Other[2]

1: satisfies ACI 318-11 Section 21.9.6.5 with $\rho_{bound} > 400/f_y$
2: satisfies ACI 318-11 Section 21.9.6.5 with $\rho_{bound} \leq 400/f_y$

In Table 7.4, normalized values are provided for embedment strength, strength of wall boundary longitudinal reinforcement crossing the embedment length, and wall demands. Specifically, $V_{n,embed}/V@M_{pe}$ is intended to assess the level of embedment provided, $A_s f_{ye}/C_b$ is intended to assess the quantity of wall reinforcement provided across the embedment length, and $\varepsilon_{s,max}/\varepsilon_y$ is

intended to assess the level of the applied maximum structural wall demands. The quantity of wall boundary transverse reinforcement provided is categorized as SBE, OBE, or Other. Referring to ACI 318-11, a special boundary element (SBE) satisfies Section 21.9.6.4, an ordinary boundary element (OBE) satisfies Section 21.9.6.5 with the longitudinal boundary reinforcement ratio greater than $400/f_y$, and conditions for no boundary element (Other) satisfy Section 21.9.6.5 with the longitudinal boundary reinforcement ratio less than or equal to $400/f_y$.

The test results reported in Table 7.4, along with nonlinear modeling recommendations developed in Section 7.2, were used to develop three behavior categories for SRC beams. These behavior categories, applicable for flexure-controlled SRC coupling beams with $2 \le (\alpha = L/h) \le 4$ and without face-bearing plates and auxiliary transfer bars, are summarized in Table 7.5 and as follows:

Category I:

- (A): Where sufficient wall longitudinal reinforcement across the embedment length exists ($A_s f_{ye}/C_b \geq 1.0$) and wall boundary transverse reinforcement is classified as either SBE (special boundary element, satisfying ACI 318-11 Section 21.9.6.4) or OBE (ordinary boundary element with 8" maximum vertical spacing of hoops and crossties, satisfying ACI 318-11 Section 21.9.6.5 with the longitudinal boundary reinforcement ratio, ρ_{bound}, greater than $400/f_y$), the maximum chord rotation for the mean value from the nonlinear response history analyses is 0.06. Minor cyclic degradation and pinching must be considered; specifically, modeling is based on SRC1 (Section 7.2) when $V_{n,embed} \geq V_{ne,limit}$ and SRC2 when $V_{n,embed} \geq 0.8 * V_{ne,limit}$.

- (B): Where sufficient wall longitudinal reinforcement across the embedment length exists ($A_s f_{ye}/C_b \geq 1.0$) and wall boundary transverse reinforcement is classified as "Other" (neither SBE nor OBE, satisfying ACI 318-11 Section 21.9.6.5 with $\rho_{bound} \leq 400/f_y$), the maximum chord rotation for the mean value from the nonlinear response history analyses is 0.03. Minor cyclic degradation and pinching must be considered; specifically, modeling is based on SRC1 (Section 7.2) when $V_{n,embed} \geq V_{ne,limit}$ and SRC2 (Section 7.2) when $V_{n,embed} \geq 0.8 * V_{ne,limit}$.

Category II:

- (A): Where modest wall longitudinal reinforcement across the embedment length exists ($0.5 \leq A_s f_{ye}/C_b < 1.0$) the maximum chord rotation for the mean value from the nonlinear response history analyses is 0.06, regardless of the classification of the wall boundary transverse reinforcement. For this case, strength is lower than for Category I and significant cyclic degradation and pinching must be considered; specifically, modeling is based on SRC3 (Section 7.2) when $V_{n,embed} \geq V_{ne,limit}$ and SRC4 (Section 7.2) when $V_{n,embed} \geq 0.8 * V_{ne,limit}$.
- (B): Where light wall longitudinal reinforcement across the embedment length exists ($A_s f_{ye}/C_b < 0.5$), the maximum chord rotation for the mean value from the nonlinear response history analyses is 0.03, regardless of the classification of the wall boundary transverse reinforcement. For this case, strength is lower than for Category I and modest cyclic degradation and pinching must be considered; specifically, modeling is based on SRC3 (Section 7.2) when $V_{n,embed} \geq V_{ne,limit}$ and SRC4 (Section 7.2) when $V_{n,embed} \geq 0.8 * V_{ne,limit}$.

Category III:

- Where light wall longitudinal reinforcement across the embedment length exists ($A_s f_{ye}/C_b < 0.5$), the maximum chord rotation for the mean value from the nonlinear response history analyses is 0.06, regardless of the classification of the wall boundary transverse reinforcement. For this case, strength is lower than for Category I and Category II and significant cyclic degradation and pinching must be considered; specifically, modeling is based on SRC4 (Section 7.2) when $V_{n,embed} \geq V_{ne,limit}$.

Table 7.5: Summary of Behavior Categories

Category		$A_s f_{ye} / C_b$	Wall Boundary Transverse Reinf.	Maximum Chord Rotation	% of $V_{ne,limit}$ used to Compute L_e	Modeling
I	A	≥ 1.0	SBE, OBE[1]	0.06	100%	SRC1
					80%	SRC2
	B		Other[2]	0.03	100%	SRC1
					80%	SRC2
II	A	≥ 0.5 & < 1.0	SBE, OBE[1], Other[2]	0.06	100%	SRC3
					80%	SRC4
	B	< 0.5		0.03	100%	SRC3
					80%	SRC4
III		< 0.5	SBE, OBE[1], Other[2]	0.06	100%	SRC4

1: satisfies ACI 318-11 Section 21.9.6.5 with $\rho_{bound} > 400/f_y$
2: satisfies ACI 318-11 Section 21.9.6.5 with $\rho_{bound} \leq 400/f_y$

The three categories describe SRC beams with robust force-deformation behavior with the highest strength and little-to-no cyclic degradation or pinching (Category I), lower strength and modest-to-significant cyclic degradation and pinching (Category II), and even lower strength with significant cyclic degradation and pinching (Category III). Appropriate modeling parameters for each category are described. Assignment of a particular SRC beam into one of

the three categories depends on the SRC coupling beam attributes (e.g. quantities of wall longitudinal and transverse boundary reinforcement and coupling beam chord rotation demands). The intent of the recommendations is to allow all SRC coupling beam behavior categories in a given building, provided that appropriate modeling parameters are used.

It is noted that the use of a ratio of $A_s f_y / C_b$ less than one is not allowed for code-based design (Equation (6.7)); however, a lower ratio is permitted for Category II and Category III for alternative design since the reduced strength and increased cyclic degradation relative to Category I are considered in the modeling parameters. Similarly, providing an embedment length that does not satisfy $V_{n,embed} \geq V_{ne,limit}$ is not permitted for code-based design (Section 6.3). For alternative design, the minimum required embedment length should be determined based on capacity design using the upper bound SRC beam strength, $V_{ne,limit}$ (in accordance with Section 6.3 and Section 7.1), unless the full embedment length may not be provided due to geometric constraints (use of a smaller steel section would eliminate this problem); however, in no case shall the embedment strength be less than $0.80 V_{ne,limit}$. If a reduced embedment length is used, lower strength and increased cyclic degradation and pinching shall be considered in the model, which is reflected in Table 7.5 and was summarized previously. Although the tests conducted in this study used reduced embedment lengths in some cases to test limiting conditions, the consistent use of a reduced embedment length represents poor practice, as reduced embedment strength leads to reduced performance, characterized by increased pinching and cyclic degradation. The use of a reduced length is not recommended but is permitted in order to address conditions where use of the full length is not practical due to configuration constraints.

It is noted that conditions for Category I (A) are most likely to exist for beams at low-to-mid levels of the building, while conditions for Category I (B) are most likely to exist for beams at low-to-mid level stories, and might exist at upper levels. Conditions for Category II (A) are most likely to exist at mid-to-upper level stories of a building, while conditions for Category II (B) and Category III are most likely to exist at upper level stories.

7.4 WALL DEMANDS

The modeling parameters for the behavior categories (Section 7.3) were developed with an understanding that local yielding above the wall base (plastic hinge) is likely to occur at a limited number of locations. This local yielding is likely due to higher mode impacts on wall moment and typically will occur at locations where moment strength changes due to cut-offs of wall boundary longitudinal reinforcement, significant changes in the quantity of wall longitudinal web reinforcement, or a reduction in wall cross section. To ensure "essentially elastic" behavior, the PEER/ATC 72-1 (2010) report recommends that yielding in the upper levels of the wall be limited to tensile strains that do not exceed twice the yield strain or plastic rotations that do not exceed 1.2 times the yield rotation. In accordance with this recommendation, it is recommended that the strain in the wall boundary longitudinal reinforcement, $\varepsilon_{s,bl}$, be limited to

$$\varepsilon_{s,bl} \leq 2\varepsilon_y \tag{7.1a}$$

or the plastic rotation, $\theta_{p,bl}$, be limited to

$$\theta_{p,bl} \leq 1.2\theta_{y,w} \tag{7.1b}$$

for at least 80% of all SRC coupling beams over the building height, where $\varepsilon_{s,bl}$ and $\theta_{p,bl}$ are computed as the mean of the maximum for the building model subjected to the requisite number of base acceleration histories, ε_y is the yield strain of wall boundary longitudinal reinforcement, and $\theta_{y,w}$ is the yield rotation of the wall. In satisfying Equation (7.1), wall strains exceeding $2\varepsilon_y$ or plastic rotations exceeding $1.2\theta_{y,w}$ would not occur for more than 20% of the coupling beams over the building height. Adopting different modeling parameters at locations where tension strains exceed $2\varepsilon_y$ or plastic rotations exceed $1.2\theta_{y,w}$ would not significantly change response results such as lateral story displacements, coupling beam chord rotations, and wall shears; therefore, a less complex modeling approach is adopted.

8 Conclusions

A testing program was undertaken to assess the performance of steel reinforced concrete (SRC) coupling beams embedded into reinforced concrete structural walls at large-scale and for realistic loading and boundary conditions. Moment and shear force were applied to the wall to generate stress/strain fields in the coupling beam embedment zones that were representative of conditions in actual structures; simultaneous reversed-cyclic loading was applied to the coupling beams, and the ratio of applied beam load to wall moment and shear force was constant for each test. Four tests were conducted on structural steel wide-flange sections to investigate the role of embedment length, coupling beam aspect ratio, wall demand, wall boundary longitudinal reinforcement, and wall boundary transverse reinforcement on SRC coupling beam strength, stiffness, energy dissipation, and ductility. The embedment models proposed by Marcakis and Mitchell (1980) and Mattock and Gaafar (1982) were used to compute the required embedment length needed to transfer bearing forces from the beam to the wall.

SRC1 was intended to represent a conservative design, with long embedment length and modest wall loading (reaching about one-half of the yield moment for the wall), whereas the embedment length for SRC2 was selected to be 75% of that used for SRC1 and the wall moment approached the yield moment. SRC3 examined the impact of beam aspect ratio by using a shorter span while the provided embedment capacity was intended to be consistent with SRC2. The embedment

length for SRC4 was the same as that of SRC2; however, lesser quantities of wall boundary longitudinal and transverse reinforcement were provided. Due to lower-than-expected concrete compressive strength for the second test specimen, the provided embedment length for SRC3 and SRC4 was determined to provide inadequate capacity based on both the Marcakis and Mitchell (1980) and Mattock and Gaafar (1982) embedment equations.

Excellent performance was observed for SRC1, with beam rotation capacity exceeding 12% with negligible strength loss and pinching. The reduced embedment length and increased structural wall demands led to lower strength and deformation capacity for SRC2 relative to SRC1, with more pinching observed in the load-deformation response. For both SRC1 and SRC2, damage concentrated at the beam-wall interface, while embedment damage was observed for SRC3 and SRC4, which led to more pinching and cyclic degradation in the load-deformation responses. The capacity of SRC4 was lower than the other three beams due to a significantly reduced quantity of wall boundary longitudinal reinforcement.

Based on the study, the following conclusions are reached:

1. The nominal plastic flexural strength, M_p, of SRC coupling beams may be computed using a plastic section analysis in which the plastic steel stress is taken as the minimum specified yield strength of structural steel, F_y, concrete in compression is modeled as a uniform magnitude (Whitney) stress block using the specified compressive strength of concrete, f'_c, and concrete tensile strength is neglected. The computation for the expected plastic flexural strength, M_{pe}, is the same as for M_p, except that the expected yield

strength of structural steel, $F_{ye} = R_y * F_y$, is used as the plastic stress. To account for a lack of fixity at the beam-wall interface, the nominal flexural strength, M_n, at the beam-wall interface is computed based on developing M_p at $L_e/3$ inside of the interface; therefore, $M_n = M_p * (L+2L_e/3)/L$.

2. Use of the Marcakis and Mitchell (1980) or Mattock and Gaafar (1982) embedment equations, modified to account for spalling as recommended by Harries et al (1993) and Harries et al (2000), leads to sufficient embedment lengths to achieve yielding of the embedded steel section. The embedment equation in the 2010 AISC Seismic Provisions, which is an extension of the Mattock and Gaafar (1982) embedment equation that includes an inherent strength reduction factor of 0.90, is recommended for design. For flexure-controlled SRC coupling beams, the expected shear force used to compute the minimum required embedment length may be determined based on developing the expected plastic flexural strength, M_{pe}, at the beam-wall interface.

3. Interface slip/extension, rather than shear and flexure deformations along the beam span, was responsible for the majority of the observed coupling beam deformations. Therefore, modeling the coupling beam span as rigid (infinite flexural and shear stiffness) with rotational springs at the beam-wall interfaces is recommended. A spring stiffness of $M_{pe}/(\theta_y=1.33\%)$, where θ_y is the chord rotation at yield, or $75M_{pe}$/radian appears appropriate and does not appear to be largely influenced by the test variables in this study (aspect ratio in particular). Rather than modeling rotational springs at the beam-wall interfaces, the spring stiffness may be converted into an equivalent flexure or shear

stiffness for a particular coupling beam, based on member cross-section and aspect ratio. Alternatively, the use of an effective bending stiffness of $0.06\alpha E_s I_{trans}$ is permitted, where α is the span-to-depth (aspect ratio), E_s is the modulus of elasticity of steel, and I_{trans} is the moment of inertia of the transformed section. (Section 6.5.2)

4. For SRC3 and SRC4, axial growth of the coupling beam was reduced relative to SRC1 and SRC2 by using a restraint system that applied a beam axial compressive load that did not exceed $\sim 0.02 A_g f'_c$. Because this level of axial restraint is assumed less than that provided by floor slabs and adjacent structural walls in actual structures, it is reasonable to conclude that significant outward ratcheting of the steel section is not a concern for SRC coupling beam used in actual structures.

5. The 2010 AISC Seismic Provisions recommend providing a quantity of wall longitudinal reinforcement crossing the embedment length with $A_s f_y$ not less than the limiting shear strength of the coupling beam, which is taken as the smaller of the expected shear strength and the shear corresponding to the expected plastic flexural strength. This recommendation was developed based on testing of shear-yielding SRC coupling beams. For flexure-yielding SRC coupling beams, providing a quantity of wall longitudinal reinforcement crossing the embedment length with $A_s f_y$ not less than the magnitude of the bearing force developed near the back of the embedded member is recommended. The AISC provision also requires two-thirds of $A_s f_y$ to be provided over the first one-half of the embedment length, which was determined to be unnecessary for flexure-yielding members. (Section 6.4.1)

6. The 2010 AISC Seismic Provisions require the use of auxiliary transfer bars attached to the flanges of the embedded steel section and the use of bearing plates provided at the embedded end of the steel section as well as at the beam-wall interface. The steel sections tested in this study did not include transfer bars and bearing plates, which complicate construction and increase cost. Acceptable performance of SRC coupling beams may be achieved without the use of face bearing plates and auxiliary transfer bars. Although face bearing plates and transfer bars could lead to improved performance for members such as SRC3 and SRC4, this improved performance also can be achieved by satisfying the recommendations for embedment capacity and vertical wall reinforcement across the embedment length. Therefore, the use of transfer bars and bearing plates is not required for flexure-controlled SRC coupling beams, which are able to develop shear loads of at least $V@M_n$ through 6% rotation without these added details.

7. Using Perform 3D computer software, simple nonlinear moment-hinge (M-Hinge) or shear-hinge (V-Hinge) models captured the load-deformation behavior of the test beams with reasonable accuracy. Modeling parameters are recommended that allow the energy dissipated for each test beam to be represented accurately. Because unloading modeling parameters are available in the computer software for the M-Hinge option but not for the V-Hinge option, the M-Hinge model provides a better match to test results in the unloading and reloading range, although the results obtained for the V-Hinge option are acceptable. If alternative nonlinear modeling platforms are used, the modeling parameters should be calibrated to the load-deformation responses of the test specimens to ensure adequate representation of observed behavior.

Appendix A – Material Properties

This appendix provides detailed information on material properties, serving as a supplement to Section 4.1, and is divided into sections for concrete (A.1), reinforcement (A.2), and structural steel (A.3).

A.1 CONCRETE

Table A.1, obtained directly from documentation provided by Catalina Pacific Concrete, shows the concrete mix design used for all three pours of both test specimens. The results of concrete cylinder compression tests, conducted at the UCLA material testing laboratory, are provided in Tables A.2 through A.5 and Figures A.1 through A.4 for all four specimens.

Table A.1: Concrete Mix Design (For All Pours)

MIX: 752EWP2S8 — 4500 psi @ 28 Days. 3/8" Gravel Pump/Place Mix. 8 Inches Slump.

GRADATIONS — with VULCAN , San Gabriel Valley (Reliance) Aggregates.

Aggregates	2"	1 1/2"	1"	3/4"	1/2"	3/8"	#4	#8	#16	#30	#50	#100	#200
W.C. SAND						100	96	81	62	41	18	6	2
3/8 AGGR					100	92	10	4	2	0	0	0	0
COMBINED	100	100	100	100	100	97	66	54	41	27	12	4	1

Materials	BATCH WEIGHTS 1 CU YD @ SSD		SPECIFIC GRAVITY			ABSOLUTE VOLUME
CEMENT - TYPE II	752 lbs	8.00 sacks	3.15	X	62.4	3.83
W.C. Sand	1839 lbs	65.1 %	2.66	X	62.4	11.08
3/8" G	984 lbs	34.9 %	2.65	X	62.4	5.95
WATER (MAXIMUM)	357.4 lbs	42.9 gals	1	X	62.4	5.73
WRDA 64	26.30 ozs					
GRACE ADVA SUP	30.10 ozs					
1.5% ENTRAPPED AIR			1.50%	X	27	0.41
TOTALS	3932.4 lbs					27.0

METHOD: California Building Code (CBC) Title 24 1905.3 - 2007 Edition

WATER/CEMENT RATIO: 5.4 gals/sack (0.48)

STRENGTH RESULTS: 4650 psi @ 7 Days, 6410 psi @ 28 Days with Laboratory Prepared Cylinders.

Table A.2: Concrete Cylinder Compression Test Results for SRC1

	Lower #1	Lower #2	Lower #3	Upper #1	Upper #2	Upper #3	Footing
$f'_{c,test}$ (ksi)	7.73	7.61	6.94	7.77	7.68	7.56	6.65
$\varepsilon_{0,test}$	0.0029	0.0030	0.0023	0.0032	0.0030	0.0030	0.0026

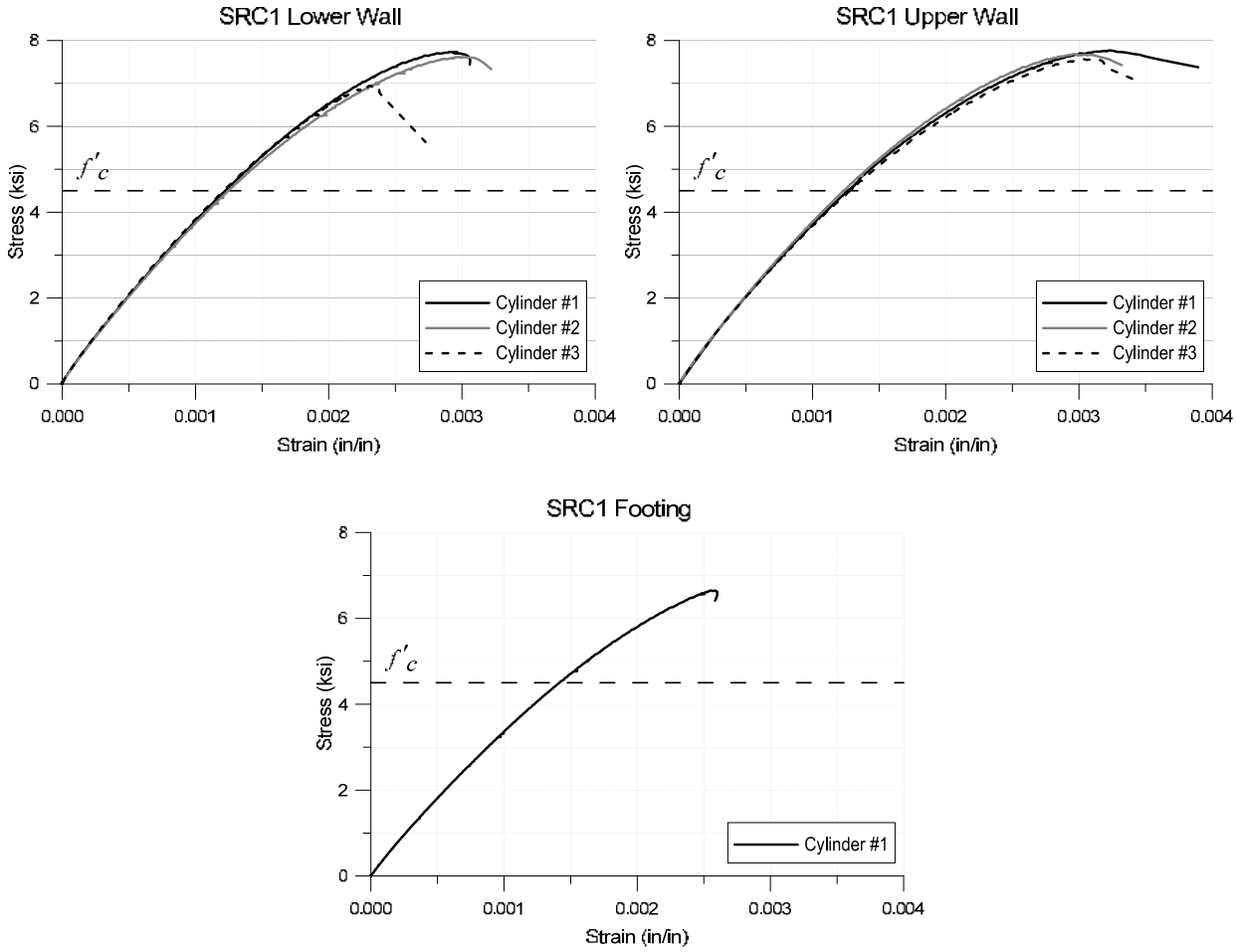

Figure A.1: Concrete Cylinder Compression Test Results for SRC1

Table A.3: Concrete Cylinder Compression Test Results for SRC2

	Lower #1	Lower #2	Lower #3	Upper #1	Upper #2	Upper #3	Footing
$f'_{c,test}$ (ksi)	7.69	7.17	N.A.	7.93	7.40	7.81	5.93
$\varepsilon_{0,test}$	0.0030	0.0027	N.A.	0.0032	0.0028	0.0032	0.0023

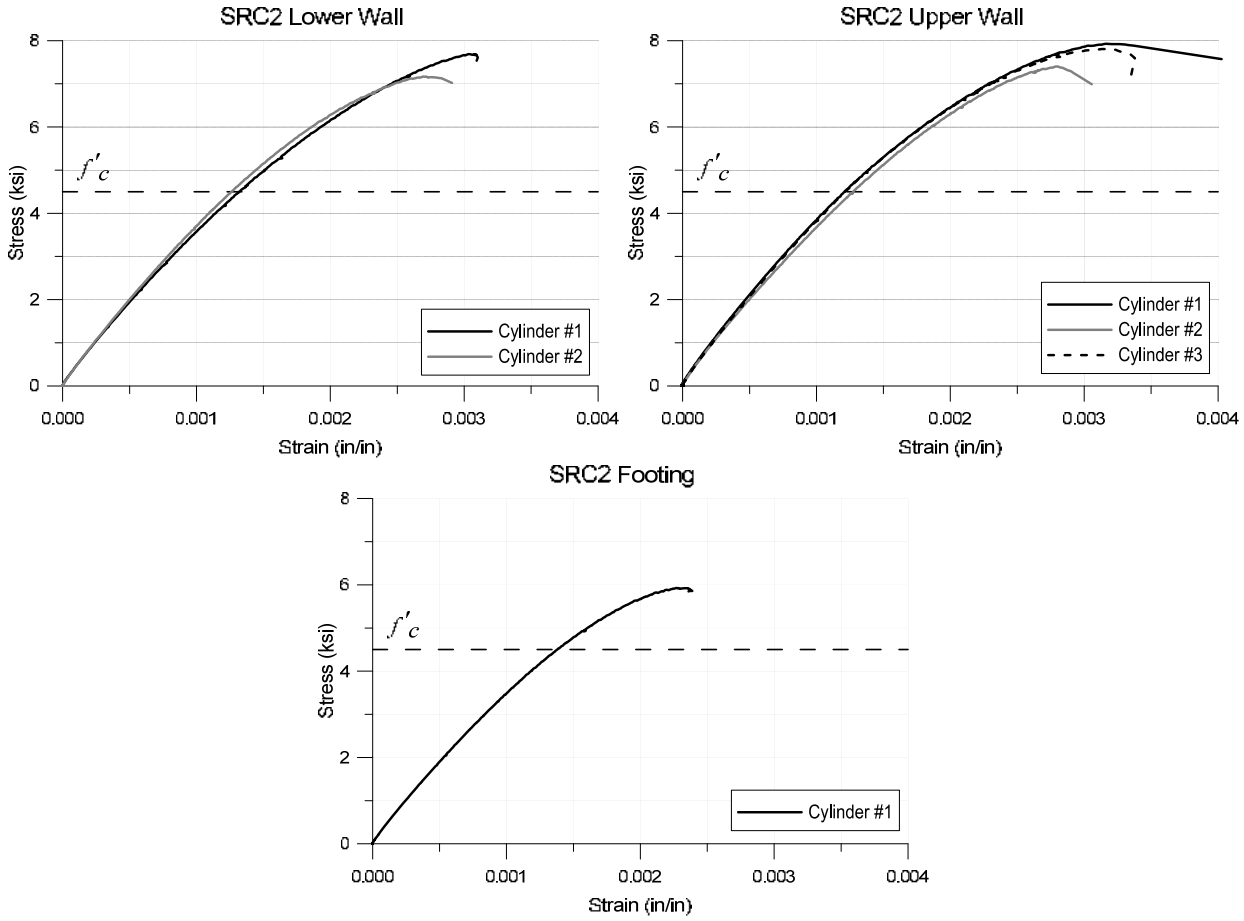

Figure A.2: Concrete Cylinder Compression Test Results for SRC2

Table A.4: Concrete Cylinder Compression Test Results for SRC3

	Lower #1	Lower #2	Lower #3	Upper #1	Upper #2	Upper #3	Footing
$f'_{c,test}$ (ksi)	4.9	5.2	5.0	4.7	4.6	4.2	5.2
$\varepsilon_{0,test}$	0.0021	0.0027	0.0022	0.0019	0.0020	0.0009	0.0013

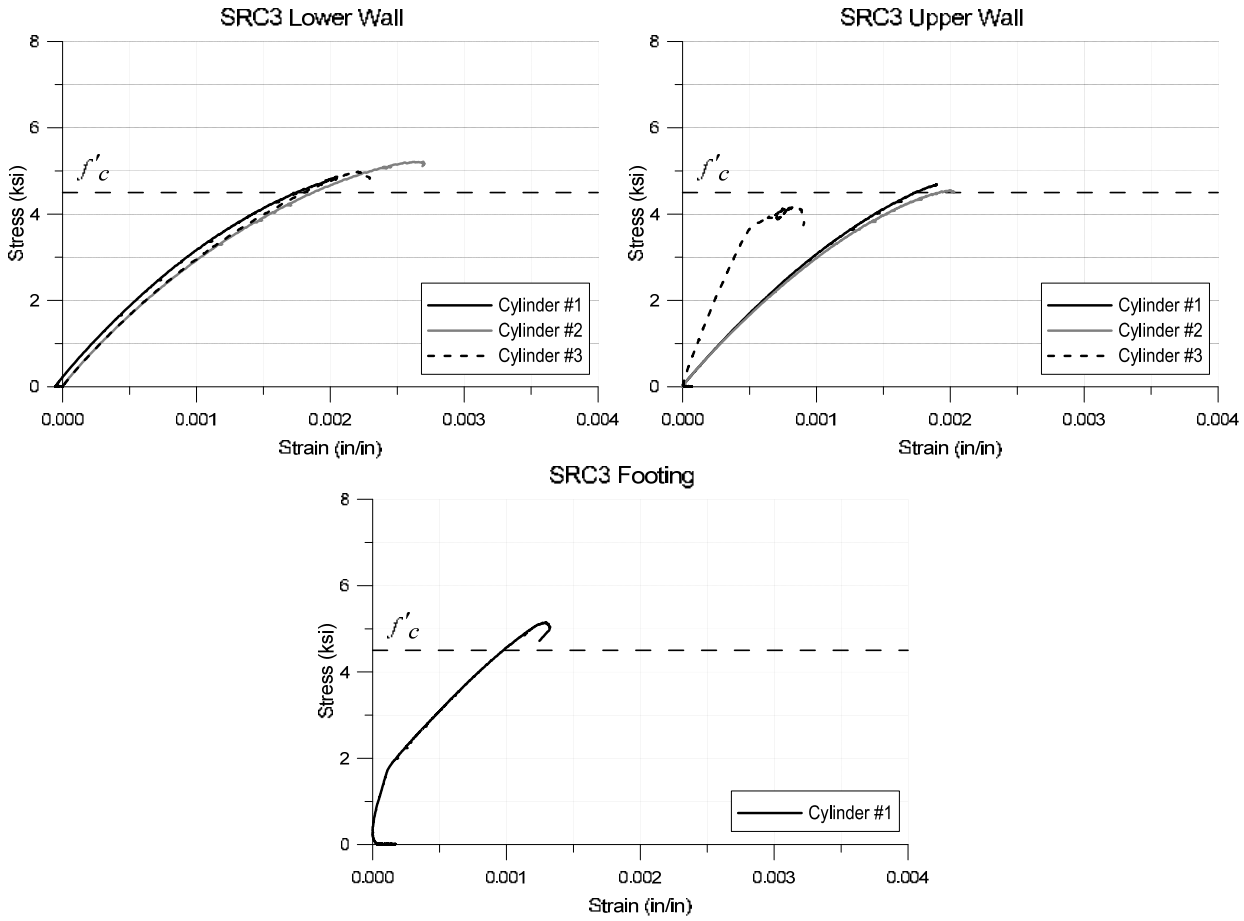

Figure A.3: Concrete Cylinder Compression Test Results for SRC3

Table A.5: Concrete Cylinder Compression Test Results for SRC4

	Footing	Lower #1	Lower #2	Lower #3	Upper #1	Upper #2	Upper #3
$f'_{c,test}$ (ksi)	6.2	5.1	4.2	4.5	5.6	5.4	5.2
$\varepsilon_{0,test}$	N.A.	N.A.	0.0015	0.0018	0.0028	0.0022	0.0024

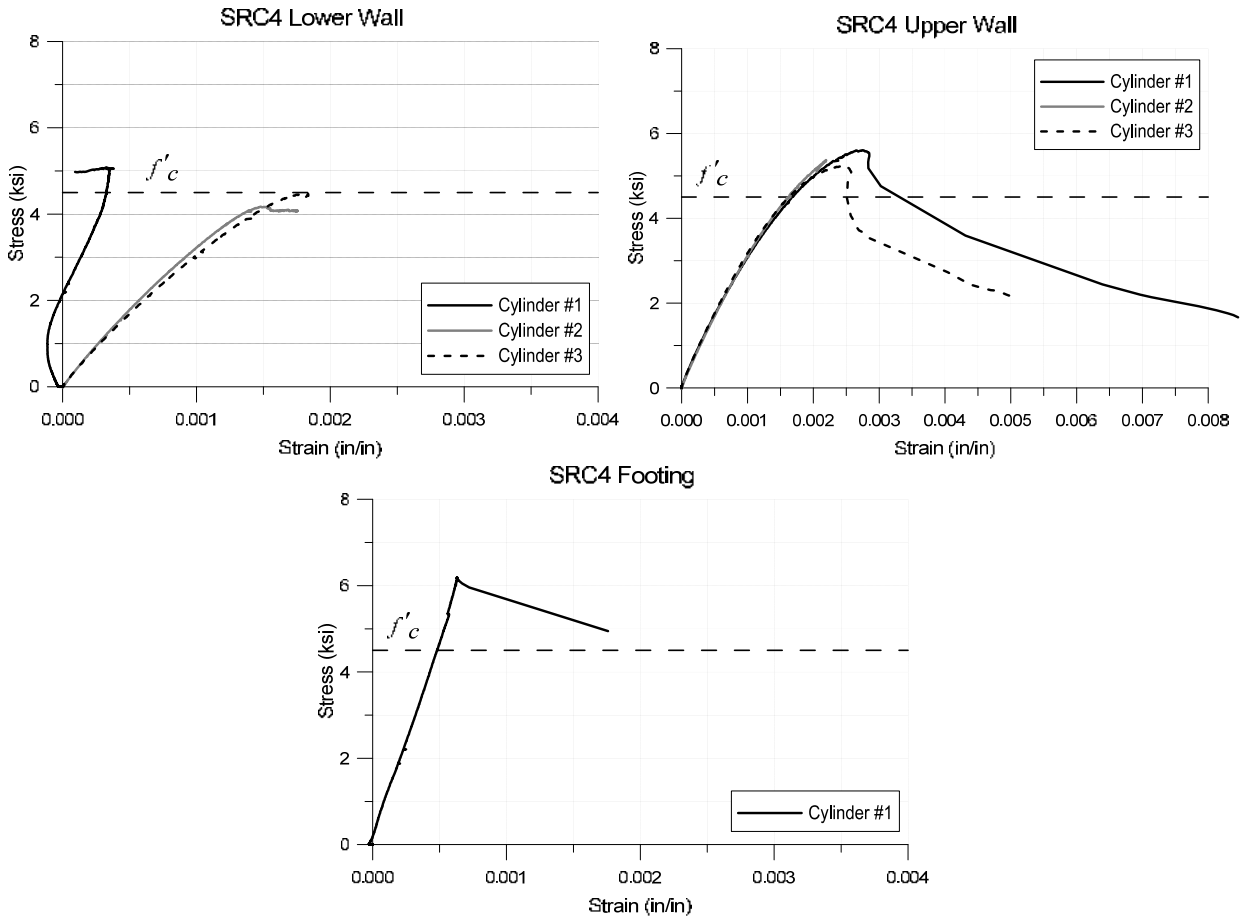

Figure A.4: Concrete Cylinder Compression Test Results for SRC4

*erroneous strain readings were recorded for the Footing and Lower #1 cylinder tests

A.2 STEEL REINFORCEMENT

The steel reinforcement tensile test results provided in Table A.6 for SRC1 and SRC2 were obtained from mill certificates provided by Gerdau Ameristeel (#9, #7, #6, and #4) and Nucor Steel Kingman LLC (#5 and #3), while those provided in Table A.7 for SRC3 and SRC4 were obtained from mill certificates provided by Gerdau Ameristeel (#9, #5, #4) and Cascade Steel Rolling Mills, Inc. (#3). The tensile test results provided for the undeformed rod used for hoops and cross-ties in all specimens (Table A.8 and Figure A.5), the threaded rod used for embedment detailing in SRC1 and SRC2 (Table A.8 and Figure A.5), and all threaded rods considered for use in embedment detailing of SRC3 (Figure A.6), were based on tests conducted at the UCLA materials testing laboratory.

Table A.6: Steel Reinforcement Tensile Test Results for SRC1 and SRC2

	#9	#7	#6	#5	#4	#3
$f_{y,test}$ (ksi)	74.5	71.0	77.5	68.7	72.0	63.9
$f_{u,test}$ (ksi)	98.5	95.5	104.0	104.4	109.0	102.5
% elong.	17	19	14	15	13	14

Table A.7: Steel Reinforcement Tensile Test Results for SRC3 and SRC4

	#9	#5	#4	#3
$f_{y,test}$ (ksi)	70.0	61.8	72.0	68.0
$f_{u,test}$ (ksi)	95.0	83.6	107.1	105.0
% elong.	13	19	15	14

Table A.8: Steel Reinforcement Tensile Test Results

	A36 1/4"-Dia. Smooth Rod			A307 gr. A 5/16"-Dia. Thrd. Rod		
	#1	#2	#3	#1	#2	#3
$f_{y,test}$ (ksi)	50.5	51.3	50.8	91.6	88.0	85.1
$f_{u,test}$ (ksi)	70.4	73.8	72.8	108.4	107.3	104.5
% elong.	19.3	21.3	22.0	2.0	2.2	1.5

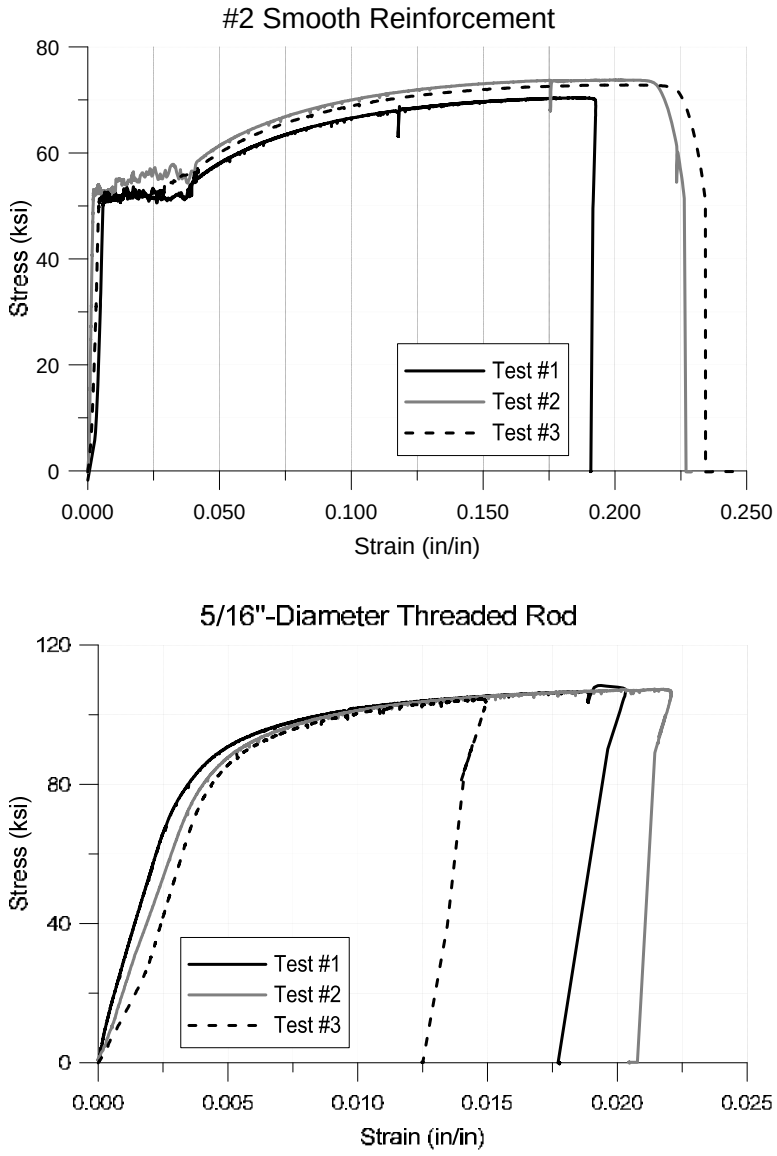

Figure A.5: Steel Reinforcement Tensile Test Results for SRC1 and SRC2

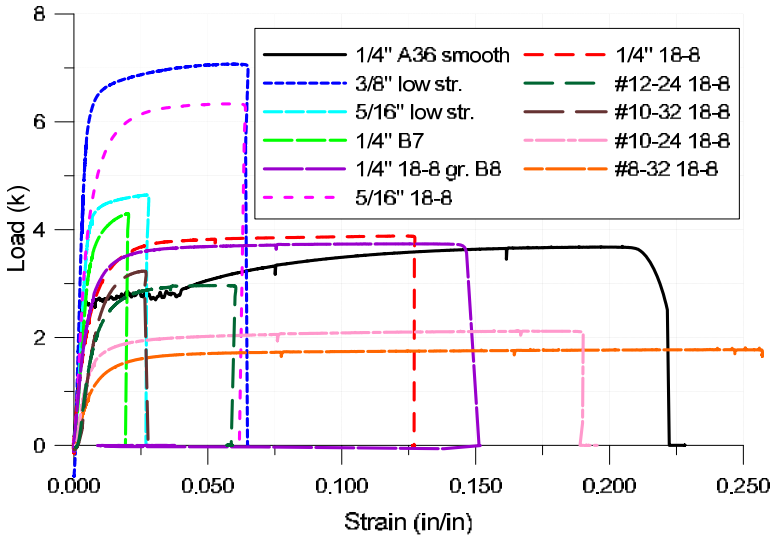

Figure A.6: Steel Reinforcement Tensile Test Results for SRC3

A.3 STRUCTURAL STEEL

Structural steel coupon tensile testing was carried out by Twining Laboratories, and the results provided in Table A.9 and Figure A.7 were obtained directly from the test report provided by Twining. It is noted that no load-strain plot was provided for Flange, Test #1.

Table A.9: Steel Coupon Tensile Test Results

	Flange			Web		
	#1	#2	#3	#1	#2	#3
$F_{y,test}$ (ksi)	62.0	51.3	51.3	62.0	63.9	55.5
$F_{u,test}$ (ksi)	84.5	75.7	76.5	80.2	81.8	76.6
% elong.	26.25	27.50	23.75	22.50	17.50	23.75

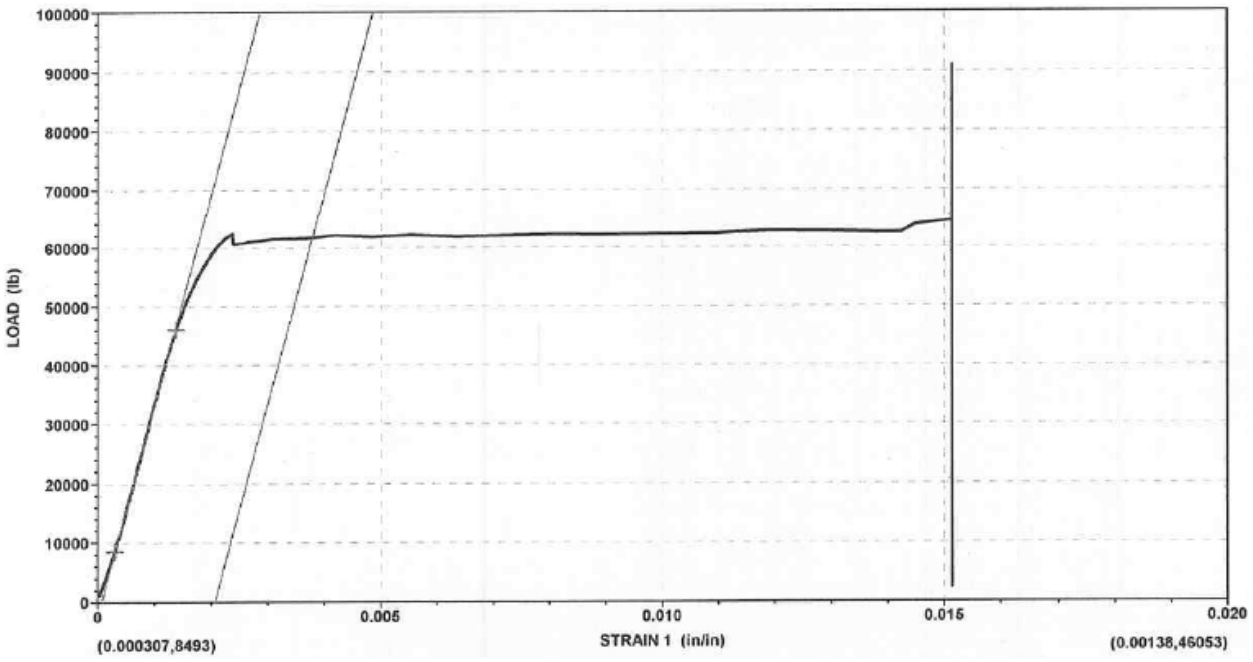

Figure A.7: Steel Coupon Tensile Test Results: a) Flange, Test #2

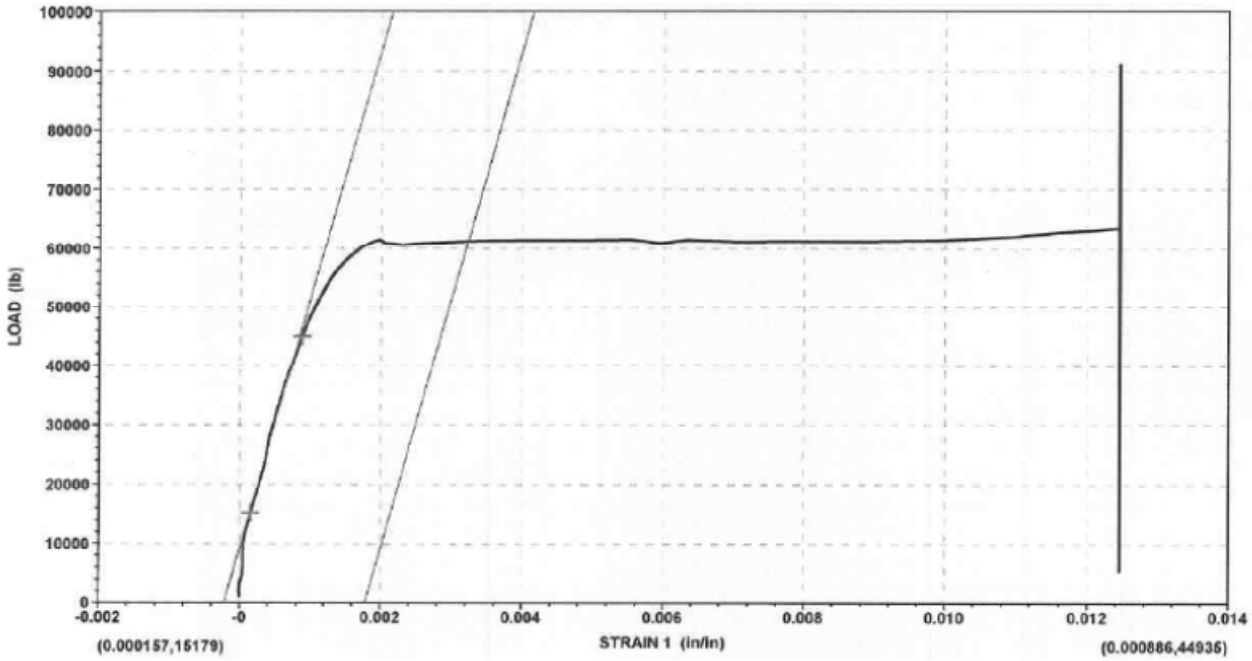

Figure A.7: Steel Coupon Tensile Test Results: a) Flange, Test #3

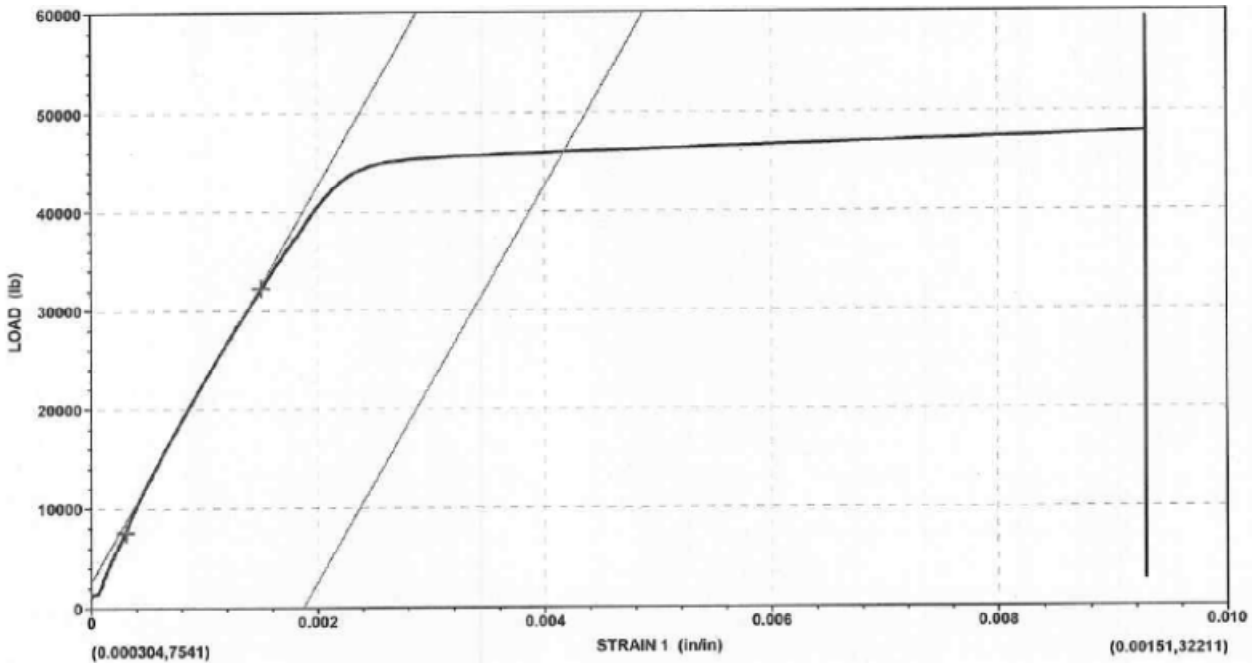

Figure A.7: Steel Coupon Tensile Test Results: a) Web, Test #1

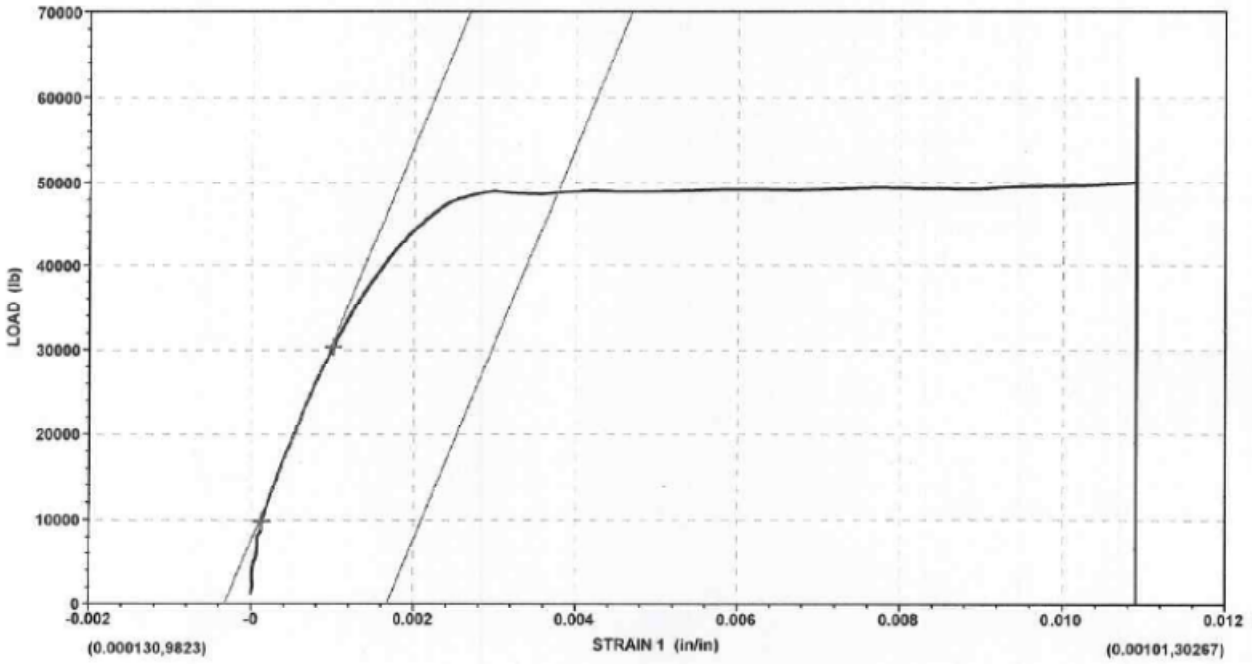

Figure A.7: Steel Coupon Tensile Test Results: a) Web, Test #2

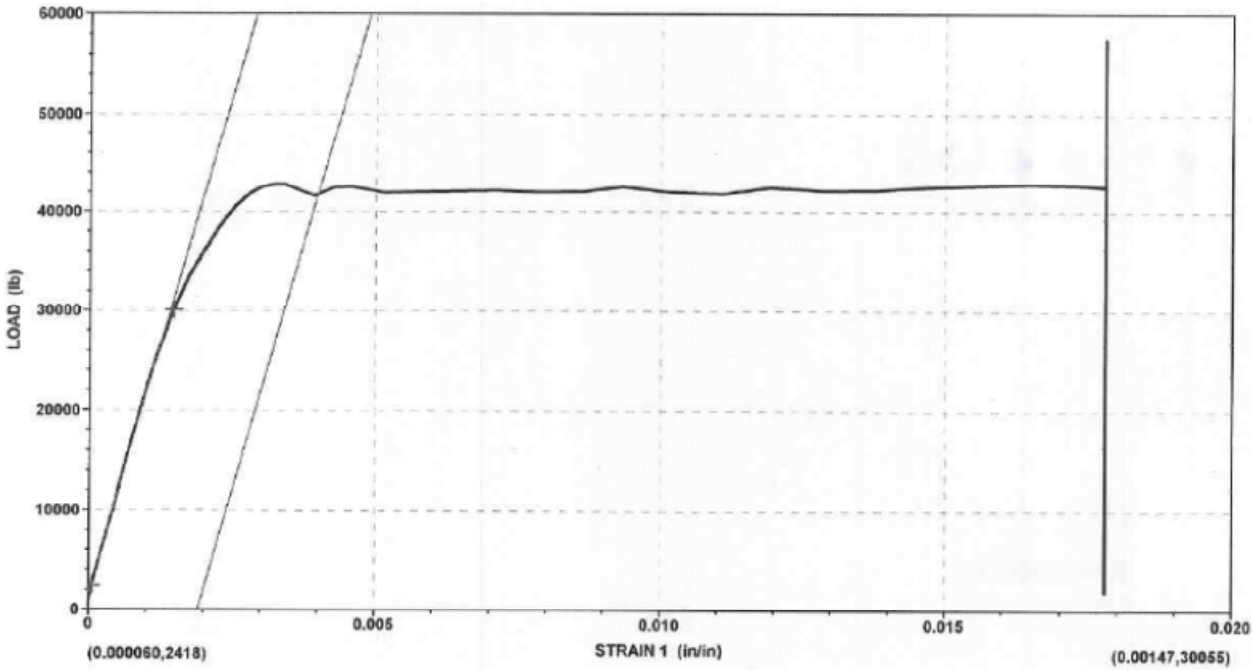

Figure A.7: Steel Coupon Tensile Test Results: a) Web, Test #3

Appendix B – Sample Computation for Flexural Strength

Plastic section analysis is recommended to compute the nominal plastic flexural strength, M_p, of an SRC coupling beam. Sample calculations for a 24"x36" SRC coupling beam containing an embedded W24x250 illustrate the computation of M_p. 6-ksi specified compressive strength of concrete (f'_c) and 50-ksi specified minimum yield strength of structural steel (F_y) was assumed for this example.

For plastic section analysis, the plastic steel stress is taken as the specified minimum yield strength of structural steel, F_y, and concrete in compression is modeled with a uniform magnitude (Whitney) stress block (consistent with the stress and force diagram shown in Figure B.1). In practice, iteration must be used to determine the neutral axis depth, x, to satisfy internal force equilibrium, and for the case of this example, the neutral axis depth was determined through iteration (not shown). In the computations provided, equilibrium of internal forces is checked, and the moment strength of the section is computed.

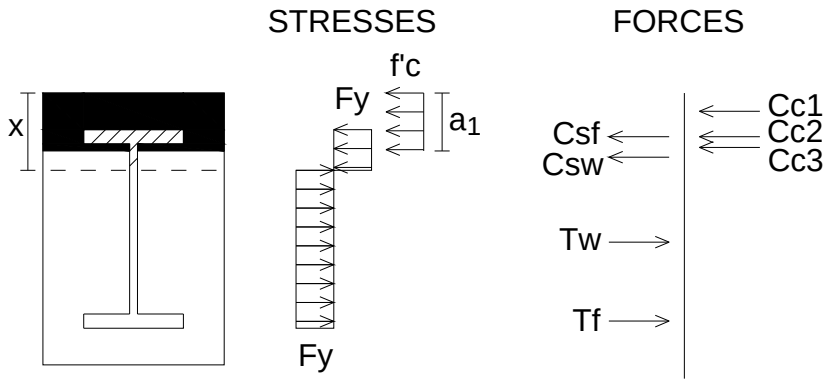

Figure B.1: Stresses and Forces on Cross-Section for Plastic Analysis

$x = 10.24$

$a_1 = \beta_1 x = (0.75)(10.24") = 7.68"$

$T_f = A_f F_y = (13.2")(1.89")(50.0^{ksi}) = 1247^k$

$T_w = (h - \text{cover} - t_f - x)t_w F_y = (36" - 4.85" - 1.89" - 10.24")(1.04")(50.0^{ksi}) = 989^k$

$\sum T = 2236^k$

$Cs_f = T_f = 1247^k$

$Cs_w = (x - t_f - \text{cover})t_w F_y = (10.24" - 1.89" - 4.85")(1.04")(50.0^{ksi}) = 182^k$

$Cc_1 = 0.85 f_c^{'}(\text{cover})b_c = 0.85(6^{ksi})(4.85")(24") = 594^k$

$Cc_2 = 0.85 f_c^{'} t_f (b_c - b_f) = 0.85(6^{ksi})(1.89")(24" - 13.2") = 104^k$

$Cc_3 = 0.85 f_c^{'}(a_1 - t_f - \text{cover})(b_c - t_w) = 0.85(6^{ksi})(7.68" - 1.89" - 4.85")(24" - 1.04") = 110^k$

$\sum C = 2237^k$

$\sum T = \sum C \rightarrow$ OK, EQUILIBRIUM

Summing moments about the neutral axis determines the nominal plastic flexural strength as:

$$M_{T_f} = T_f * \left(h - \text{cover} - \frac{t_f}{2} - x \right) = 1247^k * \left(36" - 4.85" - \frac{1.89"}{2} - 10.24" \right) = 24896^{k-in}$$

$$M_{T_w} = T_w * \frac{(h - \text{cover} - t_f - x)}{2} = 989^k * \frac{(36" - 4.85" - 1.89" - 10.24")}{2} = 9405^{k-in}$$

$$M_{Cs_f} = Cs_f * \left(x - \text{cover} - \frac{t_f}{2} \right) = 1247^k * \left(10.24" - 4.85" - \frac{1.89"}{2} \right) = 5543^{k-in}$$

$$M_{Cs_w} = Cs_w * \frac{(x - \text{cover} - t_f)}{2} = 182^k * \frac{(10.24" - 4.85" - 1.89")}{2} = 319^{k-in}$$

$$M_{Cc_1} = Cc_1 * \left(x - \frac{\text{cover}}{2} \right) = 594^k * \left(10.24" - \frac{4.85"}{2} \right) = 4642^{k-in}$$

$$M_{Cc_2} = Cc_2 * \left(x - \text{cover} - \frac{t_f}{2} \right) = 104^k * \left(10.24" - 4.85" - \frac{1.89"}{2} \right) = 462^{k-in}$$

$$M_{Cc_3} = Cc_3 * \left(x - a_1 + \frac{(a_1 - \text{cover} - t_f)}{2} \right) = 110^k * \left(10.24" - 7.68" + \frac{(7.68" - 4.85" - 1.89")}{2} \right) = 333^{k-in}$$

$$M_p = \sum M = 45600^{k-in} = 3800^{k-ft}$$

It is noted that for this particular beam cross-section (which is the prototype for the specimens tested in this study) plane-strain moment-curvature analysis without inclusion of strain hardening of steel was found to produce a similar result for computing M_p. To use a moment-curvature approach, material stress-strain relationships for concrete and steel are needed. In this example, the stress-strain relationship for concrete in compression (Figure B.2) was based on Hognestad et al (1955), and the stress-strain relationship for steel (Figure B.3) was bilinear, as strain hardening was not considered. Plane-strain moment-curvature analysis was conducted by treating the steel section as reinforcement and dividing the steel section (flanges and web) and concrete compression zone into fibers. M_p was selected as the peak moment on the moment-curvature plot. It is evident from the results of the moment-curvature analysis (Figure B.4) that M_p is nearly equivalent to the value computing using plastic analysis (within 1%) for the cross-sections in this study.

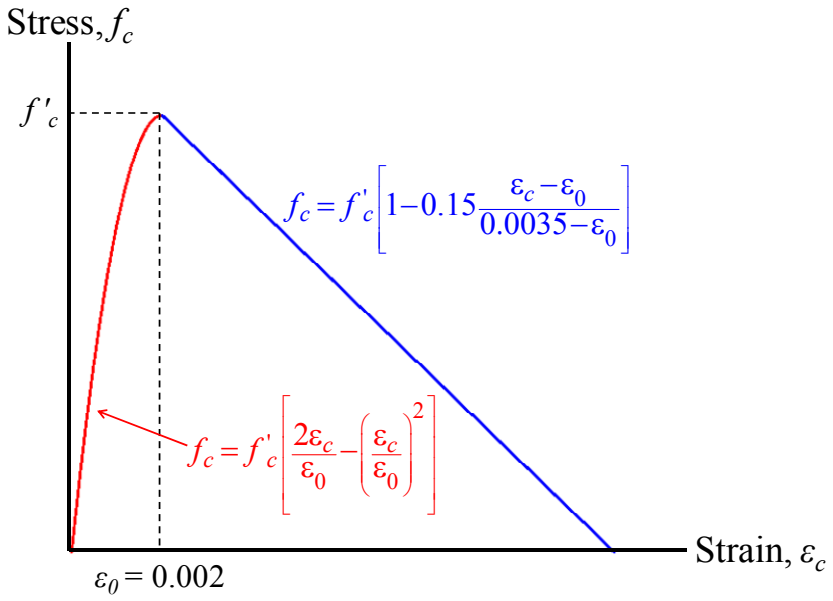

Figure B.2: Stress-Strain Relationship for Concrete in Compression (Hognestad et al, 1955)

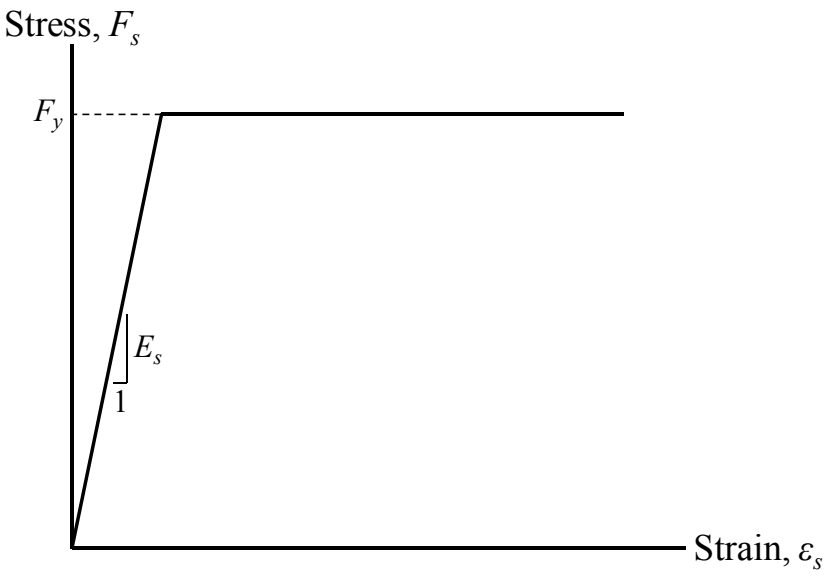

Figure B.3: Stress-Strain Relationship for Structural Steel in Tension & Compression

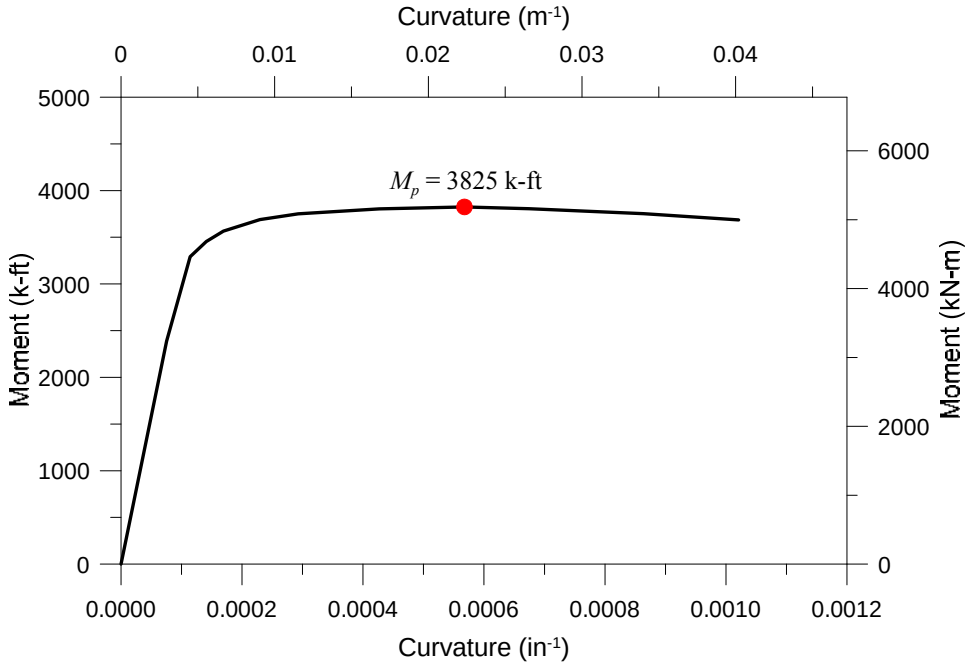

Figure B.4: Results of Plane-Strain Moment-Curvature Analysis

REFERENCES

1. ACI Committee 318. (1977). Building Code Requirements for Reinforced Concrete (ACI 318-77) and Commentary, American Concrete Institute, Detroit, MI.
2. ACI Committee 318. (2008). Building Code Requirements for Structural Concrete (ACI 318-08) and Commentary, American Concrete Institute, Farmington Hills, MI.
3. ACI Committee 318. (2011). Building Code Requirements for Structural Concrete (ACI 318-11) and Commentary, American Concrete Institute, Farmington Hills, MI.
4. AISC. (2005). Steel Construction Manual, 13th edition. American Institute of Steel Construction, Inc., Chicago, IL.
5. AISC. (2005). Seismic Provisions for Structural Steel Buildings. ANSI/AISC 341-05, American Institute of Steel Construction, Chicago, IL.
6. AISC. (2010). Seismic Provisions for Structural Steel Buildings. ANSI/AISC 341-10, American Institute of Steel Construction, Chicago, IL.
7. ASCE Task Committee on Design Criteria for Composite Structures in Steel and Concrete. (1994). Guidelines for Design of Joints between Steel Beams and Reinforced Concrete Columns. *Journal of Structural Engineering*, ASCE. 120:8, 2330-2357.
8. ASCE. (2007). ASCE/SEI Standard 41-06, Seismic Rehabilitation of Existing Buildings. American Society of Civil Engineers, Reston, VA.
9. ASTM International. (2007). Standard Test Methods and Definitions for Mechanical Testing of Steel Products. ASTM A370-07a. ASTM International, West Conshohocken, PA.
10. Collins, M. and Mitchell, D. (1991). *Prestressed Concrete Structures*, Prentice-Hall, Englewood Cliffs, NJ.

11. Computers and Structures, Inc (CSI). (2011). Perform 3D, Nonlinear Analysis and Performance Assessment for 3D Structures User Guide, Version 5. Computers and Structures, Inc., Berkeley, CA.
12. CRSI. (2008). CRSI Design Handbook, 10th Edition. Concrete Reinforcing Steel Institute, Schaumburg, IL.
13. Deierlein, G.G. (1988). Design of Moment Connections for Composite Framed Structures. *PhD Dissertation*, University of Texas at Austin.
14. Deierlein, G.G., Sheikh, T.M., Yura, J.A., and Jirsa, J.O. (1989). Beam-Column Moment Connections for Composite Frames: Part 2." *Journal of Structural Engineering*. 115:11, 2877-2896.
15. El-Tawil, S., Harries, K.A., Fortney, P.J., Shahrooz, B.M., and Kurama, Y. (2010). Seismic Design of Hybrid Coupled Wall Systems: State of the Art. *Journal of Structural Engineering*. 136:7, 755-769.
16. FEMA. (2000). Prestandard and Commentary for the Seismic Rehabilitation of Buildings (FEMA-356). Federal Emergency Management Agency, Washington D.C., 518 pp.
17. Fortney, P.J., Shahrooz, B.M., and Rassati. (2007). Large-Scale Testing of a Replaceable "Fuse" Steel Coupling Beam. *Journal of Structural Engineering*. 133:12, 1801-1807.
18. Gong, B. and Shahrooz, B.M. (1998). Seismic Behavior and Design of Composite Coupled Wall Systems," *Rep. No. UC-CII 98/01*, Cincinnati Infrastructure Institute, Cincinnati.
19. Gong, B. and Shahrooz, B.M. (2001a). Concrete-Steel Composite Coupling Beams. I: Component Testing. *Journal of Structural Engineering*. 127:6, 625-631.

20. Gong, B. and Shahrooz, B.M. (2001b). Concrete-Steel Composite Coupling Beams. II: Subassembly Testing and Design Verification. *Journal of Structural Engineering*. 127:6, 632-638.

21. Gong, B. and Shahrooz, B.M. (2001c). Steel-Concrete Composite Coupling Beams – Behavior and Design. *Engineering Structures*. 23(11), 1480-1490.

22. Harries, K.A. (1995). Seismic Design and Retrofit of Coupled Walls Using Structural Steel. *PhD thesis*, Department of Civil Engineering, McGill University, Montreal, Que.

23. Harries, K.A. (1998). Ductility and Deformability of Coupling Beams in Reinforced Concrete Coupled Walls. *Proceedings of the Eighth Canadian Conference on Earthquake Engineering*, Vancouver. 475-481.

24. Harries, K.A. (2001). Ductility and Deformability of Coupling Beams in Reinforced Concrete Coupled Walls. *Earthquake Spectra*. 17:3, 457-478.

25. Harries, K.A., Gong, B. and Shahrooz, B.M. (2000). Behavior and Design of Reinforced Concrete, Steel, and Steel-Concrete Coupling Beams. *Earthquake Spectra*. 16:4, 775-798.

26. Harries, K.A., Mitchell, D., Cook, W.D., and Redwood, R.G. (1993). "Seismic Response of Steel Beams Coupling Concrete Walls." *Journal of Structural Engineering*. 119(12), 3611-3629.

27. Harries, K.A., Mitchell, D., Redwood, R.G., Cook, W.D., (1997). "Seismic Design of Coupled Walls – A Case for Mixed Construction." *Canadian Journal of Civil Engineering*. 24, 448-459.

28. Hawkins, N.M. (1970). The Bearing Strength of Concrete for Strip Loadings. *Magazine of Concrete Research* (London). 22:71, 87-98.

29. Hognestad, E., Hanson, N.W. and McHenry, D. (1955). "Concrete Stress Distribution in Ultimate Strength Design." *ACI Journal Proceedings*. 52:12, 455-479.

30. Kriz, L.B., and Raths, C.H. (1963). Connections in Precast Concrete Structures – Bearing Strength of Column Heads. *Precast Concrete Institute (PCI) Journal*. 8:6, 45-75.

31. LATBSDC. (2014). An Alternative Procedure for Seismic Analysis and Design of Tall Buildings Located in the Los Angeles Region. Los Angeles Tall Buildings Structural Design Council, Los Angeles.

32. Lehmkuhl, E. (2002). "Renaissance – A Composite Coupled Shear Wall System." *Proceedings, 2002 SEAOC Convention*, Structural Engineering Association of California, San Francisco.

33. Liu, J., Sabelli, R., Brockenbrough, R.L. and Fraser, T.P. Expected Yield Stress and Tensile Strength Ratios for Determination of Expected Member Capacity in the 2005 AISC Seismic Provisions. *AISC Engineering Journal*. First Quarter, 15-25.

34. Marcakis, K. (1979). Precast Concrete Connections with Embedded Steel Members. *Master of Engineering thesis*, Department of Civil Engineering, McGill University, Montreal, Que.

35. Marcakis, K. and Mitchell, D. (1980). Precast Concrete Connections with Embedded Steel Members. *Precast Concrete Institute (PCI) Journal*. 25:4, 88-116.

36. Massone, L.M. and Wallace, J.W. (2004). Load-Deformation Responses of Slender Reinforced Concrete Walls. *ACI Structural Journal*. 101:1, 103-113.

37. Mattock, A.H. and Gaafar, G.H. (1982). Strength of Embedded Steel Sections as Brackets. *ACI Journal*. 79:9, 83-93.

38. Moehle, J.P., Ghodsi, T., Hooper, J.D., Fields, D.C., and Gedhada, R. (2011). Seismic Design of Cast-in-Place Concrete Special Structural Walls and Coupling Beams: A Guide for Practicing Engineers. *NEHRP Seismic Design Technical Brief No. 6*, produced by the NEHRP Consultants Joint Venture, a partnership of the Applied Technology Council and the Consortium of Universities for Research in Earthquake Engineering, for the National Institute of Standards and Technology, Gaithersburg, MD, NIST GCR 11-917-11REV-1.
39. Naish, D., Fry, A., Klemencic, R., Wallace, J. (2013a). Reinforced Concrete Coupling Beams – Part I: Testing. *ACI Structural Journal*. 110:6, 1057-1066.
40. Naish, D., Fry, A., Klemencic, R., Wallace, J. (2013b). Reinforced Concrete Coupling Beams – Part II: Modeling. *ACI Structural Journal*. 110:6, 1067-1075.
41. Naish, D., Wallace, J.W., Fry, J.A. and Klemencic, R. (2009). Reinforced Concrete Link Beams: Alternative Details for Improved Construction. *UCLA – SGEL Report 2009/06*.
42. Nowak, A.S., Szerszen, M.M., Szeliga, E.K., Szwed, A., and Podhorecki, P.J. (2008). Reliability-Based Calibration for Structural Concrete, Phase 3. SN2849, Portland Cement Association, Stokie, IL.
43. Paulay, T. (1986). "The Design of Ductile Reinforced Concrete Structural Walls for Earthquake Resistance." *Earthquake Spectra*, EERI. 2:4, 783-823.
44. PEER Tall Buildings Initiative (TBI). (2010). Guidelines for Performance-Based Seismic Design of Tall Buildings. PEER Report 2010/05, Pacific Earthquake Engineering Research Center (PEER), University of California, Berkeley.
45. PEER/ATC-72-1. (2010). Modeling and Acceptance Criteria for Seismic Design and Analysis of Tall Buildings. Pacific Earthquake Engineering Research Center (PEER) and Applied Technology Council (ATC) Joint Task Force.

46. Qin, F. (1993). Analysis of Composite Connection Between Reinforced Concrete Walls and Steel Coupling Beams. *MS thesis*, University of Cincinnati.

47. SEAONC AB-083. (2007). Recommended Administrative Bulletin on the Seismic Design and Review of Tall Buildings Using Non-Prescriptive Procedures. Structural Engineers Association of Northern California (SEAONC) AB-083 Tall Buildings Task Group, San Francisco.

48. Shahrooz, B.M., Remetter, M.E. and Qin, F. (1993). Seismic Design and Performance of Composite Coupled Walls. *Journal of Structural Engineering*. 119:11, 3291-3309.

49. Sheikh, T.M. (1987). Moment Connections between Steel Beams and Concrete Columns. *PhD Dissertation*, University of Texas at Austin.

50. Sheikh, T.M., Deierlein, G.G., Yura, J.A., and Jirsa, J.O. (1989). Beam-Column Moment Connections for Composite Frames: Part 1. *Journal of Structural Engineering*, ASCE. 115:11, 2858-2876.

51. Wallace, J.W. (1992). BIAX: Revision 1-Computer program for the analysis of reinforced concrete and reinforced masonry sections. *Rep. No. CU/CEE-92/4, Structural Engineering, Mechanics, and Materials, Clarkson University, Potsdam, N.Y.*

52. Wee, T.H., Chin, M.S., and Mansur, M.A. (1996). Stress-Strain Relationship of High-Strength Concrete in Compression," Journal of Materials in Civil Engineering. 8:2, 70-76.

53. Williams, A. (1979). The Bearing Capacity of Concrete Loaded Over a Limited Area. *Technical Report No. 526, Cement and Concrete Association, London*. 70 pp.